

**ÉCOLE DOCTORALE DES SCIENCES CHIMIQUES**

**UMR 7515 - ICPEES**

**Institut de Chimie et Procédés pour l'Énergie, l'Environnement et la Santé**

# THÈSE

présentée par

**Yeuk Ting LAW**

soutenue le : **04 Juillet 2013**

pour obtenir le grade de

**Docteur de l'université de Strasbourg**

Discipline / Spécialité : Chimie

**Investigation of Reaction Networks and  
Active Sites in Ethanol Steam Reforming  
Reaction over Ni and Co-Based Catalysts**

**THÈSE dirigée par :**

**[Mme SAVINOVA Elena]**

Professeur, Université de Strasbourg

**RAPPORTEURS :**

**[M. HENRY Claude R.]**

Directeur de Recherche, CiNaM, Marseille

**[M. MACHOCKI Andrzej]**

Professeur, University of Maria Curie-Skłodowska, Lublin

---

**MEMBRES DU JURY :**

**[M. DRILLON Marc]**

Directeur de Recherche, IPCMS, Strasbourg

**[M. PICCOLO Laurent]**

Chargé de Recherche, IRCELYON, Lyon

**[M. ZAFEIRATOS Spiros]**

Chargé de Recherche, ICPEES, Strasbourg

**[Mme SAVINOVA Elena]**

Professeur, Université de Strasbourg

# Acknowledgements

I would like to express my gratitude to many people who have supported me during my thesis.

I would like to thank Prof. Elena Savinova for her help and guidance since my master studies in 2007. I am truly grateful for the opportunities that she has given to me. I would like to express my gratitude to Dr. Spiros Zafeiratos for his supervision and assistance during my PhD studies. I am very grateful for his patience and advice from technical detail about experiments to surface science discussions.

Part of the work in this thesis was accomplished in collaboration with other laboratories. I would like to thank the people at Elettra, especially Dr. Tomas Skala, Dr. Luca Gregoratti, Dr. Matteo Amati and Mr. Martin Vondracek, who have dedicated a lot of time and effort during the beamtime, and for the data analysis afterwards. I would like to thank the staff from Bessy, Dr. Michael Hävecker, Dr. Rosa Arrigo and Dr. Detre Teschner for being very supportive and generous in sharing their time for discussion and offering technical support.

I would like to thank Prof. Andrzej Machocki for his warm welcome and assistance to his laboratory in Lublin and having accepted to be the member of the jury for this thesis defense. The co-workers in the chemical technology department in Lublin were very friendly and helpful and I appreciate their assistance during my stay in Lublin.

I would like to thank the member of the surface science group in ICPEES. Dr. Vasiliki Papaefthimiou, Dr. Roland Barbosa and Dr. Maria Sánchez have shared their experience and knowledge generously with me. I am very thankful to Dr. Won-hui Doh, from whom I have learnt very much, for being very supportive. Thank you also to the fellow PhD students in the group, Mr. Wen Luo and Miss Sylwia Turczyniak for being a good company. I appreciate very much the help and company of the past and current members of the electrochemistry group. I would like to thank Dr. Sergey Pronkin for having supervised my work during my Master studies and being a very kind advisor all along my PhD studies.

I would also like to thank the staff of the technical and administrative department in the laboratory, without whom I would not be able to finish this work. I would like to thank Dr. Thierry Dintzer who has helped in the SEM, TEM and XRD experiments. I am truly thankful also for his time in helping me on the french proof-reading. I would also like to thank Mr. Pierre Bernhardt for offering enourmous help on many technical issues and his very much insightful advice. I would also like to thank Mr. Michel Wolfe and Mr. Alain Rach, who always accept new challenges from me in making new machine parts and have always accomplished the tasks. I would also like to thank Mr Sécou Sall for his help in TPR and being a very kind and humorous neighbour in the office. Special thanks for their support all along.

I would also like to thank the members of the Jury, Dr. Claude Henry, Dr. Marc Drillon and Dr. Laurent Picollo, for their time and attention in reading this manuscript.

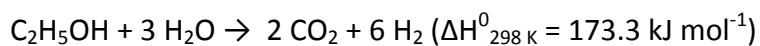
Above all, I would like to thank my parents for being always supportive.

# Résumé

## a) Introduction

Aujourd'hui, les combustibles fossiles représentent encore plus de 80% de l'énergie fournie au marché. Au cours des 20 dernières années, les émissions de CO<sub>2</sub> causées par la combustion de combustibles fossiles seuls ont augmenté de 50% [1]. L'impact environnemental de la production d'énergie a renforcé la demande en énergies alternatives. L'hydrogène, par exemple, un gaz à haute teneur énergétique, est un carburant alternatif prometteur qui ne provoque aucune émission de CO<sub>2</sub>. Il peut facilement être oxydé en se combinant avec l'oxygène pour former de l'eau, en libérant de la chaleur et de l'énergie. La production de H<sub>2</sub> à partir de l'éthanol issu de la biomasse est une méthode à émission neutre de CO<sub>2</sub>, car le CO<sub>2</sub> produit lors de la génération d'hydrogène est consommé lors de la photosynthèse pendant la croissance des plantes. L'éthanol est très approprié pour la production d'hydrogène renouvelable. Il a une teneur en hydrogène relativement élevée. Il est non-toxique et facile à manipuler et à stocker. En outre, la production d'éthanol à partir de sucre par des procédés tels que la fermentation anaérobie est une méthode ancienne et bien connue. Enfin, l'utilisation des résidus agricoles tels que la tige du blé [2] a offert depuis quelques années une nouvelle source d'éthanol, et donc à en baisser le prix [3]. Ces avantages font de lui un candidat prometteur pour la production d'hydrogène pour alimenter les piles à combustible.

Le vaporeformage de l'éthanol (ESR) est un processus qui consiste à convertir un mélange d'un rapport molaire de 1:3 d'éthanol et d'eau en hydrogène et dioxyde de carbone, comme seuls produits, suivant la réaction :



L'ESR réel implique un réseau complexe de réaction, dans lequel les voies réactionnelles sont fortement influencées par la nature des catalyseurs et des conditions de fonctionnement. Les points les plus importants à prendre en considération dans la conception d'un catalyseur de vaporeformage de l'éthanol seront: i) l'efficacité de la conversion de l'éthanol ii) la sélectivité pour l'hydrogène iii) la réduction des produits non-favorable tels que CO qui désactive le catalyseur. De plus, afin de réduire la consommation d'énergie, le catalyseur doit permettre la conversion de l'éthanol à basse température.

Les catalyseurs à base de métaux de transition, en particulier de nickel [4, 5] et le de cobalt [6-9] sont considérés comme les plus prometteurs pour la réaction d'ESR. Des rendements de conversion d'éthanol à basse température avec une sélectivité en H<sub>2</sub> comparables à celles de catalyseurs à base de métaux nobles tels que Rh, ont pu être obtenus [10, 11]. Toutefois, le défaut majeur des catalyseurs de métaux de transition reste leur propension à se désactiver par frittage [12] et à former du coke [13, 14]. L'utilisation du catalyseur bimétallique [15-18] sur des supports d'oxyde métallique [19-21] peut améliorer la stabilité du catalyseur. Des études récentes ont montré qu'un substrat de ZnO peut

## Résumé

considérablement améliorer l'efficacité de la réaction de conversion de l'éthanol et la sélectivité en hydrogène sur un catalyseur à base de Co à basse température [6, 11, 22].

Cependant, l'utilisation de catalyseurs bimétalliques rend le système plus compliqué à étudier en raison de la différence des activités catalytiques des deux métaux et leur interaction avec le support. Le but de ce travail est de comprendre l'influence des interactions bimétalliques et métaux-substrat sur le mécanisme de la réaction d'ESR à l'aide d'un système catalytique modèle. Ce système est formé de couches minces de Ni et Co déposées simultanément en phase gazeuse sur la surface d'un monocristal de ZnO sous ultravide (UHV). Ce système qui a une géométrie de surface bien définie peut être étudié grâce à des techniques d'analyse de surface, généralement difficiles à utiliser sur des catalyseurs réels en raison de la complexité de leur structure et des impuretés incorporées lors de leur synthèse.

Ce travail est constitué de quatre parties.

La première partie présente une étude des propriétés redox du matériau bimétallique Ni-Co dans 2 intervalles de pression : la plage basse pression ( $10^{-7}$  mbar) et celle de haute pression (1 bar). Une feuille polycristalline d'alliage de Ni-Co a été utilisée comme système modèle pour cette étude afin de comprendre les effets synergiques entre les deux composants de l'alliage lors de l'oxydation et ainsi que l'influence de la pression .

La deuxième partie est centrée sur l'étude de l'interaction des couches minces bimétalliques de Ni-Co (0,25 et 1,5 nm) sur le substrat polaire de ZnO (0001)-Zn et ZnO ( $000\bar{1}$ )-O. Cette étude a été réalisée sous ultra-vide (UHV) et basse pression d'oxygène ( $10^{-6}$  mbar) par spectroscopie de photoémission (PES) en utilisant le rayonnement synchrotron. Les couches de Ni et Co monométalliques ont également été caractérisées dans le but de discerner l'effet synergique de Ni-Co et l'effet venant de l'interaction métal-support. Ces deux effets majeurs sur les matériaux catalytiques ont été étudiés d'une manière cohérente grâce à l'élaboration de catalyseurs modèles préparés dans des conditions bien contrôlées.

La troisième partie est consacrée à l'étude du mécanisme d'ESR sur Ni-Co supporté sur ZnO. La spectrométrie de masse par thermodésorption (TDS) de l'éthanol sur un tel système a été réalisée afin d'identifier l'intermédiaire réactionnel et les produits de la réaction. La décomposition de l'éthanol sur ce système catalytique modèle a été discutée.

La quatrième partie se rapporte à l'étude du réseau réactionnel de l'ESR sur les nanopoudres de Ni-Co bimétalliques. Afin de se rapprocher des conditions de fonctionnement du procédé, le catalyseur est étudié *in situ* par XPS à la pression ambiante et les gaz réactionnels sont détectés simultanément par spectroscopie de masse afin de comprendre la correspondance entre les états actifs du catalyseur et les produits de réaction générés durant le processus.

## b) Résultats et interprétation

### i. L'oxydation de surface de l'alliage Ni-Co: une étude comparative par spectrométrie de photoélectrons induits par rayons X dans une large gamme de pression

L'oxydation de l'alliage NiCo a été étudiée par spectrométrie de photoélectrons induits par rayons X (XPS) sous deux régimes de pression :  $5 \times 10^{-10}$  et  $5 \times 10^{-1}$  bars. L'effet synergique entre les deux métaux de l'alliage lors de l'oxydation a été étudié. Les états d'oxydation de Ni et Co et l'évolution des compositions atomiques ont été calculés à partir de l'intensité des pics d'XPS.

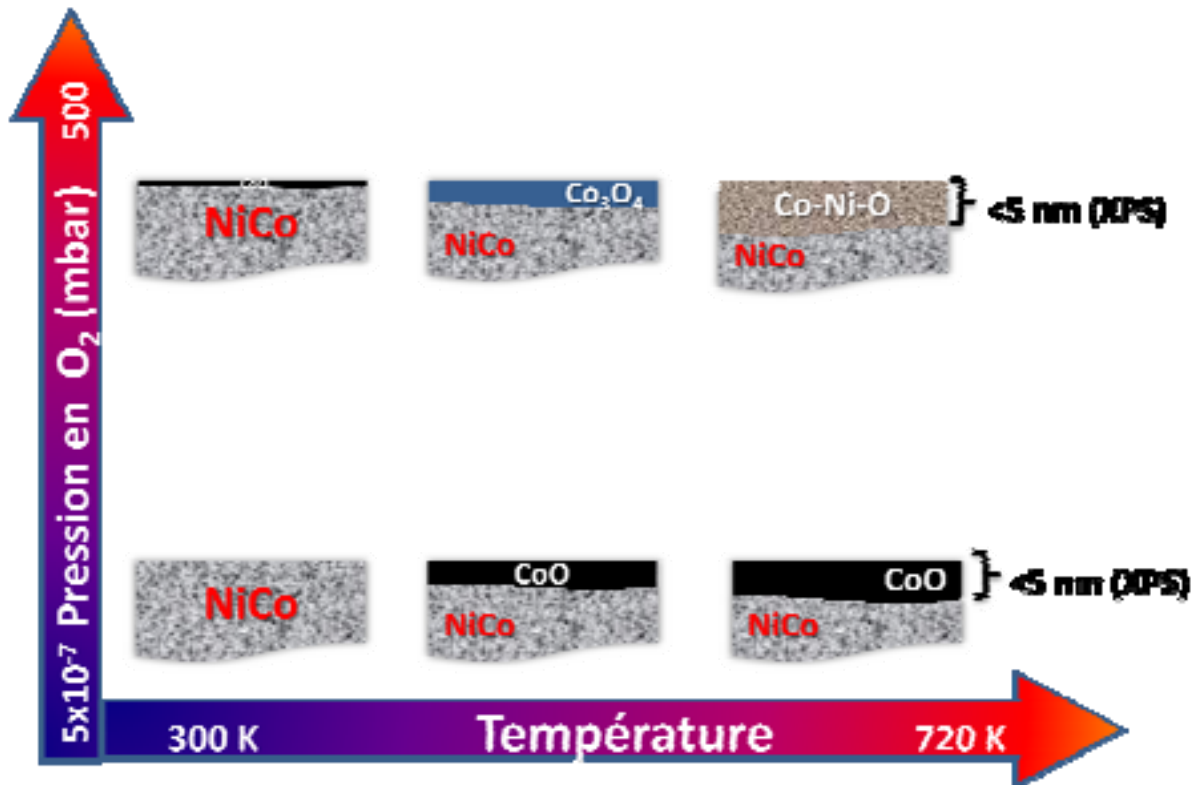


Figure 1 Illustration schématique de l'oxydation de l'alliage Ni-Co en fonction de la température sous deux régimes de pression d'oxygène.

La figure 1 est une représentation schématique des différentes étapes de l'oxydation de l'alliage Ni-Co. On peut noter qu'à basse pression d'oxygène, l'oxydation préférentielle et la ségrégation du cobalt est privilégiée, alors que l'oxydation du nickel est largement supprimée. L'espèce dominante à la surface est CoO mais il subsiste une faible quantité de  $\text{Co}^0$ , même après une oxydation de longue durée à 670 K. A 0,5 bars de pression d' $\text{O}_2$ , l'état d'oxydation de l'alliage dépend largement de la température. À 420 K le cobalt est transformé en CoO et le rapport atomique de Ni:Co à la surface atteint un minimum, ce qui est similaire aux observations faites pour les basses pressions. La formation de spinelles  $\text{Co}_3\text{O}_4$  et  $\text{Co}_x\text{Ni}_{1-x}\text{O}$  se produit à températures plus élevées (520 K à 720 K), comme indiqué par les modifications caractéristiques du pic satellite de  $\text{Ni}2p_{3/2}$ . Lors de la formation de l'oxyde spinelle, la concentration de nickel augmente de nouveau à la surface, au détriment du Co.

ii. Couches bimétalliques de nickel-cobalt nanométriques supportées sur des surfaces polaires de ZnO: interaction métal substrat et effets d'alliage étudiés par spectrométrie de photoélectrons induits par rayonnement synchrotron

La préparation des couches minces de Ni-Co et les études de PES ont été réalisées au Material Science Beamline situé au synchrotron Elettra à Trieste, en Italie. Les couches bimétalliques de Ni-Co ont été déposées par évaporation sur les monocristaux polaires d'oxyde de zinc ayant deux terminaisons: ZnO (0001)-Zn et ZnO (000 $\bar{1}$ )-O.

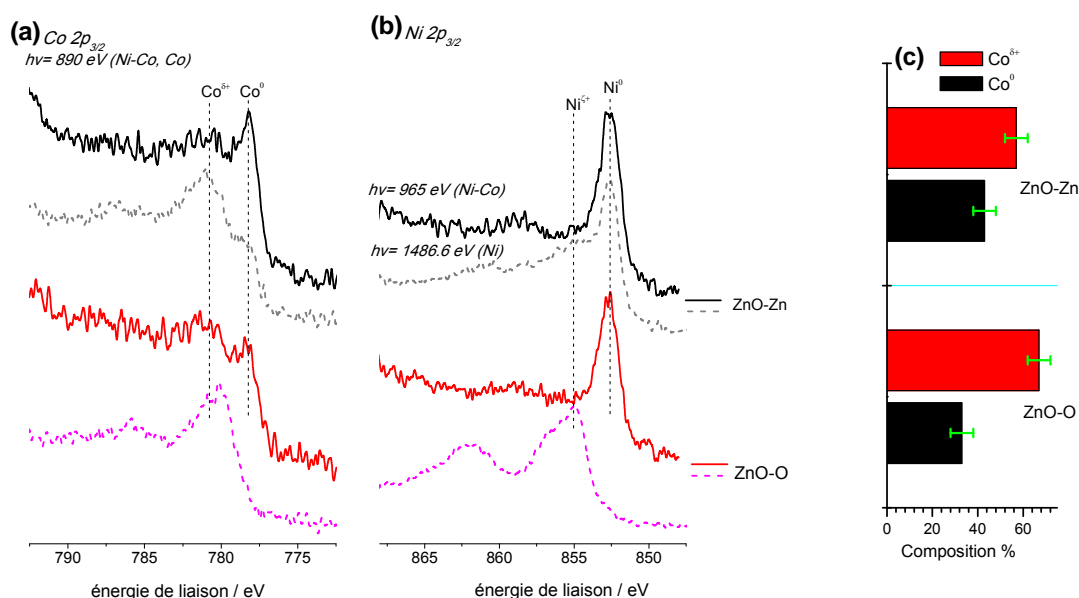


Figure 2 (a) Spectres de Co 2p<sub>3/2</sub> de Co monométallique (trait en pointillés) et Ni-Co (trait plain) déposé sur ZnO-Zn (haut) et ZnO-O (bas) après calcinations à 773 K sous UHV (l'épaisseur des couches de Co monométallique est de 0.1 nm et 0.25 nm pour Ni-Co, hv=890 eV) (b) Les spectres de Ni 2p<sub>3/2</sub> de couche monométallique (trait en pointillés) et Ni-Co (trait plain) déposé sur ZnO-Zn (haut) et ZnO-O (bas) soumis au même traitement que (a) . (c) Composition de Co<sup>0</sup> et Co<sup>2+</sup> de couche bimétallique déposée sur ZnO-Zn (haut) and ZnO-O (bas), estimée à partir de la déconvolution des spectres Co 2p<sub>3/2</sub>

L'influence de la terminaison de ZnO est indiquée en figure 2, qui représente la comparaison des spectres de Co 2p<sub>3/2</sub> et Ni 2p<sub>3/2</sub> enregistrés sur des couches minces déposées sur les deux substrats (spectres présentés en haut et en bas de chaque figure).

La présence de Co<sup>δ+</sup> ionique dans des couches bimétalliques est évidente (fig. 2a) et son intensité est plus élevée sur ZnO-O (environ 70%) que sur ZnO-Zn (environ 50%) (fig. 2c). En revanche, l'état d'oxydation du nickel est moins influencé par le substrat et ce dernier reste sous forme métallique (fig. 2b).

L'effet de substrat est plus prononcé sur les couches monométalliques (lignes pointillées). Le cobalt et le nickel déposés sur ZnO-O sont complètement oxydés en CoO et NiO [23, 24], tandis que les pics caractéristiques de Ni<sup>0</sup> et Co<sup>0</sup> sont encore visibles pour les couches déposées sur ZnO-Zn, ce qui indique une oxydation partielle.

## **Résumé**

En comparant les spectres des couches mono- et bimétalliques sur le même substrat (traits pleins et pointillés sur la fig. 2a et b), il est clair que le degré d'oxydation est influencé par les effets synergiques entre les deux éléments métalliques. En particulier, les couches bimétalliques sont plus résistantes à l'oxydation induite par l'interaction métal-support.

La couche de Ni-Co d'épaisseur plus élevée (1,5 nm) a également été caractérisée après calcination à 773 K sous UHV. Le traitement thermique n'a pas un effet prononcé sur l'état d'oxydation de Ni ou Co. L'absence de pics caractéristiques d'oxyde sur le spectre des couches d'épaisseur plus importante est due à l'influence de la taille du matériau [35] ou au confinement de l'oxydation du cobalt à l'interface métal-ZnO.

La calcination des couches minces dans des phases gazeuses différentes (UHV ou O<sub>2</sub>) engendre également des différences dans la composition de surface de Ni-Co. Celle-ci a été estimée grâce au changement d'intensité des pics 3p de Zn, Ni et Co. Une analyse quantitative comparative est présentée en figure 3. Le rapport atomique de (Ni + Co) / Zn (fig. 3a) donne la distribution de Ni et Co sur le substrat de ZnO : une valeur élevée correspond à une grande dispersion de la couche Ni-Co. En outre, le changement du rapport atomique de Ni / Co (fig. 3b) indique une ségrégation préférentielle des métaux sur la surface.

## Résumé

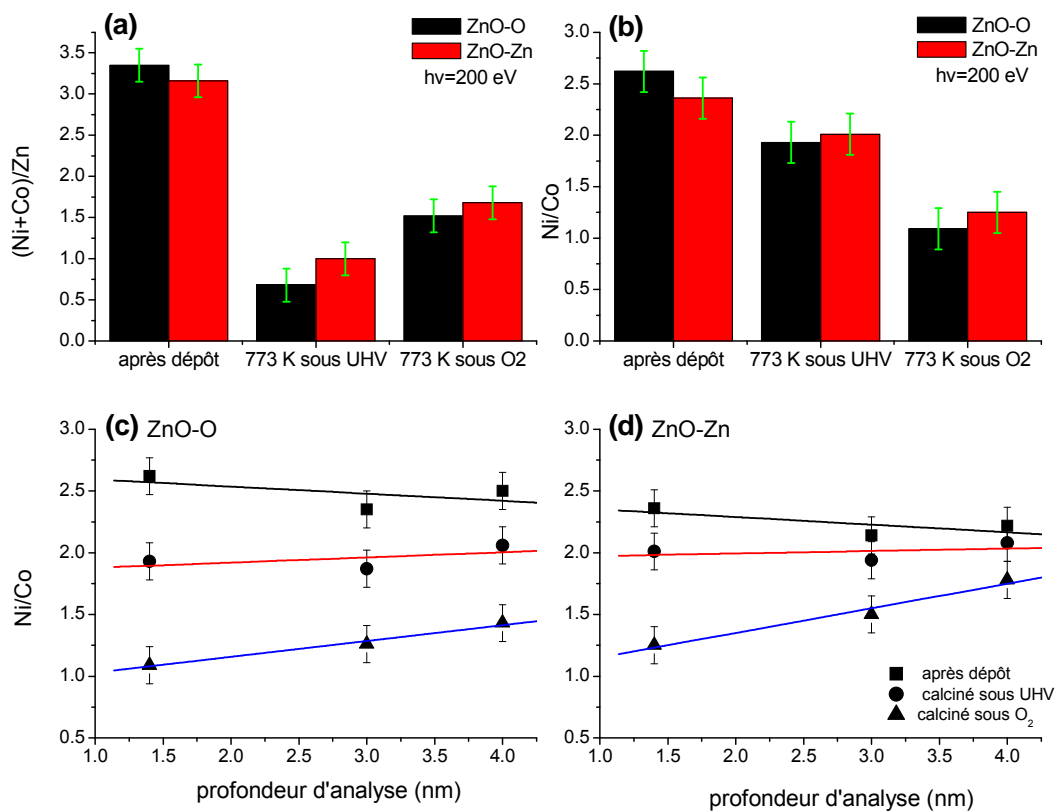


Figure 3 Calcul des rapports atomiques à partir de l'intensité de PES pour une couche mince de Ni-Co (1.5 nm) obtenue après dépôt, puis calcination à 773 K sous UHV et sous  $1 \times 10^{-6}$  mbar de O<sub>2</sub>: **(a)** (Ni+Co) / Zn **(b)** Ni / Co. Rapport atomique de Ni/Co en fonction de la profondeur de surface étudiée pour la couche bimétallique sur **(c)** ZnO-O et **(d)** ZnO-Zn

Le rapport atomique de (Ni + Co) / Zn de l'échantillon après le dépôt est comparable sur les deux substrats, ce qui indique que l'influence de la terminaison du substrat sur Ni-Co n'est pas significative à température ambiante. Toutefois, lors de la calcination sous UHV, la valeur du rapport (Ni+Co)/Zn chute à 20% de sa valeur initiale sur le substrat ZnO-O, ce qui est inférieur au rapport obtenu sur ZnO-Zn (30%). Une calcination ultérieure sous  $1 \times 10^{-6}$  mbar d'O<sub>2</sub> fait remonter la valeur de (Ni+Co)/Zn sur les deux substrats, ce qui suggère la redispersion de Ni-Co aggloméré après calcination sur ZnO. La morphologie des agglomérats de Ni-Co a été caractérisée par MEB et est présentée en figure 4.

## Résumé

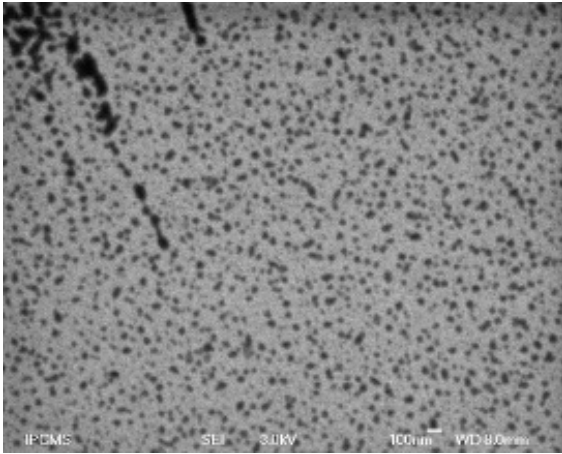


Figure 4 Image de MEB de couche mince de NiCo/ZnO-Zn (0001) d'épaisseur 1.5 nm calcinée à 773 K sous  $1 \times 10^{-6}$  mbar  $O_2$

La diminution du rapport (Ni + Co) / Zn après calcination peut être expliquée par l'agglomération de la couche de Ni-Co, qui est un phénomène généralement observé lors de la calcination des couches minces métalliques sur oxydes [26].

Ces résultats expérimentaux peuvent toutefois être également dus à la diffusion de Ni-Co dans le réseau atomique de ZnO (ou même le « spill-over » de ZnO sur Ni-Co), phénomène constaté par ailleurs pour l'interaction forte métal/support, par exemple, sur le  $TiO_2$  [27]. Si cette dernière explication est valable, l'augmentation de la valeur de (Ni + Co) / Zn après la calcination sous  $O_2$  peut être rationalisée par la re-ségrégation de la sous-surface de Ni-Co à la surface.

La calcination sous UHV induit une diminution importante du rapport atomique de Ni/Co, comme montré en fig. 3b, (75% de diminution par rapport aux valeurs initiales pour la terminaison O- et 85% pour Zn-). Une calcination successive sous  $O_2$  induit une diminution supplémentaire, ce qui indique une ségrégation importante de cobalt à la surface.

Les distributions de Ni et Co en fonction de la profondeur dans des atmosphères gazeuses différentes ont été évaluées grâce aux pics de Co 3p et Ni 3p mesurés avec des énergies de photons différentes (200 eV, 620 eV et 890 eV, qui correspondent respectivement à des profondeurs de détection de 1.4, 3 et 4 nm). Elles sont représentées dans les figures 3c et 3d. Cela nous informe sur le profil de concentration entre Ni et Co dans la couche mince. En particulier, à température ambiante, le rapport Ni / Co diminue en fonction de la profondeur de la surface détectée, alors qu'après traitement sous  $O_2$  le rapport de Ni/Co augmente avec la profondeur des couches. Le rapport de Ni/Co est plus élevé pour la sensibilité superficielle la plus haute à température ambiante. Cela indique que Ni ségrège sur Co en premier. Après calcination sous  $O_2$ , le rapport de Ni/Co présente une tendance inverse, correspondant à la restructuration de Ni-Co aggloméré avec plus de cobalt (oxyde) vers la surface pour former une structure « Ni-cœur/Co-coquille ».

Comme montré dans cette étude, le cobalt est plus réactif que le nickel aux espèces oxydantes (par exemple aux groupes -OH) et a une tendance à ségréger sur la surface. Lors

de la réaction d'ESR, la surface de cobalt peut capturer préférentiellement des espèces oxydantes (par exemple de la vapeur d'eau dans le flux réactionnel ESR) et les fournir aux sites actifs du nickel (à travers un mécanisme bi-fonctionnel) afin de limiter le dépôt de carbone.

En dehors du dépôt de carbone, nous avons montré ici que l'oxydation (due à l'interaction avec le support) est freinée sur le matériau bimétallique Ni-Co ainsi le nickel reste à l'état métallique actif.

### iii. Les étapes intermédiaires et les voies réactionnelles du reformage d'éthanol à la vapeur: les études de désorption d'éthanol à température programmée sur Ni-Co/ZnO

Le chapitre 6 est consacré à l'étude de la réaction de l'éthanol sur les couches minces de Ni, Co et Ni-Co sur ZnO (0001)-Zn. Cette étude a été réalisée par spectrométrie de masse par thermodésorption (TDS). La modification de la composition chimique et de l'état d'oxydation de Ni et de Co ont été caractérisés par XPS. Ni et Co ont été déposés sur le monocristal de ZnO (0001)-Zn par évaporation afin de créer un film homogène mince dans le but de modéliser l'interface de Ni-Co/ZnO dans un catalyseur de travail. L'épaisseur nominale de la couche de Ni-Co étudiée est d'environ 1,2 nm. La morphologie de la couche mince a été étudiée par microscopie à force atomique (AFM) (figure5).

L'alliage Ni-Co déposé à la température ambiante se compose d'une couche plane sans agglomération importante. Lors du recuit sous vide, la couche s'altère et des agglomérats de 7-8 nm d'épaisseur sont observés sur la surface.

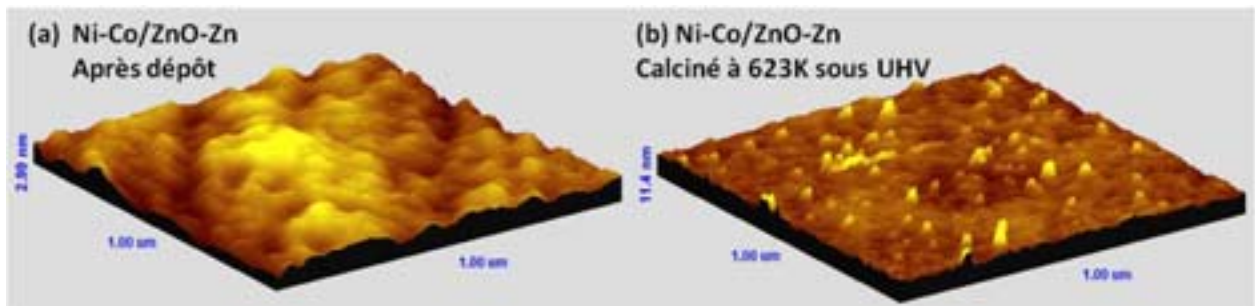


Figure 5 L'image d'AFM de couche mince de Ni-Co sur ZnO-Zn (à gauche) après dépôt et (à droite) après calcination à 623 K

L'apparition des agglomérats observés par AFM est validée par l'XPS qui montre la diminution du rapport atomique de Ni-Co/Zn lorsque la température augmente. L'XPS montre également que Ni et Co sont oxydés à température élevée, à cause de l'interaction avec ZnO.

## Résumé

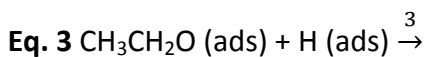
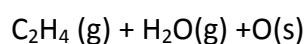
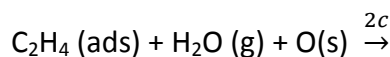
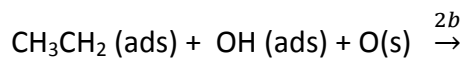
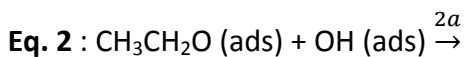
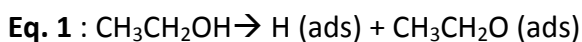
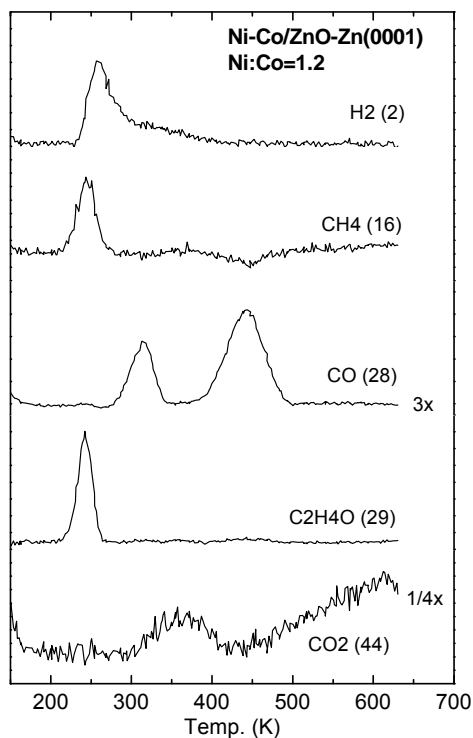


Figure 6 (à gauche) TDS des produits générés par la désorption d'éthanol et (à droite) les voies réactionnelles proposées pour la décomposition d'éthanol sur Ni-Co/ZnO-Zn (Ni/Co=1.2, épaisseur 1.4 nm)

La figure 6 représente les courbes de TDS des produits obtenus après adsorption jusqu'à saturation d'éthanol sur NiCo / ZnO. La déshydrogénation est la réaction de base de décomposition de l'éthanol car le groupe -O-H dans la molécule d'éthanol est très sensible à la dissociation. Cela conduit à la formation d'un groupe éthoxy et d'hydrogène adsorbé (Eq. 1). Le groupe éthoxy se transforme alors en acétaldéhyde par déshydrogénation ou se décompose davantage. Sur la surface du monocristal de ZnO-Zn, l'éthanol se décompose en  $\text{C}_2\text{H}_4\text{O}$ ,  $\text{H}_2\text{O}$ ,  $\text{H}_2$  et  $\text{C}_2\text{H}_4$  par deux grandes voies de réaction : la déshydrogénation (Eq. 2) et la déshydratation (Eq. 3). La décomposition du groupe éthoxy n'est pas observée sur ZnO.

Les couches minces métalliques de Ni, Co, ou Ni-Co sur ZnO-Zn sont plus efficaces en rupture des liaisons C-C et C-H. Cela se traduit par la décomposition du groupe éthoxy, qui suit cependant deux voies de réaction différentes pour Ni et pour Co.

En effet, si  $\text{H}_2$  et CO sont les produits de décomposition communs sur Ni et Co, la production de méthane a lieu exclusivement sur Ni/ZnO-Zn. La rupture de liaison C-C dans la molécule d'éthanol s'observe sensiblement plus sur Ni. Cette réaction conduit à la formation du groupe méthyle et de CO, qui désorbent alors sous forme de méthane et de CO.

Sur Co/ZnO-Zn, le groupe éthoxy se transforme en oxametallacycle, qui s'adsorbe sur Co par le groupe méthyle et l'oxygène. L'oxametallacycle subit ensuite une cassure de la liaison C-C, suivie par la déshydrogénation du groupe méthyle. Par conséquent,  $\text{H}_2$  et CO sont les seuls produits de désorption de l'éthanol sur Co/ZnO-Zn.

Ainsi, la désorption de l'hydrogène est inversement corrélée à la désorption du méthane car les réactions produisant de l'hydrogène sont en concurrence avec celle produisant du méthane. Pourtant, la sélectivité du méthane par rapport à l'hydrogène ne varie pas linéairement avec la proportion de Ni. Dans le cas des alliages de Ni-Co pour lesquels Co est majoritaire la production relative du méthane par rapport à l'hydrogène n'augmente que très légèrement avec le pourcentage de Ni. Au contraire, dans le cas des alliages plus riches en Ni qu'en Co, la sélectivité du méthane augmente considérablement avec le pourcentage de Ni. Il existe donc un pourcentage critique de Ni, qui régit la priorité des chemins réactionnels.

#### iv. **L'Étude de la Spectrométrie Photoélectronique à Pression Ambiante (APPES) et la Spectroscopie de structure près du front d'absorption de rayons X (NEXAFS) sur le réformage d'éthanol sur le catalyseur bimétallique de Ni-Co**

Nous avons étudié le vapo-réformage de l'éthanol sur les nanopoudres de Ni, Co et Ni-Co *in-situ* par APPES, NEXAFS et spectrométrie de masse en ligne. Ces techniques *in-situ* nous permettent d'étudier la correspondance de l'état de la surface du catalyseur avec les activités catalytiques en conditions opératoires.

Afin de comprendre l'interaction bimétallique dans Ni-Co sous atmosphère ambiante, la réduction des nanopoudres de Ni-Co a été étudiée dans 0,2 mbar de H<sub>2</sub>. La réduction du cobalt préoxydé, à la fois sous forme d'alliage et monométallique, suit deux étapes. La réduction de Co<sub>3</sub>O<sub>4</sub> en CoO a lieu en premier à basse température, suivie par la réduction simultanée de NiO et CoO à température plus élevée. En raison de la thermodynamique de réduction du cobalt, la réduction de Co<sub>3</sub>O<sub>4</sub> est favorisée par rapport à celle de NiO. La réduction de l'oxyde de Ni monométallique a donc lieu à une température plus basse que celle de l'alliage Ni-Co. On peut aussi remarquer que la ségrégation a lieu en même temps que la réduction de NiO et CoO. L'observation d'une augmentation importante du rapport atomique Ni/Co atteste d'une réorganisation importante de la composition chimique de surface.

Le mélange gazeux d'ESR (0.2 mbar d'éthanol et d'eau dans un rapport de débit de 1:3) constitue une atmosphère réductrice, dans laquelle le Co<sub>3</sub>O<sub>4</sub> est également d'abord réduit en CoO à basse température. Le Ni et le Co pré-oxydés sont sous forme d'oxyde NiO et CoO à 543 K. A 623 K, le NiO et le CoO de surface sont réduits en métal.

## Résumé

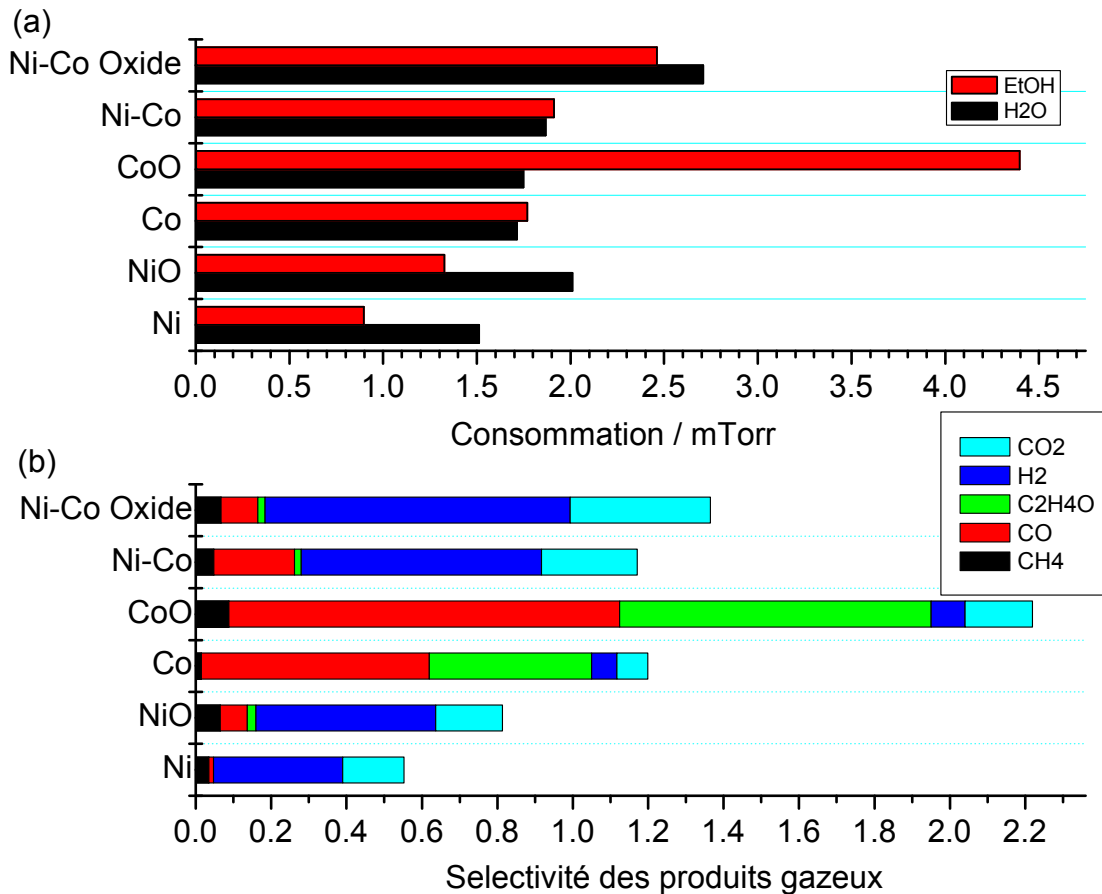


Figure 7 Consommation d'éthanol et d'eau à (a) 523 K et (b) sélectivité des produits gazeux CH<sub>4</sub>, CO, C<sub>2</sub>H<sub>4</sub>O, H<sub>2</sub> and CO<sub>2</sub> sur les échantillons de Ni, Co et alliage Ni-Co (pré-réduit sous H<sub>2</sub> à 623 K) et leurs oxydes (formés sous O<sub>2</sub> à 623 K) à 523 K

Comme l'état d'oxydation de la surface du catalyseur se modifie dynamiquement avec la composition de la phase gazeuse et la température de réaction, la réaction a du être étudiée à deux températures différentes, 543 K et 623 K, afin d'appréhender la corrélation entre l'oxydation de la surface et la réactivité.

Les principaux produits générés sont H<sub>2</sub>, CH<sub>4</sub>, CO, CO<sub>2</sub> et C<sub>2</sub>H<sub>4</sub>O. Nous avons observé, à 543K, que la consommation d'éthanol, en dehors du vaporéformage ou de la décomposition, est plus élevée sur les catalyseurs à base d'oxydes. De manière générale, Co est plus sélectif en C<sub>2</sub>H<sub>4</sub>O et en CO, tandis que Ni est plus sélectif en CH<sub>4</sub>. Mais dès que Ni est présent dans un catalyseur, qu'il s'agisse de Ni-Co ou d'oxyde de Ni-Co, l'effet du Co est grandement diminué. Cela se déduit de la faible sélectivité en C<sub>2</sub>H<sub>4</sub>O des catalyseur contenant du Ni, même lorsque la quantité de Co est supérieure de 50 % à celle de Ni. Une raison possible est le manque de groupes hydroxyles sur les catalyseurs contenant du Co, comme le montrent les spectres de O 1s.

## Résumé

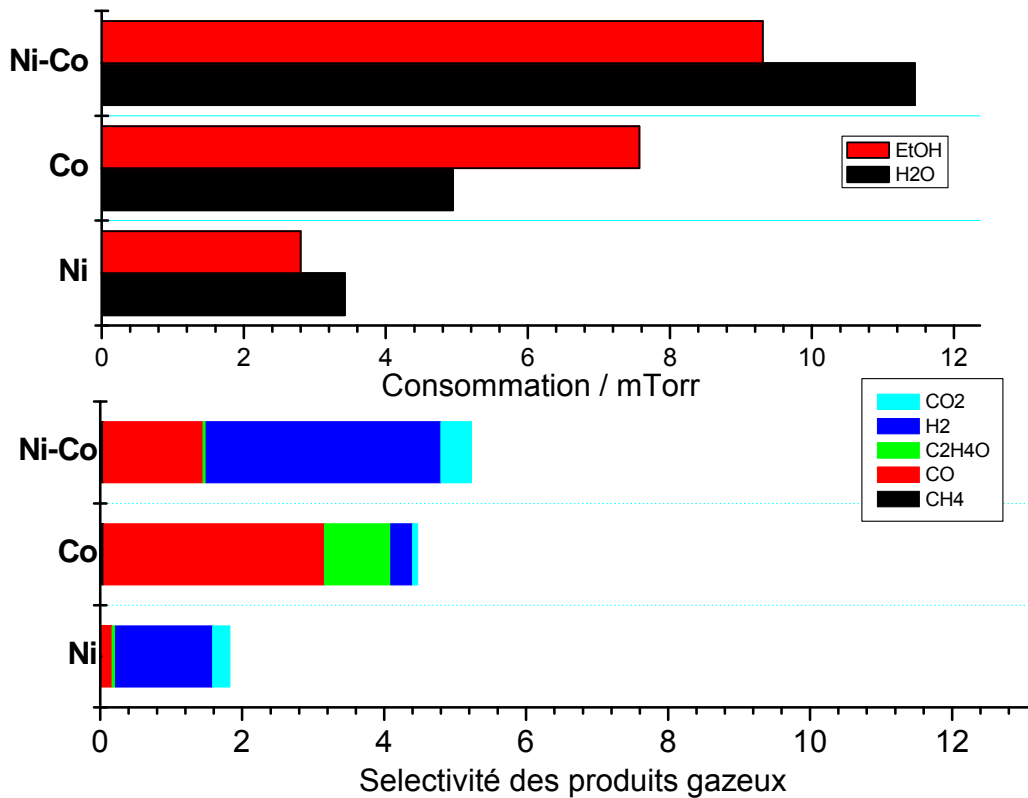


Figure 8 Consommation d'éthanol et d'eau à 623 K (b) La sélectivité de produit gazeux CH<sub>4</sub>, CO, C<sub>2</sub>H<sub>4</sub>O, H<sub>2</sub> and CO<sub>2</sub> sur les échantillons de Ni, Co et alliage Ni-Co (pré-réduit sous H<sub>2</sub> à 623 K) à 623 K

A 623 K, la consommation d'éthanol et d'eau augmente substantiellement. Les sélectivités en produits intermédiaires tels que C<sub>2</sub>H<sub>4</sub>O et CH<sub>4</sub> sont considérablement réduites, notamment sur Ni et Ni-Co. De plus, l'augmentation de la consommation d'eau et de la production de H<sub>2</sub> et de CO<sub>2</sub>, lorsque la température augmente, dénote une importante augmentation du processus de réformage de l'éthanol par rapport aux autres voies de réaction. Le réformage du méthane et de l'acétaldéhyde est également probable à cette température et peut contribuer à l'augmentation de la sélectivité en hydrogène.

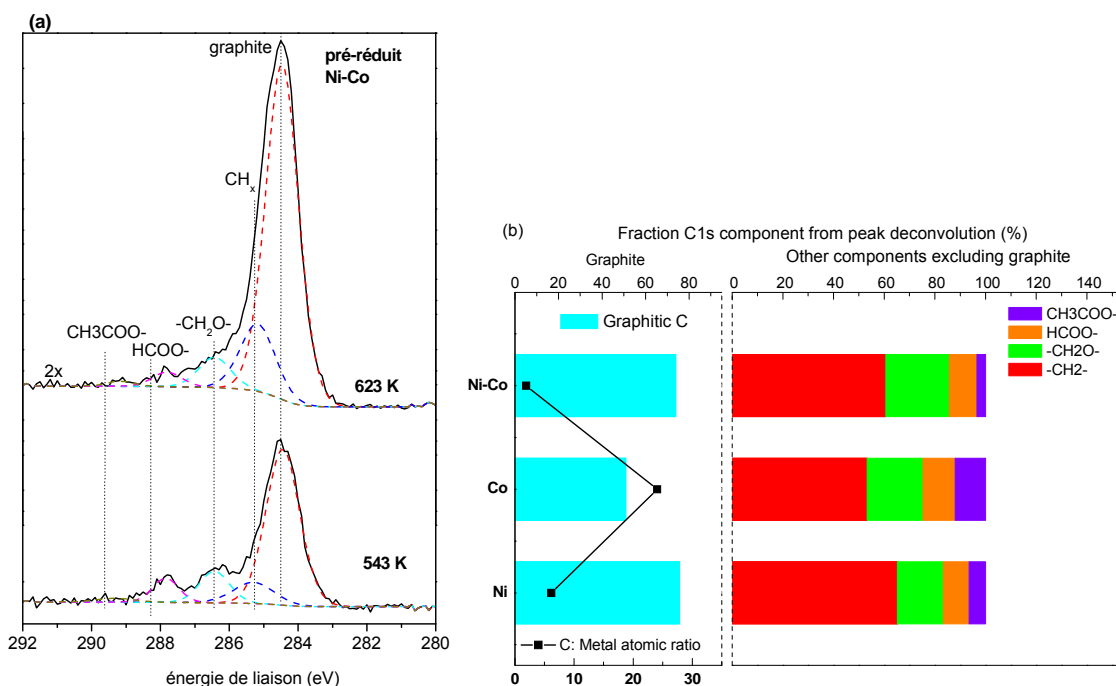


Figure 9 (a) Déconvolution du spectre C 1s du carbone sur Ni-Co à 543 K et 623 K (b) (à gauche) Rapport atomique de C 1s /métal(■) et la concentration du graphite par rapport à C1s (à droite) Concentration des autres composants de C1s en excluant le graphite sur Ni, Co et Ni-Co (pré-réduit sous H<sub>2</sub>) dans les conditions réactionnelles d'ESR à 623 K

Lorsque la température augmente, il y a une augmentation substantielle du niveau de carbone graphitique en raison de l'activité catalytique élevée à haute température. Le niveau de carbone est le plus élevé sur Co. Cela pourrait être lié à la sélectivité élevée en CO sur Co, qui favorise la formation de carbone par réaction Boudouard.

### c) Conclusions

Ce travail a permis d'améliorer la compréhension de l'influence de la synergie entre les métaux au sein des matériaux bimétalliques et de l'interaction métal-support pour le vaporéformage catalytique de l'éthanol. Un système modèle de catalyseur bimétallique a été développé, basé sur le dépôt de couches minces de Ni-Co sur un monocristal de ZnO. Ce travail a été réalisé suivant deux axes:

- la caractérisation de l'effet synergique dans l'alliage de Ni-Co ainsi que son interaction avec ZnO sous UHV et en présence de phase gazeuses (H<sub>2</sub> et O<sub>2</sub>) à pression ambiante
- l'étude de la chimie de surface et des chemins réactionnels par TDS et par des techniques d'analyse de surface *in-situ*.

Nos résultats ont montré que des phénomènes tels que la ségrégation de surface et l'oxydation induite par l'interaction métal-support peuvent jouer un rôle important pour la performance du système catalytique. La décomposition de l'éthanol sur le catalyseur bimétallique ressemble au processus réactionnel du catalyseur monométallique, puisque les

## ***Résumé***

intermédiaires majeurs sont présents sur les deux systèmes de catalyseurs. Toutefois, sous les conditions réactionnelles à pression ambiante, la sélectivité relative en produits de réformage est plus élevée pour le catalyseur bimétallique et comporte une quantité moindre d'espèces intermédiaires réactionnelles tout en limitant la contamination en carbone graphitique.

## d) References

- [1] C. Le Quéré, R.J. Andres, T. Boden, T. Conway, R.A. Houghton, J.I. House, G. Marland, G.P. Peters, G. van der Werf, A. Ahlström, R.M. Andrew, L. Bopp, J.G. Canadell, P. Ciais, S.C. Doney, C. Enright, P. Friedlingstein, C. Huntingford, A.K. Jain, C. Jourdain, E. Kato, R.F. Keeling, K. Klein Goldewijk, S. Levis, P. Levy, M. Lomas, B. Poulter, M.R. Raupach, J. Schwinger, S. Sitch, B.D. Stocker, N. Viovy, S. Zaehle, N. Zeng, *Earth Syst. Sci. Data Discuss.* 5 (2012) 1107-1157.
- [2] M.A. Kabel, G. Bos, J. Zeevalking, A.G.J. Voragen, H.A. Schols, *Bioresource Technology.* 98 (2007) 2034-2042.
- [3] S. Kim, B.E. Dale, *Biomass and Bioenergy.* 26 (2004) 361-375.
- [4] A.N. Fatsikostas, X.E. Verykios, *J. Catal.* 225 (2004) 439-452.
- [5] F. Frusteri, S. Freni, V. Chiodo, L. Spadaro, O. Di Blasi, G. Bonura, S. Cavallaro, *Appl Catal A Gen.* 270 (2004) 1-7.
- [6] J. Llorca, N. Homs, J. Sales, P. Ramírez de la Piscina, *Journal of Catalysis.* 209 (2002) 306-317.
- [7] P. Bichon, G. Haugom, H.J. Venvik, A. Holmen, E.A. Blekkan, *Topics in Catalysis.* 49 (2008) 38-45.
- [8] F. Haga, T. Nakajima, H. Miya, S. Mishima, *Catalysis Letters.* 48 (1997) 223-227.
- [9] S. Freni, S. Cavallaro, N. Mondello, L. Spadaro, F. Frusteri, *Catalysis Communications.* 4 (2003) 259-268.
- [10] J. Sun, X.P. Qiu, F. Wu, W.T. Zhu, *Int. J. Hydrogen Energy* 30 (2005) 437-445.
- [11] J. Llorca, P. Ramírez De La Piscina, J.A. Dalmon, J. Sales, N. Homs, *Applied Catalysis B: Environmental.* 43 (2003) 355-369.
- [12] F. Frusteri, S. Freni, L. Spadaro, V. Chiodo, G. Bonura, S. Donato, S. Cavallaro, *Catal. Commun.* 5 (2004) 611-615.
- [13] A.M. Karim, Y. Su, J. Sun, C. Yang, J.J. Strohm, D.L. King, Y. Wang, *Applied Catalysis B: Environmental.* 96 (2010) 441-448.
- [14] S.M. De Lima, A.M. Da Silva, L.O.O. Da Costa, U.M. Graham, G. Jacobs, B.H. Davis, L.V. Mattos, F.B. Noronha, *Journal of Catalysis.* 268 (2009) 268-281.
- [15] J. Kugai, S. Velu, C. Song, *Catalysis Letters.* 101 (2005) 255-264.
- [16] N. Homs, J. Llorca, P.R. de la Piscina, *Catalysis Today.* 116 (2006) 361-366.
- [17] F.J. Mariño, E.G. Cerrella, S. Duhalde, M. Jobbagy, M.A. Laborde, *Int. J. Hydrogen Energy* 23 (1998) 1095-1101.
- [18] A. Casanovas, M. Roig, C. De Leitenburg, A. Trovarelli, J. Llorca, *International Journal of Hydrogen Energy.* 35 (2010) 7690-7698.
- [19] H. Song, U.S. Ozkan, *Journal of Catalysis.* 261 (2009) 66-74.
- [20] Z. Zhong, H. Ang, C. Choong, L. Chen, L. Huang, J. Lin, *Physical Chemistry Chemical Physics.* 11 (2009) 872-880.
- [21] S.S.Y. Lin, D.H. Kim, S.Y. Ha, *Catalysis Letters.* 122 (2008) 295-301.
- [22] J. Llorca, N. Homs, J. Sales, J.L.G. Fierro, P.R. De La Piscina, *Journal of Catalysis.* 222 (2004) 470-480.
- [23] S.C. Petitto, E.M. Marsh, G.A. Carson, M.A. Langell, *J. Mol. Catal. A: Chem.* 281 (2008) 49-58.
- [24] M.A. Van Veenendaal, G.A. Sawatzky, *Phys. Rev. Lett.* 70 (1993) 2459-2462.
- [25] V. Papaefthimiou, T. Dintzer, V. Dupuis, A. Tamion, F. Tournus, A. Hillion, D. Teschner, M. Hävecker, A. Knop-Gericke, R. Schlögl, S. Zafeirotos, *ACS Nano.* 5 (2011) 2182-2190.
- [26] C.T. Campbell, *Surface Science Reports.* 27 (1997) 1-111.

## *Résumé*

[27] O. Dulub, W. Hebenstreit, U. Diebold, Physical Review Letters. 84 (2000) 3646-3649.

# Table of content

---

<b>Chapter 1. Introduction .....</b>	<b>- 1 -</b>
<b>1.1 Current hydrogen production status.....</b>	<b>- 1 -</b>
<b>1.1.1 Overview of energy consumption worldwide .....</b>	<b>- 1 -</b>
1.1.1.1 Demand for alternative energy .....	- 1 -
1.1.1.2 Transition from fossil fuel to renewable energy .....	- 2 -
<b>1.1.2 Current market of Hydrogen.....</b>	<b>- 3 -</b>
<b>1.1.3 Hydrogen production and efficiency .....</b>	<b>- 4 -</b>
1.1.3.1 Current production of H <sub>2</sub> .....	- 4 -
1.1.3.2 CO <sub>2</sub> emission free hydrogen production .....	- 5 -
1.1.3.3 Hydrogen from biomass .....	- 6 -
<b>1.2 Ethanol steam reforming reaction .....</b>	<b>- 6 -</b>
<b>1.2.1 Bio-ethanol for hydrogen production .....</b>	<b>- 6 -</b>
<b>1.2.2 Reaction networks and intermediates .....</b>	<b>- 7 -</b>
1.2.2.1 Initial steps of ethanol conversion .....	- 7 -
1.2.2.2 Acetaldehyde conversion .....	- 8 -
1.2.2.3 Methaneconversion.....	- 8 -
1.2.2.4 Carbon monoxide and carbon dioxide conversion.....	- 9 -
1.2.2.5 Coke formation .....	- 9 -
<b>1.2.3 Bond dissociation of ethanol .....</b>	<b>- 9 -</b>
<b>1.2.4 Consideration on reaction thermodynamics .....</b>	<b>- 10 -</b>
<b>1.2.5 Critical parameters for reaction efficiency .....</b>	<b>- 11 -</b>
<b>1.3 ESR catalyst current status .....</b>	<b>- 12 -</b>
<b>1.3.1 Transition metal catalysts-Nickel and Cobalt as ethanol steam reforming catalyst.....</b>	<b>- 12 -</b>
1.3.1.1 Nickel as ESR catalyst.....	- 13 -
1.3.1.2 Cobalt as ESR catalyst .....	- 14 -
<b>1.3.2 Bimetallic catalysts .....</b>	<b>- 16 -</b>
<b>1.3.3 Ni-Co based bimetallic catalysts.....</b>	<b>- 20 -</b>
<b>1.3.4 Metal oxide support and Metal-support interaction .....</b>	<b>- 22 -</b>
<b>1.3.5 Metal oxide support for ESR .....</b>	<b>- 23 -</b>
<b>1.3.6 Concerns of catalyst stability for ESR .....</b>	<b>- 26 -</b>
1.3.6.1 Carbon formation .....	- 26 -
1.3.6.2 Metal sintering .....	- 27 -
1.3.6.3 Metal oxidation .....	- 28 -
<b>1.4 Surface Studies of catalysts .....</b>	<b>- 28 -</b>
<b>1.4.1 Model catalyst .....</b>	<b>- 28 -</b>
<b>1.4.2 Surface chemistry of ethanol on model catalysts .....</b>	<b>- 29 -</b>
<b>1.4.3 Bridging the gap between model catalyst and real catalyst by APPES.....</b>	<b>- 33 -</b>
<b>1.5 Scope and outline of the thesis.....</b>	<b>- 37 -</b>
<b>1.6 References .....</b>	<b>- 39 -</b>

<b>Chapter 2. Experimental techniques.....</b>	<b>- 48 -</b>
<b>2.1 Methods and materials for developing model catalyst .....</b>	<b>- 48 -</b>
<b>2.1.1 Properties of ZnO.....</b>	<b>- 48 -</b>
<b>2.1.2 Material preparation .....</b>	<b>- 50 -</b>
2.1.2.1 Ni-Co bimetallic materials .....	- 50 -
2.1.2.2 Ni-Co thin film supported on polar ZnO single crystal .....	- 50 -
<b>2.2 Study of the surface composition and reactions of the catalysts ....</b>	<b>- 52 -</b>
<b>2.2.1 X-ray Photoemission spectrsocopy (XPS) .....</b>	<b>- 52 -</b>
2.2.1.1 Overview.....	- 52 -
2.2.1.2 Synchrotron radiation based photoemission spectroscopy (PES) .....	- 53 -
2.2.1.3 Chemical effects on XPS spectra .....	- 55 -
2.2.1.4 Experimental set-up .....	- 59 -
a) UHV system for low pressure studies .....	- 59 -
b) System for high pressure studies .....	- 61 -
c) Photoemission Spectroscopy (PES) in Elettra .....	- 63 -
d) Ambient Pressure Photoemission Spectroscopy (APPES).....	- 64 -
2.2.1.5 Near edge X-ray absorption fine structure (NEXAFS).....	- 66 -
<b>2.2.2 Thermal Desorption Spectroscopy (TDS).....</b>	<b>- 67 -</b>
2.2.2.1 Overview.....	- 67 -
2.2.2.2 Experimental setup for TDS.....	- 69 -
2.2.2.3 Correction of mass fragment.....	- 70 -
<b>2.3 Material characterization .....</b>	<b>- 71 -</b>
<b>2.3.1 Bulk characterization .....</b>	<b>- 71 -</b>
2.3.1.1 X-ray diffraction (XRD).....	- 71 -
<b>2.3.2 Morphological characterization .....</b>	<b>- 72 -</b>
2.3.2.1 Scanning electron microscopy (SEM) .....	- 72 -
2.3.2.2 Atomic force microscopy (AFM).....	- 74 -
2.3.2.3 Low Energy Electron Diffraction (LEED) .....	- 74 -
<b>2.4 References .....</b>	<b>- 76 -</b>
<b>Chapter 3. Surface oxidation of NiCo alloy: A comparative X-ray photoelectron spectroscopy study in a wide pressure range.....</b>	<b>- 79 -</b>
<b>3.1 Introduction .....</b>	<b>- 79 -</b>
<b>3.2 Experimental Methods .....</b>	<b>- 81 -</b>
<b>3.3 Results and discussion.....</b>	<b>- 82 -</b>
<b>3.3.1 3.1 XRD characterization.....</b>	<b>- 82 -</b>
<b>3.3.2 SEM characterization .....</b>	<b>- 82 -</b>
<b>3.3.3 Oxidation of NiCo at low O<sub>2</sub> pressure.....</b>	<b>- 84 -</b>
<b>3.3.4 Oxidation of NiCo at ambient O<sub>2</sub> pressure .....</b>	<b>- 87 -</b>
<b>3.3.5 Bimetallic synergetic effect and pressure gap .....</b>	<b>- 90 -</b>
<b>3.4 Conclusions .....</b>	<b>- 93 -</b>
<b>3.5 References .....</b>	<b>- 94 -</b>

**Chapter 4. Bimetallic nickel-cobalt nanosized layers supported on polar ZnO surfaces: metal-support interaction and alloy effects studied by synchrotron radiation X-ray photoelectron spectroscopy .....- 99 -**

<b>4.1</b>	<b>Introduction .....</b>	<b>- 99 -</b>
<b>4.2</b>	<b>Experimental Methods .....</b>	<b>- 100 -</b>
<b>4.3</b>	<b>Results .....</b>	<b>- 101 -</b>
4.3.1	Characterization of pristine polar ZnO substrates .....	- 101 -
4.3.2	Oxidation state of Ni-Co overlayers on ZnO at room temperature .....	- 103 -
4.3.3	Oxidation state of Ni-Co overlayers on ZnO annealed in UHV .....	- 104 -
4.3.4	Compositional changes of Ni-Co overlayer under different annealing environments.....	- 106 -
<b>4.4</b>	<b>Discussion .....</b>	<b>- 109 -</b>
4.4.1	Metal-support interaction at room temperature .....	- 110 -
4.4.2	Thermally induced oxidation in UHV.....	- 110 -
4.4.3	Synergetic effects between Ni and Co in O <sub>2</sub> .....	- 111 -
4.4.4	Implications in catalysis .....	- 111 -
<b>4.5</b>	<b>Conclusions .....</b>	<b>- 112 -</b>
<b>4.6</b>	<b>References .....</b>	<b>- 114 -</b>

**Chapter 5. Insight for ethanol steam reforming reaction pathways and intermediates: Ethanol desorption on ZnO supported Ni-Co bimetallic model catalyst 118**

<b>5.1</b>	<b>Introduction .....</b>	<b>-118-</b>
<b>5.2</b>	<b>Experimental methods .....</b>	<b>-119-</b>
<b>5.3</b>	<b>Results .....</b>	<b>-123-</b>
5.3.1	Ethanol desorption from ZnO-Zn .....	-123-
5.3.2	Thermal decomposition of ethanol on monometallic Ni and Co layer supported on ZnO .....	-126-
5.3.3	Ethanol decomposition on bimetallic Ni-Co alloy overlayer .....	-130-
5.3.4	Desorption products of ethanol on Ni-Co/ZnO-Zn of different Ni:Co ratio-134-	-134-
5.3.5	Susceptibility to Carbon formation .....	-138-
5.3.6	Preferences of reaction pathway on Ni-Co/ZnO-Zn of different composition... ..	-138-
<b>5.4</b>	<b>Conclusions .....</b>	<b>-140-</b>
<b>5.5</b>	<b>References .....</b>	<b>-142-</b>

<b>Chapter 6.</b>	<b>Ambient Pressure Photoemission Spectroscopy (APPEs) and Near-Edge X-ray Absorption Spectroscopy (NEXAFS) study of Ni-Co bimetallic catalyst for ethanol steam reforming.....</b>	<b>- 145 -</b>
6.1	Introduction.....	- 145 -
6.2	Experimental methods.....	- 147 -
6.3	Results.....	- 148 -
6.3.1	Reduction of Ni-Co nanopowders in ambient pressure H <sub>2</sub> .....	- 148 -
6.3.2	Coordination of Ni-Co in ethanol steam reforming mixture.....	- 153 -
6.3.3	Influence of oxidation state of Ni and Co on the catalytic performance of Ni-Co.....	- 154 -
6.3.4	Steady state reaction of 623 K.....	- 161 -
6.3.5	Carbon formation during ESR process in different temperature range...	- 163 -
6.4	Conclusions.....	- 164 -
6.5	References.....	- 166 -
<b>Chapter 7.</b>	<b>General conclusions and perspectives.....</b>	<b>- 170 -</b>
7.1	General conclusions.....	- 170 -
7.2	Perspectives.....	- 173 -
7.3	References.....	- 174 -
<b>I.</b>	<b>Appendices.....</b>	<b>- 176 -</b>
a.	Supplementary information to Chapter 3.....	- 176 -
b.	Supplementary information to Chapter 4.....	- 179 -
c.	Supplementary information to Chapter 6.....	- 184 -
d.	References.....	- 185 -
<b>II.</b>	<b>List of Publications.....</b>	<b>- 186 -</b>

---

---

# Chapter 1

## Introduction

---

---

---

---

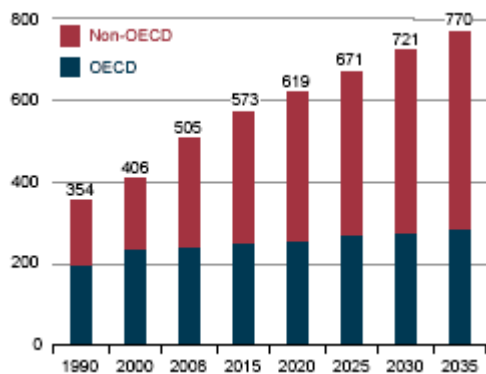
## Chapter 1. Introduction

### 1.1 Current hydrogen production status

#### 1.1.1 Overview of energy consumption worldwide

##### 1.1.1.1 Demand for alternative energy

Energy is an important driving force for modern society. Industry, transport, household users rely heavily on energy for proper operation daily. World energy consumption has gone up from 4672 kTWh to 8676 kTWh from 1973 to 2010 [2]. International Energy Agency (IEA) forecasts a 36% rise in energy demand in 2035 in respect to 2008 [3].



OECD: Countries within the Organisation for Economic Co-operation and Development [1]

Figure 1.1 World energy consumption, 1990-2035 [4]

Despite the soar of global energy demand, the source of energy has not been much diverted from the fuel used 40 years ago. Fossil fuels still account for over 80% of the energy supplied to the market in 2011. In addition to the imbalance in the demand and supply of energy resources, the growing attention on the environmental impact raised by energy production has also strengthened the demand for alternative energy sources. Rise of the emission of green house gases owing to the heavy reliance on fossil fuel is one of the major environmental concerns. Over the last 20 years CO<sub>2</sub> emission from the combustion of fossil fuel alone has increased by 50%[5]. Dependence on petroleum, especially from automotive industry has laid a heavy burden on air pollution. Although the global automobiles production has experienced some downfall due to the financial crisis in 2008 and 2009, the long term global demand is still believed to escalate due to the emerge of some developing market such as Asia[6]. Climate change brought by greenhouse gas emission results in the imbalance of the ecosystem. The adverse disturbance on the cycling of resources such as water, agricultural supply and the habitat endangers the survival of many species. The control of the emission of green house gases is now an important environmental issue worldwide. Substituting petroleum by an emission-free fuel is the ideal solution. Hydrogen, a carbon-free high energy content gas, is a promising alternative fuel. Hydrogen is an energy vector which carries high amount chemical energy [7]:

Table 1.1 Energy content of common fuels

	Lower Heating Value (MJ/kg) <sup>1</sup>	Higher Heating Value (MJ/kg) <sup>2</sup>
Natural gas	47.14127	52.22466
Gasoline	43.44804	46.5357
Coal	22.7322	23.96762
Hydrogen	120.2116	142.1814

<sup>1</sup> Lower heating value = heat released by combusting a specified quantity (initially at 25°C) and the temperature of the combustion products return to 150°C, assuming that the latent heat of vaporization of water not recovered.

<sup>2</sup> Higher heating value = heat released by a specified quantity (initially at 25°C) once it is combusted and the products have returned to a temperature of 25°C, taking into account the latent heat of vaporization of water.

It can be easily oxidized by combining with oxygen to form water, releasing heat and energy which can be utilized for other application:



Utilization of the rich chemical energy in hydrogen is made possible through hydrogen fuel cell, which converts chemical energy in the gas to electricity by the combination of hydrogen and oxygen (from air) through a catalysed electrochemical process. Unlike internal combustion engine, the theoretical efficiency is not limited to the conventional Carnot cycle. In a Carnot heat engine, the efficiency ( $\eta$ ) is limited by the temperature of isothermal heat addition ( $T_H$ ) and rejection ( $T_C$ ), e.g. at  $T_H = 700 \text{ K}$  and  $T_C = 300 \text{ K}$ ,  $\eta = 38\%$ . The conversion of chemical energy in the hydrogen to electricity or mechanical energy is highly efficient in a fuel cell and the ideal efficiency can reach up to 83% at 298 K and 1 atmosphere. Newly developed fuel cell system achieves energy conversion efficiency at around to 40-50, and is highly advantageous over gasoline-powered internal combustion engine powered, which has an efficiency of around 20%[8]. Hydrogen fuel-cell powered vehicles are regarded as one of the most promising alternative technology for future transportation. The replacement of gasoline engine, which ejects  $\text{CO}_2$  directly to the environment in automobiles, is an effective solution in abating  $\text{CO}_2$  emission in the transport sector. Usage of hydrogen fuel cell can be extended to power supply for remote locations or portable devices. In addition, it is a good medium for energy storage in complementary to other renewable energy production method such as wind power, solar power and hydrothermal power, where energy produced is mainly in form of electricity and cannot be stored easily.

#### 1.1.1.2 Transition from fossil fuel to renewable energy

The transition of the traditional fossil fuel energy system to renewable fuel system such as hydrogen is still at an early stage. The prevalence of hydrogen energy depends on the level of accomplishment in the development of a new energy chain. Unlike the current fossil fuel and nuclear energy system, where resources are extracted from the earth while the pollutants and residual are left as an open-end issue, the hydrogen energy system should be a materially closed system[9]. Renewable energy sources, such as solar light, wind or biomass should be utilized for material conversion to hydrogen. While energy is used, only

water will be emitted and could re-enter the energy chain through biomass growth or being splitted into H<sub>2</sub> and O<sub>2</sub> again.

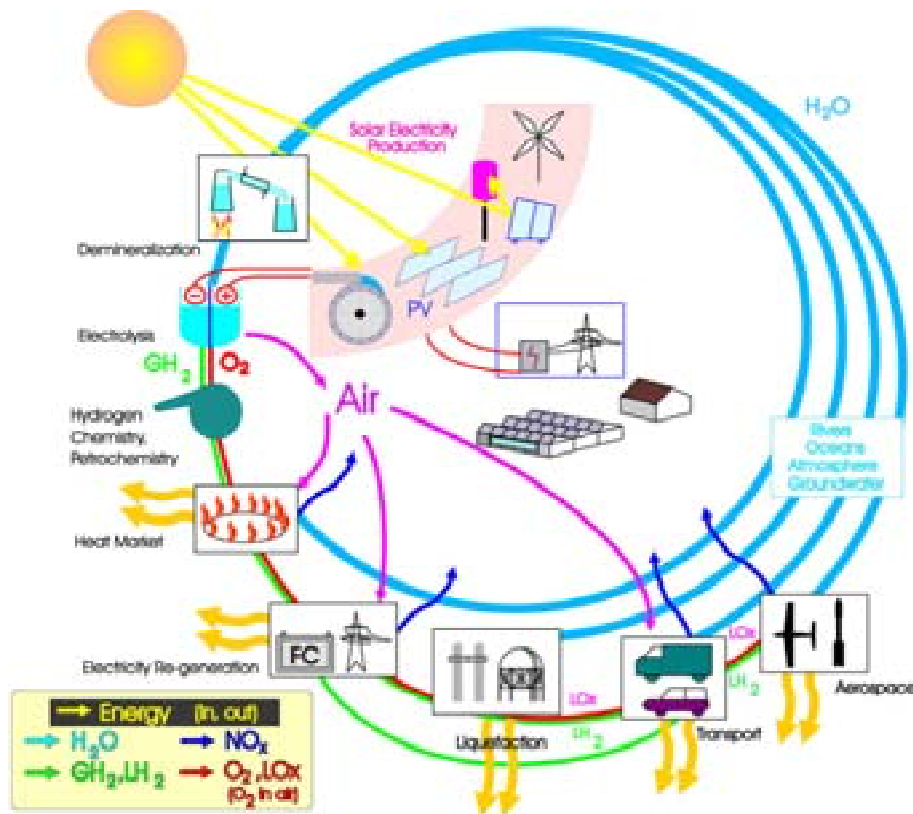


Figure 1.2 Materially closed hydrogen energy systems [9]

The establishment of this cycle has to be accomplished at different levels from production, storage, transport, dissemination to utilization. The development of infrastructure plays a critical role for the commercialisation of hydrogen. Costs other than hydrogen production account for no less than 20% of the total cost for hydrogen utilization[9]. The form in which hydrogen is stored and transported and the availability of hydrogen refuelling facility could be a very high stake in the hydrogen economy [10]. Feasibility and the risk of developing of hydrogen supply network[11-13], home fueling [14] or refuelling station[12, 15] being assessed on a region-wide or nation- wide scale[16, 17] by academics and governmental groups. Breakthrough in technology for hydrogen supply would be a key to the future success.

### 1.1.2 Current market of Hydrogen

The hydrogen production worldwide is about 65 million tonne per year nowadays[18]. Over 90% of the hydrogen produced is consumed by two industries: 1) production of ammonia, which is further utilized for fertilizer production 2) refinery of heavy petroleum to lighter hydrocarbons through hydrocracking for fuel production. Other uses of hydrogen are still confined mainly to chemical industry, such as pharmaceuticals, metal production and fabrication, food processing, laboratory research, electronics etc.

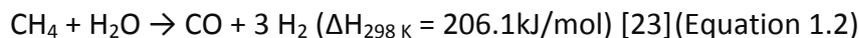
The demand of hydrogen in the first two sectors is expected to increase because of the growing demand in agriculture and extraction of fuel from non-petroleum sources[19]. Other than the conventional usage of hydrogen, hydrogen use as energy carrier is a vast emerging sector, and is expected to be a dominating sector of the hydrogen demand in the future. Major automobiles manufacturers have committed to launch commercial hydrogen fuel cell vehicles by 2015[20]. U.S. government also foresees the penetration of hydrogen fuel cell vehicles into the consumer market in 2020 [21].

### 1.1.3 Hydrogen production and efficiency

#### 1.1.3.1 Current production of H<sub>2</sub>

At present, the major resources used for hydrogen production is still fossil fuels. Natural gas provides close to 50% of total hydrogen production, while 30% comes from refinery off-gases, 18% from coal, and the rest is provided by electrolysis. Three main chemical processes are adopted for hydrogen production from natural gases<sup>[22]</sup>: (1) Steam reforming (steam methane reforming – SMR) (2) Partial oxidation (POX) (3) Autothermal reforming (ATR).

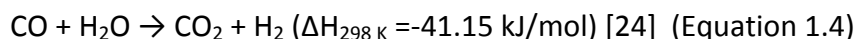
Natural gas is composed of 70-90% of methane. Steam reforming of methane is a 2-stage endothermic process. Methane reacts with high-temperature steam (700°C–850°C) at pressure 3–25 bar in the presence of a catalyst (usually nickel-based catalysts), producing hydrogen, a small amount of carbon dioxide and about 12% of carbon monoxide



Partial oxidation of natural gases is the combustion of methane with oxygen in an amount insufficient for the complete oxidation, such that hydrogen is formed instead of water:



Partial oxidation of methane is an exothermic process, such that energy requirement and heating facility for its operation is not a factor as critical as steam reforming. As seen from the reaction stoichiometry, this process initially produces less hydrogen per unit of the input fuel than is obtained by steam reforming of the same fuel. Autothermal reforming is a combination of both steam reforming (eq. 1.1) and partial oxidation (eq. 1.3) and is also exothermic. Steam reforming process is, though a more efficient process, a higher cost process as reactor units of larger scale are usually required. The carbon monoxide in the product stream of steam reforming or partial oxidation can be converted to carbon dioxide and hydrogen via water gas shift reaction:



The major exhaust of these processes is CO<sub>2</sub>. Capture of CO<sub>2</sub> from point emission source like natural gas reforming exhaust could be processed by pre-combustion or post-combustion capturing such as solvent (e.g. amine) scrubbing or oxy-fuel combustion. Despite the technology developed for CO<sub>2</sub> capture, the exhaust gas stream is still hardly completely cleaned of CO<sub>2</sub>. In addition, extra cost and energy are required for this process. The

effective solution to the abatement of CO<sub>2</sub> level should be the development of non-carbonaceous source for hydrogen production process.

### 1.1.3.2 CO<sub>2</sub> emission free hydrogen production

Water is one of the most abundant reserves of hydrogen. Hydrogen can be produced by splitting water molecule:



The reaction for this process itself does not involve any emission of CO<sub>2</sub>. Electrolysis is the most common method for water splitting nowadays. However the high amount of energy required in water splitting may engender the same problem as fossil fuel unless renewable energy is applied. Thus the development of water splitting in combination with renewable electricity production such as hydroelectric power or wind power or photovoltaic system is necessary.

Direct utilization of solar energy for water splitting through photo-catalytic process is a potential solution for hydrogen production. The energy loss through the production of electricity could be eliminated. Photo-electrochemical process [25] and photo-biological process [26-28] are now widely studied. The model of photo-electrocatalytic water splitting was proposed in 1970s by Fujishima et Honda [29]. The concept involves the use photo-electrocatalytic materials [30-34], usually a semi-conductor with a bandgap suitable for solar light absorption such as TiO<sub>2</sub>, as photoelectrode. The material surface, when excited by solar light, generates electron-hole pair which carries oxidative potential and can dissociate water. The efficiency depends largely on the intrinsic properties and morphology of the material such as bandgap of material, efficiency of light absorption. Development of photo-sensitive materials is a very critical factor for this process and long term development for materials of higher efficiency is needed. Photo-biological hydrogen production originates from plant's photosynthetic capability [35]. One important characteristic of this biological route is its convenience as it operates under ambient condition. Therefore it requires less additional energy input for production process operation. Plants like algae [26, 36, 37] and cyanobacteria [28, 38, 39] possess the enzyme hydrogenase which can catalyse water splitting during photosynthesis. The activity of hydrogenase can be inhibited by oxygen evolved during the process. Research initiative on increasing the tolerance of bacteria to oxygen is taken.

### 1.1.3.3 Hydrogen from biomass

H<sub>2</sub> derivation from biomass could be regarded as a CO<sub>2</sub> neutral route, as the CO<sub>2</sub> produced during hydrogen generation is taken back during photosynthesis for plant growth. Biomass is produced via photosynthesis during plant growth. Common biomass for hydrogen production such as sugar [40, 41] or cellulose [42, 43] are composed mainly of carbon and hydrogen and are materials of high chemical energy. Biomass could be derived from various sources ranging from agricultural waste to high energy crops such as sugar cane. Unlike fossil fuels, which requires additional energy for mining and processing, biomass is readily available for hydrogen production. Hydrogen production from biomass could be carried out via biological route through fermentation [44-46] or through thermochemical reactions such as pyrolysis and gasification [47-50]. Biomass is decomposed during pyrolysis at high temperature (650-800 K) in an inert environment to form a mixture of oxygenated compound [51] including acid, aldehyde, alcohol, ketone sugars and aromatics, which is commonly categorized as bio-oil [52]. Bio-oil can serve as feedstock for hydrogen production through catalytic steam reforming [53]. Carbon is also a common product of pyrolysis, especially for slow pyrolysis (low temperature and longer residence time), which can be used in combustion for energy generation. Other method for bio-oil production includes liquefaction, where biomass is treated at relatively low temperature (525-600 K) in water at higher pressure (5-20 MPa). The hydrogen production yield is usually lower from liquefaction, and is more adopted for bio-oil production, which can then be converted to H<sub>2</sub> by other processes such as steam reforming.

Biomass gasification is a high temperature (1200-1400 K) process, where solid carbon fuel undergoes partial oxidation to form charcoal and gas, which then combines with steam or other hydrogen sources to form syngas. The output gas mixture contains CO, H<sub>2</sub>, CO<sub>2</sub> and CH<sub>4</sub>. A series of complex reactions such as cracking, partial oxidation, steam gasification, water gas shift reaction and methanation are involved during gasification and the occurrence of each reaction depends mainly on temperature and pressure.

## 1.2 Ethanol steam reforming reaction

### 1.2.1 Bio-ethanol for hydrogen production

Among most biomass derived fuel, ethanol is a proper choice for the feedstock of renewable hydrogen production. It has high hydrogen content. It is non-toxic and easy to be handled and stored. Its convenience allows it to be a potential fuel for the on-demand production of hydrogen for fuel cells. The production of ethanol from biomass like sugar is a well-developed process. Anaerobic fermentation of sugar is one of the most widely adopted processes for ethanol production:



Ethanol has been already adapted for fuel use in complementary to gasoline in U.S. [54] and Brazil [55]. There is a strong support for the use of ethanol as fuel due to an abundant growth of energy crops such as corn and sugarcane in both countries. Though still not

commercially available in massive scale, initiative of using agricultural residue such as wheat stalk [56] has increased in order to divert the source of ethanol to lower the price of raw materials [57]. Most crop wastes are composed of lignocellulose, mixture of cellulose, hemicellulose and lignin [58, 59]. Sugar could be extracted by enzymatic hydrolysis of cellulose contained in these materials, and then ethanol could be produced by fermentation [60]. It was shown that the price for ethanol as fuel can be significantly lowered and be more competitive against traditional fuel with improved technology and mass production:

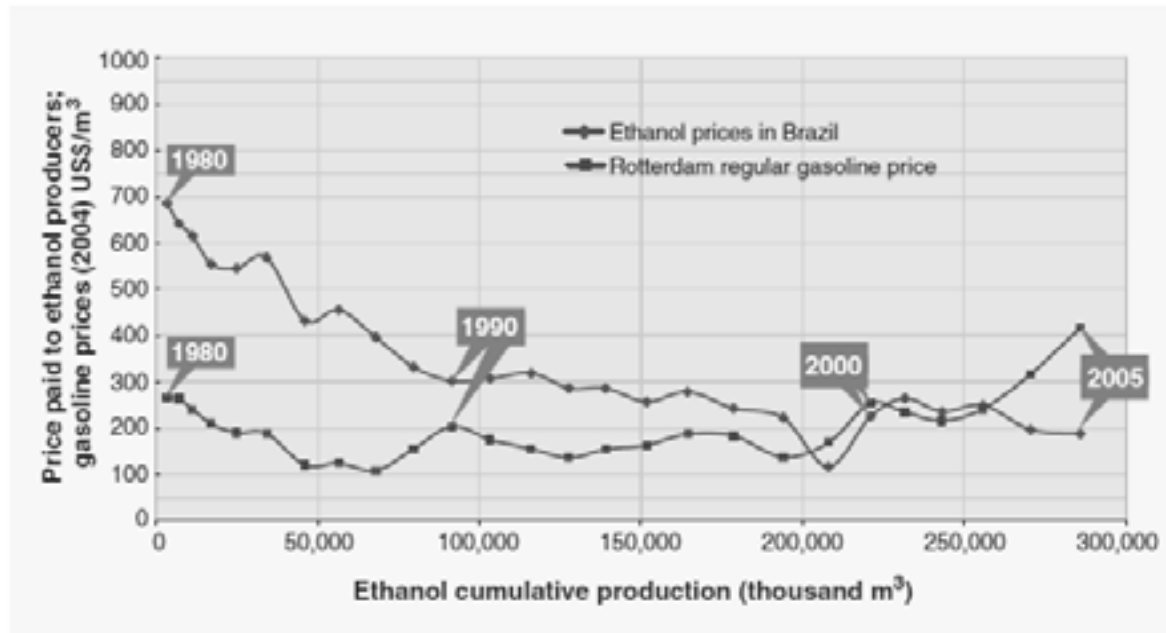
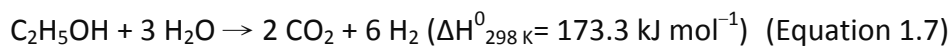


Figure 1.3 Ethanol learning curve in volume, comparing the price paid to ethanol producers in Brazil with the price of gasoline in the international market of Rotterdam [55]

## 1.2.2 Reaction networks and intermediates

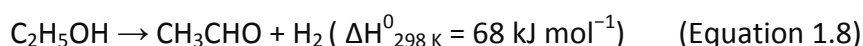
Steam reforming is a process for hydrogen production from the reaction of high temperature steam with hydrocarbon fuels. Steam reforming of ethanol is an endothermic reaction requiring the input of ethanol and water in a molecular ratio 1:3, forming  $H_2$  and  $CO_2$  as products:



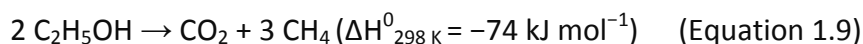
Ethanol steam reforming process involves a complex reaction network, in which the reaction pathways are strongly influenced by the nature of the catalysts and the operating condition. The major reactions involved are dehydrogenation, decarbonylation and dehydration. Apart from the production of desirable end products  $H_2$  and  $CO_2$ ,  $CO$ ,  $C$  and other more complicated reaction intermediates are also involved. Some common reaction pathways will be described in the following.

### 1.2.2.1 Initial steps of ethanol conversion

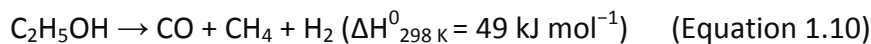
Dehydrogenation of ethanol takes place commonly as a first step in ESR, forming hydrogen and acetaldehyde:



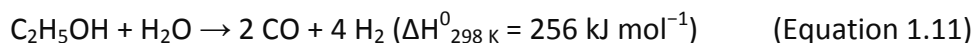
Ethanol decomposition into CO<sub>2</sub> and CH<sub>4</sub> is a probable reaction pathway, especially at low temperature as it is an exothermic reaction:



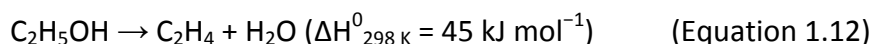
Another ethanol decomposition reaction involves the release of H<sub>2</sub> and may take place under thermodynamically favourable condition:



In case of insufficient steam supply, CO is generated in the substitution of CO<sub>2</sub>.



One of the unfavourable reactions is dehydration of ethanol, which produces ethylene. It can further polymerize and deposit as coke on the catalyst. This reaction can be easily activated on acidic metal oxide, which is a common ESR catalyst support [61, 62]



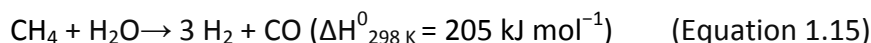
### 1.2.2.2 Acetaldehyde conversion

The reaction intermediates generated from the above reactions can undergo further reforming reaction or decomposition to form more stable end products. Acetaldehyde could undergo further reforming reaction or be decomposed to methane and carbon monoxide:

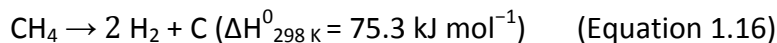


### 1.2.2.3 Methaneconversion

Generation of methane is selective to certain catalyst such as Ni[63] and Pt[64] as C-C bond scission is favoured on these surfaces. In sufficient supply of H<sub>2</sub>O and thermodynamically favourable condition, CH<sub>4</sub> could be further converted to hydrogen and CO by steam reforming:

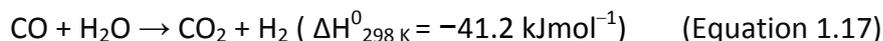


Methane decomposition is another possible reaction, which is less endothermic compared to steam reforming:

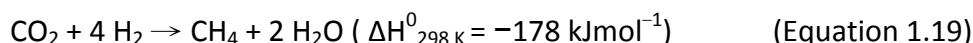
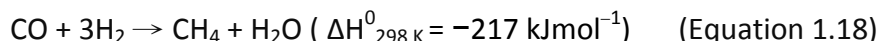


#### 1.2.2.4 Carbon monoxide and carbon dioxide conversion

In excess supply of steam, CO can also contribute to hydrogen generation via water gas shift reaction. This reaction is favoured at low temperature as it is an exothermic reaction:

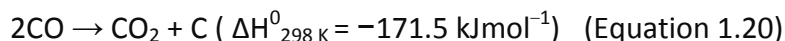


Hydrogen selectivity could be adversely affected by methanation. It is a synthetic gas production process utilizing CO, CO<sub>2</sub> and H<sub>2</sub> for the formation of CH<sub>4</sub>. It is highly exothermic and is favourable at low temperature. Therefore the control of methane production is a substantial criteria for an efficient ethanol steam reforming process

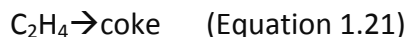


#### 1.2.2.5 Coke formation

One major catalyst deactivation mechanism is coke formation. Ethylene, CO and CH<sub>4</sub> are the major intermediate species involved in coke formation. With insufficient steam input, or at low reaction temperature, CO and CH<sub>4</sub> become the dominating products in the process with, as indicated from equation 10, 12 and 14. CO is susceptible to formation of coke via Boudouard reaction, which is a highly exothermic reaction:



Carbon can also be formed via ethylene polymerization:



Summarizing the above reactions, high level of CO, CH<sub>4</sub> and C<sub>2</sub>H<sub>4</sub> is unfavourable to both H<sub>2</sub> selectivity and catalyst stability. Catalyst with high selectivity to the above products should be avoided for ESR.

### 1.2.3 Bond dissociation of ethanol

The development of quantum theoretical methods extends the understanding of ethanol steam reforming reaction to the energy of equilibrium structures, molecule adsorption energies, activation energies for reaction paths on metal surfaces. Reaction network and intermediate formation are affected by the energy of bond cleavage in molecules on metal surfaces. Wang et al.[65] have evaluated the energy barrier of bond dissociation of ethanol on the (111) surface of selected noble and transition metals. The potential energy surface of ethanol decomposition intermediates on metal surfaces was calculated by first principle taking into account mainly four types of bond dissociation process: the cleavage of C-C, C-O, and dehydrogenation of C-H and O-H bond dissociation. The initial steps involving the lowest energy barrier is the dissociation of O-H bond such that stable intermediate CH<sub>3</sub>CH<sub>2</sub>O-M is formed. The dehydrogenation of methyl group H-CH<sub>2</sub>-CH<sub>2</sub>-O- involves then the lowest energy, notably on Rh and Ir surface. The the unit cells of Rh and Ir are of an optimum metal-metal bond distance for stable five-member ring intermediates, M-C(H<sub>2</sub>)C(H<sub>2</sub>)O(H)-M or M-C(H<sub>2</sub>)C(H<sub>2</sub>)O-M. The breaking of C-C bond as initial steps on ethanol

molecule involves high energy of dissociation compared to cleavage of other bonds such as C-O, C-H or O-H, but is energetically more favourable on intermediates  $M-C(H_2)C(H_2)O(H)-M$  and  $M-C(H_2)C(H_2)O-M$ . Subsequently decomposition could take place via C-C bond breaking through these intermediates. They have shown that among the 9 noble and non-noble metals studied, Ir, Co and Rh shows the lowest barrier to bond dissociation. In addition, the higher DOS distribution near the fermi level of Rh and Ir leads to a higher redox capability of these metals and allows them to be more efficient in CO oxidation during water gas shift reaction.

#### 1.2.4 Consideration on reaction thermodynamics

As shown in the above sections, ESR involves a complex reaction network. A number of thermodynamic studies have been conducted to illustrate the stability of different reaction intermediates and their correlation with the efficiency of ESR [66-74]. As shown from the equations (with the respective reaction enthalpy) above, reforming of ethanol (eq. 1.7), (eq. 1.11), and methane (eq. 1.15) are all endothermic while decomposition of ethanol (eq. 1.9) and steam reforming of acetaldehyde (eq. 1.3, eq. 1.14) are exothermic reactions. It could be predicted that reforming reaction would be favoured at high temperature and decomposition of ethanol proceeds at low temperature. Of the reaction intermediates involved and shown in the above reactions, CO, CO<sub>2</sub>, H<sub>2</sub> and CH<sub>4</sub> are mainly considered as stable reaction products in many thermodynamics studies [67]. Acetaldehyde, ethylene, and acetone are regarded as thermodynamically unstable and present as intermediate species of an incomplete reaction [69, 74]. Their presence implies that the operating ESR process is under kinetic control and is not in global equilibrium. These products should not be present in the gas output stream with sufficient contact time [73]. Under most reaction conditions, formation of ethylene and acetaldehyde take part as the initial step of ESR [75-77]. Presences of these two species are notably observable at low temperature [78, 79]. Mas et al. have shown that the decomposition of ethanol to acetaldehyde (eq. 1.8) increases with temperature and is in competition with the dehydration of ethanol to ethylene (eq. 1.12). The extent of ethylene generation reaches a plateau at 500 K and decreases at  $T > 500$  K. In order to avoid excessive ethylene production the minimum temperature of reaction should be maintained above this level.

When the reaction is in equilibrium, acetaldehyde is just an intermediate product and is prompt to further reaction by either reforming (eq. 1.13) or decomposition (eq. 1.14), which involves the rupture of C-C bond forming simpler molecules such as CH<sub>4</sub> and CO. Reforming of CH<sub>4</sub> (eq. 1.15) and water gas shift reaction (eq. 1.17) are side reaction that can contribute to higher hydrogen selectivity. Reforming of methane is thermodynamically favourable between 700 K and 850 K in a wide range of steam to ethanol ratio (1:1 to 10:1) [73]. The yield of CH<sub>4</sub> evolves inversely with the yield of H<sub>2</sub> both in theoretical studies [66, 67, 73] and experimental studies [80, 81], showing that it is in competition for hydrogen atom and unfavourable for formation of H<sub>2</sub>.

The utilization of CO is another important criterion for consideration in reforming process as the production of CO is inevitable. CO is poisonous to noble metal catalysts, which are commonly used for fuel cells. Consumption of CO by water gas shift reaction (eq. 1.17) is a reversible reaction. Inverse water gas shift reaction can also take place in case of a high CO<sub>2</sub> concentration in the reaction stream, where the equilibrium is shifted reversely. Owing to its exothermic nature, this reaction is favoured at low temperatures. Nevertheless, the extent of water gas shift reaction is positive under all temperature. The extent of reaction reaches a plateau and declines at  $T > 800$  K [73]. Since its energy requirement is different from reforming reactions, in practice water gas shift reaction can be treated in a separate reactor in connection with the reforming exhaust.

### 1.2.5 Critical parameters for reaction efficiency

From thermodynamic point of view, the crucial factors for the efficiency of the reaction are temperature, steam to water ratio and pressure. Garcia et al. have performed a thermodynamic study on ESR in the temperature range 400-800 K to assess the influence of the above parameters. They have assumed that the process results in 4 end products: CO, CO<sub>2</sub>, H<sub>2</sub>, CH<sub>4</sub>. Temperature is the first and foremost parameters for product yield. Hydrogen yield increases with temperature and pressure; significant amount of hydrogen can be obtained at  $T > 550$  K and. High selectivity H<sub>2</sub> and CO is obtained at high temperature, low pressure and high water to ethanol feed ratio. The selectivity to CH<sub>4</sub> decreases above 600 K. Vasudeva et al. [66] have extended the thermodynamic study to higher temperature range (800-1200 K) and water to ethanol ratio based on a model with 6 products and intermediates: C<sub>2</sub>H<sub>4</sub>O, CH<sub>4</sub>, CO, CO<sub>2</sub>, C<sub>2</sub>H<sub>4</sub> and C. The correlation between H<sub>2</sub> selectivity and operating conditions such as pressure and temperature found in their study are very similar to the study of Garcia et al. The studies of these two groups have also shown highly coherent results in the influence of water to ethanol ratio to H<sub>2</sub>, CO and CH<sub>4</sub>. CO<sub>2</sub> and H<sub>2</sub> selectivity increases with increasing steam to ethanol ratio, while selectivity to CO and CH<sub>4</sub> rises when the feed ratio is under 10:1 and decreases rapidly above this point [67]. Correspondingly, the study of Vasudeva et al. [66] shows that H<sub>2</sub> selectivity increases with increasing steam to ethanol ratio, in which the increase in the rate of hydrogen production slows down at steam to ethanol ratio above 10:1. Similar results were obtained by Rossi et al. who have shown that hydrogen production increases only for low ethanol to water ratio at high temperature [82].

The influence of process parameters on the coke formation is more disputable. Generally most studies have concluded that carbon formation is lessened with high water to ethanol ratio and at high temperature. Garcia et al. [67] suggested that C formation would not appear at steam to ethanol ratio higher than 10:1 at all temperatures. When the ratio is lowered to 2:1, process temperature has to be above 600 K to avoid carbon formation [67]. Vasudeva et al. [66] has proposed different results on carbon formation, that C formation at feed ratio 2:1 would still take place at 900 K. They have considered additionally the presence of more intermediates species such as acetaldehyde and C was treated as an

element in equilibrium in the reaction. Mas et al. estimated that coke formation could be avoided above 500 K in water to ethanol ratio 3:1. Similar scenario has been predicted by other groups at the same feed ratio [82, 83]. Rossi et al. shows that reduction of carbon formation at low steam to ethanol ratio (1:1) requires higher reaction temperature (973 K). If input of steam to ethanol is increased to 3:1, the threshold temperature to avoid carbon formation is lowered to 523 K and could be lowered to 423 K at higher steam to ethanol ratio (5:1) [83].

As described previously, the formation of unstable intermediate species is likely to be detected if the process is under kinetic control. Contact time and gas flow rate of reactant stream determines if the reaction is under kinetic control or thermodynamic control. Silva et al. [72] have performed theoretical evaluation of the performance of ESR at different contact times. At low contact time, ethanol conversion reaches 99% at  $T > 500$  K and the conversion efficiency is independent of the steam to water ratio unless temperature drops below 400 K. Hydrogen and acetaldehyde production increases with temperature and the number of moles of hydrogen and acetaldehyde produced is equivalent at low contact time.  $C_2H_4$  production is in general primarily dependent on the temperature of reaction, but the number of moles of ethylene generated is much higher at a low contact time.

In terms of carbon deposition, though the influence of steam to ethanol ratio has been described above, but its significance reduces at low contact time. Temperature remains as the most crucial factor. In contrary to previous discussion that carbon formation could be avoided at high temperature and steam to ethanol ratio, a significant amount of carbon deposition is predicted at high temperature at low contact time. At high contact times, acetaldehyde and ethylene are not present in the reaction stream. Carbon deposition is much lower and the correlation between carbon formation and other factors such as temperature and steam to ethanol ratio is in good agreement with the finding from other literature as described in previous paragraphs. Hence, high contact time provides a stable ESR system which improves significantly carbon deposition. A low contact time, unstable reaction intermediates such as acetaldehyde and ethylene is produced as a result of the loss of reaction equilibrium. This has demonstrated also the close relation between the presence of acetaldehyde and ethylene production in the product stream and carbon deposition.

### **1.3 ESR catalyst current status**

#### **1.3.1 Transition metal catalysts-Nickel and Cobalt as ethanol steam reforming catalyst**

Catalyst is the core of ethanol steam reforming reaction. Vast amount of effort has been dedicated to the catalyst research. An important consideration for catalyst design is to have high ethanol conversion efficiency, high selectivity to hydrogen and high resistance to deactivation. In order to improve energy efficiency, the catalyst developed should be able to improve the ethanol conversion efficiency at low temperature. Noble metal catalysts are commonly regarded as very efficient catalysts. Liguras et al. [62] have investigated ESR on several noble metals (Rh, Ru, Pt, Pd), in which Rh exhibits the highest activity and selectivity

in the temperature range 600–850 °C. Non-noble metal catalysts are widely investigated with raising interest as they are economically more advantageous. Ethanol conversion efficiency of certain non-noble metal catalysts such as nickel and cobalt is highly comparable to Rh. Aupretre et al. [75] has compared the activity and selectivity to H<sub>2</sub> of a range of noble metal (Rh, Pt, Pd, Ru) and non-noble metal catalysts (Ni, Cu, Zn, Fe) supported on  $\gamma$ -Al<sub>2</sub>O<sub>3</sub>. Among all metal catalysts, Rh and Ni achieve the highest selectivity to H<sub>2</sub> and CO<sub>2</sub>. Other comparison experiments have been performed on Rh, Pd, Co and Ni supported on MgO [84]. Selectivity to hydrogen of Rh, Ni and Co all reaches over 90%. However ethanol conversion on Ni and Co drops significantly after 10 hours of reaction time, while Rh maintains its high activity over a long reaction time. Post-reaction catalyst characterization such as transmission electron microscopy (TEM) and elemental analysis shows that Ni and Co suffers from severe metal sintering and coke formation.

Despite the concern in catalyst deactivation, Ni and Co are the most promising transition metal catalysts for ESR. Utilization of proper metal oxide as catalyst support has been proven to be an essential factor for the improvement on catalysts' efficiency and stability. Stable metal oxide support assists in stabilizing the distribution and thus the size of the catalyst. Moreover the properties of catalyst and its active phase can be altered by metal-support interaction.

#### **1.3.1.1 Nickel as ESR catalyst**

Nickel catalysts transform to various phases when supported on different metal oxide. Nickel located at the metal support interface tends to form oxides [85-87]. The reducibility of metal catalyst is influenced by the difference in chemical potential between metal and metal oxide, and also the defect sites available on metal support. Interfacial Ni oxide is more stable than surface Ni oxide and is more difficult to reduce. On Ni/ZrO<sub>2</sub> [85], apart from surface and interfacial Ni oxide, a third type of NiO is formed by impregnation to ZrO<sub>2</sub> oxygen vacancy. It possesses higher reactivity to the other two types of NiO. In addition, this new oxide phase can stabilize and reduces Ni particle size and improve catalyst efficiency [88].

Fatsikostas et al. has evaluated ESR on Ni catalysts supported on  $\gamma$ -Al<sub>2</sub>O<sub>3</sub>, La<sub>2</sub>O<sub>3</sub>, La<sub>2</sub>O<sub>3</sub>/ $\gamma$ -Al<sub>2</sub>O<sub>3</sub> [89]. They have deduced the roles of Ni in ESR based on the comparison of ethanol temperature programmed desorption (TPD) of bare metal oxide support and metal oxide supported nickel catalysts. At low temperature (<100°C), the reaction is primarily dominated by the decomposition of ethanol, generating CO, CH<sub>4</sub> and H<sub>2</sub> as the main products. Between 200 and 350°C, H<sub>2</sub> is observed as the only product and is mainly produced from ethanol dehydrogenation. Above this temperature, CO and CO<sub>2</sub> are given off due to the oxidation of carbonaceous species deposited at lower temperature. For Ni/Al<sub>2</sub>O<sub>3</sub>, the reaction is largely dominated by cracking and dehydrogenation of ethanol below 250°C. Water-gas shift reaction and Boudouard reaction are also involved at higher temperature. On La<sub>2</sub>O<sub>3</sub>-Al<sub>2</sub>O<sub>3</sub> supported Ni, preference to dehydrogenation increases and compete against ethanol dehydration, and thus reduces formation of C<sub>2</sub>H<sub>4</sub>. In connection with another work from this

group, which has extended the study of nickel catalyst on YSZ and MgO [90] support, it was concluded that Ni/La<sub>2</sub>O<sub>3</sub> exhibits the highest ethanol conversion efficiency (100%), hydrogen selectivity (>90%) and stability.  $\gamma$ -Al<sub>2</sub>O<sub>3</sub> supported Ni is prompt to C<sub>2</sub>H<sub>4</sub> formation and causes the most severe carbon deposition. Yang et al. [91] have compared Ni supported on ZnO, La<sub>2</sub>O<sub>3</sub>, MgO and  $\gamma$ -Al<sub>2</sub>O<sub>3</sub>. The selectivity to hydrogen on ZnO and La<sub>2</sub>O<sub>3</sub> is significantly higher than on the other two metal oxide supports. These differences in activity of supported Ni are contributed by the difference ethanol adsorption behavior of the support.

The influence of metal loading of nickel to ESR seems disputable. It was found that it can be of minor influence to the H<sub>2</sub> selectivity and ethanol conversion on certain nickel based catalytic systems Ni/CeO<sub>2</sub>, Ni/ZrO<sub>2</sub> [92] Ni/Al<sub>2</sub>O<sub>3</sub> [63]. However on ZnO supported Ni [91], increase in Ni loading (from 5% to 20%) can decrease product selectivity to other reaction products such as CO, though close to 100% ethanol conversion is obtained regardless the amount of loading. The studies of Molina et al., where they have compared the alumina supported Ni with different loading (<1 wt% and 1.7wt%), and the catalyst with low Ni loading shows a greater resistance to reduction, leaving a higher amount of inactive phase NiO. This illustrates that change in metal loading could alter nickel properties and interactions and is difficult to be considered as a single factor for the reaction.

#### 1.3.1.2 Cobalt as ESR catalyst

Activity of cobalt catalyst and its interaction with a wide range of metal oxide support (MgO,  $\gamma$ -Al<sub>2</sub>O<sub>3</sub>, SiO<sub>2</sub>, TiO<sub>2</sub>, V<sub>2</sub>O<sub>5</sub>, ZnO, La<sub>2</sub>O<sub>3</sub>, CeO<sub>2</sub>, and Sm<sub>2</sub>O<sub>3</sub>) has been studied by Llorca et al. [93]. Among all the metal oxide support, ZnO supported Co catalyst exhibits the best catalytic activity and highest H<sub>2</sub> selectivity. They have reported the advances in the synthesis of ZnO supported Co catalyst by the use of Co<sub>2</sub>(CO)<sub>8</sub> as precursor to achieve high ethanol conversion efficiency and efficient suppression of selectivity to CO at relatively low temperature (623 K) [78]. Corresponding *in-situ* infrared study [79] showed that ethoxy species is produced during ethanol-steam mixture adsorption at room temperature. The ethoxy group transforms into acetaldehyde via dehydrogenation. Similar surface species are also observed on Co/CeO<sub>2</sub> [94] and Co/ZrO<sub>2</sub> [95]. Acetaldehyde is considered as the dominating intermediate for cobalt based catalyst. The acetaldehyde group undergoes reforming or decomposition according to the temperature and generates CO<sub>2</sub>, CH<sub>4</sub> and H<sub>2</sub> as major products. Other side reactions, such as transformation of acetaldehyde into carbonate and methane via acetate formation on Co/ ZrO<sub>2</sub> by the oxidizing effect of metal oxide support has been reported by Song et al. [95].

Formation of cobalt oxide is commonly observed [78, 96] on supported catalyst. Co oxide is formed either at the catalyst-support interface due to metal support interaction or on the surface formed during synthesis. The common forms of Co oxides include: CoO in cubic structure (rocksalt) or hexagonal structure (wurtzite) and Co<sub>3</sub>O<sub>4</sub> as spinel. Surface Co oxide could be reduced in ESR reaction mixture [97], and does not remain as a stable phase under reaction condition. Catalytic activity of Co<sub>3</sub>O<sub>4</sub> is low [97]. Less than 20% of ethanol conversion is achieved at 623 K, in which conversion on metallic Co should be over 90%. The

process is selective only to acetaldehyde and H<sub>2</sub>, showing that Co<sub>3</sub>O<sub>4</sub> favours the dehydrogenation of ethanol. The reaction is activated only when reduction of Co<sub>3</sub>O<sub>4</sub> commences. The selectivity to acetaldehyde decreases and switches to CO<sub>2</sub> and CH<sub>4</sub> as Co<sub>3</sub>O<sub>4</sub> is being reduced. Similar results have been observed [98] in a study of unsupported cobalt catalyst by Llorca et al. However the catalytic performance of ZnO supported Co<sub>3</sub>O<sub>4</sub> is much inferior to the bare catalyst.

The identification of the active role of Co<sup>2+</sup> is more difficult as it is difficult to exclude the presence of metallic cobalt under reaction conditions. In addition, Co<sup>2+</sup> could be involved as cobalt oxide particles or Co ion intermixing with metal oxide support forming a solid metal oxide solution. In-situ X-ray photoelectron spectroscopy (XPS) and Extended X-ray absorption fine structure (EXAFS) techniques [99-101] have been applied to clarify the role of Co at different oxidation state in catalytic ESR. Metallic Co and Co<sup>2+</sup> usually coexist under reaction conditions [78, 99, 102, 103] and they could be both active in this reaction. Reaction of ethanol on oxidized and metallic cobalt surfaces has been studied by Hyman et al. [103] by TPD. They concluded that Co<sup>2+</sup> sites are selective to the production of acetaldehyde. The acetaldehyde species is then oxidized to acetate, which is later decomposed and desorbed as CO<sub>2</sub> on CoO surface. In comparison to CoO surface, metallic Co is more selective to decarbonylation, in which the surface is active for CO desorption at low temperature. In a later study by Martono et al. [104], the ethanol desorption behaviour of ZnO supported Co oxide (mainly CoO) was compared to unsupported Co oxide (formed by oxidation of Co foil). Much lower activity of Co<sup>2+</sup> was observed when it is present in form of ZnO-supported particles. They have attributed the poor activity mainly to the poisoning of adsorption site of ethanol on ZnO support due to the formation of Co<sup>2+</sup> on ZnO. Karim et al. [105] has extended the study of the catalytic role Co and Co<sup>2+</sup> on MgO supported Co nanoparticles. They have observed the presence of a significant amount of Co<sup>2+</sup> in the catalyst even after reduction. This demonstrates that cobalt tends to interact strongly with metal oxide support (MgO), hence cobalt oxidation, or the formation of CoO-MgO solid solution was observed. The efficiency of ethanol conversion is significantly higher on Co<sup>0</sup>, particularly the efficiency in C-C bond breaking. Therefore ethanol conversion increases with increase in Co<sup>0</sup> content. In addition, with the same ethanol conversion efficiency, catalyst of high metal cobalt concentration shows the highest selectivity to hydrogen and low selectivity to CH<sub>4</sub>. It was suggested that reactions which lead to CH<sub>4</sub> generation such as ethanol decomposition or CO/CO<sub>2</sub> methanation are more favourable on Co<sup>2+</sup> than Co<sup>0</sup>, while metallic Co can improve hydrogen yield by efficient C-C bond cleavage and water gas shift reaction.

Influence of crystalline structure of cobalt to the reaction pathway has been studied by Lin et al. [94]. Metallic cobalt is found usually in hexagonal close-packed (hcp) and face-centered cubic (fcc) Co. Hcp Co is common phase present in ambient condition as it is energetically more stable at low temperature. It could be transformed to fcc phase at high temperature (>450 °C). DRIFTS studies has shown that single carbon reaction intermediates

are mainly involved for reactions on hcp Co due to more efficient C-C bond breaking. Hence, higher ESR activity is observed over hcp Co.

### **1.3.2 Bimetallic catalysts**

Application of bimetallic materials in catalysis has demonstrated significant potential. For instance, Pt materials are the main catalyst for polymer electrolyte membrane fuel cells electrode, but it is also prone to CO poisoning. One of the solution is to introduce another component metal such as Ru, which improves oxygen absorption and can assist the oxidation of CO and improve CO poisoning resistance [106]. Bimetallic materials are also widely explored for various heterogeneous catalytic processes such as steam reforming, including Ni-Co bimetallic catalysts [107-110]. Though Ni and Co based catalyst are promising material for their high conversion efficiency and selectivity to hydrogen, their stability remains as an important concern, primarily owing to the high level of carbon deposition on Ni and Co [84, 111] which leads to deactivation of the catalyst. Tolerance to carbon deposition is improved by using bimetallic catalysts [112-114]. Bimetallic interaction leads to formation of new structure and modification of the intrinsic properties with respect to the constituent elements, which also causes alteration of catalyst's interaction to gas phase environment.

The heat of alloy formation shows the tendency of mixing of two metals. When the two metals form stronger bonding between them than the individual element, alloy formation is exothermic and favoured. Formation of ordered solid solution or intermetallic compound may take place at low temperature and disordering takes place at high temperature. In contrary, when bonding between the two metals is weaker than that of their constituent elements, alloy formation is endothermic and clustering of materials with different phases tends to occur at low temperature. Mixing of the different metal phases is possible for endothermic alloy at high temperature.

As far as catalysis is concerned, surface structure and segregation could be the more influential phenomena to be considered. In bimetallic solid solution, surface segregation of the component with the lower heat of sublimation occurs. The degree of segregation increases at higher index faces, edges, and corners. If the alloy formation is exothermic, depletion of the component enriched on the surface in the layer next to the surface would be found, while for endothermic alloy, enrichment of the surface segregated component in the layers next to the surface would occur [115].

Nowadays catalysts investigated are at nanometric scale. The structure of nano-scaled bimetallic materials could be categorized by their mixing pattern into: core/shell structure, heterostructure or homogeneous alloy.

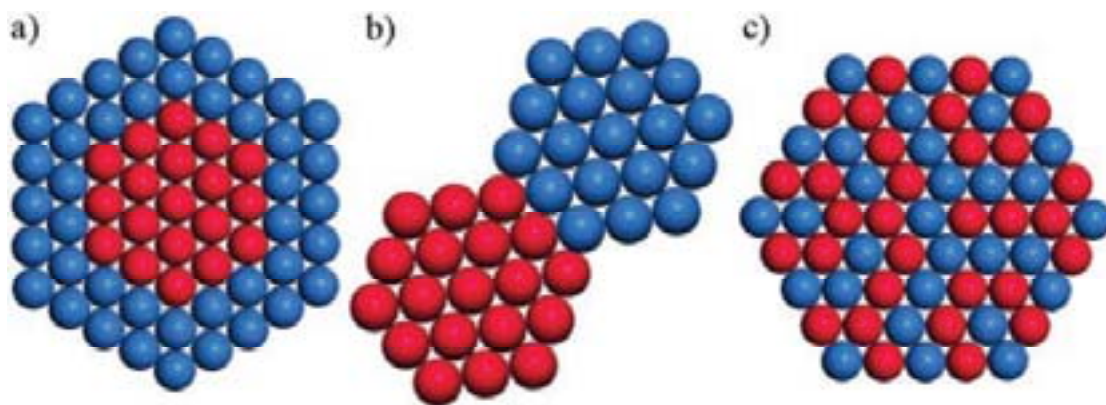


Figure 1.4. Bimetallic nanocrystal with different structures: a) core/shell; b) heterostructure; c) intermetallic or alloyed structures [116].

Formation of core-shell structure involves the segregation of one metal to the surface, resulting in the surface enrichment of one component metal covering a core composed of another metal. Heterostructured bimetallic materials involve formation of clusters of different metals sharing only interfaces between them. Homogeneous bimetallic materials refer to metals in form of randomly mixed solid solution, for example, alloy is a common form of homogenous bimetallic mixtures. Intermetallic compounds refer to metal mixture with long range atomic order, which usually involves a high level of charge transfer between the metals.

Factors concerning the atomic arrangement, such as atomic bonding and atomic size have to be considered when analyzing the segregation phenomena on nano-sized bimetallic materials. Ferrando et al. [117] has summarized the determining factors for segregation in nanoalloys: (1) Relative strengths of A-A, B-B, and A-B bonds. Mixing is favoured with stronger A-B bond and vice versa. (2) Surface energies of bulk elements A and B. Element having the lowest surface energy tends to segregate to the surface. (3) Relative atomic sizes. Smaller atoms tend to occupy the more sterically confined core. (4) Charge transfer. Strong electron transfer to more electronegative elements favors mixing. (5) Strength of binding to surface ligands (surfactants). For supported or passivated clusters, the element that binds most strongly to the support or ligands may be pulled out toward the surface. In practice, alloy structure is under strong influence of the gas environment, in which metals displaying a higher reactivity towards the gas phase are driven to the surface. (6) Specific electronic or magnetic effects. Specific sizes, compositions, or segregation arrangements may be favoured by electronic shell structure or electron spin interactions.

The above bimetallic restructuring has been demonstrated in the *in-situ* XPS study on 15 nm bimetallic Rh-Pd and Pt-Pd nanoparticles in NO, NO+CO and O<sub>2</sub> by Tao et al. [118]. The as-synthesized nanoparticles were found to be Rh-rich and Pt-rich in the surface layer, exhibiting Rh or Pt shell Pd core structure. Drastic restructuring was observed when Rh-Pd nanoparticles were exposed to CO containing gas phase environment. Migration of Rh to the core and Pd towards the surface took place while reduction of Rh and Pd took place simultaneously. The change is reversible by switching the gas composition from oxidizing to

reducing conditions. This effect was not observed on Pt-Pd nanoparticles. This was explained by the difficulty in oxidizing Pt and its high surface energy. The observed synergetic effect can explain the enhanced activity of Pd-Rh towards CO oxidation system [119], where the stronger interaction of O<sub>2</sub> with Rh and CO with Pd leads to preferential adsorption of CO on isolated Pd atoms or islands on the bimetallic catalyst surface and spillover of oxygen adsorbates from Rh to CO-covered Pd reaction sites.

Upon the formation of new structure and composition, the catalyst surface may demonstrate novel properties towards bonding and bond dissociation to reactant molecules. The modification of electronic properties due to alloying and its correlation to the surface reactivity have been tackled both by theoretical and experimental methods. It has been shown in several DFT studies that the bond energies between metal surface and adsorbates can be very well represented by the energy of d-band center. The *d*-band center varies with changes in metal bonding and coordination. It is also sensitive to the bonding with adsorbate as the *s* and *d* states of metal couple with valence states of adsorbate during adsorption. Therefore, the shift in d-band center can be regarded as an indicator for the reactivity of metal surface and the interaction of adsorbate and transition metal catalysts.

Hammer et al.[120] have shown an overview of the shift in d-band center of a supported metal overlayer or surface impurities with respect to clean metal by DFT calculations. Table 1.2 shows the estimated value of d-band center shift of metal overlayer (horizontal) on host substrate (vertical) from the DFT studies of Ruban et al.[120] The d-band center tends to shift up when “early” transition metal elements is supported on top of heavier elements, which implies an increase in interaction with adsorbate molecules such as CO.

Table 1.2 Shifts in d-band centers of surface impurities (1<sup>st</sup> column) and overlayers (2<sup>nd</sup> column) relative to the clean metal values

	Fe	Co	Ni	Cu	Ru	Rh	Pd	Ag	Ir	Pt	Au
<b>Fe</b>	<b>-0.92</b>	0.05	-0.2	-0.13	-0.29	-0.54	-1.24	-0.83	-0.36	-1.09	-1.42
		0.14	-0.04	-0.05	-0.73	-0.72	-1.32	-1.25	-0.95	-1.48	-2.19
<b>Co</b>	0.01	<b>-1.17</b>	-0.28	-0.16	-0.24	-0.58	-1.37	-0.91	-0.36	-1.19	-1.56
	-0.01		-0.2	-0.06	-0.7	-0.95	-1.65	-1.36	-1.09	-1.89	-2.39
<b>Ni</b>	0.09	0.19	<b>-1.29</b>	0.19	-0.14	-0.31	-0.97	-0.53	-0.14	-0.8	-1.13
	0.96	0.11		0.12	-0.63	-0.74	-1.32	-1.14	-0.86	-1.53	-2.1
<b>Cu</b>	0.56	0.6	0.27	<b>-2.67</b>	0.58	0.32	-0.64	-0.7	0.58	-0.33	-1.09
	0.25	0.38	0.18		-0.22	-0.27	-1.04	-1.21	-0.32	-1.15	-1.96
<b>Ru</b>	0.21	0.26	0.01	0.12	<b>-1.41</b>	-0.17	-0.82	-0.27	0.02	-0.62	-0.84
	0.3	0.37	0.29	0.3		-0.12	-0.47	-0.4	-0.13	-0.61	-0.86
<b>Rh</b>	0.24	0.34	0.16	0.44	0.04	<b>-1.73</b>	-0.54	0.07	0.17	-0.35	-0.49
	0.31	0.41	0.34	0.22	0.03		-0.39	-0.08	0.03	-0.45	-0.57
<b>Pd</b>	0.37	0.54	0.5	0.94	0.24	0.36	<b>-1.83</b>	0.59	0.53	0.19	0.17
	0.36	0.54	0.54	0.8	-0.11	0.25		0.15	0.31	0.04	-0.14
<b>Ag</b>	0.72	0.84	0.67	0.47	0.84	0.86	0.14	<b>-4.3</b>	1.14	0.5	-0.15
	0.55	0.74	0.68	0.62	0.5	0.67	0.27		0.8	0.37	-0.21
<b>Ir</b>	0.21	0.27	0.05	0.21	0.09	-0.15	-0.73	-0.13	<b>-2.11</b>	-0.56	-0.74
	0.33	0.4	0.33	0.56	-0.01	-0.03	-0.42	-0.09		-0.49	-0.59
<b>Pt</b>	0.33	0.48	0.4	0.72	0.14	0.23	-0.17	0.44	0.38	<b>-2.25</b>	-0.05
	0.35	0.53	0.54	0.78	0.12	0.24	0.02	0.19	0.29		-0.08
<b>Au</b>	0.63	0.77	0.63	0.55	0.7	0.75	0.17	0.21	0.98	0.46	<b>-3.56</b>
	0.53	0.74	0.71	0.7	0.47	0.67	0.35	0.12	0.79	0.43	

The relationship between the shift in d-band center and chemisorption of molecules on metal or alloy catalysts is of keen interest of study. Pt based surface alloy has been studied in the DFT study of Kitchin et al. [121], where they found a positive shift of surface d-band center and modification in the density of state of Pt(111) when it is modified by subsurface 3d transition metals along the periodic table. The shift in d-band center also correlates linearly to the dissociative adsorption energy of H<sub>2</sub> and O<sub>2</sub> according. Other studies on bimetallic materials on chemisorption of molecules such as CO, O<sub>2</sub> [122] atomic O or H [123] shows also similar linear correlation. These theoretical studies can provide useful fundamental knowledge to rationalize the phenomena observed in experimental studies. The studies from Skyoplyak et al. have demonstrated the high level of correspondence between theoretical studies and experimental results for catalytic reaction. They have shown that the reforming activity of ethanol obtained from TPD are linearly correlated with the d-band center [124] and binding energy [125] calculated on a model based on Ni and Pt adlayer on their respective metal single crystal. While information on the activation of reaction were obtained from DFT studies, information on reaction intermediates and pathway were determined by experimental surface techniques such as high resolution electron energy loss spectroscopy (HREELS) and TPD.

### 1.3.3 Ni-Co based bimetallic catalysts

Ni and Co have rather similar characteristics on bulk binding energies (4.446 and 4.435 eV, respectively) and nearest-neighbor distances (2.506 and 2.489 Å, respectively). As a single metal, they are usually present in different bulk crystalline structures. Face centered cubic structured nickel and hexagonal closed packed cobalt are their stable crystalline structures under ambient conditions. Cobalt, however, undergoes phase transformation to fcc phase under high temperature. Mixing of the two metals results in an alloy with a single crystalline phase of either fcc or hcp depending on the concentration of each metal [126]. On electrodeposited Ni-Co film [127], the two phases co-exist at 65-75% of Co content. Beyond this region Ni-Co film is in single phase according to the abundance of Ni or Co. Similar tendency in crystalline phase formation has also been observed on Ni-Co with other structures, such as Si single crystals supported Ni-Co film [128], unsupported nanoparticles [129] or carbon supported Ni-Co nanoparticles [130].

A number of works have been dedicated to the understanding of surface segregation of Ni-Co alloy [131-133]. Though there is little difference in terms of the surface energy of Ni and Co, calculations of the segregation energy [133] have shown that Ni tends to segregate to the surface in UHV.

Table 1.3 Surface energy of Ni and Co [134]

Surface energy – Co hcp(001)	0.94 eV
surface energy – Ni fcc (111)	0.9 eV

This has been reconfirmed by the studies by Hajcsar et al. [131] on segregation energy of Ni-Co alloy, where they have determined experimentally the energy of segregation on a Ni-Co alloy single crystal. They have deduced the surface segregation energy and entropy of such system from the Arrhenius plot of the ratio of surface to bulk Ni-Co content over a temperature range. They have observed that surface segregation of Ni is favored in UHV, with a segregation energy of  $\Delta H_{\text{seg}} = -17.8 + 1.1 \text{ kJ/mol}$  and  $\Delta S_{\text{seg}} = -11.3 \pm 1.1 \text{ J/mole K}$  for 50% Ni-Co alloy. In spite of this, adsorbate induced segregation is of a greater concern for catalysis. The potential of segregation can be deduced on a theoretical basis by the bond strength of the adsorbate [135] to the metals and the shift of d-band center [136]. Studies from Greeley et al. [137] shows that binding of oxygen on Co as an overlayer on Ni metal substrate is stronger than Ni as an overlayer, and the respective d-band center shift is more positive, resulting in the segregation of cobalt in oxidative environment.

Change in the physical properties by the formation of alloy can be reflected on the improvement of the morphology and size distribution of bimetallic Ni-Co with respect to monometallic Ni and Co. It has been observed by Hibbard et al. that the growth of grain size and the homogeneity of grain formation of nanosized Ni-Co particles obtained by electrodeposition were improved compared to its constituent elements [127]. The thermal stability also increases with increasing Co concentration compared to pure Ni nano particles.

On working catalyst, improvement of coke deposition by Ni-Co bimetallic material for reforming reaction has been observed notably for CO<sub>2</sub> reforming of CH<sub>4</sub> [138-140]. Carbon resistance was improved by increasing cobalt composition in the bimetallic catalyst [141], in which addition of cobalt content improves the oxidation of surface carbon to CO or CO<sub>2</sub>. In addition, bimetallic Ni-Co helps in stabilizing the size of nanoparticles, which also indirectly assist in improving carbon deposition. It was observed in the study by San-José-Alonso et al. [142] that addition of Ni improves the growth of small-sized nanoparticles. The diameter of carbon filament is limited by the small particle size and their growth is thermodynamically unfavourable. In addition, the gasification of carbon is also improved with small particles size. Similar improvement on the stability of nanoparticle size and reduction of carbon filament growth on the small-sized on well dispersed bimetallic Ni-Co particles [110] was also observed by Zhang et al., in which they proposed that the improvement is due to the metal-support interaction by the increase in interfacial surface area.

Apart from deactivation resistance, improvement in catalytic activities for reforming reaction on bimetallic Ni-Co was also observed, for example on Ni-Co/ZrO<sub>2</sub> [139]. Activity of ZrO<sub>2</sub> supported monometallic Co and Ni in methane conversion is very low (<50%), but the conversion of bimetallic Ni-Co/ZrO<sub>2</sub> reached almost 90% and the activity remains stable over time. From *in-situ* XAS (x-ray absorption spectroscopy) study, the bimetallic Ni-Co/ZrO<sub>2</sub> retained at metallic state under all reaction temperature while oxidation took place for monometallic Ni or Co catalyst at reaction temperature lower than 1023 K. The bimetallic catalyst showed better oxidation resistance under reaction condition. In addition, the inactivity of Co, which was due to rapid carbon deposition, was improved by alloying with nickel. The presence of adjacent nickel atoms prevents the deposition of carbon over cobalt sites, such that Co, which is active in C-H bond breaking, can serve as active sites for methane conversion. The high level of H<sub>2</sub> produced assist in maintaining both metals at reduced state. This study has demonstrated the benefit brought by the synergetic bimetallic effect as a catalyst system, in terms of the physical properties (dispersion of catalyst over support), the catalytic performance and the stability of the catalyst.

Though not as widely studied as methane reforming reaction, improvement in coke resistance has equally been observed for ethanol steam reforming. Enhancement in hydrogen yield and inhibition to production of undesirable products by the addition of Co to Ni on YSZ support has been observed in the ESR study by Resini et al. [108]. The addition of cobalt can inhibit ethanol dehydration and methane formation, which are unfavourable reactions related to associated with the support. In addition hydrogen yield at high temperature was improved due to the high activity of Ni-Co in methane steam reforming. The catalytic performance was the best for Ni-Co at a specific composition: Ni-Co (25:25). This study has illustrated that catalyst performance can be improved due to the modification in reaction pathway by the formation of bimetallic catalyst.

### 1.3.4 Metal oxide support and Metal-support interaction

Working ESR catalysts are highly dispersed on metal oxide support. Interaction derived from the formation of the metal-support interface could lead to electronic perturbation, redistribution of atoms and redox interaction [143]. Chemical interaction at metal/metal oxide interface is driven by the difference in electrochemical potential. This interaction could involve diffusion of atoms across this interface and formation of new phases of more than one monolayer. Redox reaction is the most frequently observed chemical interaction at metal/oxide interface. Oxidation of metal by lattice oxygen of the metal oxide substrate has been observed on various systems from model catalysts such as Cu/ZnO(0001) [144], Co/CeO<sub>2</sub>/YSZ(100) [145] to working catalyst system such as Co/ZnO [146] especially at elevated temperature where oxygen diffusion is enhanced [147].

The redox reaction can lead to formation of alloy or intermetallic compound if mixing of the reduced cations from oxide support with the metal layer occurs. Noted examples are noble metal catalyst such as Pt supported on SiO<sub>2</sub>, Al<sub>2</sub>O<sub>3</sub> and CeO<sub>2</sub> [148]. Pt<sub>3</sub>Me (Me = Si, Al, Ce) alloy was formed by reduction in H<sub>2</sub> at temperature up to 1073 K. Formation of the intermetallic compound could possess exceptional catalytic activities for particular system such as Pd-Zn [149]. Pd/ZnO is more reactive than Pd on other metal oxide support for methanol steam reforming due to the formation of PdZn intermetallic compound [150-152]. Interdiffusion is another form of metal and metal oxide support mixing. Diffusion and replacement of cation from metal catalyst to metal oxide creates new oxide phases such as spinel structure. This has been observed on Co/ZnO [153], Co/SiO<sub>2</sub> [154] and Co/MgO [102], where Co is oxidized to Co<sup>2+</sup> and substitute cation ion in the metal oxide, forming Me-Co-O mixed oxide.

Another type of interaction involves a more significant mass transport of oxide support onto the metal particles surface in form of catalyst encapsulation, and is commonly referred to strong metal-support interaction (SMSI). This results in the blocking of metal particles, possibly the active sites for catalysis by the oxide support. A well-known example is noble metal on TiO<sub>2</sub> [155, 156]. This also involves significant electronic interaction [157] creating differences in adsorption behaviour and in the reaction pathway for a catalytic reaction [158].

The study by Liu et al [159]. on ZnO nanorods supported Au catalyst for CO oxidation has demonstrated a catalyst system with different levels of metal-support interaction described above in oxidative and reducing gas environment. Formation of Au<sup>2+</sup> and Au<sup>3+</sup> in O<sub>2</sub> were identified by XANES and XPS. The oxidized Au species are stabilized at Au/ZnO interface due to metal oxide interaction. When treated at higher temperature in O<sub>2</sub>, SMSI was observed and ZnO migrated onto gold particles. Metal capsulation is reversible by hydrogen treatment with the formation of Au-Zn alloy. The different interactions induced in oxidative and reducing environment are closely associated to the difference in its catalytic activity on CO oxidation.

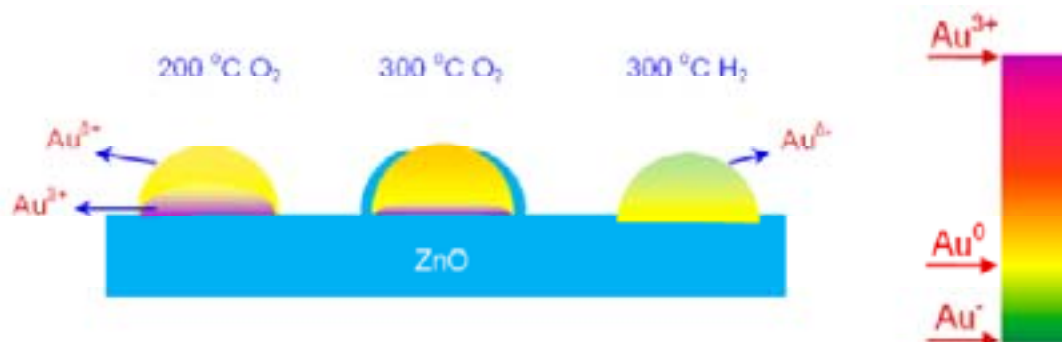


Figure 1.5 Schematic illustration for the SMSI states in the Au/ZnO nanorod system under various pretreatments. The color bar depicts the sign and degree of charging of the gold nanoparticles[159].

The metal-support interaction described above has been observed on working catalyst. Llorca et al. [93] has compared the activity of cobalt nanoparticles on a wide range of metal-oxide support. Oxidation states and chemical properties of cobalt change on different metal oxide supports. Cobalt oxide particles are formed on  $\text{SiO}_2$ . Cobalt oxidation and mixing of solid oxide occurs on  $\text{Al}_2\text{O}_3$  and  $\text{MgO}$  substrate. On  $\text{La}_2\text{O}_3$ , cobalt oxide in spinel structure  $\text{La}_2\text{CoO}_4$  is formed.

### 1.3.5 Metal oxide support for ESR

Various metal oxide supports has been studied for their effect to the catalytic activity of ESR [75, 78, 85, 92, 93, 160-163]. In the study of Llorca et al. [93],  $\text{ZnO}$ ,  $\text{La}_2\text{O}_3$ ,  $\text{Sm}_2\text{O}_3$ , and  $\text{CeO}_2$  were found to be a better support for Co catalyst than  $\text{MgO}$ ,  $\gamma\text{-Al}_2\text{O}_3$ ,  $\text{SiO}_2$ ,  $\text{TiO}_2$ ,  $\text{V}_2\text{O}_5$ , in which  $\text{ZnO}$  shows the highest selectivity to  $\text{H}_2$  and ethanol conversion efficiency. Similar studies on Ni based catalysts [91, 164] showed that  $\text{Ni/ZnO}$  exhibits the highest activities relative to other metal oxide such as  $\text{La}_2\text{O}_3$ ,  $\text{MgO}$  and  $\text{Al}_2\text{O}_3$ .

Metal oxide support itself possesses rather poor activity and does not participate directly in ethanol conversion in general. The behaviour of various metal oxides ( $\text{MgO}$ ,  $\text{Al}_2\text{O}_3$ ,  $\text{V}_2\text{O}_5$ ,  $\text{ZnO}$  from 2 synthesis methods,  $\text{La}_2\text{O}_3$ ,  $\text{CeO}_2$  and  $\text{Sm}_2\text{O}_3$ ) in ESR has been compared in a study by Llorca et al. [165].

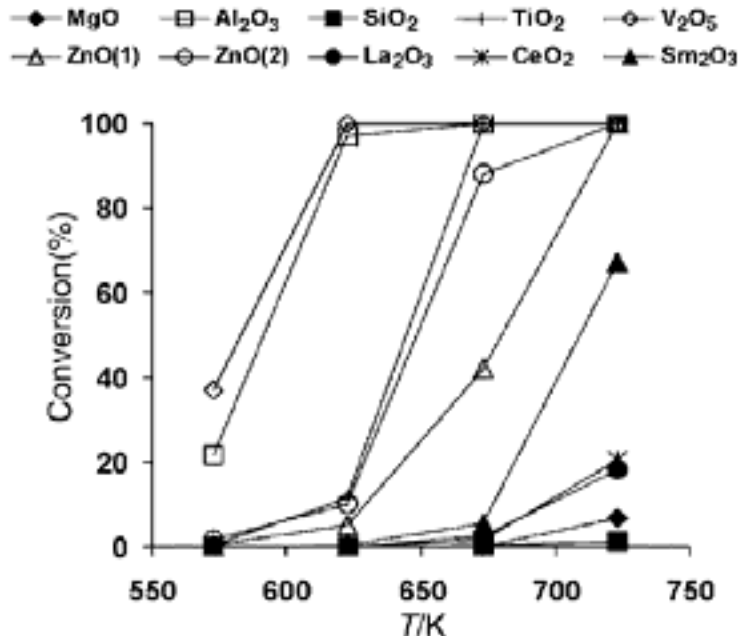


Figure 1.6 Ethanol conversion as a function of temperature for different oxides. Reaction conditions: total pressure 1 atm,  $C_2H_5OH : H_2O : Ar = 1:13:70$  (molar ratio),  $GHSV = 5000 h^{-1}$  [165].

Figure 1.6 summarizes the reactivity of the metal oxides in the temperature range of 550-750 K. The temperature for total ethanol conversion is the lowest for  $Al_2O_3$  and  $V_2O_5$ , while total conversion over ZnO and  $CeO_2$  is reached at 50 K higher. It was shown from the analysis of product selectivity that the major reactions involve over metal oxides materials are decomposition of ethanol to acetone, acetaldehyde reforming and water gas shift reaction. Other oxides show low level of ethanol conversion and selectivity to hydrogen and  $CO_2$ . ZnO is the only oxide material which is not selective to ethylene, showing that it is less susceptible to ethanol dehydration. Though ethanol conversion is efficient over  $Al_2O_3$ , its selectivity to ethylene is 100%, mainly owing to the acidity of the support [166].

The redox interaction between metal oxide supports and metal catalysts produces critical effects to the catalytic activities [83, 95, 167, 168]. The metal and metal oxide interface can also serve as an active surface for ethanol steam reforming reaction. This has been observed on  $Co/CeO_2$  [167], in which active transfer of oxygen takes place between cobalt and  $CeO_2$ , such that the metal-support interface can serve as an active center for the partial oxidation of ethanol, which facilitate the formation of  $CO_2$  and liberate the hydrogen group. Catalytic activity and selectivity can be manipulated with careful control of this redox interaction. This has been demonstrated in the study of  $Ni/CeO_2$  by Zhou et al. [169], in which selectivity of Ni to methane is reduced with the formation of  $Ce_{1-x}Ni_xO_{2-y}$  mixed oxide. They have associated the change in selectivity to the electronic perturbation of nickel brought by metal-support interaction as observed from valence band PES spectra. By increasing the interface of ceria and nickel, activity to methanation can be significantly suppressed. Other form of redox interaction has been observed on  $Co/ZnO$  [78], in which  $Co^{2+}$  substitute  $Zn^{2+}$  by calcinations such that an active Co-Zn-O phase was created. This Co oxide phase formed

by substitution creates  $\text{Co}^{2+}$  in  $T_d$  coordination instead of the more common  $O_h$ , and this new mixed oxide phase was found to be more active than other CoO formed.

Metal oxide support also assists in the catalytic reaction by mobilising useful surface adsorbed species such as oxygen or hydroxyl group to the catalyst. The enhancement of steam reforming activity by high mobility of hydroxyl group on metal oxide support has been observed in several works [75, 170, 171] and is shown to be related to the availability of oxygen vacancy in the metal oxide support. ZnO is commonly found as n-type semiconductor due to the presence of oxygen vacancy. The availability of oxygen vacancy is closely related to the oxygen partial pressure, as shown in several studies of ZnO synthesis [172-174]. Surface diffusion of oxygen vacancy is possible, making them available for surface reaction. Formation of surface oxygen vacancy on ESR catalysts support can be enhanced by the redox interaction between the catalyst and metal oxide. This has been demonstrated by the study of Song et al. [175] on Au and Cu supported on  $\text{CeO}_2$ . It was found that the deposition of metal increases the availability of oxygen vacancies on  $\text{CeO}_2$  due to the reduction effect exerted on  $\text{CeO}_2$  by the metal adlayer. The resulting oxygen vacancies play host to the oxygen from adsorbed water and induces bond dissociation of water molecule. Thus generation of hydroxyl group becomes more efficient with the presence of oxygen vacancies and increases subsequently the efficiency of water gas shift reaction. This effect has equally been observed on the Ni/ $\text{CeO}_2$  system described previously. [169].

Metal oxide support plays also an important role in the improvement of catalyst lifetime. Surface oxygen can facilitate the oxidation of adsorbed reaction species on the catalyst, in which lattice oxygen from metal oxide serves as oxidizing species of deposited carbon. Resistance to carbon deposition can be improved on metal oxide support with high oxygen mobility [95, 99, 167]. Such phenomenon has been demonstrated prominently on reducible metal oxide such as  $\text{CeO}_2$  [176, 177]. Song et al. [95] have conducted a comparison study of carbon deactivation on Co/ $\text{ZrO}_2$  with the addition of  $\text{CeO}_2$ . They have shown by isotopic experiment that oxygen exchange in  $\text{CeO}_2$  is significantly higher than  $\text{ZrO}_2$ . Also they have confirmed the high reducibility of  $\text{CeO}_2$  by  $\text{O}_2$  pulse chemisorptions experiment. This contributes to the efficient delivery of oxygen from  $\text{CeO}_2$  to catalyst surface, which promotes oxidation of carbon to  $\text{CO}_2$  and improves hydrogen yields. This explains the heavy carbon deposition observed on Co/ $\text{ZrO}_2$  compare to  $\text{CeO}_2$  containing catalyst. With the addition of  $\text{CeO}_2$ , the long term catalyst activity and stability are improved. In addition, CO and  $\text{CO}_2$  generation has increased and production of other single carbon species is reduced significantly by using  $\text{CeO}_2$  as support material. Additionally, the high oxygen mobility lead to higher oxygen consumption, which causes faster extraction of oxygen from water [167].

The improvement on catalyst deactivation by ZnO as support has been observed for Co and Ni based catalyst. Firstly, ZnO has a very moderate acidity, which helps to avoid heavy dehydration of ethanol on the catalyst system. In addition, ZnO has shown strong interaction with metal adlayer through redox reaction [159, 178-180]. This interaction can contribute to the size stabilization of metal catalyst particles, as has been shown on Ni and

Co on ZnO [181]. The interaction has led to oxidation of Ni and Co on ZnO and reduces slightly the reducibility of the metal, but it also improves the size distribution and decreases the particle size of Ni and Co. This maintains a high active surface area and the level of sintering is significantly lowered even after calcinations.

In general, though the support may not take part directly in the reaction, its influence could be exercised strongly through its interaction with the catalyst. As observed in various studies described above, this interaction can then contribute to the overall catalytic activity by improving adsorbate activation, reducing catalyst deactivation or sintering.

### 1.3.6 Concerns of catalyst stability for ESR

#### 1.3.6.1 Carbon formation

Thermodynamic studies [67, 72-74] provide the basic understanding of operating parameters to carbon formation. These studies are in agreement that carbon formation reduces at high steam to ethanol ratio and high temperature. It has been demonstrated that carbon free operating condition is not feasible at steam to ethanol ratio 1:1 [66]. Carbon free zone at steam to ethanol ratio of 2 requires an operation temperature higher than 900 K and 500 K for steam to ethanol ratio of 3 [73]. In addition, carbon formation can be improved at high contact time [72]. This has also been proven experimentally by keeping the process at low space velocity [111]. Thus carbon formation could be avoided with. However, maintaining high ethanol to steam ratio, temperature and long contact time between the catalysts and reaction gases also decreases the overall reaction efficiency and energy efficiency.

On working ESR catalyst, carbon is generally found in form of fiber [182-184] and condensed carbon, which encapsulates catalyst particles [177, 185, 186] if it is excessively accumulated. Condensed carbon on catalyst deteriorates catalytic activities by: (1) physically blocking the active sites, (2) decreasing access of reactants to metal surface (3) plugging of pores on micro- and mesoporous catalyst in which access of reactants to crystallites inside these pores is denied. On the otherhand, formation of carbon fiber induces a less severe immediate deactivation effect in comparison to condensed carbon encapsulation, as reactants still have access to catalyst surface. Mechanism of carbon fiber formation is triggered by the diffusion of surface C into the bulk of metal particles. The diffused carbon nucleates on facets for filament growth. The formation of carbon fiber on catalyst surface has been studied experimentally and theoretically by Bengaard et al. [187]. They found that small diameter (70 Å vs 1020 Å) Ni particles are less susceptible to carbon formation.

The nature of the carbon formed varies with temperature of reaction [93, 177]. Wang et al. have inspected the carbon formed on Co/CeO<sub>2</sub> in ESR by TEM. At low temperature (<450°C), carbon is mainly deposited due to the decomposition of ethanol and tends to form an amorphous layer encapsulating the Co particles. At medium temperature range (around 500 °C), decomposition is reduced and carbon is mainly formed from the cracking of methane.

Carbon is mainly in form of fibers. At higher temperature, carbon formation is significantly reduced.

Carbon formation on catalyst surface is the major catalyst deactivation mechanism for ESR process. As previously described, major reactions and species that lead to carbon formation are ethylene (Equation 1.22), carbon monoxide (Equation 1.21), and methane (Equation 1.16). Ethylene is a product of ethanol dehydration, which is easily formed on acidic metal oxide support such as  $\text{Al}_2\text{O}_3$  [166]. Two types of acidic sites could be found on metal oxide support: Brønsted acid sites and Lewis acid sites. Lewis acid sites adsorb ethanol molecule by receiving lone pair electrons from oxygen of  $-\text{OH}$  group and Brønsted acid sites donate proton to the adsorbed molecule and promotes ethanol dehydration [61, 166]. Metal oxide with strong Brønsted acid characteristics provokes severe carbon formation through this mechanism [188, 189]. Regeneration of catalyst deactivated by carbon formation is possible by oxygen treatment for the removal of surface carbonaceous species [176].

ZnO is regarded in general as a mildly acidic metal oxide support. Its acidity has been studied by the adsorption of pyridine, which is a Lewis-base possessing lone electron pair. Pyridine molecules are more strongly adsorbed on Zn site than on oxygen sites [190]. On oxygen terminated ZnO single crystal, the surface is usually highly hydroxylated. Pyridine is adsorbed on Zn terminated ZnO only by physisorption. The nature of the acidity and active sites of ZnO was studied by the model reaction of methylbutynol conversion. The availability of oxygen vacancies is correlated to the basic reactivity of ZnO [191]. The oxygen vacancies serve as acid/base pair, in which basic sites facilitate the abstraction of proton from ethanol whereas the associated acid sites stabilize the resulting anionic intermediate.  $\text{C}_2\text{H}_4$  is still formed on lewis acid site of ZnO, but is relatively mild compared to other metal oxides.

### 1.3.6.2 Metal sintering

Metal sintering is the deactivation of catalyst in physical form. Metal catalysts are usually dispersed on metal oxide support in form of particles. Sintering of the catalyst is usually the result of thermally induced restructuring, which leads to the decrease in catalytic surface area or the collapse of metal oxide support. Sintering of catalysts particles can take place via 1) Migration of the entire crystallite on support 2) Atomic migration.

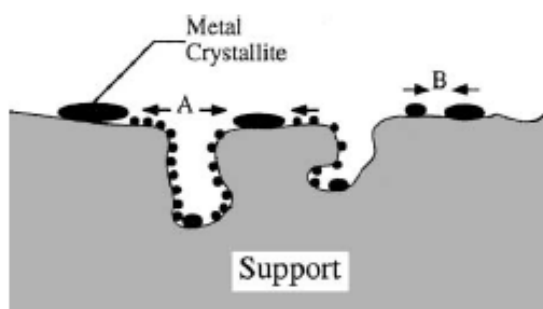


Figure 1.7 Two conceptual models for crystallite growth due to sintering by (A) atomic migration or (B) crystallite migration

Sintering of catalyst particles could be the result of a number of factors: gas phase environment, nature of metal, loading, properties of metal oxide support such as area, texture and porosity, but first and foremost, the temperature of reaction[192]. As the temperature of reaction is also a critical factor to reaction efficiency and process selectivity, improvement can be brought by modification of catalyst's crystalline structure, modification of metal oxide support, stabilization by addition of other metal or metal oxide.

Metal sintering also imposes another level of catalyst deactivation effect. It has been observed for reforming of methane that small particle size favours the oxidation of carbon formed on catalysts. Carbon species formed near the periphery of metal particles have easier access to reactive species on metal oxide support. On large size metal particles, carbon species stay on particles surfaces far away from the periphery of metal particles. Carbon tends to nucleate and cause severe deactivation in long term catalytic process. Hence, metal-support interaction increases with decrease in particle size, which helps in eliminating the carbon species formed on catalyst particles.

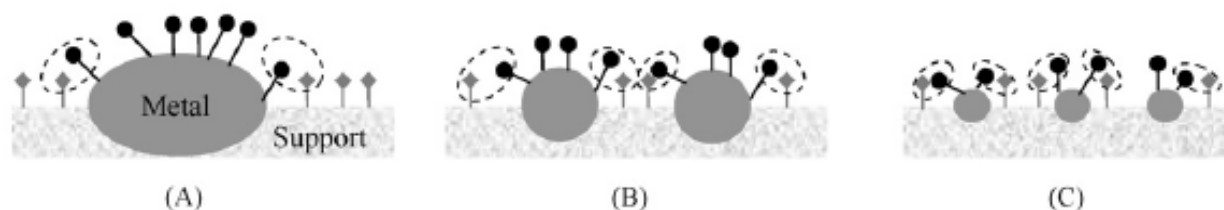


Figure 1.8 Conceptual model of carbon removal and carbon formation over the Ni-Co bimetallic catalyst for  $\text{CO}_2$  reforming of  $\text{CH}_4$ . (A) Catalyst with metal particles larger than 20 nm. (B) Catalyst with metal particles between 10 and 20 nm. (C) Catalyst with metal particles smaller than 10 nm. [110]

### 1.3.6.3 Metal oxidation

Catalyst oxidation can be induced by oxidizing species present in the reactant or from the support. According to reaction thermodynamics, oxidation of transition metal catalyst by water is probable at low temperature (<430 K)[68]. The oxide phase of transition metal catalyst such as Ni and Co was observed at low temperature in steam rich reaction stream [101, 102]. These oxides are either found to be inactive or, if active, give low selectivity to hydrogen production [97, 99].

## 1.4 Surface Studies of catalysts

### 1.4.1 Model catalyst

Working ESR catalysts are usually highly dispersed over high surface area metal oxide support in order to maximize the availability of active site for reactions. Depending on the complexity of the synthesis process and metal precursor used, working catalysts exist with complex composition and morphology and are adapted to working reaction environment. Catalytic studies on this type of system are under multilevel influence. Distinguishing the contribution of individual factor to catalytic phenomena is difficult. The complexity of a working catalyst system also impedes the utilization of surface sensitive techniques, which is

particularly powerful in terms of probing electronic structure and surface reaction at atomic or molecular level. In view of this, development of model catalyst, which involves materials of well defined structure, crystallinity and composition, provides a platform facilitating the investigations on fundamental issues with specificity.

Model catalyst are system with known and simplified geometry. Typical model catalysts include metal single crystals [193-195], or thin film or nanoparticles supported on single crystal surface [147, 178, 196, 197]. Synthesis of model catalyst requires careful cleaning of the single crystal surface by techniques such as sputtering and advanced thin film deposition techniques. Thin metal layers up to several nm are deposited onto the single crystal at a controlled deposition rate, in which metal clusters or metal films of controllable size can be obtained [198-200]. Characterization of model catalyst is possible by a number of surface techniques (such as XPS, LEED, Auger, thermal desorption etc.) in Ultra High Vacuum (UHV).



Figure 1.9 Scheme of model catalyst systems

#### 1.4.2 Surface chemistry of ethanol on model catalysts

The chemistry of biomass derived molecules such as alcohol on catalyst mimicked on these model surfaces is of increasing interest of study, in the objective of identifying reactions intermediates, mechanism and kinetics. Surface reaction of alcohol molecules could be studied by techniques like temperature programmed desorption, while surface properties of model catalysts can be characterized by techniques such as XPS or imaging techniques like AFM. Combination of these two types of techniques provides a good correspondence of the active surface sites or active intermediate species on the model catalyst surface and mechanism involved in the reaction. In order to elucidate complex effects such as metal-support interaction, studies based on pure single crystal metal catalyst[194, 201, 202], single crystal metal oxide support [195]and single crystal supported thin film[104, 178] were conducted to make the comparison effective .

Xu et al. are one of the earliest group who studied ethanol decomposition on transition metal single crystal surface with thermal desorption techniques[193]. The reaction kinetics and mechanism of ethanol on Ni (111) was studied using TPD, XPS and infrared reflection absorption spectroscopy (IRAS). They proposed that the first step of ethanol decomposition is the conversion of ethanol to adsorbed ethoxy group, in which the ethoxy group is in an orientation parallel to Ni (111) surface. This investigation was followed by another TPD studies and kinetic spectroscopy (SKS)of ethanol on Ni (111) by Gates et al.[201] aiming to

investigate of bond activation sequence. In agreement to the study of Xu et al., the dissociation of hydrogen from the OH group was indicated by desorption of acetaldehyde as the 1<sup>st</sup> step of ethanol decomposition.

The subsequent decomposition of ethoxy group is more complicated and was studied with the aid of isotope exchange. By introducing deuterium isotope in replacement of methylene H and methyl H, it was revealed that formation of methane and acetaldehyde is controlled by a single elementary reaction. The threshold temperature of both acetaldehyde and methane formation is determined by the C-H bond breaking of the methylene (-CH<sub>2</sub>- group), and should be the 2<sup>nd</sup> step of ethanol decomposition on Ni (111). This leads to the formation of a transient reaction intermediate which then take the role as the precursor for methane and CO formation via C-C bond scission. The breaking of C-C bond was further confirmed by isotopic exchange of <sup>13</sup>CO and <sup>12</sup>CO. This exchange took part in the desorption only with a very low percentage, which confirmed the unlikelihood of C-O bond breaking and C-C bond cleavage as the favourable pathway. The surface methyl groups either desorb as methane or undergo further decomposition to form hydrogen and residual C. A schematic representation of the reaction mechanism was proposed as below:

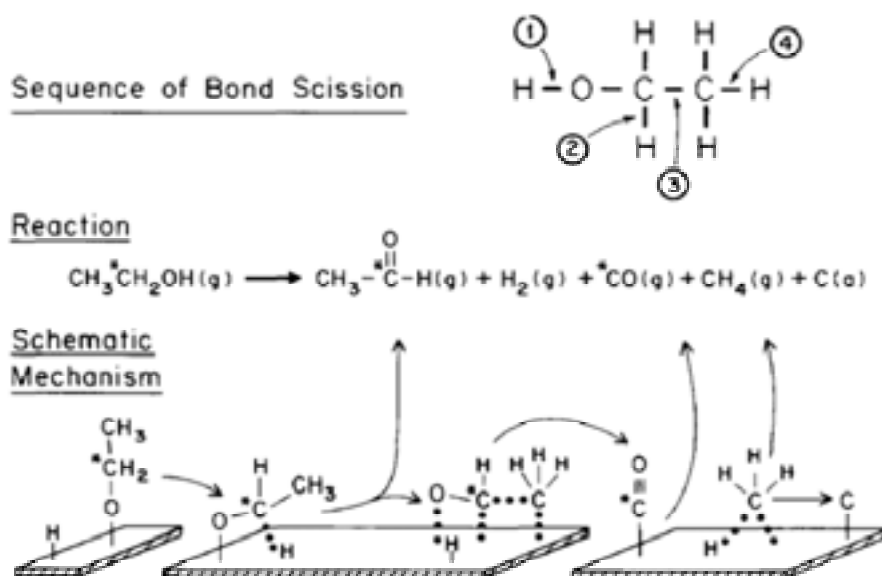


Figure 1.10 Summary of sequence of bond scission, products formed, and schematic mechanism for the decomposition and reaction of ethanol on Ni (111).

The study by Vesselli et al. [194] on ethanol decomposition on Rh (111) has revealed another ethanol decomposition mechanism and bond cleavage sequence. By the combined use of synchrotron based high resolution real time XPS and TPD, spectra of surface carbon and oxygen species on Rh surface were acquired simultaneously with ethanol thermal desorption. The evolution of C 1s and O 1s spectra during temperature ramp illustrated that formaldehyde stays as a rather stable intermediate between 250 and 400 K. The shift of 1<sup>st</sup> C 1s peak to lower binding energy also revealed that dehydrogenation of the methyl group took place simultaneously with the formation of formaldehyde. This has also given evidence for selectivity to cleavage of C-C bond with respect to C-O bond on Rh (111) surface. The

reaction species detected by TPD was coherent to the products and bond breaking sequence observed by XPS. The use of real-time XPS serves as an efficient complementary to TPD and has successfully identified the intermediate reaction occurred between 250-400 K where all intermediates remain adsorbed and cannot be observed by TPD.

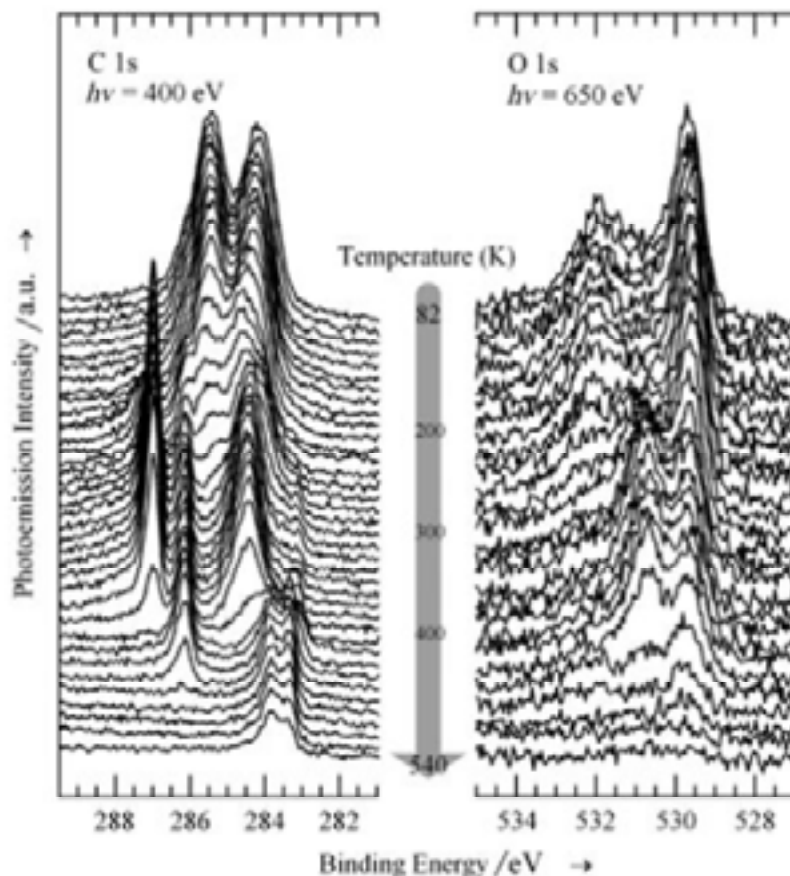


Figure 1.11 Real-time C 1s (left) and O 1s (right) sequences collected during two equivalent ethanol desorption/decomposition experiments upon surface annealing. [194]

Though metal oxide supports have been shown to be rather inactive for hydrogen production in ESR, it is a rather critical substance for ethanol dehydration. Mullins et al. has conducted a study of surface reaction of methanol, ethanol, 1-propanol, and 2-propanol on reduced and oxidized CeO<sub>x</sub>(111) thin film surfaces based on TPD and XPS recently [195]. With the use of synchrotron light source, surface sensitivity and resolution of XPS were significantly improved. CeO<sub>2</sub>(111) films were grown *in-situ* by Ce vapor deposition onto a Ru(0001) surface at 700 K under an oxygen atmosphere. The procedure has been reported previously. Reduced CeO<sub>x</sub>(111) films were produced by exposing the CeO<sub>2</sub>(111) surfaces to methanol above the methoxy decomposition temperature. Thus the surface carbonaceous species and the active Cerium species on the pre-reduced and pre-oxidized thin film could be well resolved by XPS using selected photon energy. The C 1s spectra obtained give direct information on the prevailing carbon species adsorbed on CeO<sub>2</sub> surface.

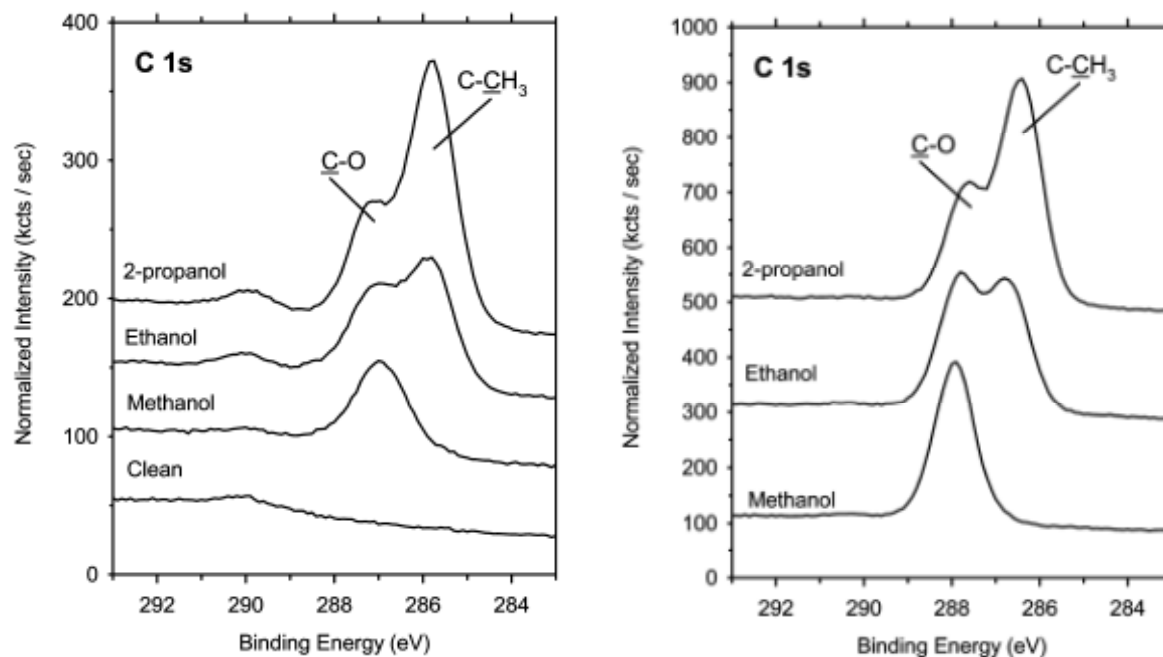


Figure 1.12 (left) C 1s XPS of methanol, ethanol, and 2-propanol adsorbed on fully oxidized CeO<sub>2</sub>(111) at 185 K and then annealed to 300 K. (right) C 1s sXPS of methanol, ethanol, and 2-propanol adsorbed on 65% reduced CeO<sub>1.67</sub>(111) at 185 K and then annealed to 300 K. [195]

The reaction pathway has been deduced from the major products of decomposition detected based on TPD results. Ethanol is decomposed into alkoxy and hydroxyl species at low temperature as the initial step. On fully oxidized CeO<sub>2</sub> surface, alkoxy groups recombine with hydroxyl groups at 200 K and form gaseous alcohol. Certain stable alkoxy groups were decomposed above 550 K. Primary alcohols produce primarily aldehydes and produce a net reduction of the ceria substrate. Secondary alcohol, undergoes dehydration and generates water and ethylene. This reaction does not modify the oxidation state of ceria. The temperature of desorption of ethylene and propene is lower than that of acetaldehyde reduced ceria surface, showing that reduced Ceria surface facilitate the breaking of the C-O bond and the breaking of O-substrate bond involves higher energy requirement. Ethanol dehydration on metal oxide has equally been observed in other TPD studies over metal oxide single crystal such as ZnO and TiO<sub>2</sub> [203, 204].

The studies of ethanol surface reaction of metal thin film or nanoparticles on metal oxide single crystal provides a proper platform for the study of metal-support interaction. Decomposition of ethanol on Co supported on yttria-stabilized ZrO<sub>2</sub>, YSZ(100), was studied by TPD and XPS in the work from Martono et al. [205]. When supported on YSZ, Co thin film exhibits a high thermal stability that catalyst dispersion is not affected after annealing. Co thin film remains in metallic state after annealing, which shows that the level of oxygen transfer over Co and YSZ support is very limited. CO was the only gaseous carbon-containing product obtained from TPD of ethanol on Co/YSZ. This shows that dehydrogenation is the important reaction, which decomposes the methyl group and the CO is generated from decarbonylation of ethoxy group. These TPD results were compared against oxygen treated

Co/YSZ, where desorption of acetaldehyde was found in addition to CO desorption. They proposed that acetaldehyde can be attributed to the abstraction of hydrogen atom from an adsorbed ethoxy intermediate by oxygen adsorbed on metal Co. Thus oxygen modified Co serves as an active site for ethanol dehydrogenation. In comparison to other system such as metal on ZnO [104], where metal-support interaction is strong causing catalyst oxidation, acetaldehyde desorption can be observed on as deposited metal film. By the comparison of the metal oxide support with different oxygen mobility, it can show that oxygen transfer to metal can assist in the primary step for ethanol decomposition.

Interaction of ZnO to metal layer is also manifested on other system such as Cu/ZnO, which is known as an efficient catalyst for methanol synthesis. The material structure and reactivity were widely studied as a model catalytic system [178, 179, 197, 200, 206]. Growth of Cu on ZnO single crystal has been characterized by STM and LEED [147]. The growth model is different on ZnO single crystal of different polarity. Cu tends to grow into 3D cluster at surface coverage higher than 0.01 ML on ZnO-Zn surface and Cu agglomeration takes place at high temperature. Interaction of Cu on ZnO-O surface is stronger which results in better wetting of copper and thus copper film grows in laminar mode.

Strong coulomb repulsion over ZnO supported Cu was observed from PES measurement, which enhances the likelihood of backbonding interaction during catalytic reaction[178]. The high catalytic activity on methanol synthesis is also closely related to the formation of  $\text{Cu}^+$  sites. These sites are in tetrahedral coordination and are specific to the incorporation of  $\text{Cu}^+$  in substitution into ZnO. Stronger CO chemisorption was observed on these Cu (I) ions than  $\text{Cu}^0$ ,  $\text{Zn}^{2+}$  or other  $\text{Cu}^+$  site such as CuCl single crystal. This also helps to explain the higher activity of methanol synthesis on this particular copper active site. This example has demonstrated by the use of model catalyst and surface techniques, the study of catalytic reaction can be tackled in terms of the material structure, electronic properties and chemical properties.

#### **1.4.3 Bridging the gap between model catalyst and real catalyst by APPES**

Though surface studies on model catalyst in UHV are informative for electronic interaction and bonding between the reactant gases and the catalytic material, it is still questionable if the effects observed in the stringent environment of UHV are analogous to the reality. In practice, catalytic processes operate at ambient condition or at more elevated pressure with a high gas flow. The knowledge learnt from well controlled surface science experiments are at stake because of this pressure gap. This risk has been demonstrated on Ru based catalyst for CO oxidation. Ru metal was shown to be a poor catalyst for CO oxidation in UHV environment compared to Rh and Pd, but contradictory results were observed for experiments conducted at 24 Torr [207]. It has been discovered later that the active sites should be  $\text{RuO}_2$ [208], an oxygen rich layer that could not be achieved in UHV, where only thin oxygen overlayer is formed.

In order to bridge the pressure gap and to study surface chemistry in realistic catalytic conditions, progress has been made on surface probing techniques adapted to high pressure environment. Development of ambient pressure photo-electron spectrometer is one of these techniques which allow *in-situ* surface analysis at working pressure up to millibar level. XPS and XAS are the most common electron spectroscopies performed at ambient pressure for surface chemistry studies. Important information such as surface composition, oxidation state and also identities of reactive species adsorbed on the surface can be directly obtained from ambient pressure XPS and XAS. This does not only bridge the pressure gap, but also enhance the understanding of reaction network. These equipments are available mainly at synchrotron radiation facility, which allows extraction of valuable information with high resolution and tunable surface sensitivity.

Though the availability of ambient pressure surface techniques is still limited due to the difficulty of hardware development, its importance on catalysis investigation has been shown by a number of representative studies. In the following, some examples on model catalyst system similar to that concerned in this thesis would be given in the following to demonstrate the necessity of techniques developed in this direction.

As mentioned previous, Cu/ZnO systems is a promising methanol synthesis catalyst [209-214]. Similar to Ni and Co, copper is also subjected to strong metal-support interaction on ZnO. Recently, some ambient pressure XPS studies have been conducted and that has enhanced our understanding to the reaction mechanism. This is a good example to demonstrate the application of Ambient pressure XPS to catalysis. It has been known that the formation of formaldehyde as intermediate species and its activity over copper surface is a critical factor to this reaction. It has been shown that the formation of aldehyde species is hindered on surface with high oxygen coverage [215, 216]. By *in situ* XPS, reaction intermediates could be identified [216]. The C 1s and O 1s spectra obtained under reaction conditions show the evolution of intermediate species, methoxy and formate group on copper surface:

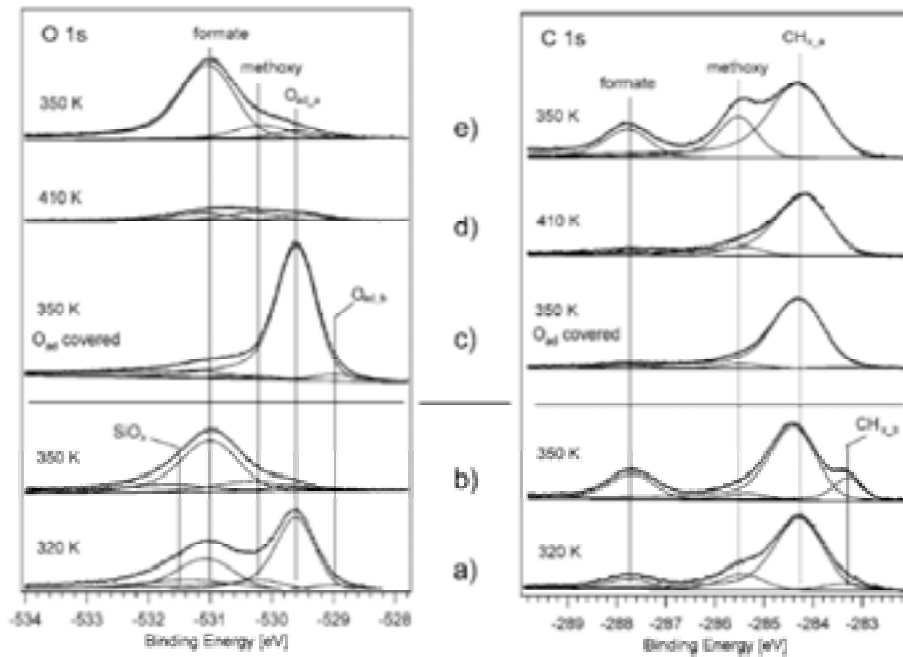


Figure 1.13 Characterization of the adsorbate species on Cu(110) by in situ photoelectron spectroscopy of the O 1s and C 1s core levels. (a) and (b) represent a stationary state of the surface. (c)–(e) spectra are transients. MR=  $p(\text{O}_2) : p(\text{CH}_3\text{OH}) = 0.3:1$  was used: a  $T=320$  K,  $p(\text{CH}_3\text{OH})=2 \times 10^{-6}$  mbar; b  $T=350$  K,  $p(\text{CH}_3\text{OH})=5 \times 10^{-6}$  mbar. c–e  $p(\text{CH}_3\text{OH})=1.4 \times 10^{-6}$  mbar and MR= $p(\text{O}_2) : p(\text{CH}_3\text{OH})=0.14:1$  before and after short annealing to 450 K. (c) at 350 K before annealing the O<sub>ad</sub> covered Cu(110) surface, (d) at  $T=410$  K during cooling down after annealing (e) during cooling down at  $T=350$  K [216]

By the quantification of the surface species, the evolution of reaction pathway can be deduced. In the mentioned example, by the deconvolution and quantification of the respective C 1 component species, it was found that surface is mainly occupied by formate at low temperature. Methoxy is detected but with a lower surface coverage when reaction is not activated. As temperature increases, oxidation of methanol to formate reduces and where oxidation to methoxy becomes the only reaction path that at high temperature it reacts spontaneously and becomes undetectable.

By in-situ NEXAFS measurement of O K-edge spectra, the ratio of bulk copper oxide, surface copper oxide, copper suboxide was distinguished. The impact of surface oxygen to the reaction was studied by *in-situ* NEXAFS measurement on O K-edge. It has been reported that copper suboxide, which is unobservable in UHV, is present under reaction conditions and is catalytically active for partial oxidation of methanol [215, 217]. The yield of formaldehyde and methanol conversion could be correlated to the abundance of different oxygen species. The active role of copper of different oxidation state could be understood by the comparison of the abundance of surface carbon intermediate and the oxidation state of copper. The increase of bulk and surface copper oxide decreases the methanol conversion. However, the abundance of copper suboxide does not affect methanol conversion and is positively correlated to CH<sub>2</sub>O yield. The copper suboxide features found from O K-edge

spectra reveal the presence of metastable oxide species under working condition, and can only be distinguished by *in-situ* mechanistic study.

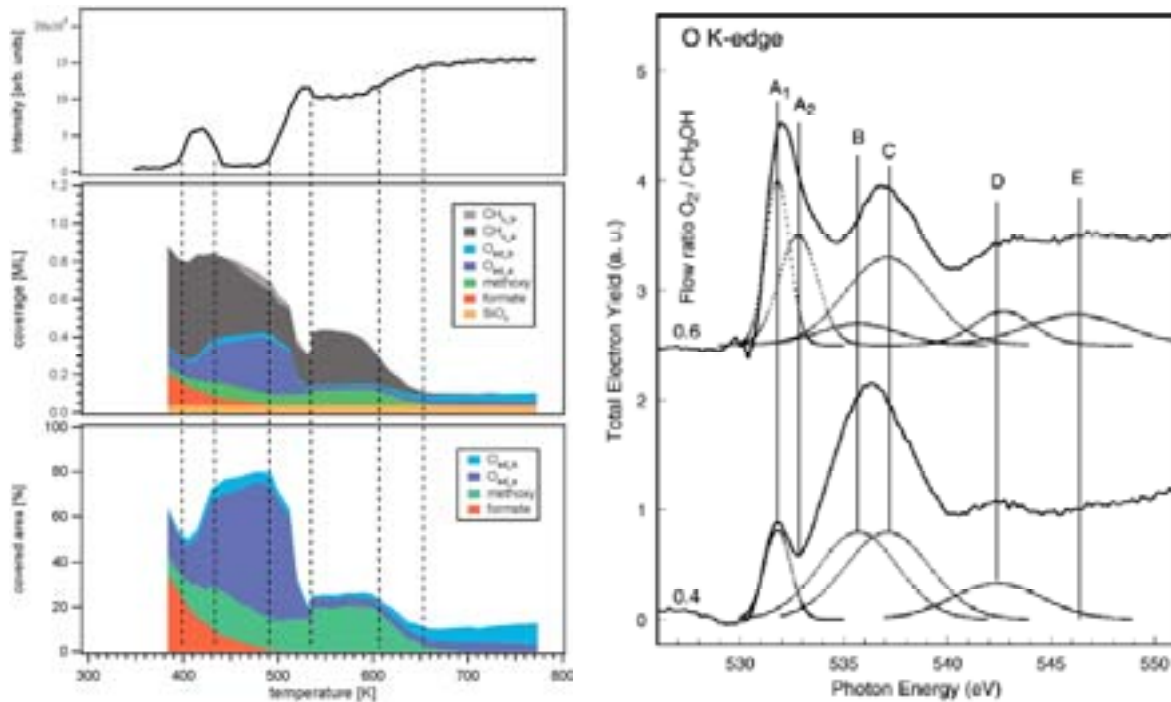


Figure 1.14 (left) Relation between adsorbate coverages and reactivity during heating up. Top: formaldehyde production rate. Middle: adsorbate coverages in monolayers. Bottom: fraction of the surface covered by the different adsorbates. Experimental conditions:  $p(\text{CH}_3\text{OH})=5 \times 10^{-6}$  mbar,  $MR = p(\text{O}_2) : p(\text{CH}_3\text{OH})=0.6:1$ . A heating rate of 5 K/min was used. (right) Two spectra are plotted to demonstrate the different oxygen species investigated in this paper. Two Gaussian peaks A1 and A2 were used to fit the oxidic structure. The suboxide phase is characterised by three Gaussian peaks B–D.

The application of these techniques on bimetallic materials is particularly interesting, as surface properties of bimetallic materials changes dynamically with the gas phase environment.

Pd/ZnO is known as a very efficient system for methanol steam reforming [218, 219]. Its advanced catalytic performance is mainly attributed to the formation of Pd-Zn alloy or intermetallic compound during reduction of the catalyst. Formation of PdZn alloy has been observed by *in-situ* EXAFS study[220] on Pd/ZnO in which the formation of the alloy changes dynamically with the reaction environment. The reduction of ZnO is initiated by hydrogen generation during methanol steam reforming. Reduction of ZnO triggers the alloying of Pd and Zn, leading to the formation of a highly reactive Pd-Zn layer at the catalyst surface. The alloy formation is sensitive to the gas phase environment as it is a reversible reaction with  $\text{O}_2$  treatment. Stability of PdZn alloy and its influence to the selectivity of methanol conversion in reaction conditions at high pressure was studied by *in-situ* XPS [221] on a model surface alloy based on Zn thin layer supported on Pd(111). The formation of PdZn alloy was indicated by the change in density of state of valence band. Growth of additional component, which is unobservable in UHV, of Zn 3d spectra was found at high water vapour

pressure. It is believed that ZnO(H) was formed due to adsorption of water. Results from ambient pressure XPS shows that this alloy is stable in different chemical environment, water (0.24 mbar), methanol (0.12 mbar), as well as CO (5 mbar) in a confined temperature range (<573 K) Above this temperature, binding energy shift of Pd 3d and appearance of "Pd-like" valence band structure is observed. The temperature of this transition corresponds well to the catalytic results of methanol dehydrogenation. The reaction gas evolution was monitored by online mass spectroscopy. Formaldehyde formation is predominant in the temperature range where PdZn is stable, and no CO is generated, showing that formaldehyde is stabilized by PdZn alloy and further dehydrogenation to form CO is hindered. Above this temperature, where Pd-Zn dealloying is observed by XPS, CO selectivity increases. Results on methanol steam reforming are highly coherent, *in-situ* XPS shows that not only PdZn alloy decomposes, but the surface O1s spectral features of water adsorbed on ZnO also disappear reaches a threshold, and is also reflected to the increase in CO selectivity. With the use of ambient pressure XPS, the surface condition of the catalyst can be directly associated with the catalytic results.

As shown in the above examples, the application of APPEs is an important and powerful technique which provides highly surface sensitive information over catalyst materials under an environment that is close to practical reaction condition.

## 1.5 Scope and outline of the thesis

The objective of this work is to perform a detailed study of the influence brought by bimetallic and metal-support interaction on a model bimetallic catalyst system, and to comprehend their influence to the active roles of the component metal and the reaction network of ethanol steam reforming on such catalyst. The catalytic system interested is a model catalyst based on bimetallic Nickel Cobalt catalyst with ZnO as the catalyst support. Nickel and Cobalt are regarded as efficient and low-cost non-noble metal catalysts for ethanol conversion and very selective to hydrogen. Majority of the studies performed focuses on the synthesis of catalytic materials and their corresponding catalytic activities, while not much work have addressed the fundamental aspects such as the synergetic effect of the component metals and metal-support to the reaction mechanism. To develop such system, Ni-Co is vapour-deposited on ZnO single crystal surface as a thin film in Ultra High Vacuum (UHV) setup. By establishing a well-ordered gas/catalyst and catalyst/support interface, surface analysis techniques could be applied and facilitate the study of surface chemistry of ethanol with the bimetallic catalyst surface at molecular level. The model system is studied by *in-situ* surface techniques such as X-ray photoelectron spectroscopy (XPS) and thermal desorption spectroscopy (TDS) for understanding its surface structural change, material properties and chemisorptions properties. In order to bridge the pressure gap and to understand better its behaviour under a more realistic operating condition, synchrotron based techniques like Ambient Pressure Photoelectron Spectroscopy (APPEs) and Near Edge X-ray Absorption Spectroscopy (NEXAFS) have been applied which allow one to study the catalyst *in-situ* in millibar pressure range. Specific aim of this thesis is to shed

light on fundamental issues which affect the catalyst's performance, but are impossible to clarify from real/industrial catalyst studies due to the high degree of complexity: (i) bimetallic synergetic effect to the catalyst's properties (ii) the effect of the support in the reaction; supports influence the catalytic reaction by mainly two routes, directly by activating the catalytic process and/or indirectly by modifying the chemical properties of the catalytic nanoparticles (iii) determination of the oxidation state and structure transformation on the surface of the catalyst under reaction conditions (iv) identify the mechanism of the reaction (v) correlation between deactivation by carbon deposition and the surface properties of the catalytic system notably the role of the support in this procedure.

The first part of this work focused on the study of the bimetallic system from a material perspective: the redox properties of bimetallic Ni-Co material in low pressure range ( $10^{-7}$  mbar) and high pressure range (1 bar). Polycrystalline NiCo foil is used as a simplified model system to understand synergetic effects of the alloy components upon oxidation. Meanwhile, the effect of the so called "pressure gap" to this process has also been investigated. The insight into the surface oxidation of NiCo alloy is crucial to rationalize the performance of NiCo in catalytic reforming reactions. The 2<sup>nd</sup> stage of the work was extended to the study of the synergetic effect of the bimetallic alloy on the ZnO supported model catalyst. Thin bimetallic Ni-Co layers (<1.5 nm) were co-deposited on polar (0001)-Zn and (000 $\bar{1}$ )-O ZnO substrates, such that two major effects, synergy of alloying and metal-support interaction, could be considered in the same study. Monometallic Ni and Co layers were also characterized to highlight the influence of Ni-Co synergetic effects to the metal-support interaction. The work accomplished at these two stages serves as the foundation for the catalytic studies of this material. The third part of the work focused on the investigation of the reaction network of ESR on Ni-Co. This was investigated at two levels: 1) the reaction mechanism on ZnO supported bimetallic Ni-Co thin film 2) the reaction mechanism on unsupported Ni-Co nanoparticles. Thermal Desorption Spectrometry (TDS) of ethanol was performed on ZnO supported bimetallic Ni-Co thin film to understand reaction intermediate and the decomposition pathway of ethanol on a supported catalyst system. In order to approach the operating conditions of the process, the catalysts were studied *in-situ* by ambient pressure XPS measurement with the reaction monitored by online mass spectroscopy in order to understand the correspondence of the active states of the catalysts and the reaction products released in the process.

## 1.6 References

- [1] O.f.E.C.-o.a.D. (OECD), OECD, Paris.
- [2] I.E. Agency, World Energy Outlook 2010, IEA PUBLICATIONS, France, 2010.
- [3] OECD/IEA, International Energy Agency, France, 2012, p. 80.
- [4] U.S.E.I. Administration, U.S. Energy Information Administration, U.S., 2011.
- [5] C. Le Quéré, R.J. Andres, T. Boden, T. Conway, R.A. Houghton, J.I. House, G. Marland, G.P. Peters, G. van der Werf, A. Ahlström, R.M. Andrew, L. Bopp, J.G. Canadell, P. Ciais, S.C. Doney, C. Enright, P. Friedlingstein, C. Huntingford, A.K. Jain, C. Jourdain, E. Kato, R.F. Keeling, K. Klein Goldewijk, S. Levis, P. Levy, M. Lomas, B. Poulter, M.R. Raupach, J. Schwinger, S. Sitch, B.D. Stocker, N. Viovy, S. Zaehle, N. Zeng, *Earth Syst. Sci. Data Discuss.* 5 (2012) 1107-1157.
- [6] I.O.o.M.V. Manufacturers, France, 1998-2011.
- [7] U.S.D.o.E.H.A.R. Center, Jan 2012 ed., U.S. Department of Energy Hydrogen Analysis Resource Center, United States, 2012.
- [8] C. Song, *Catalysis Today.* 77 (2002) 17-49.
- [9] C.J. Winter, *International Journal of Hydrogen Energy.* 34 (2009) S1-S52.
- [10] B. Gross, I. Sutherland, H. Mooiweer, General Motors Research and Development Center, Detroit, MI, 2007.
- [11] N. Johnson, J. Ogden, *International Journal of Hydrogen Energy.* 37 (2012) 5421-5433.
- [12] H. Dagdougui, A. Ouammi, E. Garbolino, R. Sacile, 2012, pp. 34-39.
- [13] H. Dagdougui, *International Journal of Hydrogen Energy.* 37 (2012) 5318-5327.
- [14] G.G. Tao, B. Butler, A.V. Virkar, 2010.
- [15] L. Zhiyong, P. Xiangmin, M. Jianxin, *International Journal of Hydrogen Energy.* 35 (2010) 6822-6829.
- [16] W. Dougherty, S. Kartha, C. Rajan, M. Lazarus, A. Bailie, B. Runkle, A. Fencel, *Energy Policy.* 37 (2009) 56-67.
- [17] L.I. Lubis, I. Dincer, G.F. Naterer, M.A. Rosen, *International Journal of Hydrogen Energy.* 34 (2009) 1631-1637.
- [18] **I.E. Agency, 2007.**
- [19] MarketsandMarkets, 2011.
- [20] I.P.f.H.a.F.C.i.t. Economy, International Partnership for Hydrogen and Fuel Cells in the Economy, Berlin, Germany, 2010.
- [21] U.S.D.o. Energy, 2007 ed., U.S. Department of Energy, 2007.
- [22] J.N. Armor, *Applied Catalysis A: General.* 176 (1999) 159-176.
- [23] J. Xu, G.F. Froment, *AIChE Journal.* 35 (1989) 88-96.
- [24] M.A. Peña, J.P. Gómez, J.L.G. Fierro, *Applied Catalysis A: General.* 144 (1996) 7-57.
- [25] K. Shankar, J.I. Basham, N.K. Allam, O.K. Varghese, G.K. Mor, X. Feng, M. Paulose, J.A. Seabold, K.-S. Choi, C.A. Grimes, *The Journal of Physical Chemistry C.* 113 (2009) 6327-6359.
- [26] O. Kruse, J. Rupprecht, K.P. Bader, S. Thomas-Hall, P.M. Schenk, G. Finazzi, B. Hankamer, *Journal of Biological Chemistry.* 280 (2005) 34170-34177.
- [27] J.R. Benemann, K. Miyamoto, P.C. Hallenbeck, *Enzyme and Microbial Technology.* 2 (1980) 103-111.
- [28] A.N. Rai, E. Söderbäck, B. Bergman, *New Phytologist.* 147 (2000) 449-481.
- [29] A. Fujishima, K. Honda, *Nature.* 238 (1972) 37-38.
- [30] R. Asahi, T. Morikawa, *Chemical Physics.* 339 (2007) 57-63.

- [31] O. Diwald, T.L. Thompson, E.G. Goralski, S.D. Walck, J.T. Yates, *The Journal of Physical Chemistry B*. 108 (2004) 52-57.
- [32] S.U.M. Khan, M. Al-Shahry, W.B. Ingler Jr., *Science*, 2002, p. 2243.
- [33] R. Nakamura, T. Tanaka, Y. Nakato, *The Journal of Physical Chemistry B*. 108 (2004) 10617-10620.
- [34] Z. Zhang, J.B.M. Goodall, D.J. Morgan, S. Brown, R.J.H. Clark, J.C. Knowles, N.J. Mordan, J.R.G. Evans, A.F. Carley, M. Bowker, J.A. Darr, *Journal of the European Ceramic Society*. 29 (2009) 2343-2353.
- [35] H. Gaffron, J. Rubin, *The Journal of General Physiology*. 26 (1942) 219-240.
- [36] J.R. Benemann, *International Journal of Hydrogen Energy*. 22 (1997) 979-987.
- [37] F.P. Healey, *Planta*. 91 (1970) 220-226.
- [38] K. Schütz, T. Happe, O. Troshina, P. Lindblad, E. Leitão, P. Oliveira, P. Tamagnini, *Planta*. 218 (2004) 350-359.
- [39] G.D. Smith, G.D. Ewart, W. Tucker, *International Journal of Hydrogen Energy*. 17 (1992) 695-698.
- [40] O. Mizuno, R. Dinsdale, F.R. Hawkes, D.L. Hawkes, T. Noike, *Bioresource Technology*. 73 (2000) 59-65.
- [41] H. Yokoi, R. Maki, J. Hirose, S. Hayashi, *Biomass and Bioenergy*. 22 (2002) 389-395.
- [42] D.B. Levin, R. Islam, N. Cicek, R. Sparling, *International Journal of Hydrogen Energy*. 31 (2006) 1496-1503.
- [43] Y.C. Lo, W.M. Chen, C.H. Hung, S.D. Chen, J.S. Chang, *Water Research*. 42 (2008) 827-842.
- [44] V.L. Martínez, R.E. García, G. Curutchet, A. Sanguinetti, H.J. Fasoli, J.I. Franco, *International Journal of Hydrogen Energy*. 37 (2012) 14920-14925.
- [45] F.R. Hawkes, I. Hussy, G. Kyazze, R. Dinsdale, D.L. Hawkes, *International Journal of Hydrogen Energy*. 32 (2007) 172-184.
- [46] H.H.P. Fang, H. Liu, T. Zhang, *International Journal of Hydrogen Energy*. 30 (2005) 785-793.
- [47] N. Muradov, *Journal of Power Sources*. 118 (2003) 320-324.
- [48] A. Demirbaş, G. Arin, *Energy Sources*. 26 (2004) 1061-1069.
- [49] G. Chen, J. Andries, H. Spliethoff, M. Fang, P.J. van de Enden, *Solar Energy*. 76 345-349.
- [50] M. Asadullah, S.-i. Ito, K. Kunimori, M. Yamada, K. Tomishige, *Environmental Science & Technology*. 36 (2002) 4476-4481.
- [51] X. Zhang, J. Li, W. Yang, W. Blasiak, *Energy and Fuels*. 25 (2011) 3739-3746.
- [52] S. Czernik, J. Scahill, J. Diebold, *Journal of Solar Energy Engineering, Transactions of the ASME*. 117 (1995) 2-6.
- [53] D. Wang, S. Czernik, D. Montané, M. Mann, E. Chornet, *Industrial and Engineering Chemistry Research*. 36 (1997) 1507-1518.
- [54] A.F.D. Center, U.S. Department of Energy - Energy Efficiency and Renewable Energy.
- [55] J. Goldemberg, *Science*. 315 (2007) 808-810.
- [56] M.A. Kabel, G. Bos, J. Zeevalking, A.G.J. Voragen, H.A. Schols, *Bioresource Technology*. 98 (2007) 2034-2042.
- [57] S. Kim, B.E. Dale, *Biomass and Bioenergy*. 26 (2004) 361-375.
- [58] C.N. Hamelinck, G.v. Hooijdonk, A.P.C. Faaij, *Biomass and Bioenergy*. 28 (2005) 384-410.
- [59] J. Blackburn, Y. Liang, D. Das, *International Journal of Hydrogen Energy*. 34 (2009) 7428-7434.
- [60] I. del Campo, I. Alegría, M. Zazpe, M. Echeverría, I. Echeverría, *Industrial Crops and Products*. 24 (2006) 214-221.

- [61] Z. Zhong, H. Ang, C. Choong, L. Chen, L. Huang, J. Lin, *Physical Chemistry Chemical Physics*. 11 (2009) 872-880.
- [62] D.K. Liguras, D.I. Kondarides, X.E. Verykios, *Applied Catalysis B: Environmental*. 43 (2003) 345-354.
- [63] J.W.C. Liberatori, R.U. Ribeiro, D. Zanchet, F.B. Noronha, J.M.C. Bueno, *Applied Catalysis A: General*. 327 (2007) 197-204.
- [64] Y. Cong, V. Van Spaendonk, R.I. Masel, *Surface Science*. 385 (1997) 246-258.
- [65] J.H. Wang, C.S. Lee, M.C. Lin, *Journal of Physical Chemistry C*. 113 (2009) 6681-6688.
- [66] K. Vasudeva, N. Mitra, P. Umasankar, S.C. Dhingra, *International Journal of Hydrogen Energy*. 21 (1996) 13-18.
- [67] E.Y. García, M.A. Laborde, *International Journal of Hydrogen Energy*. 16 (1991) 307-312.
- [68] C.N. de Ávila, C.E. Hori, A.J. de Assis, *Energy*. 36 (2011) 4385-4395.
- [69] I. Fishtik, A. Alexander, R. Datta, D. Geana, *International Journal of Hydrogen Energy*. 25 (2000) 31-45.
- [70] S. Freni, G. Maggio, S. Cavallaro, *Journal of Power Sources*. 62 (1996) 67-73.
- [71] T. Ioannides, *Journal of Power Sources*. 92 (2001) 17-25.
- [72] A. Lima da Silva, C.d.F. Malfatti, I.L. Müller, *International Journal of Hydrogen Energy*. 34 (2009) 4321-4330.
- [73] V. Mas, R. Kipreos, N. Amadeo, M. Laborde, *International Journal of Hydrogen Energy*. 31 (2006) 21-28.
- [74] G. Rabenstein, V. Hacker, *Journal of Power Sources*. 185 (2008) 1293-1304.
- [75] F. Auprêtre, C. Descorme, D. Duprez, *Catalysis Communications*. 3 (2002) 263-267.
- [76] P. Bichon, G. Haugom, H.J. Venvik, A. Holmen, E.A. Blekkan, *Topics in Catalysis*. 49 (2008) 38-45.
- [77] A. Chica, S. Sayas, *Catalysis Today*. 146 (2009) 37-43.
- [78] J. Llorca, P. Ramírez De La Piscina, J.A. Dalmon, J. Sales, N. Homs, *Applied Catalysis B: Environmental*. 43 (2003) 355-369.
- [79] J. Llorca, N. Homs, P. Ramirez de la Piscina, *Journal of Catalysis*. 227 (2004) 556-560.
- [80] J. Comas, F. Marino, M. Laborde, N. Amadeo, *Chemical Engineering Journal*. 98 (2004) 61-68.
- [81] A.J. Vizcaíno, A. Carrero, J.A. Calles, *International Journal of Hydrogen Energy*. 32 (2007) 1450-1461.
- [82] C.C.R.S. Rossi, C.G. Alonso, O.A.C. Antunes, R. Guirardello, L. Cardozo-Filho, *International Journal of Hydrogen Energy*. 34 (2009) 323-332.
- [83] H. Song, L. Zhang, R.B. Watson, D. Braden, U.S. Ozkan, *Catalysis Today*. 129 (2007) 346-354.
- [84] F. Frusteri, S. Freni, L. Spadaro, V. Chiodo, G. Bonura, S. Donato, S. Cavallaro, *Catal. Commun.* 5 (2004) 611-615.
- [85] J.D.A. Bellido, E.M. Assaf, *Journal of Power Sources*. 177 (2008) 24-32.
- [86] A.M. Diskin, R.H. Cunningham, R.M. Ormerod, *Catalysis Today*. 46 (1998) 147-154.
- [87] R. Molina, G. Poncelet, *Journal of Catalysis*. 173 (1998) 257-267.
- [88] S. Li, M. Li, C. Zhang, S. Wang, X. Ma, J. Gong, *International Journal of Hydrogen Energy*. 37 (2012) 2940-2949.
- [89] A.N. Fatsikostas, X.E. Verykios, *J. Catal.* 225 (2004) 439-452.
- [90] A.N. Fatsikostas, D.I. Kondarides, X.E. Verykios, *Chemical Communications* (2001) 851-852.
- [91] Y. Yang, J. Ma, F. Wu, *International Journal of Hydrogen Energy*. 31 (2006) 877-882.
- [92] P. Biswas, D. Kunzru, *International Journal of Hydrogen Energy*. 32 (2007) 969-980.

- [93] J. Llorca, N. Homs, J. Sales, P. Ramírez de la Piscina, *Journal of Catalysis*. 209 (2002) 306-317.
- [94] S.S.Y. Lin, D.H. Kim, S.Y. Ha, *Applied Catalysis A: General*. 355 (2009) 69-77.
- [95] H. Song, X. Bao, C.M. Hadad, U.S. Ozkan, *Catalysis Letters*. 141 (2011) 43-54.
- [96] J. Llorca, J.A. Dalmon, P. Ramírez De la Piscina, N. Homs, *Appl. Catal. A Gen.* 243 (2003) 261-269.
- [97] V.A. de la Peña O'Shea, N. Homs, E.B. Pereira, R. Nafria, P. Ramírez de la Piscina, *Catalysis Today*. 126 (2007) 148-152.
- [98] J. Llorca, P. Ramírez De La Piscina, J.A. Dalmon, N. Homs, *Chemistry of Materials*. 16 (2004) 3573-3578.
- [99] B. Bayram, I.I. Soykal, D. Von Deak, J.T. Miller, U.S. Ozkan, *Journal of Catalysis*. 284 (2011) 77-89.
- [100] K.S. Kim, H.R. Seo, S.Y. Lee, J.G. Ahn, W.C. Shin, Y.K. Lee, *Topics in Catalysis*. 53 (2010) 615-620.
- [101] S.S.Y. Lin, D.H. Kim, M.H. Engelhard, S.Y. Ha, *Journal of Catalysis*. 273 (2010) 229-235.
- [102] S. Tuti, F. Pepe, *Catalysis Letters*. 122 (2008) 196-203.
- [103] M.P. Hyman, J.M. Vohs, *Surf. Sci.* . 605 (2011) 383-389.
- [104] E. Martono, M.P. Hyman, J.M. Vohs, *Physical Chemistry Chemical Physics*. 13 (2011).
- [105] A.M. Karim, Y. Su, M.H. Engelhard, D.L. King, Y. Wang, *ACS Catalysis*. 1 (2011) 279-286.
- [106] D. Kardash, C. Korzeniewski, N. Markovic, *Journal of Electroanalytical Chemistry*. 500 (2001) 518-523.
- [107] I. Luisetto, S. Tuti, E. Di Bartolomeo, *International Journal of Hydrogen Energy*. 37 (2012) 15992-15999.
- [108] C. Resini, M. Concepción Herrera Delgado, S. Presto, L.J. Alemany, P. Riani, R. Marazza, G. Ramis, G. Busca, *International Journal of Hydrogen Energy*. 33 (2008) 3728-3735.
- [109] D. San-José-Alonso, J. Juan-Juan, M.J. Illán-Gómez, M.C. Román-Martínez, *Applied Catalysis A: General*. 371 (2009) 54-59.
- [110] J. Zhang, H. Wang, A.K. Dalai, *Applied Catalysis A: General*. 339 (2008) 121-129.
- [111] A.M. Karim, Y. Su, J. Sun, C. Yang, J.J. Strohm, D.L. King, Y. Wang, *Applied Catalysis B: Environmental*. 96 (2010) 441-448.
- [112] M. Scott, M. Goeffroy, W. Chiu, M.A. Blackford, H. Idriss, *Topics in Catalysis*. 51 (2008) 13-21.
- [113] Q. Shi, B. Li, W. Chen, C. Liu, B. Huang, 2012, pp. 314-319.
- [114] V. Palma, F. Castaldo, P. Ciambelli, G. Iaquaniello, *Chemical Engineering Transactions*. 29 (2012) 109-114.
- [115] W.M.H. Sachtler, R.A.V. Santen, in: H.P.a.P.B.W. D.D. Eley (Ed.), *Advances in Catalysis*, Academic Press, 1977, pp. 69-119.
- [116] D. Wang, Y. Li, *Advanced Materials*. 23 (2011) 1044-1060.
- [117] R. Ferrando, J. Jellinek, R.L. Johnston, *Chemical Reviews*. 108 (2008) 845-910.
- [118] F. Tao, M.E. Grass, Y. Zhang, D.R. Butcher, J.R. Renzas, Z. Liu, J.Y. Chung, B.S. Mun, M. Salmeron, G.A. Somorjai, *Science*. 322 (2008) 932-934.
- [119] J.R. Renzas, W. Huang, Y. Zhang, M.E. Grass, D.T. Hoang, S. Alayoglu, D.R. Butcher, F.F. Tao, Z. Liu, G.A. Somorjai, *Physical Chemistry Chemical Physics*. 13 (2011) 2556-2562.
- [120] A. Ruban, B. Hammer, P. Stoltze, H.L. Skriver, J.K. Nørskov, *Journal of Molecular Catalysis A: Chemical*. 115 (1997) 421-429.
- [121] J.R. Kitchin, J.K. Nørskov, M.A. Barteau, J.G. Chen, *Journal of Chemical Physics*. 120 (2004) 10240-10246.

- [122] Y. Xu, A.V. Ruban, M. Mavrikakis, *Journal of the American Chemical Society*. 126 (2004) 4717-4725.
- [123] A.V. Ruban, H.L. Skriver, J.K. Nørskov, *Physical Review B - Condensed Matter and Materials Physics*. 59 (1999) 15990-16000.
- [124] O. Skoplyak, M.A. Barteau, J.G. Chen, *Journal of Physical Chemistry B*. 110 (2006) 1686-1694.
- [125] O. Skoplyak, M.A. Barteau, J.G. Chen, *Surface Science*. 602 (2008) 3578-3587.
- [126] T. Nishizawa, K. Ishida, *Bulletin of Alloy Phase Diagrams*. 4 (1983) 390-395.
- [127] G.D. Hibbard, K.T. Aust, U. Erb, *Materials Science and Engineering: A*. 433 (2006) 195-202.
- [128] O. Ergeneman, K.M. Sivaraman, S. Pané, E. Pellicer, A. Teleki, A.M. Hirt, M.D. Baró, B.J. Nelson, *Electrochim. Acta* 56 (2011) 1399-1408.
- [129] H. Zhang, T. Yao, Z. Sun, Y. Li, Q. Liu, F. Hu, Z. Pan, B. He, Z. Xie, S. Wei, *J. Phys. Chem. C* 114 (2010) 13596-13600.
- [130] G. Zhang, S. Sun, M. Bostetter, S. Poulin, E. Sacher, *Journal of Colloid and Interface Science*. 350 (2010) 16-21.
- [131] E.E. Hajcsar, P.R. Underhill, W.W. Smeltzer, *Surface Science*. 297 (1993) 186-192.
- [132] R. Jayaganthan, G.M. Chow, *Materials Science and Engineering B: Solid-State Materials for Advanced Technology*. 95 (2002) 116-123.
- [133] P.R. Underhill, *Surface Science*. 195 (1988) 557-565.
- [134] H.L. Skriver, N.M. Rosengaard, *Physical Review B*. 46 (1992) 7157-7168.
- [135] J. Greeley, M. Mavrikakis, *Nature Materials*. 3 (2004) 810-815.
- [136] C.A. Menning, J.G. Chen, *Journal of Chemical Physics*. 130 (2009).
- [137] J. Greeley, J.K. Nørskov, *Surface Science*. 592 (2005) 104-111.
- [138] K. Takanabe, K. Nagaoka, K. Nariai, K.-i. Aika, *J. Catal.* . 232 (2005) 268-275.
- [139] V.M. Gonzalez-Delacruz, R. Pereñiguez, F. Ternero, J.P. Holgado, A. Caballero, *Journal of Physical Chemistry C*. 116 (2012) 2919-2926.
- [140] J. Zhang, H. Wang, A.K. Dalai, *Journal of Catalysis*. 249 (2007) 300-310.
- [141] A.C.W. Koh, L. Chen, W. Kee Leong, B.F.G. Johnson, T. Khimyak, J. Lin, *International Journal of Hydrogen Energy*. 32 (2007) 725-730.
- [142] D. San-José-Alonso, J. Juan-Juan, M.J. Illán-Gómez, M.C. Román-Martínez, *Applied Catalysis A: General*. 371 (2009) 54-59.
- [143] Q. Fu, T. Wagner, *Surface Science Reports*. 62 (2007) 431-498.
- [144] K. Ozawa, Y. Oba, K. Edamoto, *Surface Science*. 601 (2007) 4053-4057.
- [145] E. Martono, J.M. Vohs, *Journal of Catalysis*. 291 (2012) 79-86.
- [146] X. Chu, J. Liu, B. Sun, R. Dai, Y. Pei, M. Qiao, K. Fan, *Journal of Molecular Catalysis A: Chemical*. 335 (2011) 129-135.
- [147] O. Dulub, M. Batzill, U. Diebold, *Topics in Catalysis*. 36 (2005) 65-76.
- [148] S. Penner, D. Wang, D.S. Su, G. Rupprechter, R. Podlucky, R. Schlögl, K. Hayek, *Surface Science*. 532-535 (2003) 276-280.
- [149] T. Conant, A.M. Karim, V. Lebarbier, Y. Wang, F. Girgsdies, R. Schlögl, A. Datye, *Journal of Catalysis*. 257 (2008) 64-70.
- [150] S. Liu, K. Takahashi, H. Eguchi, K. Uematsu, *Catalysis Today*. 129 (2007) 287-292.
- [151] M.P. Hyman, J.M. Vohs, 2008.
- [152] S. Kameoka, T. Kimura, A.P. Tsai, *Catalysis Letters*. 131 (2009) 219-224.
- [153] J.A. Dumont, M.C. Mugumaoderha, J. Ghijsen, S. Thiess, W. Drube, B. Walz, M. Tolkiehn, D. Novikov, F.M.F. De Groot, R. Sporken, *Journal of Physical Chemistry C*. 115 (2011) 7411-7418.

- [154] D. Potoczna-Petru, L. Krajczyk, *Catalysis Letters*. 87 (2003) 51-56.
- [155] O. Dulub, W. Hebenstreit, U. Diebold, *Physical Review Letters*. 84 (2000) 3646-3649.
- [156] S. Bernal, J.J. Calvino, M.A. Cauqui, J.M. Gatica, C. López Cartes, J.A. Pérez Omil, J.M. Pintado, *Catalysis Today*. 77 (2003) 385-406.
- [157] Q. Fu, T. Wagner, S. Olliges, H.-D. Carstanjen, *The Journal of Physical Chemistry B*. 109 (2004) 944-951.
- [158] A. Dandekar, M.A. Vannice, *Journal of Catalysis*. 183 (1999) 344-354.
- [159] X. Liu, M.H. Liu, Y.C. Luo, C.Y. Mou, S.D. Lin, H. Cheng, J.M. Chen, J.F. Lee, T.S. Lin, *Journal of the American Chemical Society*. 134 (2012) 10251-10258.
- [160] M.A. Martin-Luengo, P.A. Sermon, Y. Wang, *Journal of Catalysis*. 135 (1992) 263-268.
- [161] S. Freni, S. Cavallaro, N. Mondello, L. Spadaro, F. Frusteri, *Catalysis Communications*. 4 (2003) 259-268.
- [162] M.C. Sánchez-Sánchez, R.M. Navarro, J.L.G. Fierro, *Int. J. Hydrogen Energy*. 32 (2007) 1462-1471.
- [163] O. Akdim, W. Cai, V. Fierro, H. Provendier, A. van Veen, W. Shen, C. Mirodatos, *Topics in Catalysis*. 51 (2008) 22-38.
- [164] A. Denis, W. Grzegorzczuk, W. Gac, A. Machocki, *Catalysis Today*. 137 (2008) 453-459.
- [165] J. Llorca, P. Ramírez de la Piscina, J. Sales, N. Homs, *Chemical Communications* (2001) 641-642.
- [166] H. Knözinger, *Angewandte Chemie International Edition in English*. 7 (1968) 791-805.
- [167] H. Song, U.S. Ozkan, *Journal of Catalysis*. 261 (2009) 66-74.
- [168] H. Song, U.S. Ozkan, *Journal of Physical Chemistry A*. 114 (2010) 3796-3801.
- [169] G. Zhou, L. Barrio, S. Agnoli, S.D. Senanayake, J. Evans, A. Kubacka, M. Estrella, J.C. Hanson, A. Martínez-Arias, M. Fernández-García, J.A. Rodríguez, *Angewandte Chemie - International Edition*. 49 (2010) 9680-9684.
- [170] S. Bernal, J.J. Calvino, M.A. Cauqui, J.M. Gatica, C. Larese, J.A. Pérez Omil, J.M. Pintado, *Catalysis Today*. 50 (1999) 175-206.
- [171] D. Duprez, P. Pereira, A. Miloudi, R. Maurel, *Journal of Catalysis*. 75 (1982) 151-163.
- [172] R. Martins, P. Barquinha, I. Ferreira, L. Pereira, G. Goñalves, E. Fortunato, *Journal of Applied Physics*. 101 (2007).
- [173] Y. Ma, G.T. Du, S.R. Yang, Z.T. Li, B.J. Zhao, X.T. Yang, T.P. Yang, Y.T. Zhang, D.L. Liu, *Journal of Applied Physics*. 95 (2004) 6268-6272.
- [174] J.N. Zeng, J.K. Low, Z.M. Ren, T. Liew, Y.F. Lu, *Applied Surface Science*. 197-198 (2002) 362-367.
- [175] J.A. Rodríguez, P. Liu, J. Hrbek, J. Evans, M. Pérez, *Angewandte Chemie International Edition*. 46 (2007) 1329-1332.
- [176] H.S. Roh, A. Platon, Y. Wang, D.L. King, *Catalysis Letters*. 110 (2006) 1-6.
- [177] H. Wang, Y. Liu, L. Wang, Y.N. Qin, *Chemical Engineering Journal*. 145 (2008) 25-31.
- [178] S.V. Didziulis, K.D. Butcher, S.L. Cohen, E.I. Solomon, *Journal of the American Chemical Society*. 111 (1989) 7110-7123.
- [179] K.H. Ernst, A. Ludviksson, R. Zhang, J. Yoshihara, C.T. Campbell, *Physical Review B*. 47 (1993) 13782-13796.
- [180] M.C. Mugumaoderha, R. Sporken, J. Ghijsen, J.A. Dumont, *Journal of Physical Chemistry C*. 115 (2011) 20603-20609.
- [181] J.F. Da Costa-Serra, R. Guil-López, A. Chica, *Int. J. Hydrogen Energy*. 35 (2010) 6709-6716.
- [182] A.L. Alberton, M.M.V.M. Souza, M. Schmal, *Catalysis Today*. 123 (2007) 257-264.

- [183] M. Bilal, S.D. Jackson, *Catalysis Science & Technology*. 2 (2012) 2043-2051.
- [184] F. Frusteri, S. Freni, V. Chiodo, L. Spadaro, O. Di Blasi, G. Bonura, S. Cavallaro, *Appl Catal A Gen.* 270 (2004) 1-7.
- [185] F. Wang, Y. Li, W. Cai, E. Zhan, X. Mu, W. Shen, *Catalysis Today*. 146 (2009) 31-36.
- [186] J. Rass-Hansen, C.H. Christensen, J. Sehested, S. Helveg, J.R. Rostrup-Nielsen, S. Dahl, *Green Chemistry*. 9 (2007) 1016-1021.
- [187] H.S. Benggaard, J.K. Nørskov, J. Sehested, B.S. Clausen, L.P. Nielsen, A.M. Molenbroek, J.R. Rostrup-Nielsen, *Journal of Catalysis*. 209 (2002) 365-384.
- [188] V.K. Díez, C.R. Apesteguía, J.I. Di Cosimo, *Catalysis Today*. 63 (2000) 53-62.
- [189] V.K. Díez, C.R. Apesteguía, J.I. Di Cosimo, *Journal of Catalysis*. 215 (2003) 220-233.
- [190] S. Hövel, C. Kolczewski, M. Wühn, J. Albers, K. Weiss, V. Staemmler, C. Wöll, *Journal of Chemical Physics*. 112 (2000) 3909-3916.
- [191] C. Drouilly, J.M. Krafft, F. Averseng, H. Lauron-Pernot, D. Bazer-Bachi, C. Chizallet, V. Lecocq, G. Costentin, *Applied Catalysis A: General*. 453 (2013) 121-129.
- [192] C.H. Bartholomew, *Applied Catalysis A: General*. 212 (2001) 17-60.
- [193] J. Xu, X. Zhang, R. Zenobi, J. Yoshinobu, Z. Xu, J.T. Yates Jr, *Surface Science*. 256 (1991) 288-300.
- [194] E. Vesselli, A. Baraldi, G. Comelli, S. Lizzit, R. Rosei, *ChemPhysChem*. 5 (2004) 1133-1140.
- [195] D.R. Mullins, S.D. Senanayake, T.L. Chen, *Journal of Physical Chemistry C*. 114 (2010) 17112-17119.
- [196] N.A. Khan, M.B. Zellner, L.E. Murillo, J.G. Chen, *Catalysis Letters*. 95 (2004) 1-6.
- [197] E.D. Batyrev, N.R. Shiju, G. Rothenberg, *Journal of Physical Chemistry C*. 116 (2012) 19335-19341.
- [198] D.R. Rainer, D.W. Goodman, *Journal of Molecular Catalysis A: Chemical*. 131 (1998) 259-283.
- [199] K. Biedermann, M. Gubo, L. Hammer, K. Heinz, *Journal of Physics Condensed Matter*. 21 (2009).
- [200] J. Yoshihara, J.M. Campbell, C.T. Campbell, *Surface Science*. 406 (1998) 235-245.
- [201] S.M. Gates, J.N. Russell Jr, J.T. Yates Jr, *Surface Science*. 171 (1986) 111-134.
- [202] T. Kratochwil, M. Wittmann, J. Küppers, *Journal of Electron Spectroscopy and Related Phenomena*. 64-65 (1993) 609-617.
- [203] J.M. Vohs, M.A. Barteau, *Surface Science*. 221 (1989) 590-608.
- [204] E. Farfan-Arribas, R.J. Madix, *Journal of Physical Chemistry B*. 106 (2002) 10680-10692.
- [205] E. Martono, J.M. Vohs, *ACS Catalysis*. 1 (2011) 1414-1420.
- [206] C.T. Campbell, A. Ludviksson, 4 ed., AVS, Orlando, Florida (USA), 1994, pp. 1825-1831.
- [207] C.H.F. Peden, D.W. Goodman, *The Journal of Physical Chemistry*. 90 (1986) 1360-1365.
- [208] H. Over, Y.D. Kim, A.P. Seitsonen, S. Wendt, E. Lundgren, M. Schmid, P. Varga, A. Morgante, G. Ertl, *Science*. 287 (2000) 1474-1476.
- [209] T. Shishido, Y. Yamamoto, H. Morioka, K. Takaki, K. Takehira, *Applied Catalysis A: General*. 263 (2004) 249-253.
- [210] T. Fujitani, J. Nakamura, *Applied Catalysis A: General*. 191 (2000) 111-129.
- [211] M. Saito, T. Fujitani, M. Takeuchi, T. Watanabe, *Applied Catalysis A: General*. 138 (1996) 311-318.
- [212] J. Toyir, P. Ramírez De La Piscina, J.L.G. Fierro, N. Homs, *Applied Catalysis B: Environmental*. 29 (2001) 207-215.
- [213] N. Takezawa, N. Iwasa, *Catalysis Today*. 36 (1997) 45-56.

- [214] T. Shishido, M. Yamamoto, D. Li, Y. Tian, H. Morioka, M. Honda, T. Sano, K. Takehira, *Applied Catalysis A: General*. 303 (2006) 62-71.
- [215] A. Knop-Gericke, M. Hävecker, T. Schedel-Niedrig, R. Schlögl, *Topics in Catalysis*. 15 (2001) 27-34.
- [216] S. Günther, L. Zhou, M. Hävecker, A. Knop-Gericke, E. Kleimenov, R. Schlögl, R. Imbihl, *Journal of Chemical Physics*. 125 (2006).
- [217] H. Bluhm, M. Hävecker, A. Knop-Gericke, E. Kleimenov, R. Schlögl, D. Teschner, V.I. Bukhtiyarov, D.F. Ogletree, M. Salmeron, *Journal of Physical Chemistry B*. 108 (2004) 14340-14347.
- [218] Y.H. Chin, R. Dagle, J. Hu, A.C. Dohnalkova, Y. Wang, *Catalysis Today*. 77 (2002) 79-88.
- [219] N. Iwasa, S. Masuda, N. Ogawa, N. Takezawa, *Applied Catalysis A: General*. 125 (1995) 145-157.
- [220] K. Föttinger, J.A. van Bokhoven, M. Nachttegaal, G.n. Rupprechter, *The Journal of Physical Chemistry Letters*. 2 (2011) 428-433.
- [221] C. Rameshan, C. Weilach, W. Stadlmayr, S. Penner, H. Lorenz, M. Hävecker, R. Blume, T. Rocha, D. Teschner, A. Knop-Gericke, R. Schlögl, D. Zemlyanov, N. Memmel, G. Rupprechter, B. Klötzer, *Journal of Catalysis*. 276 (2010) 101-113.

---

# Chapter 2

## Experimental techniques

---

---

---

---

## Chapter 2. Experimental techniques

An overview on the materials, methodology and experimental techniques used in the present research study will be given in this chapter. Two types of catalyst systems will be discussed in the current work: 1) study of bimetallic interaction of Ni-Co and its catalytic properties as a bulk system without influence of support. 2) study of a model catalyst of Ni-Co thin film supported on ZnO single crystal to understand the metal-support interaction and its influence to ethanol steam reforming.

The use of X-ray photoelectron spectroscopy (XPS) and temperature desorption spectroscopy (TDS) will be discussed with particular focus as they are the two major in-house techniques involved in this work. A number of other characterisation techniques were also used, including: Scanning electron microscopy (SEM), X-Ray Diffraction (XRD), Atomic Force Microscopy (AFM) and Low Energy Electron Diffraction (LEED) to study the material's bulk structure, crystallinity and surface morphology. Part of the experiments were conducted in Elettra synchrotron facility and Bessy II synchrotron facility, in order to obtain high resolution Photoemission Spectroscopy (PES) spectra with high surface sensitivity (Elettra) and to carry out surface studies of the catalysts *in-situ* in reaction gases using Ambient Pressure PhotoEmission Spectroscopy (APPES) in Bessy II.

### 2.1 Methods and materials for developing model catalyst

#### 2.1.1 Properties of ZnO

Some properties of Ni-Co bimetallic materials have been reviewed in chapter 1. ZnO is an important catalyst support material, and its intrinsic properties also affect material's catalytic properties. Some characteristics of ZnO will be reviewed in this section.

ZnO is a wide band-gap semiconductor (band gap  $\sim 3.37$  eV). It has been widely applied to optoelectronics, gas sensing, energy, biomedical sciences and spintronics.[1-5] Development of nanostructured ZnO is of wide research interest in recent years [6-8]. This has paved the way to the development of high surface area and efficient catalyst support based on ZnO.

ZnO lattice has a hexagonal closed packing (hcp) wurtzite crystal structure. A schematic representation of wurtzite ZnO structure is shown in Fig. 2.1. The unit cell is composed of two overlapping hcp sublattices. Each sublattice is composed of four atoms per unit cell and every atom of one kind is surrounded by four atoms of the other kind, such that each atom is tetrahedral coordinated. This forms a bulk crystal composed of alternating planes from each type of atom. These planes are displaced with respect to each other along *c*-axis. This arrangement results in a net dipole moment normal to the polar surface of the crystal. The plane along the *c*-axis contains equal amount of oxygen and Zn atom and is the non-polar face of ZnO crystal.

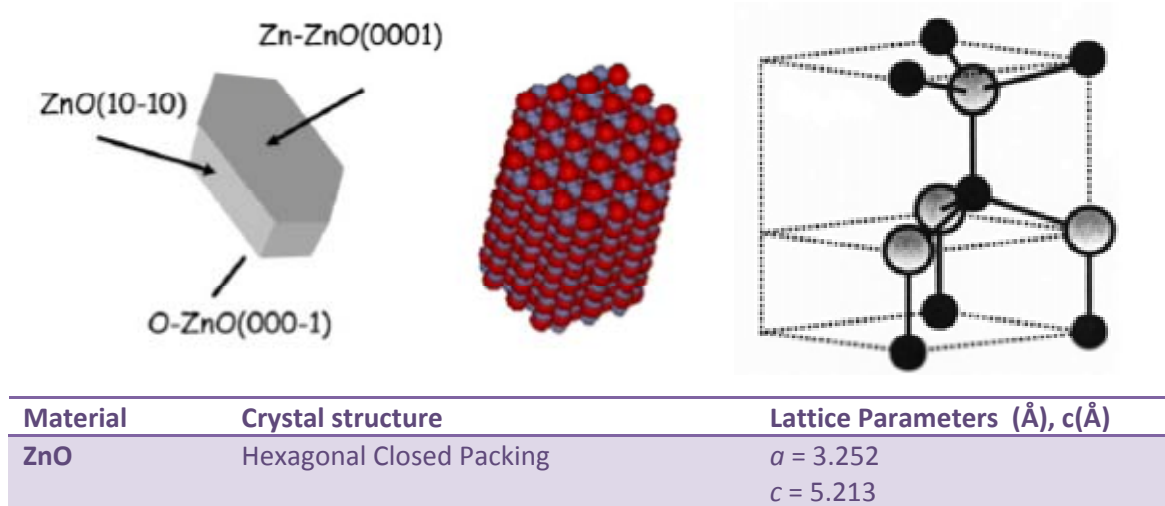


Figure 2.1 Schematic representation and lattice parameters of ZnO crystallite. [5, 9]

ZnO single crystals are usually available as Zn terminated ZnO (0001) (denoted as ZnO-Zn) and O terminated ZnO (000-1) (denoted as ZnO-O) and non-polar ZnO (1010). In this work, polar ZnO single crystals were used. Clean ZnO-Zn or ZnO-O single crystal shows a (1x1) diffraction pattern in LEED, which is coherent with its hexagonal bulk structure:

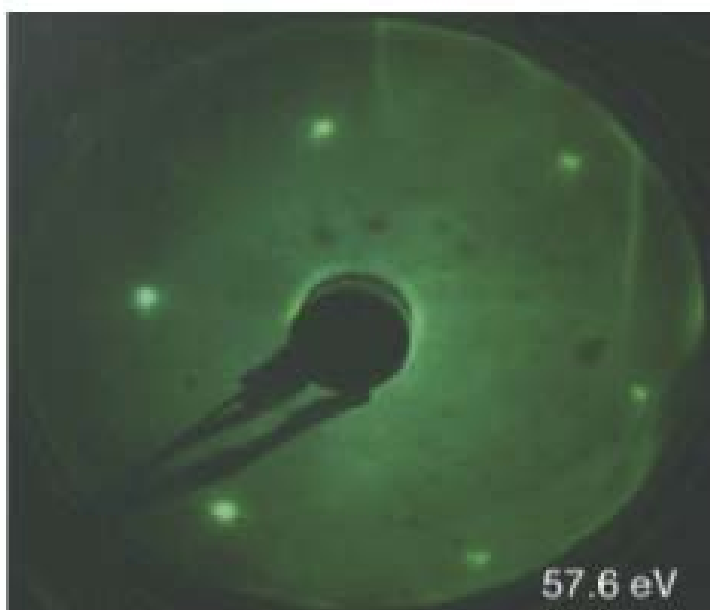


Figure 2.2 LEED pattern of Zn-terminated, polar ZnO - Zn surface. [9]

Polar ZnO surfaces are less stable due to the presence of dipole moment. ZnO-Zn and ZnO-O surfaces are stabilized through different surface restructuring mechanism. On ZnO-Zn, formation of triangular islands and pits with O atom occupying the edge of the islands have been predicted both theoretically by DFT [10] and experimentally by STM [11, 12]. On polar ZnO surface, water tends to adsorb dissociatively as hydroxyl group. On ZnO-Zn, the adsorption sites are found along step edges of the triangular pits and islands at the Zn atom, leaving the hydrogen group to oxygen [13]. Water adsorption on ZnO-O also results in formation of hydroxyl group. Dissociative adsorption of water are detected at low

temperature (200 K on ZnO-O) [14]. Bare ZnO-O tends to restructure as (1x3) oxygen vacancy structure and the formation of hydroxylated ZnO-O-H surface tend to stabilize the (1x1) surface structure on ZnO-O [12, 13, 15]. Because of their surface instability, polar surfaces exhibits higher catalytic activities towards reactions such as methanol synthesis[16].

The activity of ZnO in catalytic reaction is closely associated to the presence of oxygen vacancy [17]. Wurtzite ZnO are commonly found as n-type semiconductor which possesses intrinsic defects such as O vacancies and Zn interstitials. Surface oxygen vacancy could serve as adsorption site for O atom in a molecule, exposing the other groups for further reactions. This functionality has been discussed for the activation of CO<sub>2</sub> [18] and the adsorption of ethanol [19]. The reducibility of molecules by the function of lattice oxygen of ZnO has been shown in methanol steam reforming reaction [16]. It has also been proposed by Douilly et al. [20] that the formation of oxygen vacancy increases the electron density and hence the basicity of these sites, which increases the reactivity of ZnO towards reactant molecules.

## **2.1.2 Material preparation**

### **2.1.2.1 Ni-Co bimetallic materials**

Two types of unsupported Ni-Co materials, planar polycrystalline Ni-Co foil and Ni-Co nanopowder, have been studied in this work. Planar polycrystalline Ni-Co foil was used to study bimetallic interaction of Ni-Co in oxidative environment. Reactions that are specific to certain geometry and crystal structure are generalized on polycrystalline material and thus the phenomena observed could be associated mainly to materials' chemical properties such as chemical potential difference. In addition, a better correspondence of these results to later study by APPES could be made, since the sample used was in powder form in order to achieve a satisfactory level of catalytic activities. This also reduces the geometric specificity of the sample. Reference experiments on monometallic Ni and Co foils or powder were also studied for a better comparison of the bimetallic effect.

The Ni, Co and Ni-Co foils (50% Ni and 50% Co, 99.9+% purity) used were of size 1 cm x 1 cm x 0.01mm from Mateck. The metal foils were cleaned by Ar<sup>+</sup> sputtering (600V, 40 min) and annealed subsequently at 670 K in UHV to remove surface impurities. The sputtering-annealing cycle was repeated until no C signal was detected from XPS.

Ni-Co powders were used for the study of reactions under ambient pressure gas phase environment in synchrotron based APPES setup. Ni-Co (99%, <150nm, Sigma Aldrich) nanopowders were used in this study. The results were compared with those from monometallic Ni (99.9%, <100nm, Sigma Aldrich), Co (99%, 50-80nm, Alfa Aesar) nanopowders. The nanopowder was treated at 623 K in O<sub>2</sub> to oxidize surface carbonaceous species as the cleaning procedure before experiments.

### **2.1.2.2 Ni-Co thin film supported on polar ZnO single crystal**

The model catalyst used for the study of metal-support interaction (experiments conducted in Elettra, presented in chapter 4) and the TDS study of ethanol (presented in chapter 5) is

based on Ni-Co thin overlayers supported on polar ZnO single crystal. The thin overlayers were prepared by e-beam evaporation. One side polished O- and Zn- terminated (1cm x 1cm x 0.33mm) ZnO single crystal (obtained from Crystec) were used as the substrate. The polished side were used as the surface for thin film deposition. It was cleaned by a 600 eV Ar<sup>+</sup> ion sputtering at Ar pressure 1x10<sup>-4</sup> mbar for 40 minutes to remove surface impurities. The ZnO single crystals were then annealed at 773 K in 5x10<sup>-7</sup> mbar of O<sub>2</sub> for 10 minutes to restore the oxygen vacancies created. The sputtering-annealing procedure was repeated until no carbon was detected by XPS. The single crystal surface structure was confirmed by LEED.

Ni and Co thin layers were deposited on ZnO single crystal by e-beam deposition. The e-beam water-cooled evaporator (Mantis depositions Ltd., model: QUAD-EV-C) consists of four independent pockets, allowing 4-metal simultaneous evaporation. The target metals for deposition (Ni and Co) were biased to 2000 V. Electrons was generated from a tungsten filament and hit the biased metal target. The target metal tip was locally heated and evaporated. A manual shutter was used to control the time of deposition. The rate of evaporation was measured by intergrated metal plates which collects the current of the ionised fraction of the evaporant stream for flux monitoring.

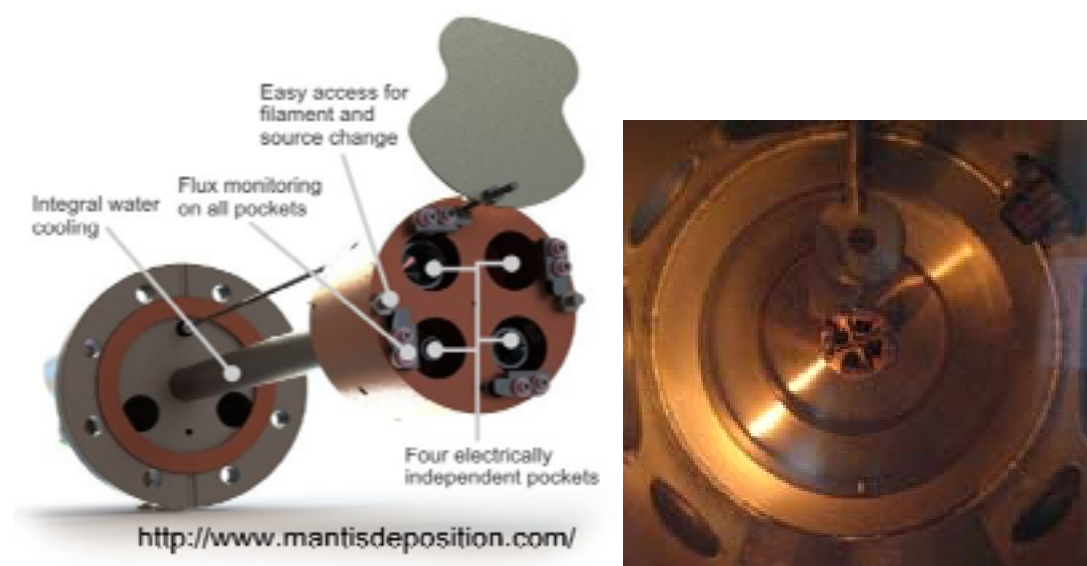


Figure 2.3 Scheme of the e-beam evaporator and real image of the evaporator[21]

This evaporation source was used for the experiments performed in the in-house UHV setup and the end station of the beamline in Elettra. The distance of the evaporation head and the sample was above 6 cm in the in-house UHV setup and in the end station of beamline to ensure the overlapping of the beam coverage from each evaporation pocket on the sample.

The rate of evaporation was controlled at ion flux of 4 nA in case of single metal evaporation or bimetallic evaporation for Ni:Co of 1:1 ratio. The thickness of the deposited film was controlled by varying the time of deposition. In case of deposition of Ni-Co bimetallic layer of different composition, the flux of the respective pocket was adjusted in proportion to the composition desired.

## 2.2 Study of the surface composition and reactions of the catalysts

### 2.2.1 X-ray Photoemission spectroscopy (XPS)

#### 2.2.1.1 Overview

XPS is the major characterization technique used for the study of catalysts' surface properties. XPS provides information on the energy level of core level and valence electrons, from which one can obtain information on the type of elements, their chemical state and the surface composition. It is a rather surface sensitive technique that information is acquired from the outermost layers (e.g. ~3 nm of the surface layer for Ni, Co and ZnO), which is also the critical region to catalytic reaction. The basic principles of XPS is based on photoelectric effect. In particular, when a material is illuminated by photon, their energy is absorbed by electrons in the atoms, which is transferred from initial state into an excited final state.

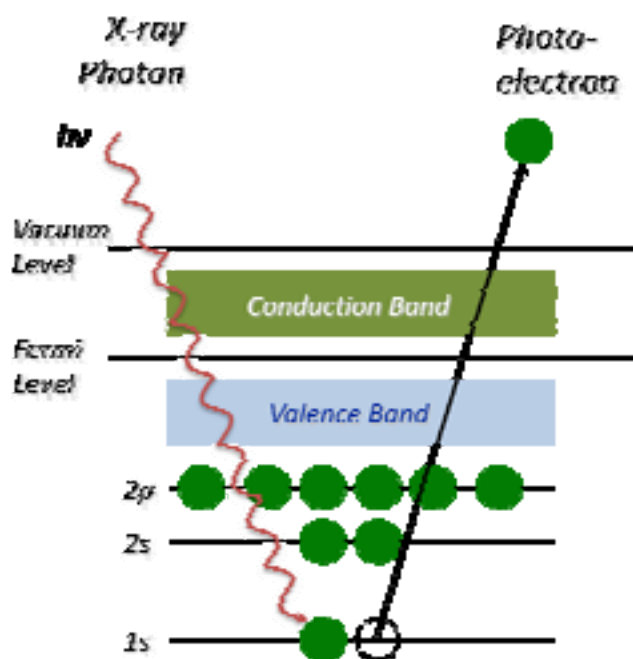


Figure 2.4 Photoemission of a core level electron

When excited with sufficient energy, electrons ejects from the atoms. The kinetic energy (K.E.) of these photoelectrons is given by

$$\text{K.E.} = h\nu - \text{B.E.} - \phi$$

where  $h\nu$  is the energy of photon, B.E. is the binding energy of the photoelectron and  $\phi$  is the work function of spectrometer.

Conventional lab-based XPS is usually equipped with a dual anode (Al  $k\alpha$  and Mg  $k\alpha$ ) X-ray as the photon source. The respective photon energy is 1486.7 eV and 1253.6 eV. The energy of photoelectrons is identified by an energy analyser. The energy analyzer used in the XPS systems involved in this work all belongs to hemispherical analyser. A scheme of the electron trajectory in the analyzer is shown in figure 2.5. In order to improve energy resolution with an analyser of reasonable size, the energy of photoelectrons is retarded to a

constant energy, commonly referred as pass energy ( $E_0$ ) by a lens system before entering the energy analyser. The passage of electrons is controlled by entrance and exit slits. The two plates of the hemisphere are charged with different potentials ( $V_1$  and  $V_2$ ). The electrons are deflected along the analyser by the attractive/repulsive force created by the potential difference. The potential of the electron at pass energy ( $V_0$ ) is given by:

$$V_0 = V_1 \frac{R_1}{2R_0} + V_2 \frac{R_2}{2R_0} \quad \text{and} \quad E_0 = eV_0$$

The notations are indicated in figure 2.5. Only electrons with selected energy can travel along the spherical trajectory and be refocused to leave the analyzer from the exit slit.

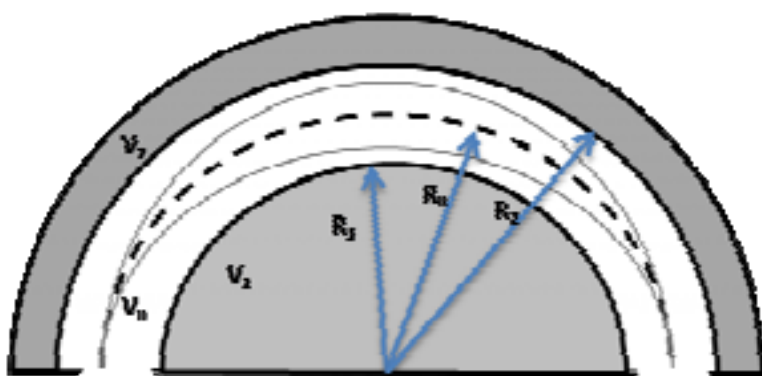


Figure 2.5 Concentric hemispherical analyzer

The photoelectron detector is a channel electron multiplier which has a spiral tube along which a potential difference is applied. The electrons entering the spiral collide with the wall and produces secondary electrons. These electrons are accelerated and deflected by the potential applied and multiplies itself when being collected at the exit of the channeltron.

### 2.2.1.2 Synchrotron radiation based photoemission spectroscopy (PES)

Conventional laboratory-based X-ray has in general confined photon intensity (number of photons). In addition, the incident photon energy is fixed and the resolution is limited by the line width of the X-ray. Synchrotron radiation, where electromagnetic radiation is generated from accelerated electron travelling in orbital trajectory, can be applied for advanced spectroscopic techniques to overcome the short-coming of common X-ray. In synchrotron facility, electrons are accelerated in a linear accelerator, and enter a large storage ring when they are accelerated to their final energy level. The trajectories of electrons are manipulated in a curved path by the magnetic fields generated by surrounding bending magnets. Energy is lost in form of light during the circular movement and is known as synchrotron radiation. These light beams are of very high intensities and spread over a wide energy range. The light beam is then directed toward "beamlines" where they are focused and monochromatised by specialised optics for usage at the end station.

Synchrotron radiation has shown some exceptional qualities over conventional x-ray:

- Radiation is generated with brilliance orders of magnitude higher than conventional X-rays.
- Light beams have high level of polarization (linear, elliptical or circular).
- The wavelength of photon spans over a wide range and can be monochromatised.
- The light beam consists of almost parallel rays and is highly collimated.
- The light beam is focused over a very small area.
- Photons are emitted with highly precise pulsed time interval

Part of the experiment was conducted in two synchrotron radiation facilities. The characteristics of the respective beamlines are summarized as the following:

Table 2.1 Characteristics of Material Science beamline and ISIS beamline used

	<b>Elettra- Material Science beamline</b>	<b>Bessy II- ISIS beamline</b>
<b>Photon energy window</b>	22-1000 eV	80-2000 eV
<b>Spot size</b>	100 μm in diameter	150 μm x 80 μm (h x v)
<b>Monochromator</b>	Plane grating monochromator Bestec (SX 700 design) with a single grating	Plane grating monochromator
<b>Flux</b>	2x10 <sup>9</sup> - 6x10 <sup>10</sup> ph/s 0.3mA ring current (25-500eV)	5x10 <sup>9</sup> - 6x10 <sup>10</sup> ph/s 0.1A ring current (100-1400eV), 111μm exit slit
<b>Polarisation</b>	~80% linear horizontal	linear horizontal

Thanks to the wide applicable range of photon energy in synchrotron, the kinetic energy of the photoelectrons can be selected to control the surface sensitivity of the photoelectron. In general the overall depth of the surface probed by XPS or PES is regarded as 3 times of the Inelastic Mean Free Path (IMFP) of the photoelectrons. The IMFP adopted in this work is estimated from TPP-2M equation[23], where the major parameters are the solid density ( $\rho$ ), the number of valence electrons per atom or molecule for a compound ( $N_v$ ), the plasmon frequency ( $E_p$ ) and the energy of the bandgap ( $E_g$ ):

$$\lambda = \frac{E}{E_p^2 \left[ \beta \ln(\gamma E) - \left(\frac{C}{E}\right) + \left(\frac{D}{E^2}\right) \right]}$$

where

$$\beta = -0.1 \pm 0.944(E_p^2 + E_g^2)^{-\frac{1}{2}} + 0.069\rho^{0.1}$$

$$\gamma = 0.191\rho^{-1/2}$$

$$C = 1.97 - 0.91U$$

$$D = 53.4 - 20.8U$$

$$U = \frac{N_v \rho}{M} = E_p^2 / 829.4$$

$$E_p = 28.8(N_v \rho / M)^{1/2}$$

The corresponding IMFP for the elements studied is shown as the following:

Table 2.2 IMFP of Ni 2p, Co 2p and Zn 2p from different photon sources

Element	IMFP(Å)		
	In-house XPS Al $\kappa\alpha$ ( $h\nu=1487$ eV)	Synchrotron based PES at Bessy II (K.E.=145eV)	Synchrotron based PES at Elettra (K.E.=115eV)
Ni 2p	11.1	4.7	4.2
Co 2p	12	4.7	4.3
Zn 2p (ZnO)	11.5	--	--

The results obtained from synchrotron based PES is more surface sensitive to those from conventional XPS due to the low photon energy used. By the variation of photon energy, depth-dependent analysis was performed to study the surface composition of the catalyst at different surface region. This experiment was performed at Elettra. Depth profiling technique helps to differentiate the effects at the outermost surface and at the metal-support interface. The photon energy used and the corresponding IMFP are shown in the following table:

Table 2.3 IMFP of Ni 3p, Co 3p and Zn 3p from different photon sources

Element	IMFP(Å)		
	Synchrontron based PES at Elettra		
	$h\nu = 890\text{eV}$	$h\nu = 620\text{eV}$	$h\nu = 200\text{eV}$
Ni 3p	13.4	10.1	4.5
Co 3p	13.4	10.2	4.6
Zn 3p (ZnO)	16.9	12.6	5.6

### 2.2.1.3 Chemical effects on XPS spectra

XPS spectra features allow the identification of the binding energy (B.E.) difference between photoelectrons excited from different local chemical environment. B.E. depends on the initial and final state of the atom. Shift in core level binding energy is likely to be associated to a change in chemical bonding. In addition, a number of relaxation processes, such as shake-up/shake off process and plasmon excitation can also affect the final state of the atom and contribute to the characteristic feature of XPS spectra for each chemical state.

The initial state of Ni 2p and Co 2p electrons are subjected to spin-orbit splitting. The coupling between the electron spin and the angular momentum vector of p orbital gives rise to the splitting of two states at different energy. The total angular momentum ( $j$ ) for p subshell is 3/2 and 1/2, which is shown as two separate peaks: Ni 2p<sub>3/2</sub> and Ni 2p<sub>1/2</sub>; Co 2p<sub>3/2</sub> and Co 2p<sub>1/2</sub>. Most of the XPS data shown will refer to Ni 2p<sub>3/2</sub> and Co 2p<sub>3/2</sub> only.

Shake-up or shake-off satellites are features of the final state configuration, where energy is made available for excitation of atoms (shake-up) or ejection of outer shell electron (shake-

off) during photoemission process. The B.E. of the main peak and satellite peak of Ni and Co and the respective oxides has been reported by several studies:

Table 2.4 binding energy of the main peak and satellite peak of Ni and Co in different oxidation state

	B.E. (Main)	B.E. (Satellite)	References
<b>Ni</b>	852.6		[24, 25]
	852.5		[26]
	852.2		[27]
<b>Ni<sup>2+</sup> (NiO)</b>	854.1		[28]
	854.6		[29]
	854		[26]
	854.1	855.6; 861	[27]
<b>Co</b>	778.2		[30]
	778.2		[31]
<b>Co<sup>2+</sup> (CoO)</b>	780.2-780.7		[32]
	780.1-780.9		[31]
	780.5	787.1	[33]
<b>Co<sup>3+</sup> (Co<sub>3</sub>O<sub>4</sub>)</b>	779.6-780.5	786-789.5	[32]
	779.8	788.8	[34]

The XPS spectra of Ni and Co oxide contain characteristic secondary structure from shake-up satellite. Ni 2p<sub>3/2</sub> spectra is consisted of the main line at 854.5 eV, corresponding to the final state of  $\underline{c}3d^9\underline{L}$ , and a charge-transfer shake-up satellite at 861 eV, corresponding to the final state of  $\underline{c}3d^8$  and  $\underline{c}3d^{10}\underline{L}^2$  ( $\underline{c}$  denotes for a hole in the Ni 2p core level and  $\underline{L}$  denotes a hole in the ligand band)[35]. The origin of the shoulder observed at 855.5 eV has been a controversial issue. It has been interpreted as a non-local screening effect from O 2p electrons in the NiO<sub>6</sub> cluster[36]. Recent studies from Mossaneck et al. [37] has indicated that the contribution of surface cluster NiO<sub>5</sub> to this feature should be considered in addition to the bulk model cluster NiO<sub>6</sub>.

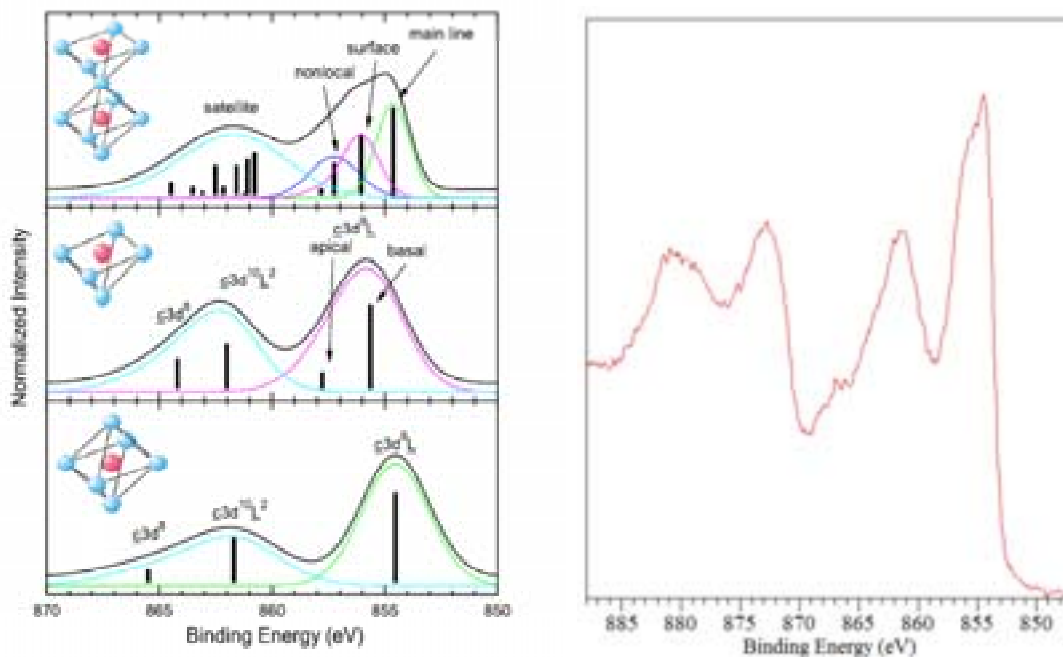


Figure 2.6 (left) Simulated Ni  $2p_{3/2}$  for NiO [38] and (right) experimental Ni  $2p_{3/2}$  of NiO from Al  $K\alpha$

CoO has an intense satellite peak at about 787 eV. The high intensity of the satellite is associated to the high-spin  $Co^{2+}$  of the CoO lattice, which allows significant charge-transfer between cobalt  $3d^7$  band with neighbouring lattice oxygen [39]. The presence of satellite could be understood with a similar cluster model as Ni oxide. The energy of satellite is the difference between coulomb interaction of  $2p$ - $3d$  hole and the charge-transfer energy between a  $3d$  and  $2p$  hole [40].

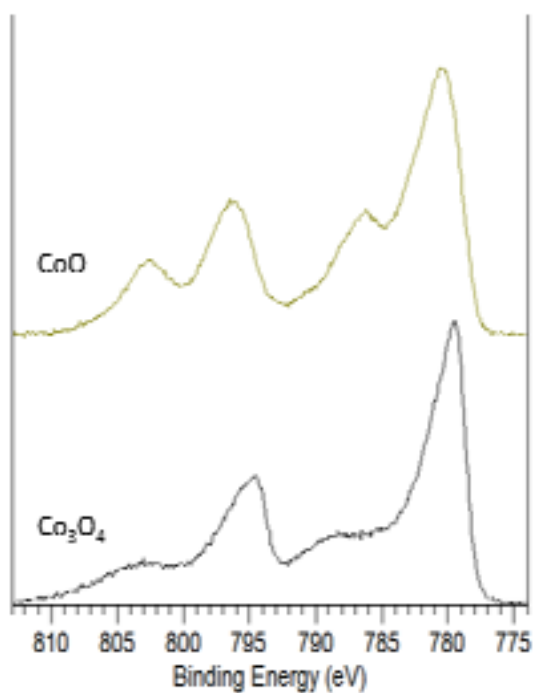


Figure 2.7 Co  $2p_{3/2}$  spectra of CoO and  $Co_3O_4$

On the other hand, Co<sub>3</sub>O<sub>4</sub> has a weak satellite at around 787 eV. This is explained by the extra stability of O<sub>h</sub> Co<sup>3+</sup> ion, which is a low-spin d<sub>6</sub> cation with totally spin-paired t<sub>2g</sub> and empty e<sub>g</sub> levels. This electronic configuration has suppressed charge transfer between orbitals by shake-up mechanism.[39]

The B.E. value and the peak shape provide information on the local electronic environment of the element. In the experimental results presented, the binding energy was calibrated to the Fermi level of the sample. The proportion of metal oxide to the entire peak was obtained by subtraction of reference spectra of metallic Ni and Co from the experimental spectra. The reference spectra of metals were obtained from Ni or Co metal foil after cycles of sputtering and cleaning cycle. The reference spectra were normalized to the intensity of the experimental spectra at the B.E. of the main peak for subtraction. The background signal was subtracted by using Shirley background. C 1s and O 1s were fitted with Gaussian/Lorentzian line shape (G/L ratio = 0.3).

The surface composition of the samples was calculated from the atomic ratio between the elements, which was calculated from the following formula for conventional XPS measurement:

$$\frac{N_A}{N_B} = \frac{I_A/A.S.F._A}{I_B/A.S.F._B}$$

where

N<sub>x</sub> is atomic concentration of element X

I<sub>x</sub> is the intensity of the peak of photoemission of element X

A.S.F.<sub>x</sub> is the atomic sensitivity of element X obtained from the empirical value estimated by Wagner et al. [41].

Table 2.5 Atomic sensitivity factor [41]

Element	A.S.F.
Ni 2p 3/2	3
Co 2p 3/2	2.5
Zn 2p3/2	4.8
O 1s	0.66
C 1s	0.25

The quantification of data obtained from synchrotron was treated with different correction factors. As the photon energy can be easily adjusted in synchrotron, the spectra were collected with about the same kinetic energy to ensure that the information depth for each element is the same. The photon intensity is affected by the photon flux and the electrons in the storage ring. The current of electron in the storage ring in Elettra was maintained at a constant level. The intensity of the peak area was normalised to the photon flux and photoionization cross section[42] prior to the calculation of atomic ratio. The data obtained from Bessy was normalised with the above two factors and the ring-current, as electron injection to the storage ring was made only at defined time interval (12 hours).

The XPS quantification for the ZnO supported thin film was based on the calculation model for a layered structure. The surface coverage of metal layer deposition was estimated by the attenuation of the signal of substrate ( $I_A$ ). Thickness ( $d_M$ ) of metal layer deposited was obtained from:

$$I_A = I_A^\infty \exp\left[-\frac{d_M}{\lambda_M \cos\theta}\right], \text{ where}$$

$d_M$  is the thickness of the metal overlayer

$I_A^\infty$  is the intensity of the substrate element from an infinitely thick layer. For model with ZnO as substrate, the intensity of the Zn 2p or Zn 3p peak measured on a clean ZnO single crystal substrate were used as  $I_A$ .

$\lambda_M$  is the IMFP of photoelectrons of the deposited layer

$\theta$  is the emission angle of electron

In this work, XPS measurement has been conducted in several set-ups, including:

- XPS system works at UHV or low pressure ( $<10^{-6}$  mbar) gas pressure
- XPS system with high pressure cell

which are both in-house XPS systems in the laboratory of l'Institut de chimie et procédés pour l'énergie, l'environnement et la santé (ICPEES). In addition, selected experiments were conducted in the following two synchrotron based PES facilities, in order to gain results with higher resolution, surface sensitivity and to perform *in-situ* PES measurement under reaction condition:

- Material science beamline in Elettra, Trieste, Italy
- ISSS beamline in Bessy II, Berlin, Germany

The configuration of each system will be described in the following.

#### 2.2.1.4 Experimental set-up

##### a) UHV system for low pressure studies

This XPS system is adapted for general surface science studies in UHV. The UHV system is separated into three compartments: 1) a load-lock chamber 2) a preparation chamber with  $\text{Ar}^+$  sputtering gun for sample cleaning and the evaporation source for metal deposition and 3) an analysis chamber. The main analysis chamber is equipped with an  $\text{Ar}^+$  sputtering gun, a ultraviolet light source for Ultraviolet Photoemission Spectroscopy (UPS), a gas/vapour doser and a differentially pumped mass spectrometer for thermal desorption spectroscopy (TDS). The base pressure of the system is maintained at  $2 \times 10^{-9}$  mbar.

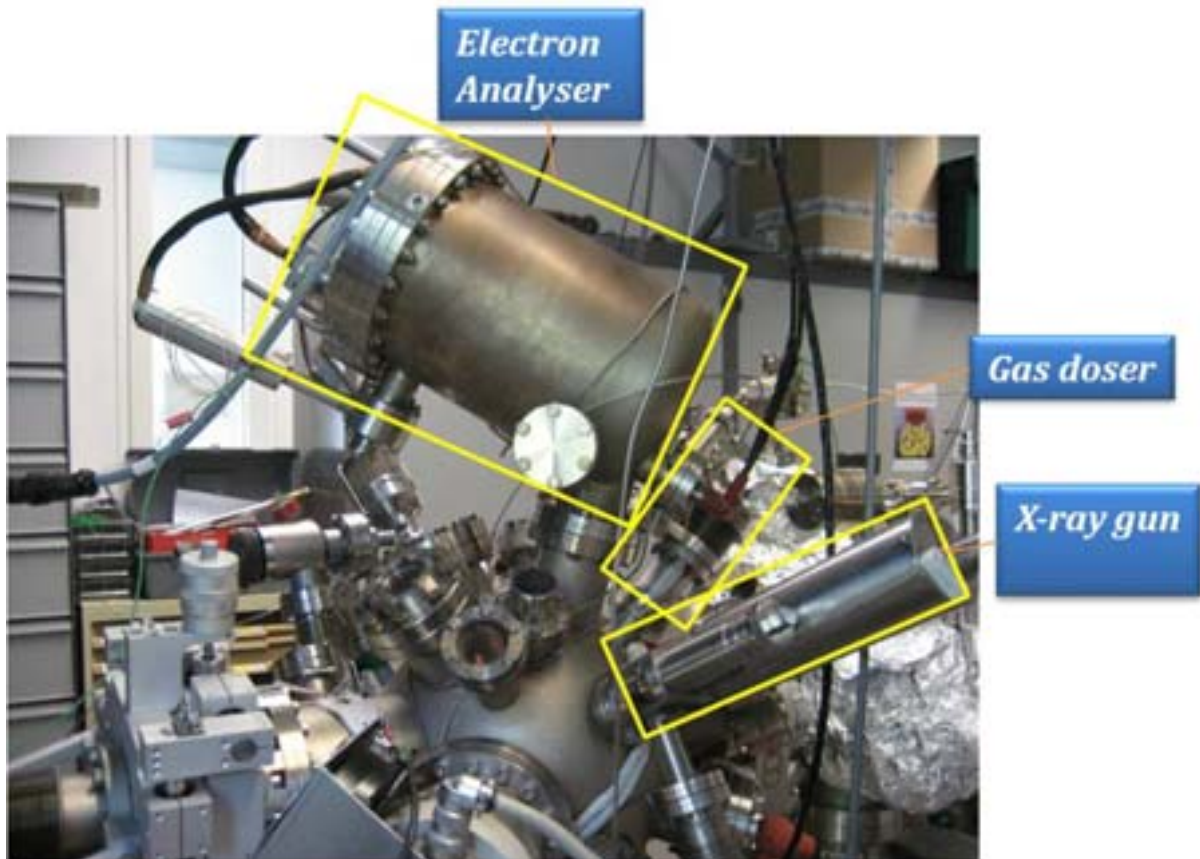


Figure 2.8 UHV system for low pressure XPS and TDS studies

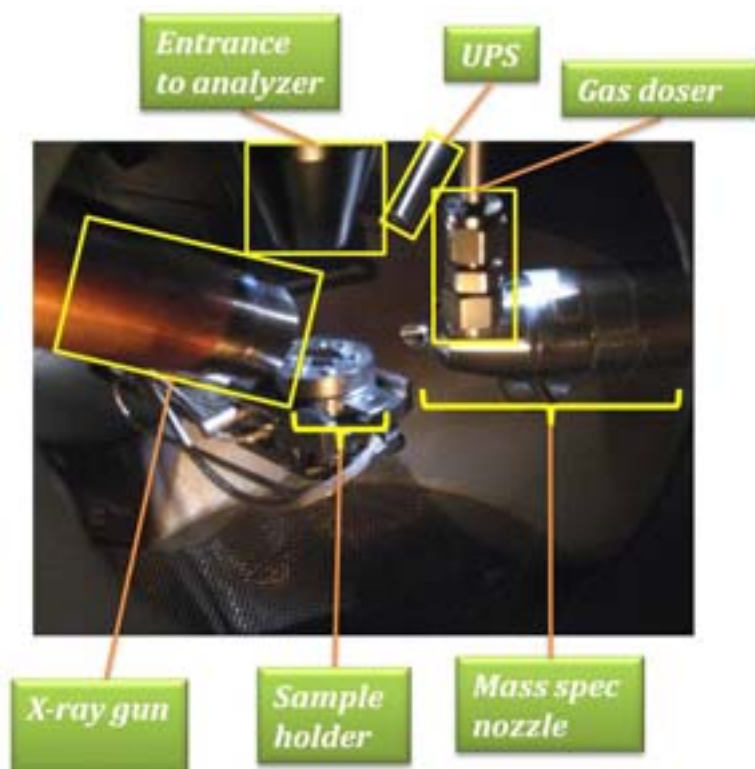


Figure 2.9 Analysis UHV system for low pressure XPS and TDS studies

The XPS consists of a non-monochromatic dual anode (Al  $\text{K}\alpha$  and Mg  $\text{K}\alpha$ ) X-ray source and a VG microtechClam 2 electron analyser. The XPS spectra in this work were measured with Al  $\text{K}\alpha$  X-ray source. The angle of incidence of the X-ray tube is 30 degree with respect to the sample and the emission angle is 15 degree to the normal of the sample surface unless otherwise specified. The energy of electrons was detected by a 1-channel concentric hemispherical analyzer. The pass energy for high resolution spectra was 20 eV and the survey scan was recorded with pass energy at 50 eV. The sample can be heated by electron bombardment from a Tungsten filament embedded in the molybdenum sample holder. The temperature of the sample was measured by a chromel/alumel (K-type) thermocouple, pressed onto the surface of the sample. Unless otherwise stated, the heating ramp was maintained at 1 K/s for most heating process. The sample can be cooled to 110 K by a cold finger located at the base of the sample. This cold finger is sealed from the UHV system and is connected to the atmosphere by an isolated circuit, where liquid nitrogen is introduced. The cold finger is supported on a mobile stage which is levelled by compressed air, and thus controls the contact of cold finger to the sample holder. Gas exposure ( $<1 \times 10^{-6}$  mbar) to the chamber was manually controlled by a leak valve, with the pressure monitored by ion gauge.



*Figure 2.10 Sample holder for the XPS system for low gas pressure/UHV studies*

***b) System for high pressure studies***

Another UHV system used was dedicated for studies of atmospheric pressure gas treatment. This system consists of a main chamber equipped with XPS and a preparation chamber with an enclosed high pressure cell, and an  $\text{Ar}^+$  sputtering gun (3000 eV). This system allows the sample to be introduced to the analysis chamber after high pressure gas treatment without being exposed to the atmosphere.

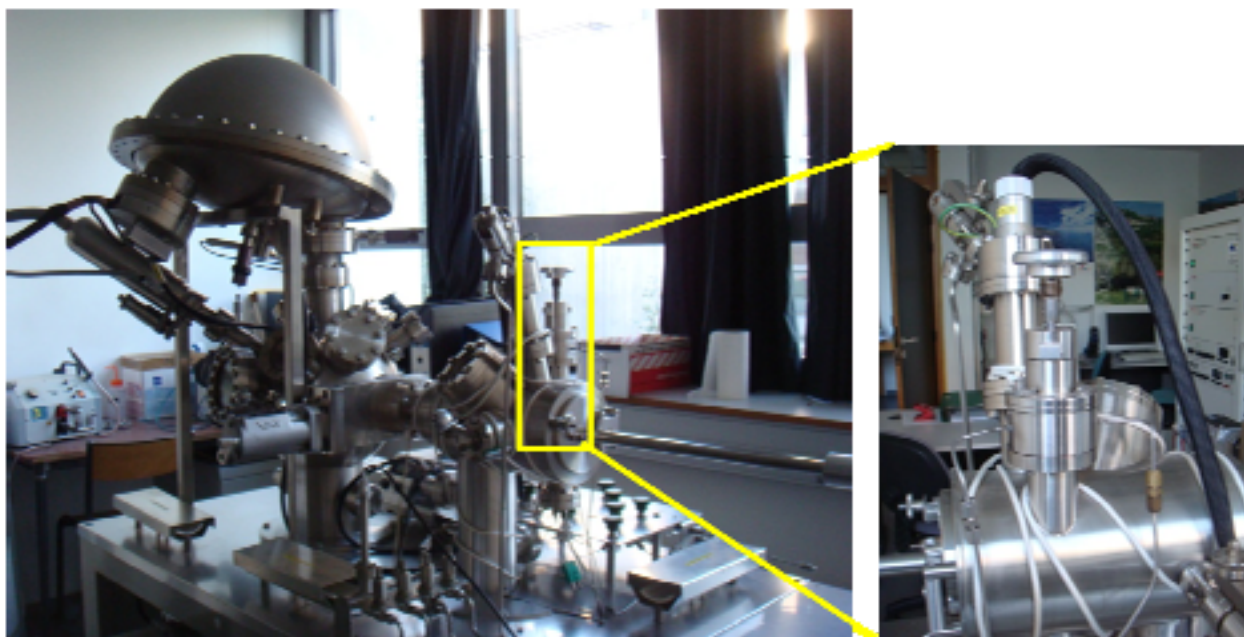


Figure 2.11 UHV system for high pressure studies (right) high pressure cell installed in the preparation chamber

The XPS system consists of a non-monochromatic dual anode (Al  $\kappa\alpha$  and Mg  $\kappa\alpha$ ) X-ray source, and a 9-channeltron CLAM MCD analyser. The XPS spectra were measured with Al  $\kappa\alpha$  X-ray in this system. The angle of incidence of the X-ray tube was at  $38^\circ$  incident angle and the emission angle was normal to the sample surface. The pass energy for high resolution spectra was 20 eV and the survey scan was recorded with pass energy at 50 eV.

The high pressure cell is composed of a sample support assembly equipped with gas inlet and outlet, sample heater, a thermocouple, and a movable top part which seals the cell by a retaining ring with gold plated C-ring. A pressure gauge is connected to the inlet to monitor the pressure and the outlet line is connected to a roughing pump. The gas cell was operated with continual gas flow with inlet gas pressure at 1 bar.

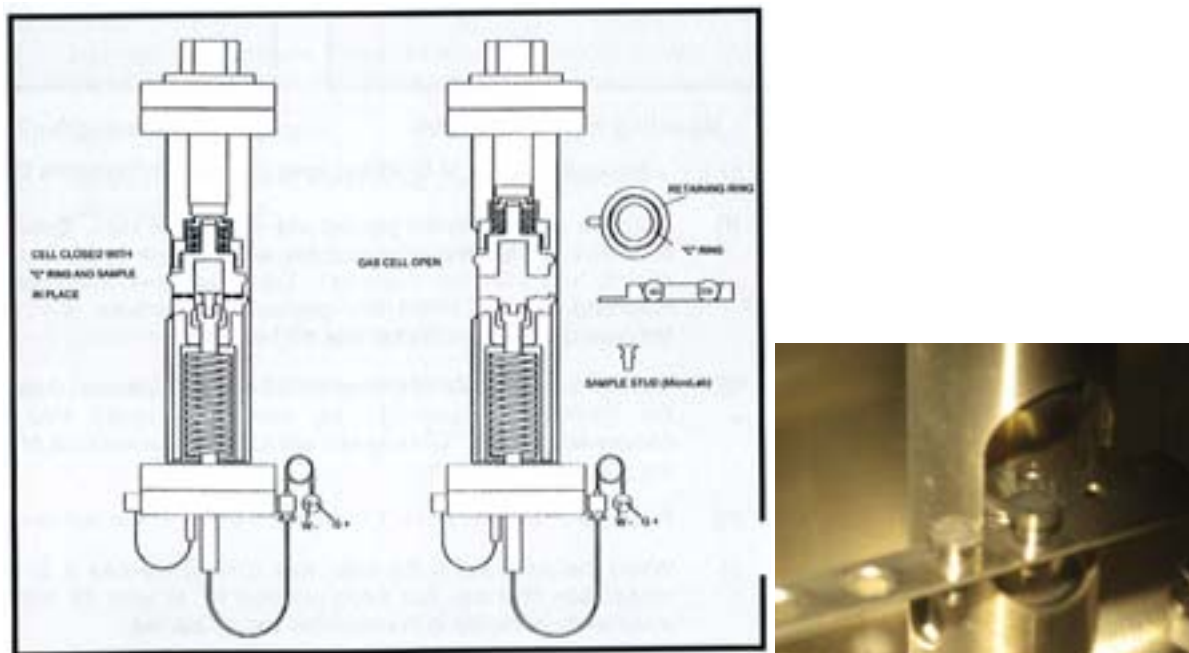


Figure 2.12 (left) Schematic representation [43] and (right) image of the interior of high pressure cell

**c) Photoemission Spectroscopy (PES) in Elettra**

The material science beamline at Elettra is well-adapted for investigation of systems with low dimensionality such as thin film or nanostructure at surfaces and interfaces as high signal intensity can be obtained at low photon energy. Therefore the beamline can be specialised for studies requiring high surface sensitivity. The top view of the end station is shown in figure 2.13.

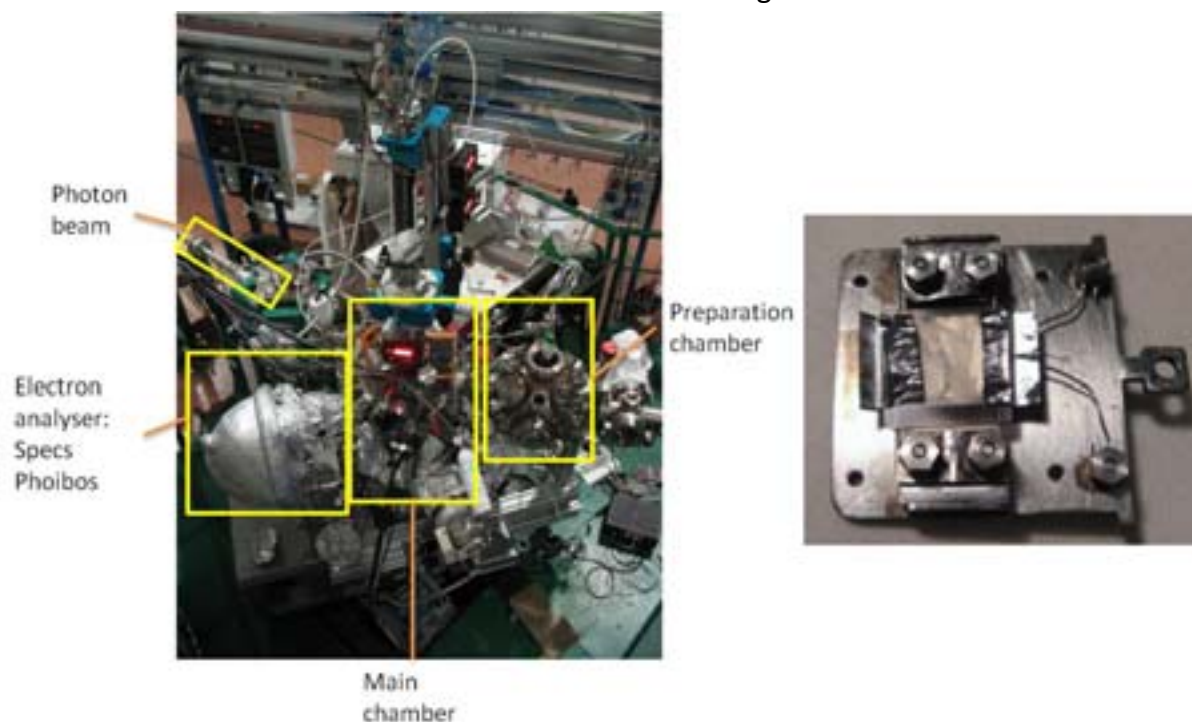


Figure 2.13 End station of material science beamline of Elettra (left) and the sample holder (right)

The energy analyzer is a hemispherical analyzer (SPECS Phoibos 150) and is installed to the main chamber with an inclination of  $60^\circ$  from the beamline axis. The chamber is also equipped with  $\text{Ar}^+$  sputtering and a number of gas lines controlled by precision leak valves for gas exposure. Gas exposure was performed in the main chamber with the pressure monitored by an ion gauge. The sample was heated by a resistive heater on the tantalum sample holder located at the back of the sample. A K-type thermocouple was pressed onto the sample for temperature monitoring. The Ni-Co e-beam evaporator was installed to a fast entry port in the preparation chamber for metal deposition. The chamber is also equipped with a non-monochromated X-ray source for general XPS measurement.

**d) Ambient Pressure Photoemission Spectroscopy (APPES)**

The development of APPES is a progress in bridging the pressure gap between UHV experimental conditions and catalytic processes in real practice. Surface emitted particles or electrons are heavily influenced by absorption and scattering from the surrounding, which makes the strict control of environment necessary. The mean free path of electron ( $\lambda_e$ ) is inversely proportional to pressure. Shown in figure 2.14,  $\lambda_e$  is in mm range below 8 mm for electrons of K.E. from 0-1000 eV. As pressure increases to 100 mbar,  $\lambda_e$  decreases to 30  $\mu\text{m}$  [44].

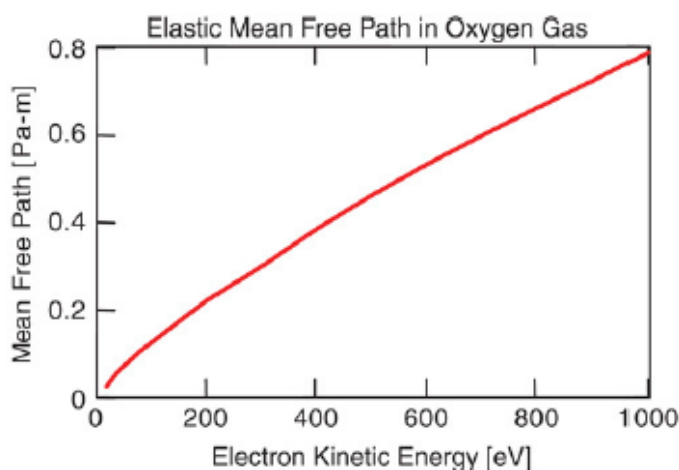


Figure 2.14 Electron elastic mean free path through an oxygen gas environment as a function of kinetic energy. At 100 Pa (1 mbar) a 400 eV electron travels approximately 4 mm before suffering an inelastic collision. Ten Pa-meter represents the same number of molecules as approximately 1 monolayer, if condensed on a surface.[44]

The design of ambient pressure photo-electron spectrometer copes with the short travel distance of electrons by the addition of electrostatic lens and differential pumping scheme. The concept and schematic representation of ISISS beamline is shown in figure 2.15 and 2.16 respectively. Gas flow and reactions are processed in a high pressure chamber. The signal intensity is dependent on the (1) the flux of the photon source, (2) the transmission through the X-ray window, (3) the absorption of photon by the gas in the high pressure cell, (4) the efficiency of photoionization and scattering of photoelectrons in solids, (5) the

scattering of photoelectrons by gas-phase molecules, and (6) the efficiency of photoelectron collection by the spectrometer [45].

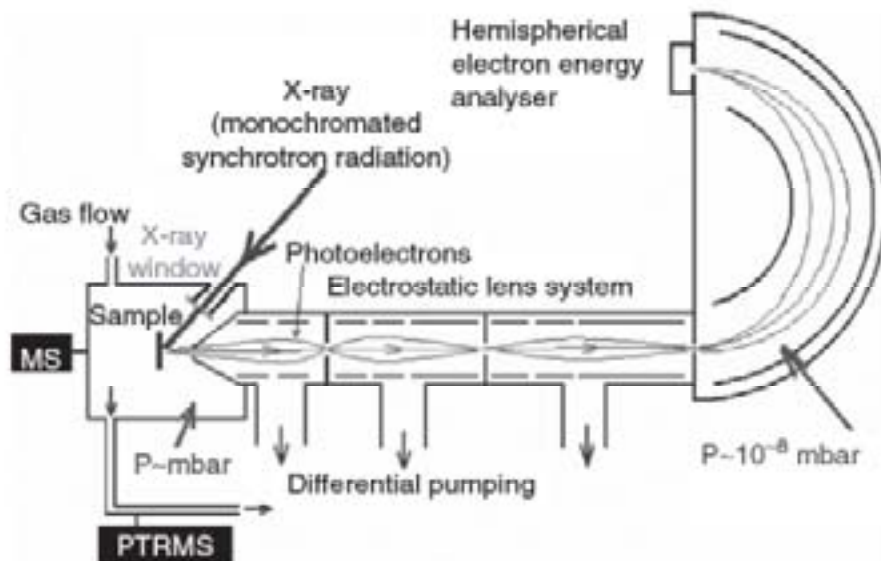


Figure 2.15 XPS equipment with electrostatic lens system [45].

Photon beam enters the high pressure chamber through a Si membrane window which prevents gases from entering the beam line and the storage ring. Photoelectrons emitted from the sample enter the electron analyzer through a series of differential pumping stages, which evacuate the gases from the analyzer and minimize the collision of photoelectrons by gas-phase molecules. Electrostatic lenses at each pumping stage focus the electrons through the aperture and prevent them from diverging. The maximum pressure achieved at this beamline is up to several mbar for gases such as hydrogen.

The gases in the high pressure cell are monitored on line by a quadrupole mass spectrometer (QMS) (Prisma QMS200 M). The quadrupole mass spectrometer is connected to the cell through a leak valve. The leak valve together with the turbo-pump controls the working pressure in the QMS in the range of  $10^{-7}$  –  $10^{-6}$  mbar.

The sample can be heated from the back by using an infrared laser. The radiation of the laser is directed onto the back of the sample through a glass fiber. Disks of SiC or stainless steel are used as heating plates. They were mounted below the catalyst in the case the sample has a high reflectivity. The temperature is measured with a thermocouple mounted on the top of the sample.

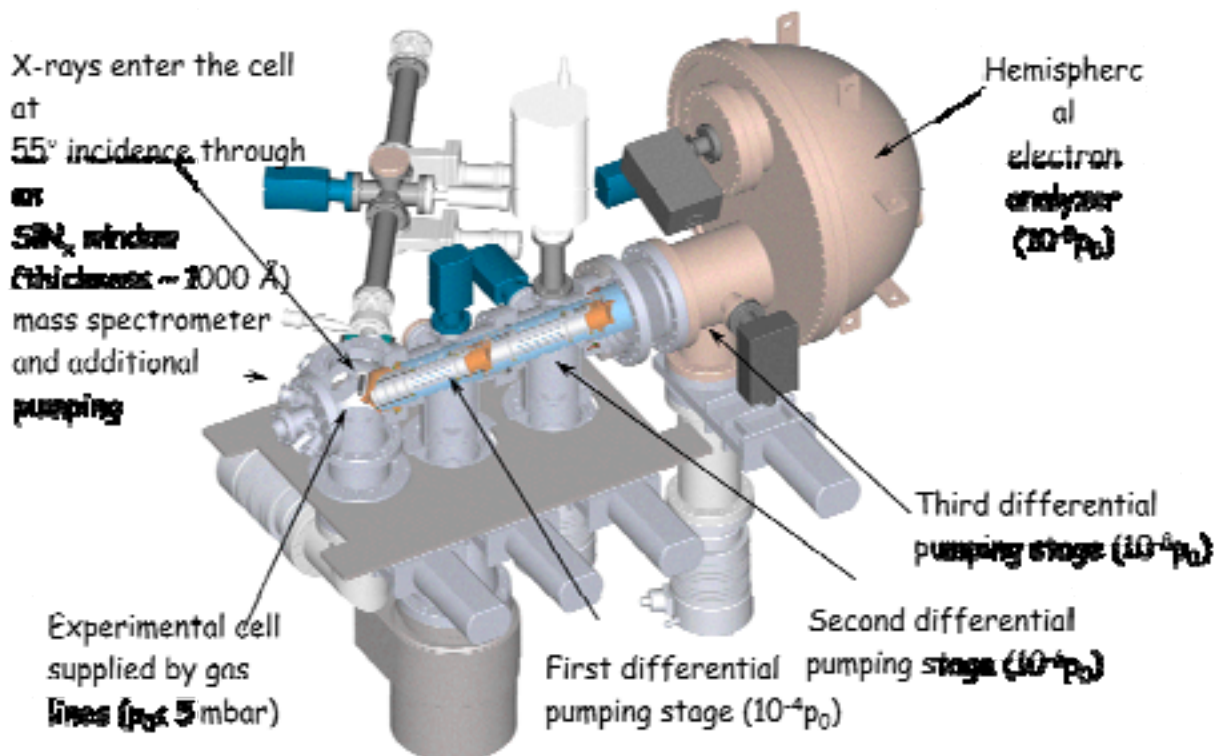


Figure 2.16 End station and the ambient pressure XPS gas flow cell is ISS beamline at Bessy II

**2.2.1.5 Near edge X-ray absorption fine structure (NEXAFS)**

X-ray absorption spectroscopy (XAS) is a technique that is sensitive to intra-molecular bonding of atoms in a molecule or an inorganic compound. Its sensitivity to intra-molecular electronic and geometric structure also enables the determination the molecular orientation of adsorbates on surfaces. Detection of photo absorption is described by the X-ray absorption cross section  $\sigma_x$ , which is defined as the number of electrons excited per unit time divided by the number of incident photon per unit time unit area.

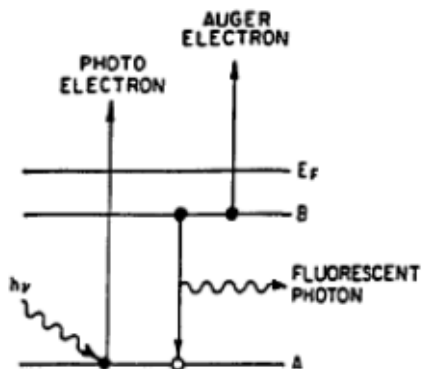


Figure 2.17 Energy scheme of creation and annihilation of a core hole as a result of X-ray absorption.[46]

Photon absorption leads to the emission of photoelectron and creation of core hole, which is filled by electron from a higher shell. The energy relaxation of the atom can take place in form of fluorescent emission or Auger electron emission. Measurement of these two

processes represents the probability of the existence of core hole created by photon absorption, and is regarded as a representative measurement for  $\sigma_x$ . Thus NEXAFS data is commonly measured in electron yield mode and fluorescence yield mode.

Electron yield signals are measured by an electron collection grid (collection plate for the setup in Bessy II) located closed to the sample. Electron yield measurement can be further differentiated into Auger Electron Yield (AEY), Partial Electron Yield (PEY) and Total Electron Yield (TEY). The intensity of the emitted primary Auger electrons is a direct measure of the x-ray absorption process and is used in "Auger electron yield" measurements. Measurement by partial electron yield filters the electrons with energy lower than threshold energy, such that measurement of the photoemission peak of the sample with the same kinetic energy window is avoided. For TEY, electrons of all energies are collected. Low energy electron from inelastically scattered auger electrons contributes to a significant part of the spectra. This also leads to a higher total count-rate and lower signal to background ratio of spectra obtained from TEY mode.

NEXAFS spectra refer to the region of x-ray absorption spectrum within 50 eV of the absorption edge. The absorption edge is dependent on the ionization energy of core electrons and is affected by the oxidation state (chemical shift). The main edge shifts to higher energy with increasing oxidation state. Pre-edge features are influenced by electronic transitions to empty bound states. The probability of transition is controlled by local geometry around the absorbing atom and can be used to differentiate bonding characteristics such as bond length between adsorbates and sample surfaces. The near-edge region is dominated multiple-scattering resonances. The photoelectrons ejected is at a relatively low kinetic energy, such that excited electrons tends to interact with neighbouring atoms and is described as multiple-scattering. Thus features in this range are affected by multiple factors such as the atomic position of neighbours, interatomic distances and bond angles.

The X-ray absorption spectra shown in this study were measured in TEY mode. It is particularly useful for the identification of the oxidation state of cobalt. XPS Co 2p spectra of Co metal and Co oxides contain overlapping features and are difficult to distinguish. The near-edge structure of CoO and Co<sub>3</sub>O<sub>4</sub> produces characteristic features and hence is used as a fingerprinting technique.

## **2.2.2 Thermal Desorption Spectroscopy (TDS)**

### **2.2.2.1 Overview**

Thermal Desorption Spectroscopy (TDS), also named temperature programmed desorption (TPD) is a direct method to study interaction of gases with solid surfaces. It is a straightforward technique, in which the surface of sample is exposed to gases and the desorption of the gas molecules or products from surface reaction is monitored (by mass spectrometer) during a controlled linear heating process. TDS is commonly applied on

planar samples such as single crystals, or model catalysts, which can largely eliminate the ambiguity caused by structure-specific reactions and diffusion processes [47, 48].

Adsorption of molecules can take place by physisorption and chemisorptions. Physisorption is a physical interaction between particles and surface by weak van-der-Waals forces. Chemisorptions involve chemical bond formation between the adsorbed molecules and the surface atoms. Chemical bond formed between surface and adsorbate may involve electron transfer that can weaken the intramolecular bonding. In case of intramolecular bond breaking, the adsorption is known as dissociative adsorption.

The heat of desorption ( $q_{des}$ ) describes the energy barrier that the adsorbate overcomes when approaching the surface to arrive into a chemisorbed state.  $q_{des}$  is the bond strength of the adsorbate and the surface, which is equal to the difference in energy of desorption ( $E_{des}$ ) and energy barrier of adsorption ( $E_{ads}$ ). In case of dissociative adsorption,  $q_{des}$  is given by the difference between the binding energy of the adsorbates and the dissociation energy of the intramolecular bond.

The heat of desorption is a coverage dependent function as it varies with the level of lateral interaction. The rate of desorption ( $r_{des}$ ) can be represented by the Polanyi-Wigner equation:

$$r_{des} = -\frac{\partial\theta}{\partial t} = k_n\theta^n$$

where  $\theta$  is the surface coverage of adsorbate and  $n$  is the reaction order

The rate constant ( $k_n$ ) can be represented by Arrhenius equation:

$$k_n = \nu_n \exp\left(-\frac{E_{des}}{RT}\right)$$

where  $\nu_n$  is the pre-exponential factor of reaction

A linear temperature ramp ( $\beta$ ) is applied during TDS, such that sample temperature is a time dependent variable:

$T_s = T_0 + \beta t$ , where  $T_s$  is the sample temperature,  $T_0$  is the initial temperature.

This transforms the Polanyi-Wigner equation into:

$$\frac{E_{des}}{RT_p^2} = \frac{n\nu_n}{\beta} \theta_p^{n-1} \exp\left(-\frac{E_{des}}{RT_p^2}\right),$$

where  $T_p$  is the desorption peak temperature and assuming that  $\nu_n$  and  $E_{des}$  are independent of coverage

This equation can assist in understanding qualitatively the desorption order from the results of TDS. Zero order desorption ( $n=0$ ) is independent of surface coverage and increases exponentially with temperature. Multilayer adsorption or molecules of unlimited supply are typical processes of zero order kinetics. Desorption peaks of different surface coverage in

the TDS spectra originate from the same edge and the desorption reaches a maximum when the coverage starts to decrease.

Peak intensity of 1<sup>st</sup> order desorption ( $n=1$ ) is proportional to instantaneous surface coverage.  $T_p$  is dependent of temperature ramp and it results in asymmetric desorption peak. It is mainly related to non-dissociative adsorption. 2<sup>nd</sup> order desorption ( $n=2$ ) produces nearly symmetric desorption peaks. The temperature of desorption peak decreases with increasing coverage and. It describes usually recombinative desorption.

TDS is widely used for the investigation of kinetics on simple molecules such as CO, O<sub>2</sub> or H<sub>2</sub> on single crystal metal surface. TDS on reactive molecules such as alcohol [50, 51] or other hydrocarbon [52-54] can provide extensive information on reaction mechanism. The analysis of spectra focuses more on the desorption products resulting from surface reaction. Desorption peaks generated from surface reaction may desorb at temperature different from normal gas phase adsorption and is referred to reaction-limited desorption peaks. The time sequence of desorption peak also provides useful information to the clarification of reaction mechanism. By varying the structure or composition of the model catalyst, one can address specifically to issues such as influence of surface structure or surface pretreatment to reaction pathway.

### **2.2.2.2 Experimental setup for TDS**

Two major parts are involved in a TDS setup: a gas dosing system and mass spectrometer for gas detection. The gas dosing is usually performed in two approaches: 1) by backfilling the UHV chamber at a constant pressure for a measured period of time 2) introduce a tubular gas doser, directing the gases on to the sample. By the 2nd method, gas dosing could be confined to the sample area and the background pressure could be maintained at a low level. After gas exposure, the sample is brought closed to the detector of the mass spectrometer. Quadrupole mass spectrometer (QMS) was used for mass detection in TDS. Multiple masses can be detected simultaneously with QMS. QMS consists of a hot filament, which ionizes the molecules to be detected and accelerates them towards the detector. The trajectory of the ionized species is affected by the applied potential of a quadrupole mass filter, which directs only those with selected mass to charge ratio to the detector.

The gas doser and mass spectrometer used in the experiment is installed in the UHV system for low pressure studies described in section 2.2.1.4 (a). Gases and Vapour were directed through a stainless steel tube (6mm) to the sample. A pinhole diaphragm (15 $\mu$ m) was put to the end of the doser to control the uniformity of gas exposure. The doser was connected to a reservoir of ethanol and gas exposure was manually controlled by a leak valve. The doser was brought to a distance about 2mm away from the sample surface to avoid excessive increase of background pressure. The QMS is a VGQ100 mass spectrometer. The mass spectrometer was differentially pumped to increase the amount of desorbed gas entering the detector. The mass spectrometer's head ends with a nozzle with an oblique angle of 45<sup>o</sup> and major axis length 1cm in order to cope with the orientation of the sample manipulator.

During TDS measurement, the nozzle was at about 1 mm above the sample, such that signal from the background could be minimized.

### 2.2.2.3 Correction of mass fragment

Hydrogen, carbon monoxide, acetaldehyde, methane and carbon dioxide are the major ethanol desorption products. Ionization of these species generates mass fragments which overlapped with the signals from other products. Reference of the ionization mass spectra is available from NIST database[55]. In order to determine the exact mass ionization pattern for the experimental set-up, the mass fragment of each decomposition products were calibrated. This was done by dosing the pure gas of the decomposition product at different partial pressure while measuring the corresponding mass signal with the same configuration as TDS experiment. The mass fragments are expressed in terms of relative intensity against the mass fragment with the highest mass signal. For example, ionization of acetaldehyde generates three mass fragments:  $m/z$  44,  $m/z$  28 and  $m/z$  27, with the highest-signal fragment being  $m/z$  29. The increase in signal intensity of the mass fragments with respect to the increase in pressure is shown in figure 2.18.

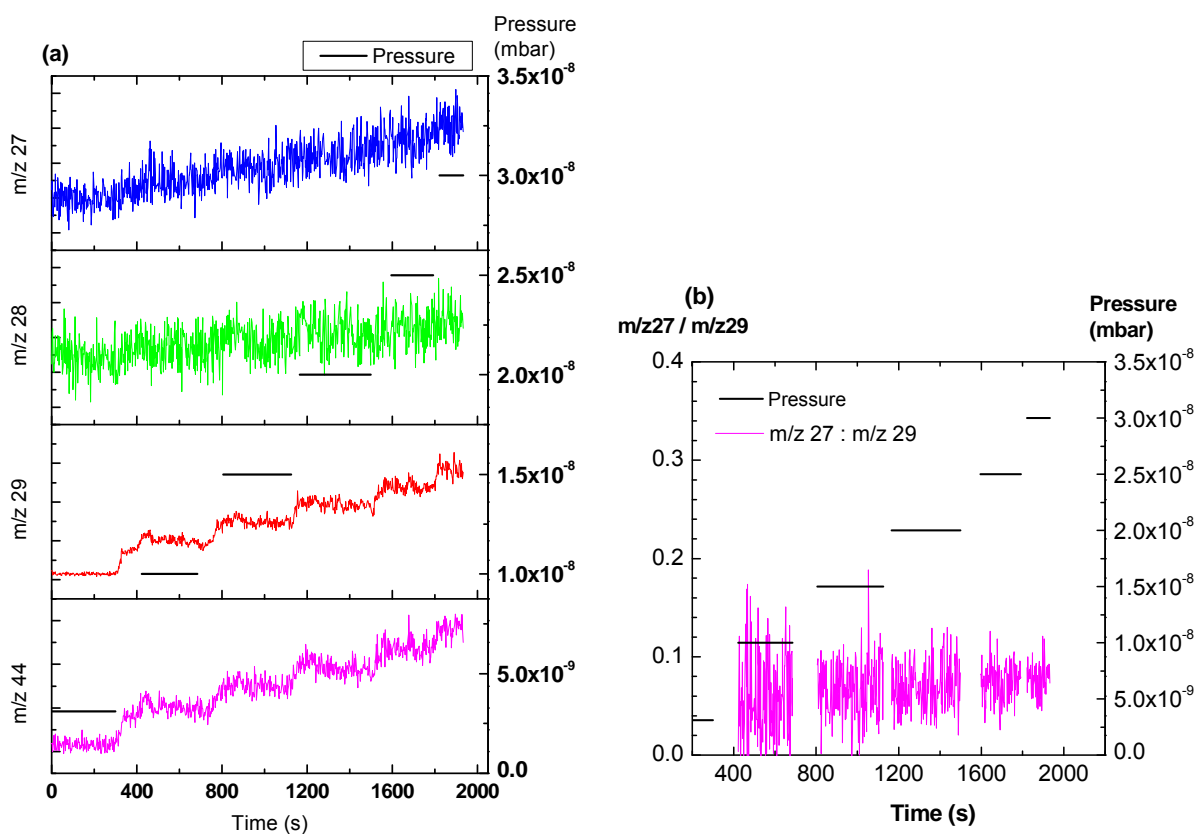


Figure 2.18 (a) Mass signal of  $m/z$ 44,  $m/z$ 29,  $m/z$ 28 and  $m/z$ 27 corresponding to increase in acetaldehyde partial pressure (b) the ratio of mass signal intensity of  $m/z$ 27 to  $m/z$  29

Mass 27 is the principal fragment for ethylene. From NIST database, ionization of acetaldehyde gives a fraction of 3.3 for signal  $m/z$  27 vs 100 for signal  $m/z$  29. The experimental relative intensity was obtained from the difference of mass signal of  $m/z$ 27 at a known exposure pressure relative to that of  $m/z$  29.

$$\text{Relative intensity of } m/z \ 27 = \frac{[I_{27}(P = 1 \times 10^{-8}) - I_{27}(P = 0)]}{[I_{29}(P = 1 \times 10^{-8}) - I_{29}(P = 0)]}$$

The above calculation results in a ratio which scatters between 0.025-0.09 (figure 2.18 right), and the average value is around 0.06. Therefore in the experimental setup, a fraction (0.06) of the signal from  $m/z$  29 is subtracted from  $m/z$  27 for the actual intensity of ethylene. This data correction was performed also for the desorption products below:

Table 2.6 Mass fragment generated and requiring subtraction upon desorption of respective ethanol decomposition products

Desorption products	Mass fragment for subtraction
CO- $m/z$ 28	$m/z$ 16
C <sub>2</sub> H <sub>4</sub> O- $m/z$ 29	$m/z$ 16, 27, 28, 44
C <sub>2</sub> H <sub>5</sub> OH- $m/z$ 31	$m/z$ 27, 29
CO <sub>2</sub> - $m/z$ 44	$m/z$ 16, 28

## 2.3 Material characterization

### 2.3.1 Bulk characterization

#### 2.3.1.1 X-ray diffraction (XRD)

XRD is applied for the identification of bulk crystal structure of bimetallic Ni-Co material. The crystal structure of a material is defined by the order of repeated unit cell. The atomic arrangement in a crystal can be found as a series of aligned planes. This also creates planes of electrons, which interact with the incident X-ray beam and oscillate at the same frequency. The X-ray is diffracted with constructive interference of radiation as the atoms are organised into repeated planes in the crystal. Diffraction from different planes of atoms produces a diffraction pattern, which contains information about the atomic arrangement within the crystal.

The parameters obtained from X-ray diffraction can be described by Bragg's law:

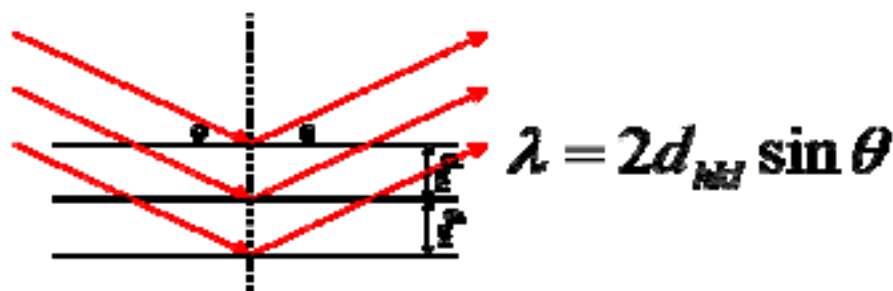


Figure 2.19 Bragg's law and X-ray diffraction at atomic plane

The distance between atom planes ( $d_{hkl}$ ) is a function of the wavelength ( $\lambda$ ) of X-ray and the angle between the atomic plane and the sample ( $\theta$ ). For common lab-based X-ray diffraction, the wavelength of X-ray is a constant value, such that an ensemble of parallel lattice planes produces diffraction peak only at one specific angle. The space between diffracting planes of atoms determines peak positions. Different atom planes in a lattice results in a series of diffraction peak with different intensity which produces a characteristic

pattern for a crystalline phase. Thus the X-ray diffraction pattern of a pure substance is like a fingerprint of the substance and is suited for the characterization and identification of polycrystalline phases.

The XRD was performed in a Bruker AXS-D8 Advance XRD system with a Cu K $\alpha$  X-ray source of wavelength 1.54 Å. The measurement was conducted from 2 $\theta$ =30-100°. The sample remained in horizontal position and the detector changed its orientation during measurement.

### 2.3.2 Morphological characterization

The surface morphology and structure of Ni-Co bimetallic materials and the ZnO support Ni-Co thin layers were inspected by SEM and AFM respectively. LEED was used for the identification of ZnO surface crystal structure after cleaning while SEM was used for the identification of surface morphology..

#### 2.3.2.1 Scanning electron microscopy (SEM)

SEM is a common technique to visualize fine morphological features on surfaces. Instead of light, it uses a beam of electrons in which signals are derived from electron interaction or scattering with the sample surfaces. These electrons are focused by electromagnetic or electrostatic lenses and collected as signals for SEM. The interactions of electron with sample that are collected for SEM include: reflection of high-energy electrons by elastic scattering, emission of secondary electrons by inelastic scattering and the emission of electromagnetic radiation. Electron transmission is also possible for ultra-thin specimen and the collection of these electrons is the basis for Transmission Electron Microscopy (TEM). Information on sample's composition can also be obtained by Energy-dispersive X-ray spectroscopy (EDX). But unlike the surface techniques mentioned above, this chemical analysis method provides information of a much higher depth.

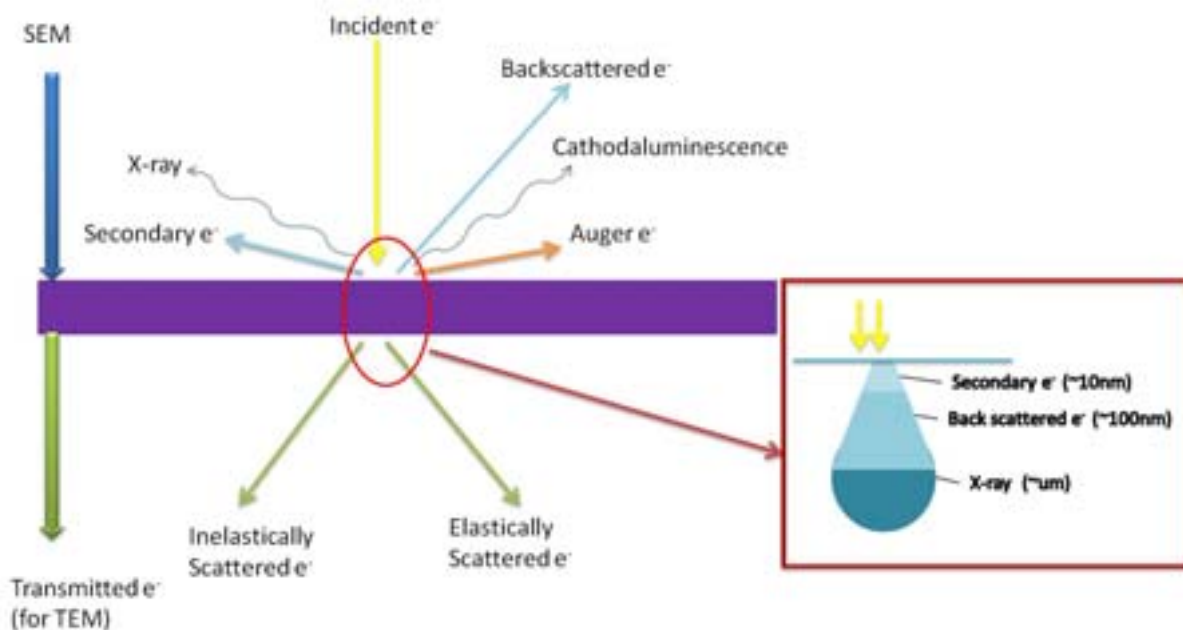


Figure 2.20 Electrons interaction for SEM

The incident electrons lose energy by random scattering and absorption within a teardrop-shaped volume known as interaction volume. This volume extends from less than 100 nm to around 5  $\mu\text{m}$  into the surface. The size of the interaction volume depends on the electron's energy, the atomic number of the sample and sample's density. The information delivered by different types of electron-surface interaction is summarized as below:

Table 2.7 Characteristics of different electron scattering mechanism for SEM

Type of signal	Origin of emission	Type of information delivered
<b>Backscattered <math>e^-</math></b>	Inelastic collisions between primary electrons and atoms	<ul style="list-style-type: none"> <li>• Contrast in zones of different chemical compositions resulting from collection of high energy electrons</li> <li>• Brightness controlled by the power of backscattering (atomic number of the atoms)</li> </ul>
<b>Secondary <math>e^-</math></b>	Inelastic collisions between primary electrons (the beam) and loosely bound electrons of the conduction band or valence electrons	<ul style="list-style-type: none"> <li>• Information on the morphology of the surface resulting from collection of low energy electrons (&lt; 50 eV)</li> <li>• Brightness controlled by the intensity of electrons reflected</li> </ul>
<b>X-ray</b>	Energy dissipation in form of electromagnetic waves, coming from the difference in energy between the higher-energy shell and the lower energy shell as higher-energy shell fills the hole created by electron emission	<ul style="list-style-type: none"> <li>• Elemental composition resulting from the X-rays with energy corresponding to the characteristic of the difference in energy between the two shells, and of the atomic structure of the element from which they were emitted</li> </ul>
<b>Cathodo-luminescence</b>	Emission of light resulting from atoms excited by high-energy electrons return to their ground state	<ul style="list-style-type: none"> <li>• Show the actual colour of the sample</li> </ul>

In a typical SEM, electron beam can be emitted from thermionic source or field emission source. Field emitters like Schottky and cold-field emitters, which are made of fine Tungsten needles, are superior to thermionic sources in terms of source size, brightness, and lifetime. The electron beam is focused by condenser lenses to a small spot.

Due to the highly planar nature of the ZnO and the high level of conformity of the Ni-Co thin layer to ZnO, SEM shows relatively few information on the surface morphology of the deposited layer. The technique was mainly applied on Ni-Co bulk materials which form different crystallite structure after different gas or thermal treatment. The SEM system is a JEOL JSM-6700F microscope. It is equipped with an In-lens Schottky field emission gun. The sample was briefly transferred into the atmosphere from the UHV chamber before putting into the SEM system.

### 2.3.2.2 Atomic force microscopy (AFM)

AFM belongs to the family of scanned probe microscopy, in which images are obtained by scanning a sharp probe across a surface and the surface topography are reconstituted by the tip-sample interaction. The measurement is made in three dimensions, which allows the establishment of 3 dimensional images of a sample surface.

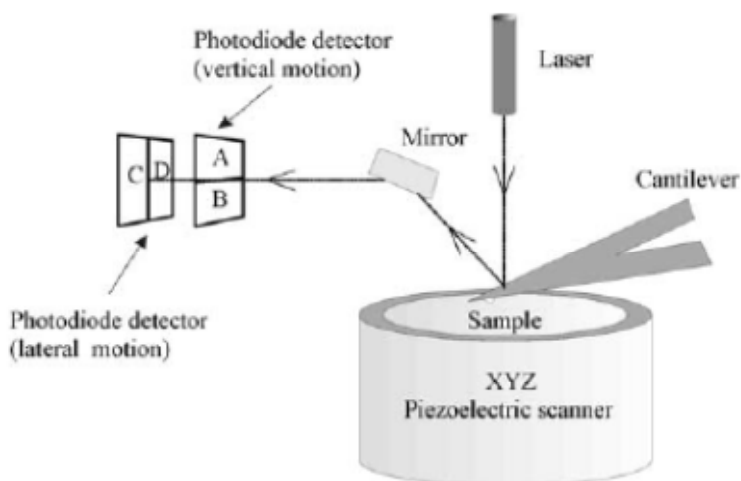


Figure 2.21 Configuration of AFM [49]

AFM consists of a probing tip attached to a cantilever. During scanning, the sample is moved relative to the tip, where it is subjected to different types of interaction such as direct physical contact, electrostatic force or van der Waal's forces. This results in movement of the z-axis as the tip scans across surface features, which is then detected by the reflection of a laser beam from the cantilever to a photodiode. The force between the tip and the sample is determined by Hooke's Law.

$$F = -kx$$

where F is force, k is the spring constant, and x is the cantilever deflection,

In this study, The AFM system used is from RHK Technology. Contact mode AFM was applied, in which the tip is in physical contact with the surface. Thus the major interaction comes from the contact force for image interpretation.

### 2.3.2.3 Low Energy Electron Diffraction (LEED)

LEED is a highly surface sensitive technique in which information is obtained from the outermost 2-5 monolayers. It was used mainly for the determination of long range surface ordering. Therefore it is exclusively applied on single crystals which have a well-ordered surface. LEED measures only elastically scattered electrons. When the sample surface is struck by low energy electron, these electrons interact strongly with surface and is scattered by localised electron density of surface atoms. The wavelength of electrons is given by Broglie's wavelength:

$$\lambda = h/\sqrt{2mve}$$

where  $h$  is Planck constant,  $m$  is electron mass,  $v$  is electron velocity and  $e$  is electron charge. The energy of electrons used ranges between 20-200 eV, which corresponds to wavelength between 0.87-2.7Å. This value is comparable to interlayer distances in crystals. LEED apparatus is constituted of two major components: (1) Electron gun producing monochromatic electrons (2) electron detector system. The detector is composed of concentric grids, which filters the inelastically scattered electrons, and a phosphor screen. The pattern is viewed through a transmission screen and a viewport. The relationship of incident electrons and the lattice parameters is analogous to X-ray diffraction. The diffracted electrons correspond to a reciprocal space image of the surface lattice.

LEED was mainly performed at the beamline in Trieste. The LEED system was from Omicron and was attached to the main chamber of the end station. The ZnO surface structure was inspected by LEED after sputtering-annealing cycles. A (1x1) diffraction pattern was obtained for both ZnO-Zn and ZnO-O single crystals, which conforms to the hexagonal structure of ZnO.

## 2.4 References

- [1] K.S. Leschkes, R. Divakar, J. Basu, E. Enache-Pommer, J.E. Boercker, C.B. Carter, U.R. Kortshagen, D.J. Norris, E.S. Aydil, *Nano Letters*. 7 (2007) 1793-1798.
- [2] W.J.E. Beek, M.M. Wienk, M. Kemerink, X. Yang, R.A.J. Janssen, *Journal of Physical Chemistry B*. 109 (2005) 9505-9516.
- [3] Q. Wan, Q.H. Li, Y.J. Chen, T.H. Wang, X.L. He, J.P. Li, C.L. Lin, *Applied Physics Letters*. 84 (2004) 3654-3656.
- [4] J. Xu, Q. Pan, Y. Shun, Z. Tian, *Sensors and Actuators, B: Chemical*. 66 (2000) 277-279.
- [5] Ü. Özgür, Y.I. Alivov, C. Liu, A. Teke, M.A. Reshchikov, S. Doğan, V. Avrutin, S.J. Cho, H. Morkoç, *Journal of Applied Physics*. 98 (2005) 1-103.
- [6] X. Feng, L. Feng, M. Jin, J. Zhai, L. Jiang, D. Zhu, *Journal of the American Chemical Society*. 126 (2004) 62-63.
- [7] Z.R. Tian, J.A. Voigt, J. Liu, B. McKenzie, M.J. McDermott, *Journal of the American Chemical Society*. 124 (2002) 12954-12955.
- [8] P. Gao, Z.L. Wang, *Journal of Physical Chemistry B*. 106 (2002) 12653-12658.
- [9] C. Wöll, *Progress in Surface Science*. 82 (2007) 55-120.
- [10] M.-H. Du, S.B. Zhang, J.E. Northrup, S.C. Erwin, *Physical Review B*. 78 (2008) 155424.
- [11] O. Dulub, M. Batzill, U. Diebold, *Topics in Catalysis*. 36 (2005) 65-76.
- [12] O. Dulub, L.A. Boatner, U. Diebold, *Surface Science*. 519 (2002) 201-217.
- [13] A. Önsten, D. Stoltz, P. Palmgren, S. Yu, M. Göthelid, U.O. Karlsson, *Journal of Physical Chemistry C*. 114 (2010) 11157-11161.
- [14] M. Kunat, S.G. Girol, U. Burghaus, C. Wöll, *Journal of Physical Chemistry B*. 107 (2003) 14350-14356.
- [15] M. Kunat, S. Gil Girol, T. Becker, U. Burghaus, C. Wöll, *Physical Review B*. 66 (2002) 081402.
- [16] H. Lorenz, M. Friedrich, M. Armbrüster, B. Klötzer, S. Penner, *Journal of Catalysis*. 297 (2013) 151-154.
- [17] J. Kiss, A. Witt, B. Meyer, D. Marx, *The Journal of Chemical Physics*. 130 (2009) 184706-184714.
- [18] G. Dutta, A.A. Sokol, C.R.A. Catlow, T.W. Keal, P. Sherwood, *ChemPhysChem*. 13 (2012) 3409-3409.
- [19] K. Geunjae, Y. Kijung, *Journal of Physical Chemistry C*. 112 (2008) 3036-3041.
- [20] C. Drouilly, J.M. Krafft, F. Averseng, H. Lauron-Pernot, D. Bazer-Bachi, C. Chizallet, V. Lecocq, G. Costentin, *Applied Catalysis A: General*. 453 (2013) 121-129.
- [21] M. deposition, Mantis deposition, Oxfordshire UK.
- [22] C.C. Chusuei, D.W. Goodman, in: A.M. Editor-in-Chief: Robert (Ed.), *Encyclopedia of Physical Science and Technology (Third Edition)*, Academic Press, New York, 2003, pp. 921-938.
- [23] S. Tanuma, C.J. Powell, D.R. Penn, *Surface and Interface Analysis*. 20 (1993) 77-89.
- [24] M.C. Biesinger, B.P. Payne, L.W.M. Lau, A. Gerson, R.S.C. Smart, *Surface and Interface Analysis*. 41 (2009) 324-332.
- [25] A.R. González-Elipe, J.P. Holgado, R. Alvarez, G. Munuera, *J. Chem. Phys.* . 96 (1992) 3080-3086.
- [26] M.A. Langell, M.H. Nassir, *Journal of Physical Chemistry*. 99 (1995) 4162-4169.
- [27] S. Uhlenbrock, C. Scharfschwerdt, M. Neumann, G. Illing, H.J. Freund, *Journal of Physics: Condensed Matter*. 4 (1992) 7973-7978.

- [28] A.R. González-Elipe, R. Alvarez, J.P. Holgado, J.P. Espinos, G. Munuera, J.M. Sanz, *Applied Surface Science*. 51 (1991) 19-26.
- [29] G.-E.A. R., M. G., E.J. S., S.J. M., *Surf. Sci.* 220 (1989) 368.
- [30] M. Oku, Y. Sato, *Appl. Surf. Sci.* . 55 (1992) 37-41.
- [31] V.M. Jiménez, A. Fernández, J.P. Espinós, A.R. González-Elipe, *Journal of Electron Spectroscopy and Related Phenomena*. 71 (1995) 61-71.
- [32] H.A.E. Hagelin-Weaver, G.B. Hoflund, D.M. Minahan, G.N. Salaita, *Applied Surface Science*. 235 (2004) 420-448.
- [33] T.J. Chuang, C.R. Brundle, D.W. Rice, *Surf. Sci.* . 59 (1976) 413-429.
- [34] E.M. Marsh, S.C. Petitto, G.S. Harbison, K.W. Wulser, M.A. Langell, *Journal of Vacuum Science and Technology A: Vacuum, Surfaces and Films*. 23 (2005) 1061-1066.
- [35] R.J.O. Mossaneck, I. Preda, M. Abbate, J. Rubio-Zuazo, G.R. Castro, A. Vollmer, A. Gutiérrez, L. Soriano, *Chemical Physics Letters*. 501 (2011) 437-441.
- [36] D. Alders, F.C. Voogt, T. Hibma, G.A. Sawatzky, *Phys. Rev. B: Condens. Matter Mater. Phys.* . 54 (1996) 7716-7719.
- [37] R.J.O. Mossaneck, I. Preda, M. Abbate, J. Rubio-Zuazo, G.R. Castro, A. Vollmer, A. Gutiérrez, L. Soriano, *Chemical Physics Letters*. 501 (2011) 437-441.
- [38] J.F. Moulder, W.F. Stickle, P.E. Sobol, K.D. Bomben, *Handbook of X-ray Photoelectron Spectroscopy*, Perkin-Elmer Corporation Physical Electronics Division, 1992.
- [39] A.W. Moses, H.G.G. Flores, J.-G. Kim, M.A. Langell, *Applied Surface Science*. 253 (2007) 4782-4791.
- [40] Z.X. Shen, J.W. Allen, P.A.P. Lindberg, D.S. Dessau, B.O. Wells, A. Borg, W. Ellis, J.S. Kang, S.J. Oh, I. Lindau, W.E. Spicer, *Physical Review B*. 42 (1990) 1817-1828.
- [41] C.D. Wagner, L.E. Davis, M.V. Zeller, J.A. Taylor, R.H. Raymond, L.H. Gale, *Surf. Interface Anal.* . 3 (1981) 211-225.
- [42] J.J. Yeh, I. Lindau, *Atomic Data and Nuclear Data Tables*. 32 (1985) 1-155.
- [43] T.E.C.S.I. division, Issue 2 ed., Thermo Electron Corporation.
- [44] M. Salmeron, R. Schlögl, *Surface Science Reports*. 63 (2008) 169-199.
- [45] A. Knop-Gericke, E. Kleimenov, M. Hävecker, R. Blume, D. Teschner, S. Zafeirotos, R. Schlögl, V.I. Bukhtiyarov, V.V. Kaichev, I.P. Prosvirin, A.I. Nizovskii, H. Bluhm, A. Barinov, P. Dudin, M. Kiskinova, in: C.G.a.H.K. Bruce (Ed.), *Advances in Catalysis*, Academic Press, 2009, pp. 213-272.
- [46] J.G. Chen, *Surface Science Reports*. 30 (1997) 1-152.
- [47] J. Xu, J.T. Yates Jr, *Surface Science*. 327 (1995) 193-201.
- [48] T. Matsushima, H. Akiyama, A. Lesar, H. Sugimura, G.E.D. Torre, T. Yamanaka, Y. Ohno, *Surface Science*. 386 (1997) 24-33.
- [49] K.W. Kolasinski *Surface Science: Foundations of Catalysis and Nanoscience*, Second Edition ed., John Wiley & Sons Ltd., 2008.
- [50] K. Kähler, M.C. Holz, M. Rohe, J. Strunk, M. Muhler, *ChemPhysChem*. 11 (2010) 2521-2529.
- [51] S. Chaturvedi, D.R. Strongin, *The Journal of Physical Chemistry B*. 102 (1998) 2970-2978.
- [52] D. Stacchiola, L. Burkholder, W.T. Tysoe, *Surface Science*. 542 (2003) 129-141.
- [53] H. Guo, F. Zaera, *Surface Science*. 547 (2003) 284-298.
- [54] D. Chrysostomou, A. Chou, F. Zaera, *Journal of Physical Chemistry B*. 105 (2001) 5968-5978.
- [55] P.J. Linstrom, W.G. Mallard, NIST Standard Reference Database No. 69, June 2005 ed., National Institute of Standards and Technology, Gaithersburg, MD, 20899, 2005.

---

# Chapter 3

## Surface oxidation of NiCo: A comparative X-ray photoelectron spectroscopy study in a wide pressure range

---

---

---

---

## **Chapter 3. Surface oxidation of NiCo alloy: A comparative X-ray photoelectron spectroscopy study in a wide pressure range**

### **3.1 Introduction**

Transition metal catalysts such as nickel [1-3] and cobalt [4-6] are gaining extensive interest in hydrocarbon reforming for renewable fuels production [7] mainly due to their economic advantage over noble metals. The activity and life-time of the catalyst can be significantly improved by properly selecting the support material [8-10] and/or by employing multiple metal catalysts [11]. Oxide-supported bimetallic nickel-cobalt catalysts [12, 13] have been reported to have superior catalytic activity and lower coke formation rates in methane reforming, compared to their monometallic counterparts. It has been proposed that alloying of Ni with Co inhibits undesirable metal oxidation providing better performed reforming catalyst [14]. Therefore it is important to understand the interaction and synergy between the two metals in oxidative environments in order to further optimize their performance for catalytic application. Since heterogeneous catalytic reactions are mainly surface located processes, an investigation using a surface sensitive approach is essential.

Early works on metals oxidation have developed the theory of the kinetics of oxide growth [15, 16]. Since the 70s, surface sensitive techniques have been applied such that surface oxide growth could be studied thoroughly. Most of the studies were conducted over clean single crystalline metal surfaces exposed to oxygen at low O<sub>2</sub> pressure conditions (up to 10<sup>-6</sup>-6 mbar)[17-20]. Oxidation of nickel at low O<sub>2</sub> partial pressure and room temperature can be considered as a three stage process [20, 21]: (i) dissociative chemisorption of oxygen on various surface sites according to the orientation of Ni substrate [22], (ii) epitaxial NiO island formation, and (iii) lateral growth of NiO island till a film of NiO of about 3 monolayers is formed upon oxygen saturation. As NiO islands coalesce on the surface, the rate of NiO formation diminishes sharply. It was shown by Lambers and co workers that this thin passivation layer remains even at high O<sub>2</sub> partial pressure [23]. Formation of thicker NiO films is temperature dependent [24], where diffusion of cation from the bulk and oxygen anion into the bulk, is the rate determining factor. Similar processes were also observed for cobalt [25]. Initial exposure of oxygen at temperature lower than 420 K results in a stable dissociative adsorbed phase of oxygen on cobalt surface. The cobalt oxide formation, however, follows a different mechanism from the island-growth model of nickel, in which oxygen dissolution to the bulk is not hindered by passivation. Further oxygen exposure leads to the diffusion of oxygen into near surface region and eventually into the bulk, where cobalt oxide formation takes place [26]. Cobalt oxides exist commonly as CoO and Co<sub>3</sub>O<sub>4</sub>. In rocksalt CoO, Co<sup>2+</sup> occupies octahedral site while Co<sub>3</sub>O<sub>4</sub> is a spinel structure with Co<sup>2+</sup> and Co<sup>3+</sup> occupying octahedral and tetrahedral sites respectively. Oxidation of CoO to Co<sub>3</sub>O<sub>4</sub> is possible under high O<sub>2</sub> partial pressure. Transformation of CoO to Co<sub>3</sub>O<sub>4</sub> has been studied at different conditions [27-30]. At low temperature, oxygen diffusion is slow such that Co<sub>3</sub>O<sub>4</sub> can be easily formed as diffusion of oxygen to the bulk is limited and the surface is saturated with oxygen [17]. As temperature increases, oxygen diffusion is facilitated and

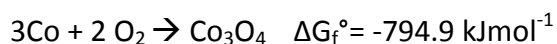
Co<sub>3</sub>O<sub>4</sub> could be reduced to CoO at low O<sub>2</sub> partial pressure [31]. Thus the formation of CoO or Co<sub>3</sub>O<sub>4</sub> depends strongly on the kinetics of oxygen diffusion.

When the system involves two metals, the oxidation mechanism is further complicated since apart from the reactivity towards oxygen, metal segregation effects are coming into play. Nickel and cobalt situate successively in the periodic table and they have very similar electronic structure. They are miscible in the bulk and form alloys with hexagonal closed pack (hcp) or face centered cubic (fcc) structures depending on composition and temperature. Metal segregation on alloy surfaces could occur during oxidation when there is a difference in the oxygen affinity of the constituent elements.

The preference of Ni and Co to form an oxide could be reflected by the Gibbs free energy of formation ( $\Delta_f G^\circ$ ) of the respective bulk oxides. At low oxygen pressure, the complete oxidation of Co to Co<sub>3</sub>O<sub>4</sub> is not favoured due to the shortage of oxygen. Thus formation of Ni and Co mono-oxides should be the main reactions to be considered under this condition [32, 33]:



The  $\Delta_f G^\circ$  value of CoO formation is slightly lower. Therefore at low oxygen partial pressure, formation of CoO is preferential to NiO. Under ambient temperature and pressure, where oxygen is in excess, CoO will further oxidize to the more stable Co<sub>3</sub>O<sub>4</sub>:



Apart from the thermodynamic considerations, the higher oxidation rate of cobalt compared to nickel has been also attributed to the abundance of cation vacancies in CoO and thus higher diffusion rates of Co ions [34]. Preferential oxidation of cobalt occurs via cobalt segregation towards the surface of NiCo, [35]. A gradient profile of mixed nickel and cobalt oxides is developed with higher Co concentration close to the outermost surface layers and possible spinel Co<sub>3</sub>O<sub>4</sub> formation [35]. Mixed spinel oxides having two different metallic cation have been also observed after oxidation of bimetallic alloys, but for other metal combinations (e.g. Co-Fe) [36]. Most studies of Ni-Co alloy oxidation were conducted at high temperatures (>1000K) where mixed Ni-Co-O spinel-like structure are not stable [37].

In this work, we study NiCo surface oxidation under two O<sub>2</sub> pressure regimes by X-ray photoelectron spectroscopy (XPS). At low O<sub>2</sub> pressure ( $5 \times 10^{-7}$  mbar), the different stages of oxidation involved proceeds sequentially, which permits the primary interaction of the two metals to exhibit clearly. The studies of oxidation of the alloy system in ambient pressure provide more insight of its behavior under catalytically relevant conditions. This pressure gap could alter the nucleation of metal oxides layer on the alloy surface [38]. We have also

compared NiCo alloy with pure Ni and Co so as to clarify the synergetic effect of alloying to the oxidation process.

### **3.2 Experimental Methods**

The Ni, Co and NiCo (50% Ni, 99.9+%) alloy foils (10x10x0.1 mm) were purchased from MaTeck GmbH, Germany. Samples were cleaned by ultrasonification in ultra pure water, acetone and ethanol sequentially, immediately prior to each experiment. After being introduced into the ultra high vacuum (UHV) apparatus, the surface was further cleaned by successive cycles of Ar<sup>+</sup> sputtering and annealing at 670 K for the removal of residual impurities. The analysis was carried out in two instruments, a VG Microtech and a Thermo-VG multilab 2000 spectrometers (base pressure < 2x10<sup>-9</sup> mbar), using non-monochromatic Al K $\alpha$  and Mg K $\alpha$  X-ray sources. Spectra were obtained at perpendicular take off angle, using pass energies 100 eV (survey) and 20 eV (Ni 2p, Co 2p, C 1s and O 1s spectra). Oxidation at low pressure regime was performed by annealing the sample in the XPS analysis chamber filled with pure oxygen (99.9995%) up to 5x10<sup>-7</sup> mbar. Each spectrum was taken consecutively with the time interval accumulated to prior oxidation duration. The oxidation at high pressure regime was performed in a sealed stainless-steel compartment equipped with a gas inlet and outlet and attached to a UHV analysis chamber. Prior to ambient pressure oxidation experiments, the metal and alloy samples were pretreated by annealing in oxygen (0.5 bar, 720 K) and subsequently in hydrogen (0.5 bar, 720 K) until most of carbon and oxygen impurities were not detected by XPS. Oxidation of the metal and alloy foil was performed by annealing for 5 min at various temperatures in 0.5bar O<sub>2</sub>. Subsequently the sample was cooled down and transferred to the UHV XPS analysis chamber, without being exposed to the atmosphere.

The spectra obtained were processed with background subtraction by Shirley method and normalized using atomic sensitivity factors [39]. The ratio of the metal oxide component and metallic component of nickel and cobalt was obtained by the difference of the normalized metal spectra at reduced state, which were obtained by the initial XPS measurement before oxidation and the normalised metal oxide spectra. The mean valence values of nickel and cobalt were obtained from the average of the oxidation state of metal and metal oxide content. The bulk crystalline structure of the sample was characterized by X-ray diffraction (XRD, Bruker AXS D8 Advance). The morphology of nickel cobalt alloy before and after oxidation was inspected by scanning electronic microscopy (SEM) and energy-dispersive X-ray spectroscopy (EDX) using a Jeol JSM-6700F field emission scanning electron microscope.

### **3.3 Results and discussion**

#### **3.3.1 XRD characterization**

Pure nickel is commonly found with fcc phase and it is stable over a wide range of temperature. Pure cobalt exists in hcp phase at low temperature and it undergoes phase transition to fcc phase above 690 K. The bulk structure of NiCo alloys is known to depend on the chemical composition [40, 41]. At low nickel content, the NiCo alloy is in hcp structure, while from 50% Ni concentration and above, fcc becomes the dominant phase. In this work, pure Ni, pure Co and NiCo alloy foil were characterised by X-ray diffraction (see *supplementary data, S1*). As expected pure nickel and cobalt foils were in the fcc and hcp phases respectively. The diffractograms of the NiCo alloy used in this experiment corresponds to fcc crystalline phase, in agreement with literature results for NiCo alloys containing 50% Ni. No indications of other (e.g. oxide structures) were found by XRD after multiple oxidation treatment, pointing out that oxidation is restricted to the near surface region and does not influence the bulk structure of the foil.

#### **3.3.2 SEM characterization**

Figure 3.1 shows two representative SEM images of NiCo alloy oxidized in 0.5 bar O<sub>2</sub> at 720 K. It is evident that well defined crystallites are formed in a variety of sizes and shapes. From low magnification image, it was found that larger crystallites are mainly organized into long and narrow chains-like structures. The dense rock-like masses in the SEM image are mainly due to Co<sub>3</sub>O<sub>4</sub> spinel oxide formation as indicated by XPS results (shown later) and EDX analysis. Crystalline cobalt oxide formation on fcc cobalt at room temperature has been reported [42], therefore it is not surprising that at 720 K, crystallites of Co<sub>3</sub>O<sub>4</sub> are formed over our alloy surface. Since, as mentioned before, XRD did not indicate any oxide-related features, one can assume that Co<sub>3</sub>O<sub>4</sub> crystallites are restricted to the surface region. The organization of large crystallites in chain-like structures can be rationalized by preferential growth of the cobalt oxide at the grain boundaries of the alloy, since in this region oxidation is faster due to increase in defect sites and easier diffusion of ions.

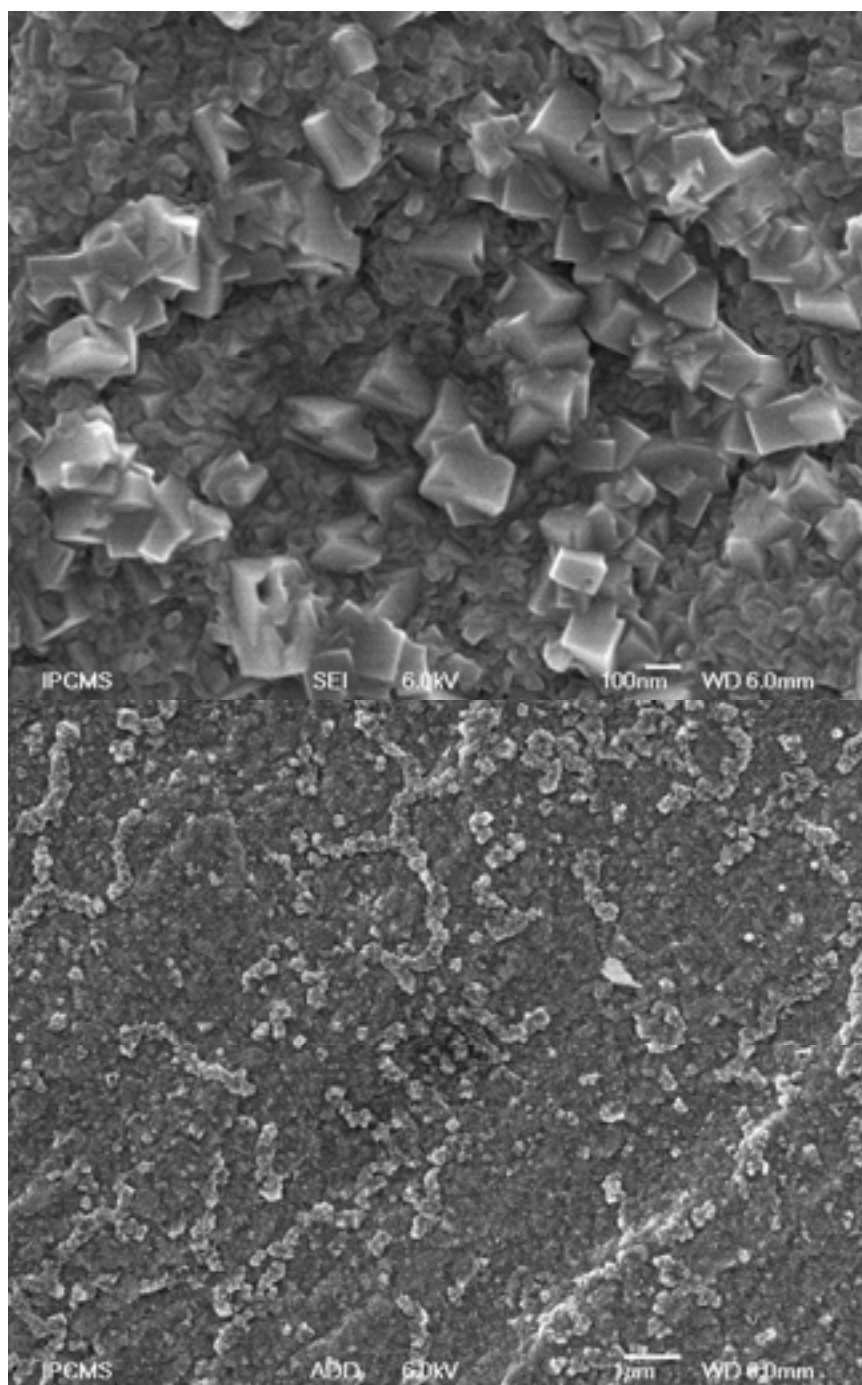


*Figure 3.1 Characteristic SEM images in two magnifications of NiCo surface oxidized in 0.5 bar O<sub>2</sub> at 720 K.*

Figure 3.2 shows SEM images taken on NiCo alloy cleaned by multiple Ar<sup>+</sup> sputtering and annealing at 673K in UHV chamber. It should be noted that surface oxide was significantly reduced after this treatment, however the sample was briefly exposed to the atmosphere upon removal from the XPS chamber for microscopy. The SEM images show a rough, but quite homogeneous, surface morphology. The reduction of oxide reveals an alloyed surface with certain rugosity and pits of ~100nm. The grains observed in higher magnification image are systematically lower in number and size than before and have lost the characteristic

crystalline shape. This can be attributed to the shrinkage of the initial oxide crystallites during reduction.

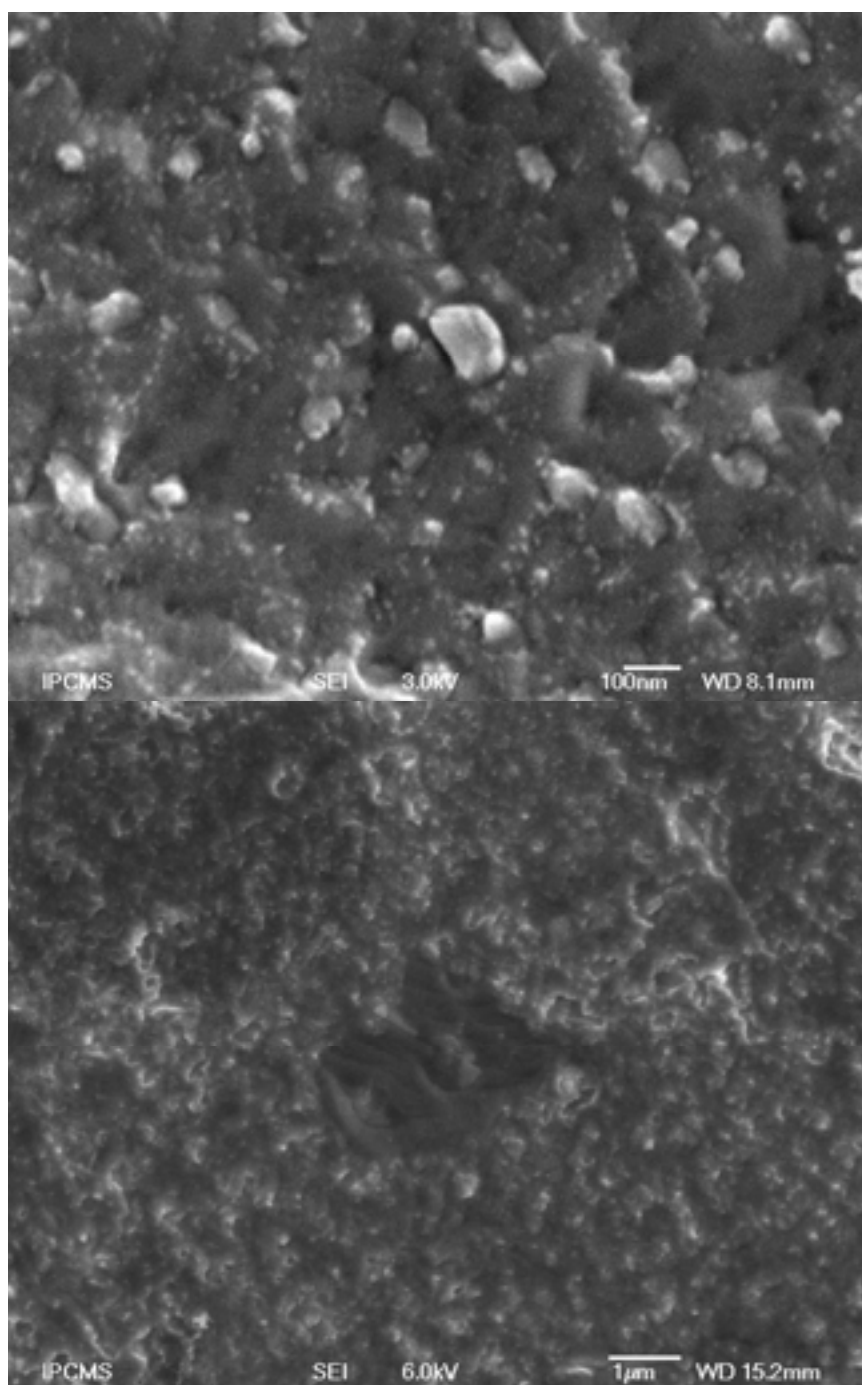


*Figure 3.2 Characteristic SEM images in two magnifications of pre-oxidized NiCo surface cleaned by Ar<sup>+</sup> sputtering and annealing cycles under UHV.*

### **3.3.3 Oxidation of NiCo at low O<sub>2</sub> pressure**

NiCo alloy was exposed to  $5 \times 10^{-7}$  mbar oxygen and photoelectron spectra were obtained at fixed time intervals up to 90 min of O<sub>2</sub> exposure. As reference, pure Ni and Co polycrystalline foils were measured under identical conditions. Experiments performed at

570 and 670 K indicated similar trends, however the lower the temperature the slower the oxidation process, therefore for clarity only the highest temperature experiments will be presented in detail.

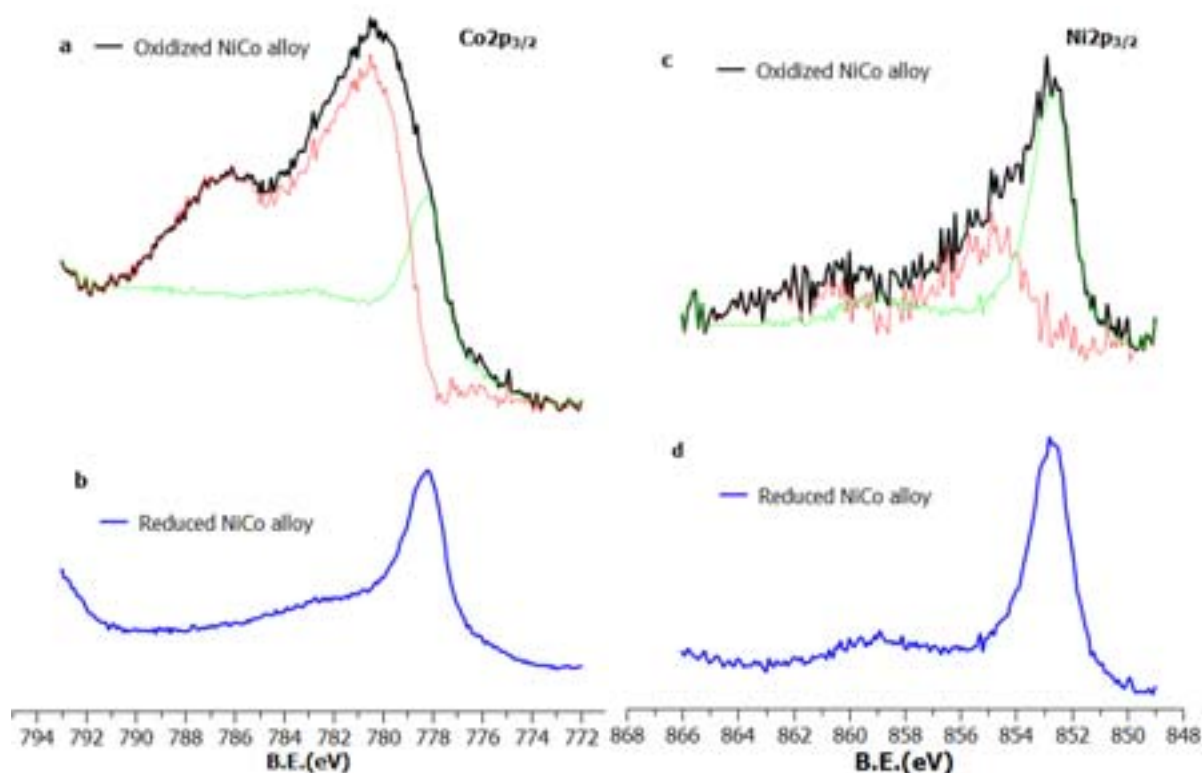


*Figure 3.3 (a) Normalised XPS spectrum of  $\text{Co}2p_{3/2}$  for NiCo alloy foil exposed to  $\text{O}_2$  at  $5 \times 10^{-7}$  mbar at 670 K for 30min and the decomposition of the peak to metallic Co and Co Oxides (b) Normalised XPS spectrum of  $\text{Co}2p_{3/2}$  for clean NiCo alloy foil (c) Normalised XPS spectrum of  $\text{Ni}2p_{3/2}$  for NiCo alloy foil exposed to  $\text{O}_2$  at  $5 \times 10^{-7}$  mbar at 670 K for 30min and the decomposition of the peak to metallic Ni and NiO components (d) Normalised XPS spectrum of  $\text{Ni}2p_{3/2}$  for clean NiCo alloy foil.*

The  $\text{Ni}2p_{3/2}$  and  $\text{Co}2p_{3/2}$  core level peaks of NiCo alloy before and after 30 min oxygen exposure at 670 K are shown in figure 3.3. The  $\text{Co}2p_{3/2}$  peak of NiCo alloy before oxygen exposure is located at 778.1eV (fig.3b), which is coherent to the binding energy measured on monometallic Co foil and literature values [43]. The peak is broadened and a strong satellite structure is built up at higher binding energies when the alloy is exposed to  $\text{O}_2$  (fig.3a). Subtraction of normalized metallic cobalt spectrum from that of the oxidized NiCo, indicates that the overall  $\text{Co}2p_{3/2}$  peak is a convolution of two components related to  $\text{Co}^0$  and  $\text{Co}^{x+}$  (oxide species). The main peak of oxidized cobalt is at 780.4eV with a characteristic strong satellite at about 6 eV higher in BEs. This is in good agreement with literature values of rocksalt CoO [44, 45]. In addition, the residual spectrum obtained after subtraction of the metallic Co component was compared to a reference Co  $2p_{3/2}$  spectrum taken on pure CoO grown over Co(0001) (as confirmed by X-ray absorption spectroscopy [46], please refer to supplementary information in appendices). The strong coherence between residual and the CoO reference spectra indicates that the majority of oxidized cobalt is in rocksalt CoO-like

phase. No indication of  $\text{Co}_3\text{O}_4$  phase formation was found, and if  $\text{Co}_3\text{O}_4$  exists, it should be of trace amount that do not produce measurable modification in the Co  $2p_{3/2}$  peak (estimated less than 10%).

Similar results were found for nickel. The  $\text{Ni}2p_{3/2}$  peak at 852.7 eV (initially at metallic state [47]), becomes broader after 30 minutes of oxygen exposure. After subtracting the metallic component from the overall spectra (fig. 3c), an additional peak at 854.5eV with a satellite at 861.5eV due to NiO formation was evident.

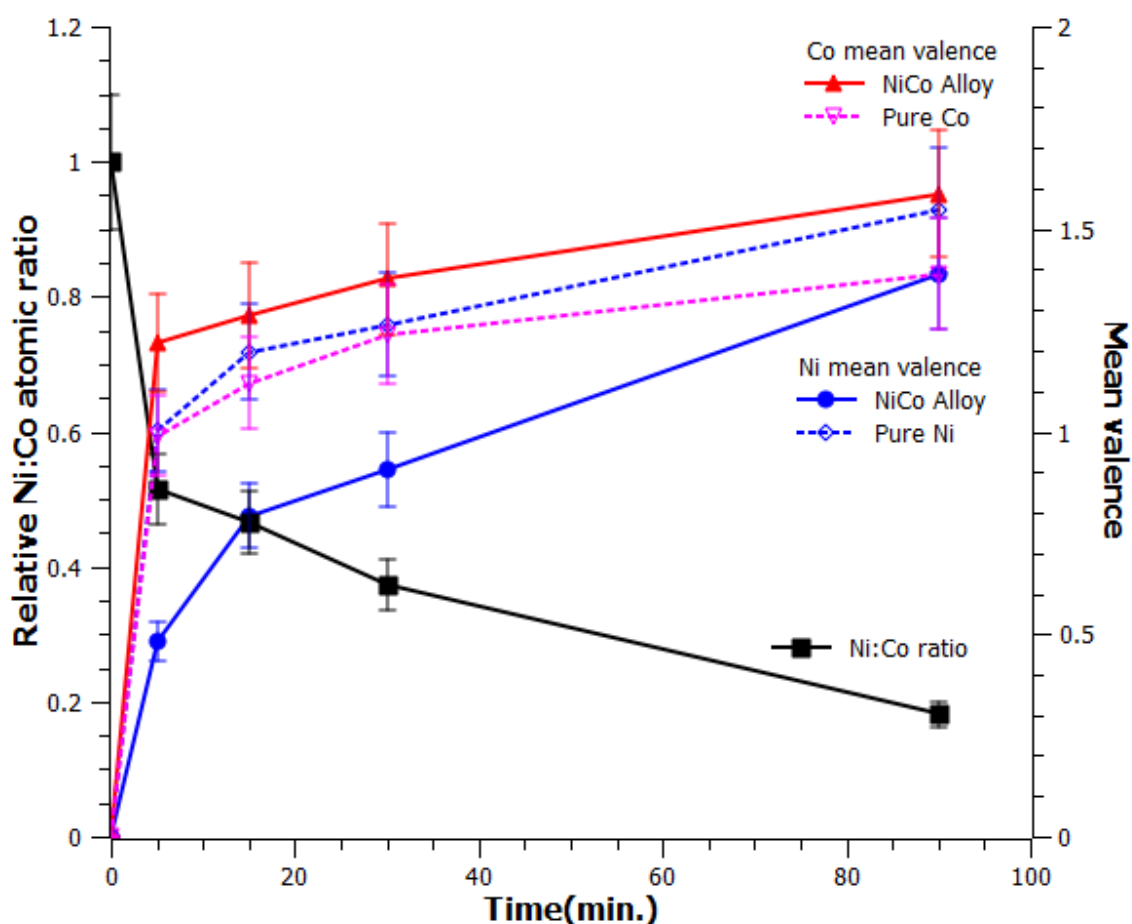


Figure 3.4. Cobalt and nickel mean valence values (right y-axis) and relative Ni:Co atomic ratio (left y-axis) recorded after exposure of monometallic Co, monometallic Ni and alloyed NiCo foils to  $5 \times 10^{-7}$  mbar  $\text{O}_2$  at 670 K for various time intervals.

In order to reveal possible synergetic effects of alloying to the oxidation process, the mean valence values (MVs) of pure and alloyed NiCo are presented in figure 3.4, together with the Ni to Co atomic ratio. Ni and Co oxidation occurs simultaneously as oxygen diffuses promptly into the surface alloy layer. The steep increase of Ni and Co MVs and decrease of Ni:Co ratio, indicate that oxide formation is followed by significant cobalt segregation. However, after the rapid (5 min) built-up, further growth of the initial oxide layer proceeds much slower. This shows that development of thicker oxide layers depends to a great extent on cation diffusion, which most probably at 670 K is still kinetically hindered. Adsorption-driven Co segregation contributes to the higher composition of cobalt oxide on the alloy

surface, as indicated by the decrease of Ni:Co atomic ratio. Similar segregation behavior was also observed by Hajcsar et al.[48] in their Auger electron spectroscopy study of NiCo alloy nanoparticles at 733 K in  $10^{-6}$  Torr  $O_2$ .

As shown in figure 3.4, the MV of Co for the alloy is systematically higher than that in pure form, whereas the reverse trend is observed for Ni. This signifies a synergetic effect at the Ni/Co interface [49, 50], which hinders oxidation of nickel in the alloy. In addition, as shown by the Ni:Co atomic ratio, nickel tends to be depleted as cobalt oxide formation takes place on the surface. Consequently nickel outward diffusion for the formation of oxide is further suppressed. Thus, NiCo alloy is deprived of nickel oxide on the surface compared to nickel metal.

Ruban et al. [51] estimated the segregation energy of bimetallic transition metal alloys in vacuum by first principle calculations. They predicted that nickel ion impurities in cobalt (host metal), has the tendency to segregate moderately to the surface (energy of segregation=-0.13eV/atom), and *vice versa* for cobalt impurities into nickel. In addition, Menning et al. [52] has deduced the general trend of adsorbate-induced segregation of bimetallic surfaces from the thermodynamic potential of segregation obtained by DFT calculations. It was found that surface configuration with a cobalt monolayer over Ni(111) host is thermodynamically preferred when the surface is covered by 0.5 monolayers of oxygen, compared to configurations where the surface is terminated by a nickel layer with subsurface cobalt. It should be noted that first principle calculations are not directly applicable to our relatively complex system where the actual surface composition, surface ordering and external environment are radically different. However, our experimental results are coherent with the trends predicted by theory, therefore these studies can be used as the base to rationalize the initial stages of alloy oxidation.

Although the difference in the free energy of formation of CoO and NiO is little (please refer to the introduction for the corresponding values), cobalt oxidation is known to be faster than nickel [53] due to the higher concentration of mobile cation vacancies in cobalt oxide [34]. This might serve as the driving force for preferential cobalt segregation during the oxidation in NiCo alloy, especially for polycrystalline surfaces where the high degree of grain boundaries might enhance kinetic effects.

#### **3.3.4 Oxidation of NiCo at ambient $O_2$ pressure**

The oxidation of NiCo alloy was studied after 5 min annealing in 0.5 bar  $O_2$  at different temperatures and the Ni  $2p_{3/2}$  peaks are shown in the stack plot of Figure 3.5a. Results of a reference Ni foil measured under the same conditions are shown in figure 3.5b.

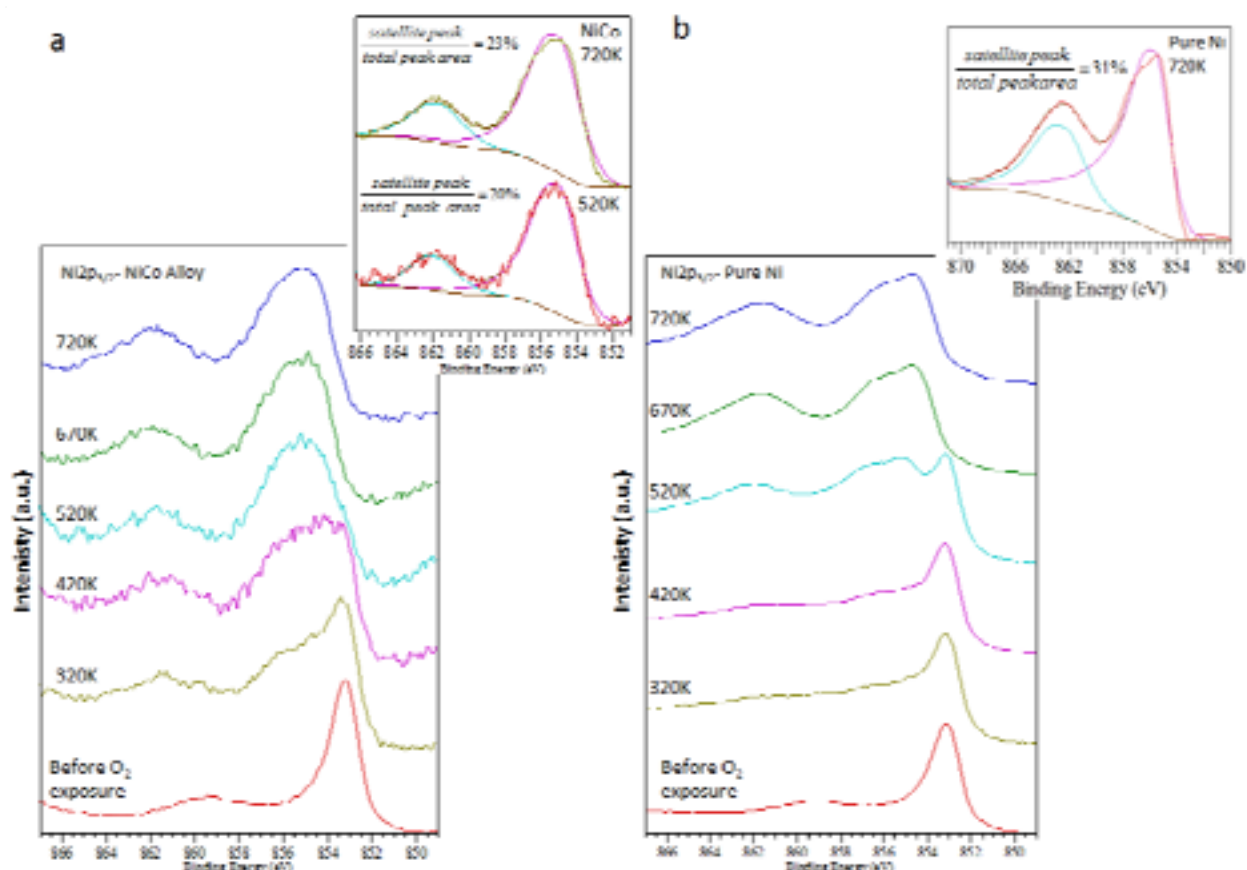


Figure 3.5. Normalised  $Ni2p_{3/2}$  XPS spectra of (a) NiCo alloyed foil and (b) monometallic Ni foil, after 5 min exposure to 0.5bar  $O_2$  at 320, 420, 520, 670 and 720 K. The inset graphs show characteristic cases of peak fitting the  $Ni2p_{3/2}$  peak into main photoelectron and satellite components.

On pure Ni, the ratio of NiO to metallic Ni remains similar from 320 K to 420 K reflecting surface passivation phenomena [23], in which the thin outermost NiO layer prevents further nickel oxidation. At more elevated temperature ( $T > 520$  K), diffusion of nickel ion is enhanced and thicker nickel oxide layer is formed, as clearly indicated by the appearance of the new component around 855 eV. At higher temperature ( $T > 670$  K) the  $Ni2p_{3/2}$  spectrum has the main peak at 854.5 eV and two distinct satellite peaks at 856eV and 861.2eV. The satellite peaks are characteristic for bulk-like NiO and have been attributed to the non-local screening effect of neighboring nickel oxide cluster [54].

In case of NiCo alloy, the oxide component in the  $Ni2p_{3/2}$  spectrum increases gradually up to 670 K, where total oxidation is observed. Comparison between the  $Ni2p_{3/2}$  peaks of monometallic and alloy foil in the fully oxidized state, indicates differences in the relative intensity of the 856 eV satellite compared to the main line. As shown by Sawatzky and co. workers [54] the intensity of 856 eV satellite is strongly influenced not only by the nearest-neighbor, but also from the next-nearest-neighbor, configuration around Ni ions. In addition, Alders et al. have reported similar modification of 856 eV satellite intensity when a monolayer of NiO is epitaxially grown on MgO [55], due to the strong influence of MgO in

the proximity to NiO. In a similar manner, a well mixed Ni-Co-O spinel-like solid solution could produce analogous modifications in the satellite structure. Another supporting evidence of mixed Ni-Co-O oxide formation can be derived from analyzing the satellite peak at 861eV. The relative intensity of the 861 eV satellite peak compared to the main line is suppressed for the alloy compared to the pure NiO spectrum (see inset of figure 3.5). In an XPS study of  $\text{Co}_x\text{Ni}_{1-x}\text{O}$  ( $0 \leq x \leq 1$ ) by Nydegger et al. [56], similar suppression of the 861 eV satellite structure was attributed to the deviation of NiO structure from rocksalt stoichiometry, either due to lattice oxygen vacancies or spinel oxide formation. Overall, the features of Ni 2p spectrum of the NiCo alloy indicate that upon annealing at ambient pressure a non-stoichiometric mixed oxide of Co and Ni is likely to form on the surface. The  $\text{Co}2p_{3/2}$  spectra for pure cobalt metal and NiCo alloy change in a similar fashion (see supplementary data, S3). At 420 K, there is almost complete transformation of Co to CoO. At higher temperature, CoO is further oxidized to  $\text{Co}_3\text{O}_4$ , where the main peak lies at 779.9 and corresponds to the characteristic value of  $\text{Co}_3\text{O}_4$  [57]. In addition, the main satellite of CoO at 786.5 is reduced at 520 K, which further affirms the transformation of CoO to  $\text{Co}_3\text{O}_4$ .

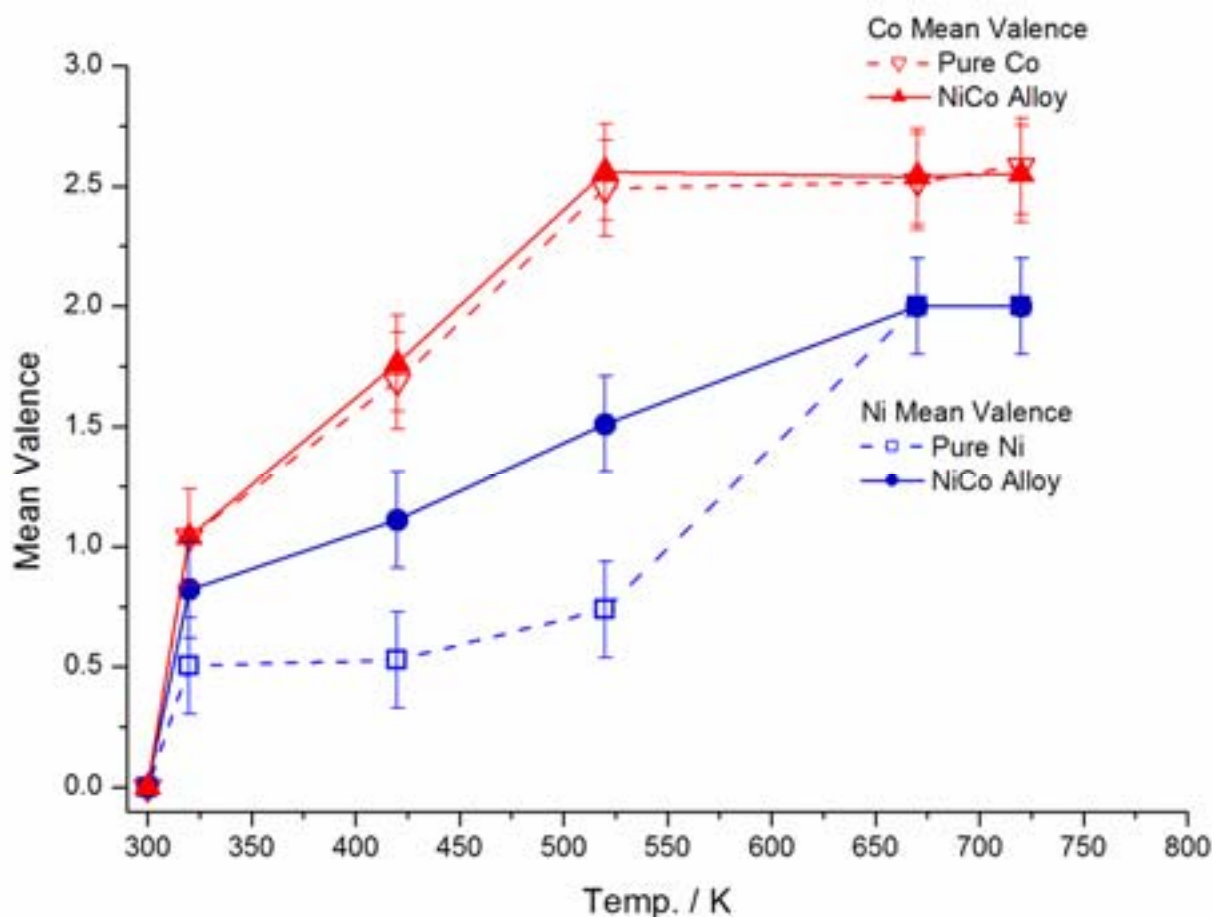


Figure 3.6 Nickel and Co mean valence values of monometallic Ni and Co foils as well as of alloyed NiCo foil after 5 min exposure to 0.5bar  $\text{O}_2$  at various temperatures.

Figure 3.6 summarizes the changes of nickel and cobalt MV values during oxidation at successive temperatures. Only very slight differences between cobalt MV values of pure

cobalt and NiCo alloy were found. Since high O<sub>2</sub> partial pressure leads to rapid cobalt segregation on the surface of the alloy (see figure 3.7), influence brought by alloying and redox coupling with nickel is suppressed. Conversely, there is a much larger difference in the chemical state of Ni in pure metal and alloy forms. One must also take into account the fact that the amount of nickel on the alloy surface is much lower than that of the nickel metal foil, due to the effect of cobalt segregation as described previously for oxidation at low O<sub>2</sub> pressure. This reduces the amount of metallic nickel that can be detected by our surface sensitive method (estimated probing depth < 5nm).

### 3.3.5 Bimetallic synergetic effect and pressure gap

Differences between Ni, Co and NiCo alloy at the two O<sub>2</sub> pressure regimes (5x10<sup>-7</sup> and 500 mbar) indicates the effect of the so called “pressure gap” in the oxidation process.

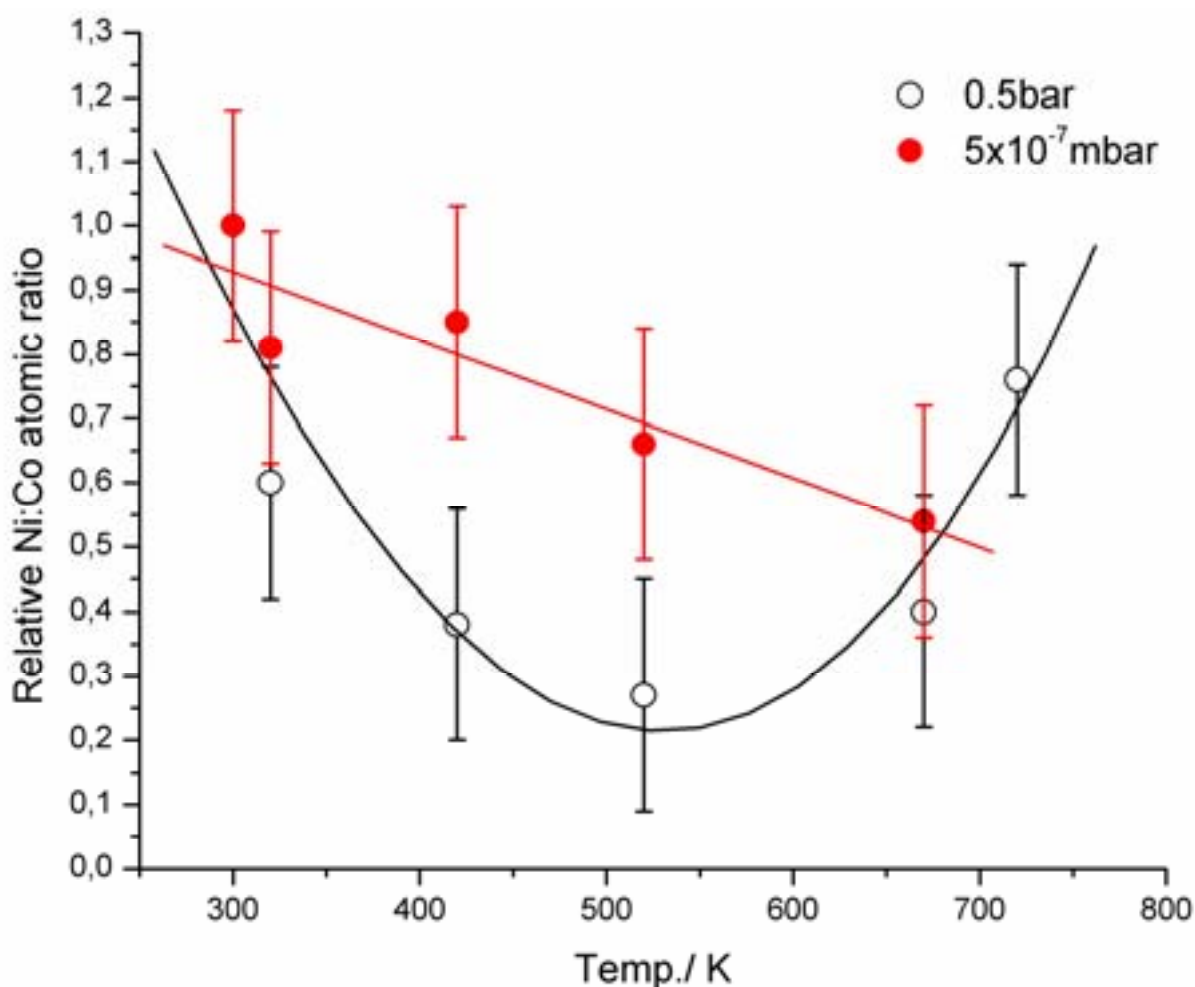


Figure 3.7. Comparison of Ni:Co atomic ratio relative to the initially measured value (before oxidation) as a function of temperature in two O<sub>2</sub> pressure regimes.

As summarized in figure 3.7, Ni:Co atomic ratio at low O<sub>2</sub> pressure undergoes a continual decrease with increasing temperature, while that at high O<sub>2</sub> pressure initially decreases up to 520 K, but then increases as Co<sup>2+</sup> is further oxidized to Co<sub>3</sub>O<sub>4</sub>. At low O<sub>2</sub> pressure, the surface layer of the alloy behaves as predicted from the reactivity of the two metals. The

more reactive species, in this case cobalt, is segregated to the gas-solid interface and its higher oxygen affinity induces a redox effect between the interfacial cobalt and nickel. Consequently, nickel oxidation of NiCo alloy is suppressed, which causes the large difference in the mean valence value of Ni between pure metal and NiCo alloy as shown previously in figure 3.4. Meanwhile, the mean valence value of cobalt undergoes a substantial increase, which can be interpreted by the extensive formation of cobalt oxide nuclei on the surface of alloy, displacing nickel into the bulk.

Similar segregation effect is also observed at high O<sub>2</sub> pressure and it is further amplified due to the higher abundance of oxygen in the gas phase. Ni to Co atomic ratio decreases as the oxidation temperature moves from 320 to 520 K. Subsequent increase in temperature increases the Ni to Co atomic ratio, but please note that it remains lower than that found of clean/reduced NiCo alloy. Since at high O<sub>2</sub> pressure more oxygen is available, cobalt is sequentially oxidized to CoO and Co<sub>3</sub>O<sub>4</sub> according to the ascent of temperature. At 420 K, the mean valence of cobalt is close to 2, thus metallic cobalt has been transformed to CoO. Cobalt segregation slows down, indicating that the preference for oxygen reactivity has switched to nickel. Meanwhile, nickel ion mobility also increases with temperature. The Ni:Co atomic ratio reaches a minimum at 520K, where CoO is further oxidized to Co<sub>3</sub>O<sub>4</sub> (mean valence of cobalt is 2.5 and that of Co<sub>3</sub>O<sub>4</sub> is 2.67). Above 520K, Ni ions diffuse back to the surface, such that the Ni to Co atomic ratio increases. With the formation of Co<sub>3</sub>O<sub>4</sub> spinel structure at higher temperature, exchange of nickel and cobalt in the octahedral site of the spinel can take place. This suggests that the formation of mixed Ni-Co-O layer on the alloy surface is probable at high temperature and O<sub>2</sub> pressure, as supported by the increase in Ni:Co atomic ratio. The reduction of NiO satellite peak from the XPS spectra, as shown previously, provides also supportive information for the formation of mixed Ni-Co-O spinel-like oxide. A schematic overview of the modifications induced on the NiCo alloy surface as a function of temperature and oxygen pressure is presented in figure 3.8.

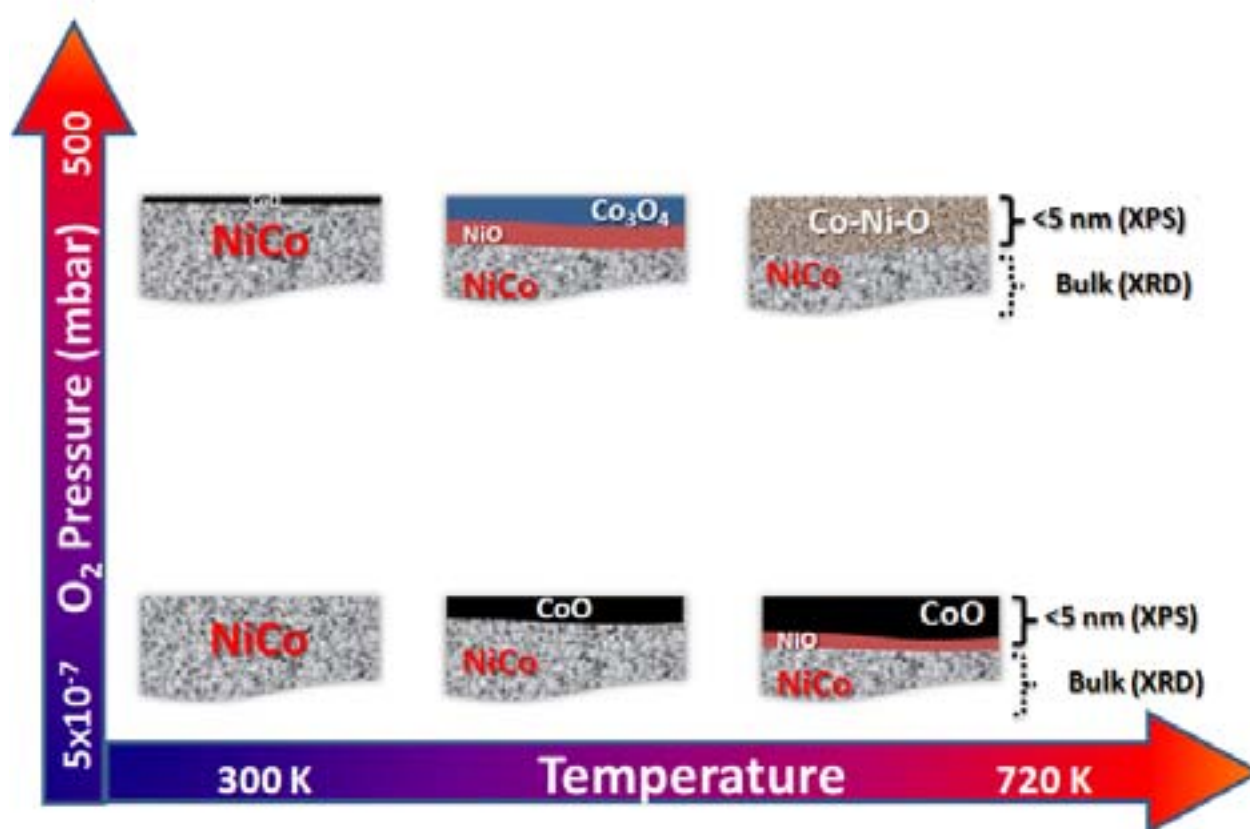


Figure 3.8. Illustration of the surface oxidation of NiCo alloy under two different O<sub>2</sub> pressure regimes in ascending temperature. At low pressure ( $5 \times 10^{-7}$  mbar), CoO enriches the surface of the alloy under ascending temperature of annealing. At high pressure regime (500 mbar), CoO is mainly found at low temperature and Co<sub>3</sub>O<sub>4</sub> is formed at moderate temperature. With the formation of Co<sub>3</sub>O<sub>4</sub>, Ni<sup>2+</sup> may exchange with Co<sup>2+</sup> ions in octahedral sites of Co<sub>3</sub>O<sub>4</sub> spinel, forming a layer of mixed nickel-cobalt spinel-like oxide. Thus cobalt surface enrichment is suppressed at high pressure and temperature. The bulk NiCo alloy structure was not affected as confirmed by the x-ray diffraction (XRD) results.

The results presented here, can help to elucidate the performance of NiCo alloys when used as catalysts, as for example during ethanol steam reforming reaction. It has been shown recently that the oxidation state of cobalt can determine the selectivity paths [58]. In particular, Co<sup>0</sup> is highly active for decarbonylation of ethoxide species to form CO, while Co<sup>2+</sup> is more selective to dehydrogenation of ethoxide to acetaldehyde. Under working catalytic conditions the oxidation state of cobalt is mainly determined by the composition of the reaction mixture (ethanol and water), the pressure, as well as the temperature. As shown here, alloying Co with Ni has a profound effect on the oxidation state and the abundance of surface cobalt species. This can be used to manipulate the surface state, so as to turn favour or suppress different reaction pathways, obtaining desired reaction products.

### **3.4 Conclusions**

Surface oxidation of NiCo (1:1) alloy exposed to O<sub>2</sub> at two pressure regimes (5x10<sup>-10</sup> and 5x10<sup>-1</sup> bar) has been studied by X-ray photoelectron spectroscopy. Cobalt is more reactive towards oxidation compared to nickel, such that at both pressure regimes cobalt segregation on the surface was observed. Saturation of oxygen on the surface takes place rapidly at both pressures and beyond that oxidation depends greatly on cation diffusion. At low pressure regime, the redox effect between nickel and cobalt accompanied by the segregation effect, leads to a higher oxidation state achieved for cobalt on alloy compared to pure cobalt, while the opposing result is observed for nickel. At high pressure regime, cobalt segregation occurs in a much faster rate. Complete transformation to cobalt monoxide occurs above 420 K. Cobalt segregation reaches a maximum at 520 K, where CoO undergoes further oxidation to form Co<sub>3</sub>O<sub>4</sub>. Subsequently, above this temperature cobalt segregation is reduced and a layer of mixed nickel-cobalt spinel-like oxide is formed, as Ni<sup>2+</sup> replace Co<sup>2+</sup> ions at octahedral sites during the segregation process.

### **3.5 References**

- [1] A.N. Fatsikostas, X.E. Verykios, Reaction network of steam reforming of ethanol over Ni-based catalysts, *Journal of Catalysis*, 225 (2004) 439-452.
- [2] P. Bichon, G. Haugom, H.J. Venvik, A. Holmen, E.A. Blekkan, Steam Reforming of Ethanol Over Supported Co and Ni Catalysts, *Topics in Catalysis*, (2008) 1-8.
- [3] F. Frusteri, S. Freni, V. Chiodo, L. Spadaro, O. Di Blasi, G. Bonura, S. Cavallaro, Steam reforming of bio-ethanol on alkali-doped Ni/MgO catalysts: hydrogen production for MC fuel cell, *Applied Catalysis A: General*, 270 (2004) 1-7.
- [4] F. Haga, T. Nakajima, H. Miya, S. Mishima, Catalytic properties of supported cobalt catalysts for steam reforming of ethanol, *Catalysis Letters*, 48 (1997) 223-227.
- [5] J. Llorca, J.A. Dalmon, P. Ramírez De la Piscina, N. Homs, In situ magnetic characterisation of supported cobalt catalysts under steam-reforming of ethanol, *Applied Catalysis A: General*, 243 (2003) 261-269.
- [6] F. Frusteri, S. Freni, L. Spadaro, V. Chiodo, G. Bonura, S. Donato, S. Cavallaro, H<sub>2</sub> production for MC fuel cell by steam reforming of ethanol over MgO supported Pd, Rh, Ni and Co catalysts, *Catalysis Communications*, 5 (2004) 611-615.
- [7] H. Tanaka, R. Kaino, Y. Nakagawa, K. Tomishige, Comparative study of Rh/MgO modified with Fe, Co or Ni for the catalytic partial oxidation of methane at short contact time. Part II: Catalytic performance and bed temperature profile, *Applied Catalysis A: General*, 378 (2010) 187-194.
- [8] J.F. Da Costa-Serra, R. Guil-López, A. Chica, Co/ZnO and Ni/ZnO catalysts for hydrogen production by bioethanol steam reforming. Influence of ZnO support morphology on the catalytic properties of Co and Ni active phases, *International Journal of Hydrogen Energy*, 35 (2010) 6709-6716.
- [9] M.C. Sánchez-Sánchez, R.M. Navarro, J.L.G. Fierro, Ethanol steam reforming over Ni / M<sub>x</sub> O<sub>y</sub>-Al<sub>2</sub>O<sub>3</sub> (M = Ce, La, Zr and Mg) catalysts: Influence of support on the hydrogen production, *International Journal of Hydrogen Energy*, 32 (2007) 1462-1471.
- [10] J. Sun, X.P. Qiu, F. Wu, W.T. Zhu, H<sub>2</sub> from steam reforming of ethanol at low temperature over Ni/Y<sub>2</sub>O<sub>3</sub> and Ni/La<sub>2</sub>O<sub>3</sub> catalysts for fuel-cell application, *International Journal of Hydrogen Energy*, 30 (2005) 437-445.
- [11] F.J. Mariño, E.G. Cerrella, S. Duhalde, M. Jobbagy, M.A. Laborde, Hydrogen from steam reforming of ethanol. characterization and performance of copper-nickel supported catalysts, *International Journal of Hydrogen Energy*, 23 (1998) 1095-1101.
- [12] J. Xu, W. Zhou, Z. Li, J. Wang, J. Ma, Biogas reforming for hydrogen production over a Ni-Co bimetallic catalyst: Effect of operating conditions, *International Journal of Hydrogen Energy*, 35 (2010) 13013-13020.
- [13] K. Takanabe, K. Nagaoka, K. Nariai, K.-i. Aika, Titania-supported cobalt and nickel bimetallic catalysts for carbon dioxide reforming of methane, *Journal of Catalysis*, 232 (2005) 268-275.
- [14] M.S. Fan, A.Z. Abdullah, S. Bhatia, Utilization of greenhouse gases through carbon dioxide reforming of methane over Ni-Co/MgO-ZrO<sub>2</sub>: Preparation, characterization and activity studies, *Appl. Catal., B* 100 (2010) 365-377.
- [15] K.R. Lawless, The oxidation of metals, *Reports on Progress in Physics*, 37 (1974) 231-316.
- [16] N. Cabrera, N.F. Mott, Theory of the oxidation of metals, *Reports on Progress in Physics*, 12 (1949) 163-184.

**Chapter 3 Surface oxidation of NiCo alloy: A comparative X-ray photoelectron spectroscopy study in a wide pressure range**

- [17] G. Benitez, J.L. Carelli, J.M. Heras, L. Viscido, Interaction of oxygen with thin cobalt films, *Langmuir*, 12 (1996) 57-60.
- [18] K.S. Kim, N. Winograd, X-ray photoelectron spectroscopic studies of nickel-oxygen surfaces using oxygen and argon ion-bombardment, *Surface Science*, 43 (1974) 625-643.
- [19] H. Bu, C.D. Roux, J.W. Rabalais, Oxygen induced added-row reconstruction of the Ni{110} surface, *The Journal of Chemical Physics*, 97 (1992) 1465-1470.
- [20] P.H. Holloway, J.B. Hudson, Kinetics of the reaction of oxygen with clean nickel single crystal surfaces: I. Ni(100) surface, *Surface Science*, 43 (1974) 123-140.
- [21] P.H. Holloway, CHEMISORPTION AND OXIDE FORMATION ON METALS: OXYGEN-NICKEL REACTION, *Journal of vacuum science & technology*, 18 (1980) 653-659.
- [22] D.F. Mitchell, M.J. Graham, A kinetic study of the initial oxidation of Ni (111) and (211) surfaces by rheed and X-ray emission, *Surface Science*, 114 (1982) 546-562.
- [23] E.S. Lambers, C.N. Dykstal, J.M. Seo, J.E. Rowe, P.H. Holloway, Room-temperature oxidation of Ni(110) at low and atmospheric oxygen pressures, *Oxidation of Metals*, 45 (1996) 301-321.
- [24] W.D. Wang, N.J. Wu, P.A. Thiel, Structural steps to oxidation of Ni(100), *The Journal of Chemical Physics*, 92 (1990) 2025-2035.
- [25] T. Matsuyama, A. Ignatiev, LEED-AES study of the temperature dependent oxidation of the cobalt (0001) surface, *Surface Science*, 102 (1981) 18-28.
- [26] T. Matsuyama, A. Ignatiev, LEED-AES study of the temperature dependent oxidation of the cobalt (0001) surface, *Surf. Sci.*, 102 (1981) 18-28.
- [27] R.B. Moyes, M.W. Roberts, Interaction of cobalt with oxygen, water vapor, and carbon monoxide : X-Ray and ultraviolet photoemission studies, *Journal of Catalysis*, 49 (1977) 216-224.
- [28] G.R. Castro, J. Küppers, Interaction of oxygen with hcp (0001) recrystallized cobalt surfaces, *Surface Science*, 123 (1982) 456-470.
- [29] M. Oku, Y. Sato, In-situ X-ray photoelectron spectroscopic study of the reversible phase transition between CoO and Co<sub>3</sub>O<sub>4</sub> in oxygen of 10<sup>-3</sup> Pa, *Applied Surface Science*, 55 (1992) 37-41.
- [30] M.E. Bridge, R.M. Lambert, Oxygen chemisorption, surface oxidation, and the oxidation of carbon monoxide on cobalt (0001), *Surface Science*, 82 (1979) 413-424.
- [31] G.R. Castro, J. Küppers, Interaction of oxygen with hcp (0001) recrystallized cobalt surfaces, *Surf. Sci.*, 123 (1982) 456-470.
- [32] J. Chase, M.W., C.A. Davies, J. Downey, J.R., D.J. Frurip, R.A. McDonald, A.N. Syverud, NIST JANAF THERMOCHEMICAL TABLES 1985, in: NIST JANAF THERMOCHEMICAL TABLES, 1985.
- [33] Lange's handbook of chemistry, 15th Edition ed., McGraw-Hill, Inc., 1999.
- [34] G.C. Wood, I.G. Wright, J.M. Ferguson, The oxidation of Ni and Co and of Ni/Co alloys at high temperatures, *Corrosion Science*, 5 (1965) 645-661.
- [35] B. Chattopadhyay, G.C. Wood, The transient oxidation of alloys, *Oxidation of Metals*, 2 (1970) 373-399.
- [36] B.D. Bastow, G.C. Wood, D.P. Whittle, The segregation of alloy components in scales and subscales formed by binary alloys of Mn, Fe, Co and Ni, *Corrosion Science*, 25 (1985) 253-285.
- [37] M. Cabo, E. Pellicer, E. Rossinyol, O. Castell, S. Suriñach, M.D. Baró, Mesoporous NiCo<sub>2</sub>O<sub>4</sub> spinel: Influence of calcination temperature over phase purity and thermal stability, *Crystal Growth and Design*, 9 (2009) 4814-4821.

- [38] G. Zhou, Nucleation-induced kinetic hindrance to the oxide formation during the initial oxidation of metals, *Physical Review B - Condensed Matter and Materials Physics*, 81 (2010).
- [39] C.D. Wagner, L.E. Davis, M.V. Zeller, J.A. Taylor, R.H. Raymond, L.H. Gale, EMPIRICAL ATOMIC SENSITIVITY FACTORS FOR QUANTITATIVE ANALYSIS BY ELECTRON SPECTROSCOPY FOR CHEMICAL ANALYSIS, *Surface and Interface Analysis*, 3 (1981) 211-225.
- [40] O. Ergeneman, K.M. Sivaraman, S. Pané, E. Pellicer, A. Teleki, A.M. Hirt, M.D. Baró, B.J. Nelson, Morphology, structure and magnetic properties of cobalt-nickel films obtained from acidic electrolytes containing glycine, *Electrochimica Acta*, 56 (2011) 1399-1408.
- [41] H. Zhang, T. Yao, Z. Sun, Y. Li, Q. Liu, F. Hu, Z. Pan, B. He, Z. Xie, S. Wei, Structural study on Co-Ni bimetallic nanoparticles by X-ray spectroscopy, *Journal of Physical Chemistry C*, 114 (2010) 13596-13600.
- [42] G. Hassnain Jaffari, H.-Y. Lin, C. Ni, S. Ismat Shah, Physiochemical phase transformations in Co/CoO nanoparticles prepared by inert gas Condensation, *Materials Science and Engineering: B*, 164 (2009) 23-29.
- [43] J.F. Moulder, W.F. Stickle, P.E. Sobol, K.D. Bomben, *Handbook of X-ray Photoelectron Spectroscopy*, Perkin-Elmer Corporation Physical Electronics Division, 1992.
- [44] S.C. Petitto, E.M. Marsh, G.A. Carson, M.A. Langell, Cobalt oxide surface chemistry: The interaction of CoO(1 0 0), Co<sub>3</sub>O<sub>4</sub>(1 1 0) and Co<sub>3</sub>O<sub>4</sub>(1 1 1) with oxygen and water, *Journal of Molecular Catalysis A: Chemical*, 281 (2008) 49-58.
- [45] Y.E. Roginskaya, O.V. Morozova, E.N. Lubnin, Y.E. Ulitina, G.V. Lopukhova, S. Trasatti, Characterization of bulk and surface composition of Co<sub>x</sub>Ni<sub>1-x</sub>O<sub>y</sub> mixed oxides for electrocatalysis, *Langmuir*, 13 (1997) 4621-4627.
- [46] S. Zafeiratos, T. Dintzer, D. Teschner, R. Blume, M. Hävecker, A. Knop-Gericke, R. Schlögl, Methanol oxidation over model cobalt catalysts: Influence of the cobalt oxidation state on the reactivity, *Journal of Catalysis*, 269 (2010) 309-317.
- [47] A.R. González-Elipe, J.P. Holgado, R. Alvarez, G. Munuera, Use of factor analysis and XPS to study defective nickel oxide, *Journal of Physical Chemistry*, 96 (1992) 3080-3086.
- [48] E.E. Hajcsar, P.R. Underbill, W.W. Smeltze, Initial stages of oxidation on Co-Ni alloys: Island nucleation and growth, *Langmuir*, 11 (1995) 4862-4872.
- [49] R. De Masi, D. Reinicke, F. Müller, P. Steiner, S. Hüfner, The interface of Mn, Fe, Co and Au metal films on NiO(0 0 1), investigated by photoemission and low energy electron diffraction, *Surface Science*, 515 (2002) 523-537.
- [50] T.J. Regan, H. Ohldag, C. Stamm, F. Nolting, J. Lüning, J. Stöhr, R.L. White, Chemical effects at metal/oxide interfaces studied by x-ray-absorption spectroscopy, *Physical Review B - Condensed Matter and Materials Physics*, 64 (2001) 2144221-21442211.
- [51] A.V. Ruban, H.L. Skriver, J.K. Nørskov, Surface segregation energies in transition-metal alloys, *Physical Review B - Condensed Matter and Materials Physics*, 59 (1999) 15990-16000.
- [52] C.A. Menning, J.G. Chen, General trend for adsorbate-induced segregation of subsurface metal atoms in bimetallic surfaces, *Journal of Chemical Physics*, 130 (2009).
- [53] G.J. Koel, P.J. Gellings, The contribution of different types of point defects to diffusion in CoO and NiO during oxidation of the metals, *Oxidation of Metals*, 5 (1972) 185-203.
- [54] M.A. Van Veenendaal, G.A. Sawatzky, Nonlocal screening effects in 2p x-ray photoemission spectroscopy core-level line shapes of transition metal compounds, *Physical Review Letters*, 70 (1993) 2459-2462.

**Chapter 3 Surface oxidation of NiCo alloy: A comparative X-ray photoelectron spectroscopy study in a wide pressure range**

- [55] D. Alders, F.C. Voogt, T. Hibma, G.A. Sawatzky, Nonlocal screening effects in 2p x-ray photoemission spectroscopy of NiO (100), *Physical Review B - Condensed Matter and Materials Physics*, 54 (1996) 7716-7719.
- [56] M.W. Nydegger, G. Couderc, M.A. Langell, Surface composition of  $\text{Co}_x\text{Ni}_{1-x}\text{O}$  solid solutions by X-ray photoelectron and Auger spectroscopies, *Appl. Surf. Sci.* , 147 (1999) 58-66.
- [57] T.J. Chuang, C.R. Brundle, D.W. Rice, Interpretation of the x-ray photoemission spectra of cobalt oxides and cobalt oxide surfaces, *Surface Science*, 59 (1976) 413-429.
- [58] M.P. Hyman, J.M. Vohs, Reaction of ethanol on oxidized and metallic cobalt surfaces, *Surf. Sci.* , 605 (2011) 383-389.

---

## Chapter 4

Bimetallic nickel-cobalt  
nanosized layers supported  
on polar ZnO surfaces:  
metal-support interaction  
and alloy effects studied by  
synchrotron radiation X-ray  
photoelectron

---

---

---

## **Chapter 4. Bimetallic nickel-cobalt nanosized layers supported on polar ZnO surfaces: metal-support interaction and alloy effects studied by synchrotron radiation X-ray photoelectron spectroscopy**

### **4.1 Introduction**

Zinc oxide is a wide band-gap semiconductor with a wide range of applications in photocatalysis [1-3], photovoltaics [4, 5], gas sensing [6, 7] and heterogeneous catalysis [8, 9]. It crystallizes in hexagonal wurtzite structure with Zn atoms tetrahedrally coordinated with four O atoms, such that planes of only Zn or O atoms arrange alternately along (0001) axis. This results in a net dipole moment developed along this axis with two polar ZnO(0001)-Zn and ZnO(000 $\bar{1}$ )-O surface terminations, (for brevity will be denoted as ZnO-Zn and ZnO-O respectively). Non-polar (10 $\bar{1}$ 0) surface contains equal number of O and Zn atoms on the same plane, and is energetically more stable. A (1x1) diffraction pattern from low-energy electron diffraction (LEED) should be observed on clean, un-reconstructed ZnO-Zn or ZnO-O as determined by the bulk hexagonal structure. Different stabilization mechanism has been suggested for these two surfaces [10]. Dulub et al. have observed the formation of triangular islands on Zn-terminated surface where O occupies most of the step edges [11]. They suggested that the O-termination of these islands reduces the quantity of Zn surface atoms and hence stabilizes the surface. This has been further supported by their later DFT calculations [12]. More recently honeycomb structures were found for the O-terminated ZnO surface [10]. It has been suggested that clean O-terminated surface is very difficult to achieve even in vacuum as the O atom can readily react with residual H<sub>2</sub> and H<sub>2</sub>O in the chamber, forming a hydroxyl group saturated surface. The (1x1) structure commonly observed is a result of the stabilization by this OH termination, forming a H(1x1) O-ZnO surface. The existence of adsorbed hydroxyl group on ZnO surface has been confirmed by photoelectron spectroscopy (PES), where the contribution of -OH groups is almost always visible at the higher binding energy side of the O 1s peak. With special cleaning procedure, (1x3) pattern could be observed on ZnO-O surface [13]. The presence of OH groups has an effect on the adsorption properties of ZnO-O [14]. For example, pyridine adsorption on polar ZnO surfaces has been studied by Hovel et al. [15] and they found that interaction between the lone pair electrons of N and Zn sites on ZnO-Zn is stronger and pyridine is mainly physisorbed on H-ZnO-O surface. This has reinforced the idea of the Lewis acid nature of Zn sites on ZnO-Zn, which can be analogously applied to the adsorption of other molecules such as alcohol and organic acids.

The interaction of ZnO with metal overlayers is influenced by the ZnO surface termination [16, 17]. From a general point of view, the chemical potential established across the metal/oxide interface and the transport mechanism between defects or metal and oxygen ions could create different chemical interactions such as redox reactions, or encapsulation of metal by the oxide support [18]. Redox reactions and interdiffusion of metal layers onto ZnO upon annealing have been experimentally confirmed in several cases [19-22]. In heterogeneous catalysis ZnO is used as a support for metal nanoparticles. In particular,

recent studies have shown that ZnO substrate improves conversion and selectivity of cobalt catalysts at relatively low temperatures during (bio)ethanol steam reforming reaction (ESR) [23-25]. Cobalt [25-28] as well as nickel [29, 30] have been regarded as the most promising and effective non-noble metal catalysts for ESR reaction. However, a major short-coming is their fast deactivation due to sintering [31] and surface coke formation [32, 33]. Utilization of bimetallic catalysts [34-37] and suitable metal oxide support [38-40] can enhance the catalyst stability. Homs et al. showed that addition of Ni to Co supported on ZnO improves the performance of the catalyst at low temperatures[35]. Improvement of efficiency and durability of Ni-Co has been reported also on hydrotalcite [41] and yttria-stabilized zirconia (YSZ) [42] substrates.

In this respect, we aim to investigate a model systems consisted of Ni-Co overlayer supported on well defined ZnO-O and ZnO-Zn single crystal surfaces for better understanding the metal-support interaction on a bimetallic catalyst. The sample was developed by co-evaporation of thin Ni-Co layers (in nanometer dimension) on polar ZnO surfaces and characterization was mainly performed by synchrotron-based PES. It must be stressed that despite the substantial “material gap” between the model system studied here and technical ESR catalysts, the results of this study might be used as guidance for improving the properties of ZnO-based catalysts, taking into account the substantial progress made in the synthesis of tailored ZnO nanostructures and surfaces.

## **4.2 Experimental Methods**

The preparation of Ni-Co overlayers and PES studies were conducted at the Materials Science Beamline at Elettra synchrotron light source facility in Trieste. The end station of the beamline is equipped with SPECS Phoibos 150 electron energy analyser, LEED optics, Ar<sup>+</sup> ion sputtering gun and a gas inlet system. Detailed description of the mechanical design and the beamline properties has been given elsewhere[43]. The samples were mounted on a resistively heated tantalum sample holder and the temperature was monitored with K-type thermocouple. One-side polished ZnO (0001)-Zn and ZnO(000  $\bar{1}$  )-O single crystals (10x10x0.33mm, Crystec) were cleaned by repeated cycles of Ar<sup>+</sup> sputtering and annealing at 773 K in  $1 \times 10^{-6}$  mbar O<sub>2</sub>. A (1x1) hexagonal pattern was observed by LEED on the clean ZnO surfaces for both surface terminations (*Please refer to supplementary information in appendices*). Ni-Co bimetallic layers were co-evaporated on ZnO using a commercial e-beam evaporator (Mantis Deposition Ltd). The photoemission spectra were obtained at normal emission using various photon energies (from 50 to 965 eV). In addition to synchrotron radiation, a non-monochromatic AlK $\alpha$  excitation source (1486.6 eV) was used. Ni-Co overlayers as deposited and subjected to 5 min heating in UHV or  $1 \times 10^{-6}$  mbar O<sub>2</sub> were studied. The PES measurements were taken at room temperature. The thickness of the as deposited Ni-Co, Ni and Co layers was estimated from the intensity of the Zn 3p substrate signal supposing its exponential attenuation with overlayer thickness. For the evaluation of atomic ratios between the elements, the spectra were normalized to incident photon flux (measured by a photodiode) and photoionization cross sections[44, 45]. For Ni-Co bimetallic

layers the resulting nominal thickness was 0.25 and 1.5 nm, and the Ni:Co atomic ratio was about 2.5. For reference pure monometallic layers nominal thickness of 0.1 nm was used for either Ni or Co, so as the amount of Co could be comparable in both mono and bi-metallic samples. The inelastic mean free path (IMFP) used for the calculation of Ni-Co layer thickness was obtained from TPP-2M formula[46] and the information depth presented in this work is the estimation of 3 times of the IMFP. The morphology of Ni-Co/ZnO after annealing in O<sub>2</sub> was inspected by scanning electronic microscopy (SEM) using a Jeol JSM-6700F field emission scanning electron microscope.

## 4.3 Results

### 4.3.1 Characterization of pristine polar ZnO substrates

Figure 4.1 shows the O 1s and Zn 3p core level spectra of clean ZnO-Zn and ZnO-O single crystals. The Zn3p peak could be resolved as Zn 3p<sub>3/2</sub> and Zn 3p<sub>1/2</sub> doublet. The O 1s peak is composed of two components, a major component which corresponds to the O in ZnO lattice at binding energy (B.E.) 530.7 eV for ZnO-Zn and 529.9 eV for ZnO-O [13] and a second component attributed to adsorbed hydroxyl (OH) groups at B.E.= 532.4 eV (ZnO-Zn) and 531.9 eV (ZnO-O) [47, 48]. Depth-dependent measurements of the O 1s peak using different photon energies (*Please refer to supplementary information in appendices*) confirms that OH groups are located at the outermost surface layer.

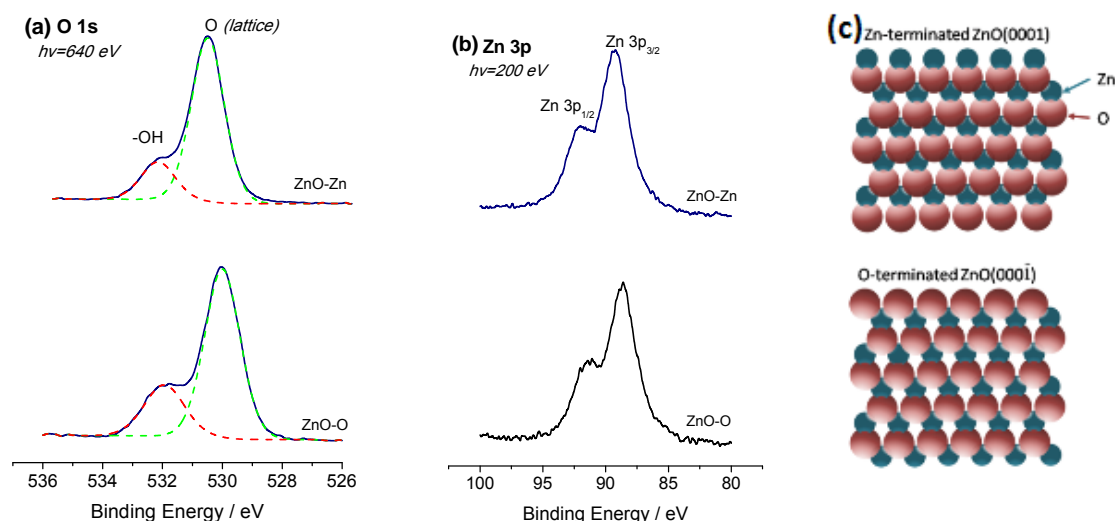


*Figure 4.1. (a) O 1s spectra of clean ZnO-O and ZnO-Zn measured with 640 eV photon energy. Constituent components, O from ZnO lattice and adsorbed OH species, are shown by the dotted line with the spectra. (b) Zn 3p spectra measured with 200 eV photon energy. (c) Schematic representation of the ideal ZnO-Zn (top) and ZnO-O (bottom) substrates.*

The B.E. difference of the O 1s peaks between ZnO-O and ZnO-Zn surfaces has also been observed by Ozawa et al. and is attributed to differences in the bulk doping of the crystals and to the different direction and magnitude of band bending at the surfaces [49]. Adsorbed

hydroxyl species have been reported before for polar ZnO surfaces prepared under UHV condition [10, 14]. Their source is either residual H<sub>2</sub> and H<sub>2</sub>O gases, traces of which are always present in UHV environment, or hydrogen diluted in the bulk of ZnO crystal that segregates and form OH species with the surface O atoms of ZnO [10, 14]. In the O 1s spectrum presented in fig. 4.1 the relative contribution of the OH groups to the total spectrum area is 25% on ZnO-O and 18% on ZnO-Zn surface. The coverage of hydroxyl species is estimated to be 0.6 and 0.4 equivalent monolayers, respectively. The Zn 3p to O 1s atomic ratio calculated from these spectra is 0.72 for ZnO-O and 0.81 for ZnO-Zn. The kinetic energy of the photoelectrons in both cases was 110 eV and the estimated analysis depth being 1.7 nm, i.e. about the first 7 surface atomic layers. Comparison between the Zn:O ratio of the two substrates confirms that Zn-terminated substrate contains relatively more Zn atoms and vice versa for O-terminated. The lower Zn:O ratio compared to the ideal ZnO stoichiometry (Zn:O=1) could be due to the surface stabilization by forming O-edge terminated islands, as proposed by Dulub et al.[12] for ZnO-Zn.

### 4.3.2 Oxidation state of Ni-Co overlayers on ZnO at room temperature

Figure 4.2 illustrates the interaction of 0.25 nm bimetallic Ni-Co with polar ZnO substrates (Zn- and O-terminated). For comparison the spectra of single metal deposition are also presented (dashed lines).

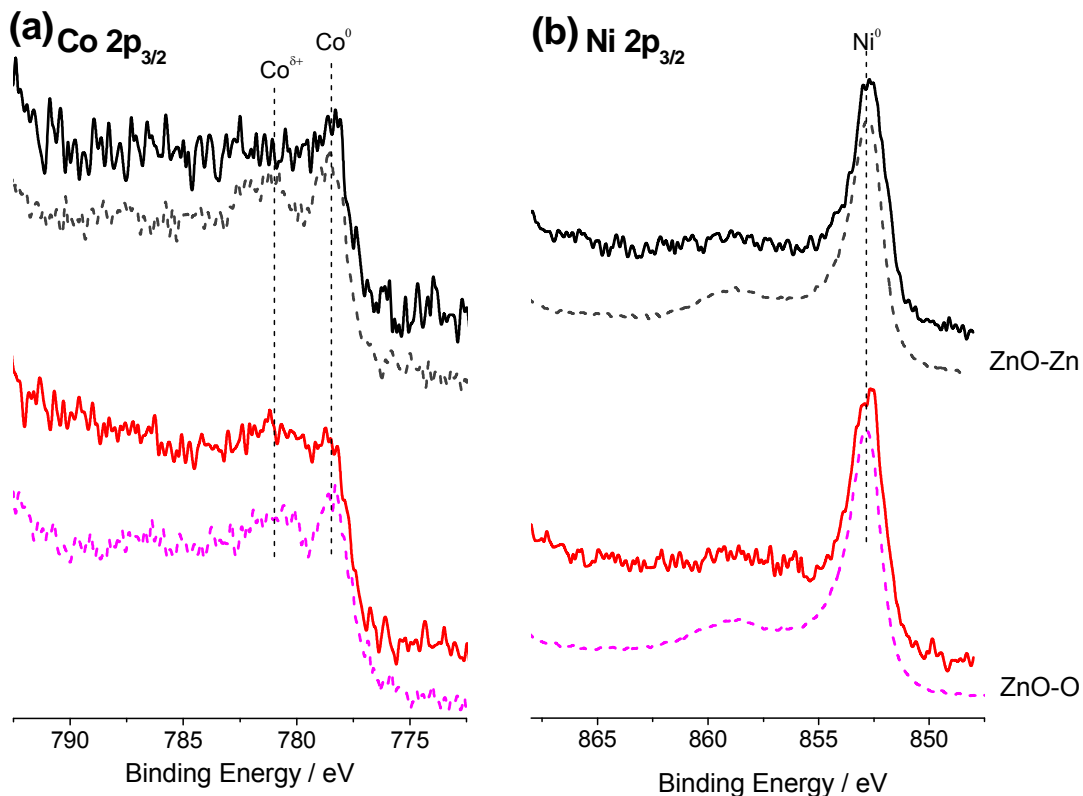


Figure 4.2. (a) Co2p<sub>3/2</sub> core level spectra of Co (dash line) and Ni-Co (solid line) deposited on ZnO-Zn (top) and ZnO-O (bottom) substrates (spectra were recorded on 0.1 (for Co) and 0.25 (for Ni-Co) nm layers using 890 eV photon energy) (b) as in (a) for Ni 2p<sub>3/2</sub> (spectra were recorded using photon energies 965 eV for Ni-Co and 1486.6 eV for Ni).

The Co2p<sub>3/2</sub> photoelectron peak (Fig. 4.2a) contains two components, metallic Co<sup>0</sup> (B.E.=778.4 eV) and ionic Co<sup>δ+</sup> (B.E.= 780.6 eV), [50] showing that cobalt is partially oxidized due to the immediate interaction with the support. The Ni 2p<sub>3/2</sub> peak of both monometallic Ni and bimetallic Ni-Co (Fig. 4.2b) at 852.6 eV is characteristic of zero valence Ni<sup>0</sup>. [50] The Co2p<sub>3/2</sub> and Ni 2p<sub>3/2</sub> photoelectron peaks recorded on monometallic and bimetallic overlayers are highly similar, indicating minor synergetic effects between the two metals. In addition, apart from a slight intensity increase of ionic Co<sup>δ+</sup> on ZnO-O supported Ni-Co, ZnO surface termination does not significantly affect the oxidation state of Ni and Co overlayers at room temperature. For higher Ni-Co deposition amount (1.5 nm) only a small portion of the overall Co 2p<sub>3/2</sub> spectrum (ca. 20%) is composed of Co<sup>δ+</sup>, whereas nickel is in the metallic

state (data not shown). This indicates that the immediate interaction of cobalt with ZnO support is influenced by the deposition amount as will be discussed in the next paragraph.

### 4.3.3 Oxidation state of Ni-Co overlayers on ZnO annealed in UHV

The Co  $2p_{3/2}$  and Ni  $2p_{3/2}$  photoelectron peaks of mono- and bi-metallic Ni-Co overlayers (0.25 nm) on ZnO recorded after annealing at 773 K in UHV are presented in Figure 4.3. The influence of the ZnO surface termination is indicated by comparing the corresponding Ni and Co photoelectron peaks recorded on each substrate (spectra presented at the top and at the bottom of each figure).

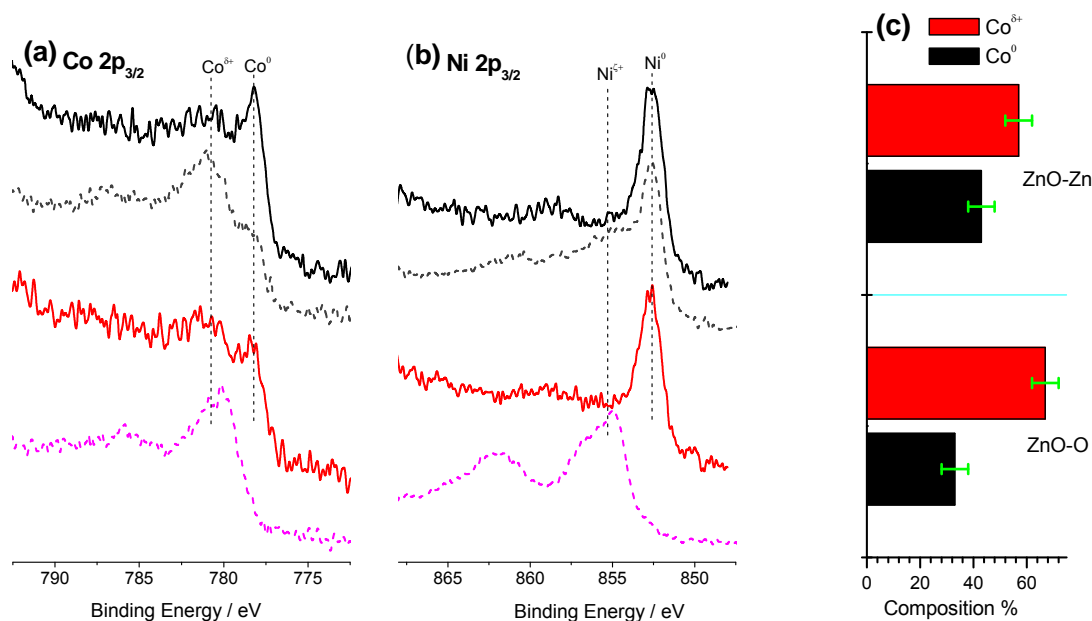


Figure 4.3. (a) Co  $2p_{3/2}$  core level spectra of Co (dash line) and Ni-Co (solid line) on ZnO-Zn (top) and ZnO-O (bottom) substrates after annealing at 773 K in UHV (spectra were recorded on 0.1 (for Co) and 0.25 (for Ni-Co) nm thick layers using 890 eV photon energy) (b) as in (a) for Ni  $2p_{3/2}$  (spectra were recorded using 965 eV and 1486.6 eV photon energies). (c) Composition of  $Co^0$  and  $Co^{2+}$  in the bimetallic Ni-Co on ZnO-Zn (top) and ZnO-O (bottom), estimated after deconvolution of Co  $2p_{3/2}$  spectrum.

For bimetallic Ni-Co layers, ionic  $Co^{\delta+}$  is evident (fig. 4.3a) and is relatively more for ZnO-O (ca. 70%) compared to ZnO-Zn (ca. 50%) substrate (fig. 4.3c). In contrast, nickel is not influenced by the support and remains as  $Ni^0$  (Fig. 4.3b). The substrate effect is much more pronounced for monometallic samples (dashed lines). In that case, cobalt and nickel supported on ZnO-O are completely transformed to CoO and NiO-like oxides [51, 52], while for ZnO-Zn the spectral components due to  $Ni^0$  and  $Co^0$  are still evident, indicating partial oxidation. Cobalt oxidation induced by annealing in UHV has been previously observed for monometallic Co deposited on ZnO-Zn [19]. By comparing the spectra of mono- and bi-metallic Ni Co layers on the same support (solid and dashed lines in fig. 4.3a and b), it is

clear that the degree of Ni and Co oxidation is influenced by synergetic effects occurring between the two metal components. In particular, bimetallic Ni-Co is more resistant to oxidation caused by interaction with the support, which might indicate weaker overlayer-support interaction.

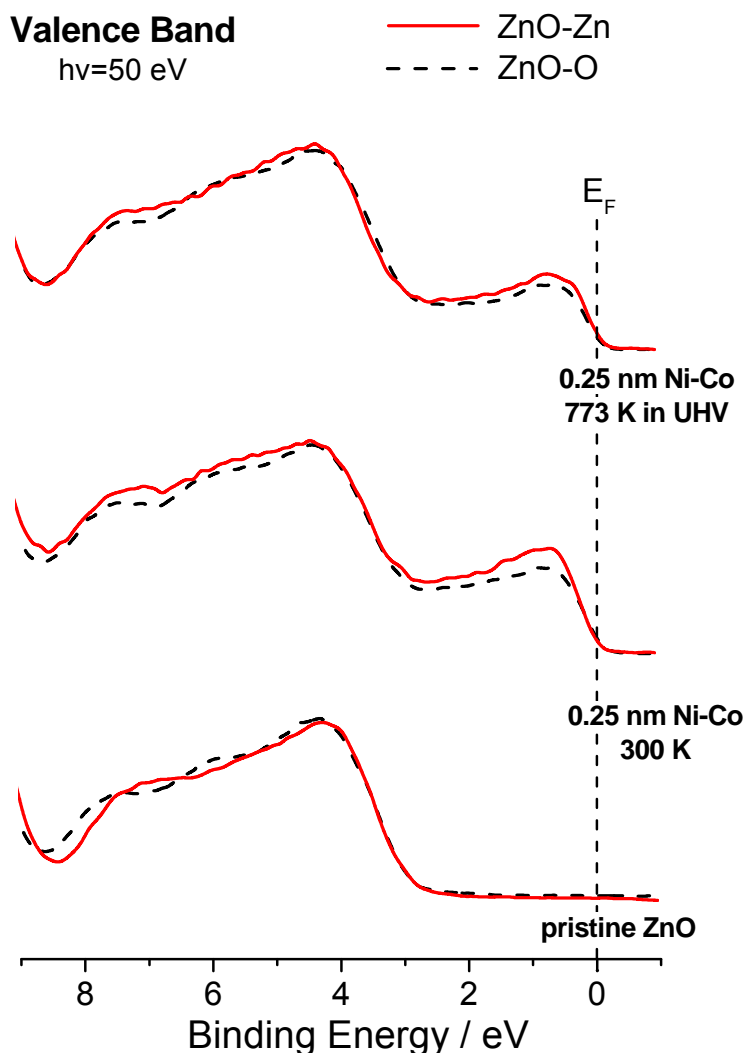


Figure 4.4. Valence band spectra of clean ZnO-O and ZnO-Zn substrates (bottom), after deposition of 0.25 nm Ni-Co at room temperature (middle) and after annealing in UHV at 773 K (top).

Figure 4.4 shows the normal emission valence band (VB) spectra recorded on clean ZnO-O and ZnO-Zn substrates (bottom spectra), following deposition of 0.25 nm Ni-Co (middle spectra) and after UHV annealing (top spectra). According to previous studies the feature located between 4-5 eV is assigned to O 2p state and the structure between 4-9eV is mainly derived from hybridized Zn 4sp-O 2p states [53]. As expected deposition of Ni-Co gives rise to 3d states at the Fermi edge, providing evidence to the metallic nature of the majority of the Ni-Co layer. This is coherent with the results observed from core level PES, where the as deposited Ni-Co layer is composed of metallic Ni and partly metallic Co. Annealing in UHV

induces a slight decrease of Ni and Co 3d states close to the Fermi edge, coherent to core level peaks observations, showing minor modifications of Ni and Co spectra. In addition, by comparing the Ni and Co 3d states on the Fermi edge (which is entirely due to metallic Ni and Co) between Zn and O terminated substrates, it could be deduced that the intensity at the FE is systematically higher on Zn-terminated substrate compared to that of O-terminated, confirming the core PES results which show higher metallic character of the deposit on Zn-polar substrate. It is also interesting to note that the VB features related to the support are not significantly affected by the deposition.

Annealing of 1.5 nm Ni-Co at 773 K in UHV does not have pronounced effect to the oxidation state of Ni or Co (data not shown). As discussed above for untreated samples, even at room temperature oxidation of cobalt is more pronounced at low coverage (0.25 nm) compared to high one (1.5 nm). The absence of pronounced oxide features at high deposition amount can be attributed either to size-dependent oxidation effect [54] or to restriction of cobalt oxidation at the interface with ZnO. In the later case for high deposition amounts the signal of ionic Co species is attenuated by metallic Co above it and therefore is much less pronounced to the overall spectrum.

#### **4.3.4 Compositional changes of Ni-Co overlayer under different annealing environments**

The influence of annealing environment (UHV or O<sub>2</sub>) to the surface composition of Ni-Co overlayers is examined by the relative intensity change of Zn, Ni, and Co 3p peaks which appear very close in the B.E. scale (Zn 3p at 89 eV, Ni 3p at 67 eV and Co 3p at 60 eV), therefore photoelectrons from practically the same information depth were collected for all elements. Due to the poor signal to noise ratio of these spectra for the 0.25 nm sample, no reliable data could be collected. Thus we focus on the analysis of 1.5 nm deposited layer.

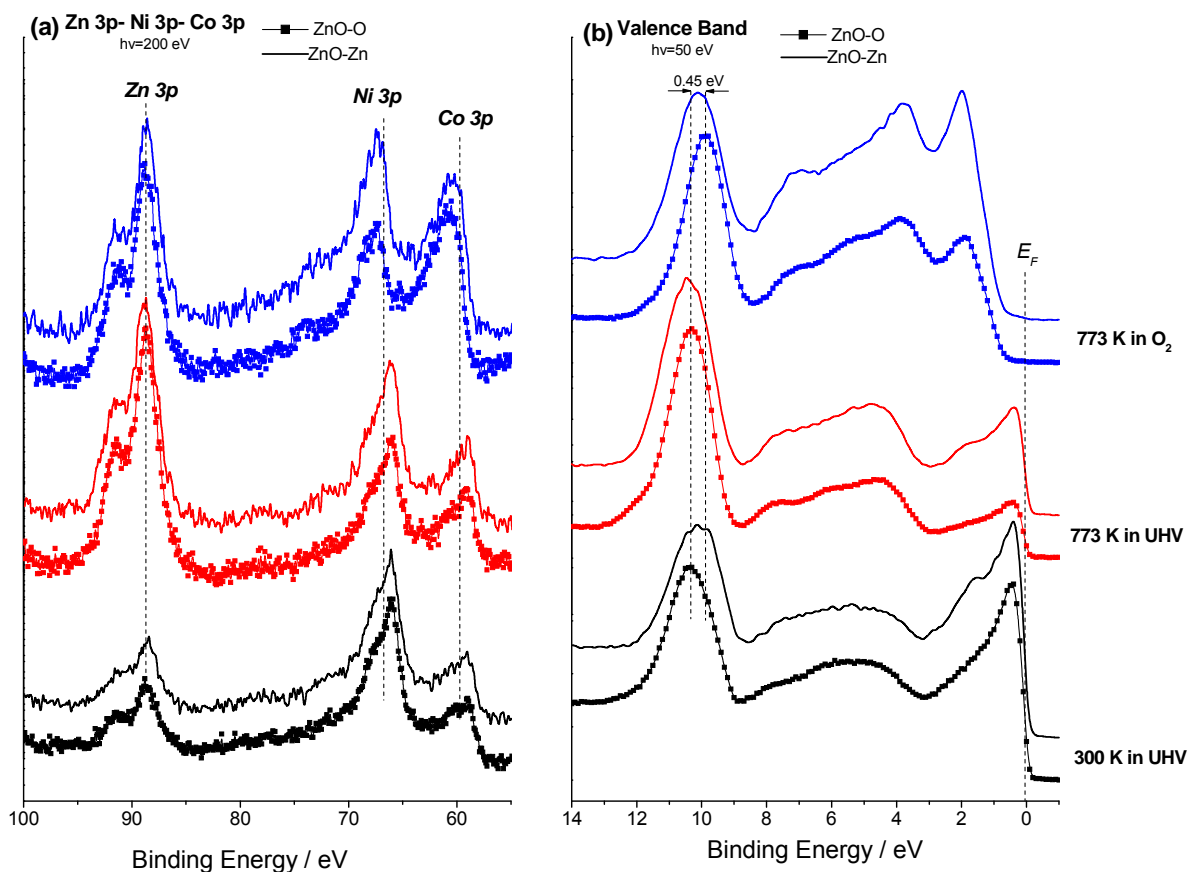
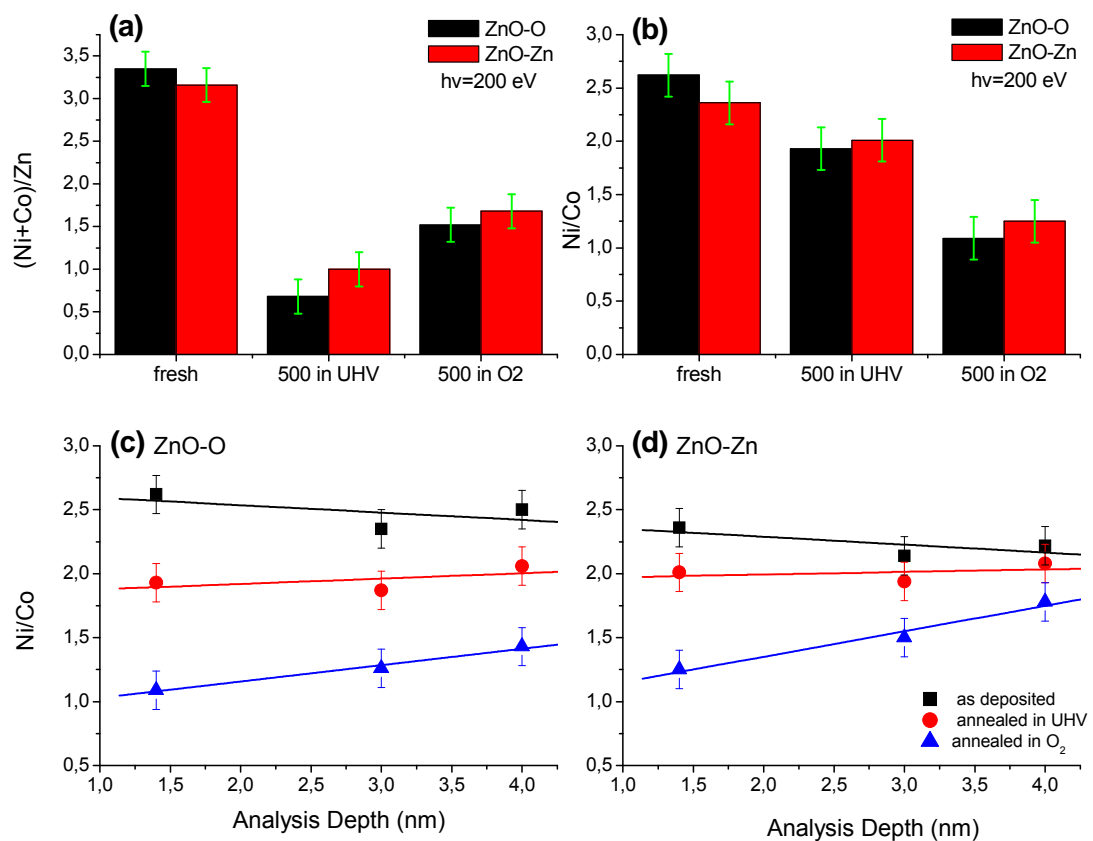


Figure 4.5. Zn, Ni, Co3p core-level (a) and valence band (b) spectra of 1.5 nm Ni-Co layer on ZnO-Zn(—) and ZnO-O(■) substrates as deposited (bottom), annealed at 773 K in UHV (middle) and after  $1 \times 10^{-6}$  mbar O<sub>2</sub> at 773 K (top).

As shown in figure 4.5 initial annealing in UHV leads to a sharp decrease of Ni-Co intensity with respect to Zn, while the Ni and Co 3p intensity partially recovers by subsequent annealing in O<sub>2</sub>. From the valence band spectra (fig. 4.5b), the appearance of intense Ni and Co 3d features at the E<sub>F</sub> confirms the metallic character of the high loading deposition, as described in the previous section. Since the information depth of photoelectron with 50 eV photon energy is around 1.5 nm, the high intensity of the Zn 3d features at about 11 eV indicates that Ni and Co do not form a dense layer over the substrate but rather arrange as particles covering only part of the support, which is typical for metallic particles on weakly interacting oxides [47]. Formation of nanosized particles is also confirmed by electron microscopy images of the post treated sample (*Please refer to supplementary information in appendices*). After annealing in UHV the metallic Ni and Co feature at the E<sub>F</sub> remains but has diminished relative to Zn 3d peak. Finally after annealing in O<sub>2</sub> the disappearance of intensity at the Fermi edge and the appearance of a new component overlapping with Zn 4sp-O 2p bands at around 2 eV is a solid confirmation for the complete oxidation of the metal overlayer [55, 56]. There is also a B.E. shift of Zn3d peak for ZnO-O after annealing in O<sub>2</sub>, which is very likely to be caused by the upward band bending at the Ni-Co oxide/ZnO-O

interface. Compared to ZnO-Zn, where the shift and thus the band bending are relatively minor, this could be an implication of an extended charge transfer at Ni-Co/ZnO-O compared to Ni-Co/ZnO-Zn interface.

A comparative quantitative analysis under various conditions is presented in fig. 4.6. The (Ni+Co)/Zn atomic ratio (fig. 4.6a) can be used as a measure of the distribution of Ni and Co on the ZnO substrate, with higher values referring to higher dispersion of Ni-Co adlayer. In addition, the Ni/Co ratio (fig. 4.6b) is used to evaluate the preferential surface segregation of the alloy constituents upon various treatments.



*Figure 4.6. Quantitative calculation based on PES core level intensities for 1.5 nm Ni-Co layer on ZnO as deposited, after annealing at 773 K in UHV and in  $1 \times 10^{-6}$  mbar O<sub>2</sub>: (a) (Ni+Co) to Zn and (b) Ni to Co atomic ratio. The Ni to Co atomic ratio a function of information depth for bimetallic Ni-Co deposited on (c) ZnO-O and (d) ZnO-Zn.*

The (Ni+Co)/Zn ratio of the as-deposited sample is very similar for both substrates, indicating that at room temperature Ni-Co distribution is not significantly influenced by the substrate termination, as also stated above. However, upon annealing in UHV the (Ni+Co)/Zn ratio drops to 20% of its initial value for ZnO-O supported Ni-Co, which is significantly larger than that observed on the ZnO-Zn substrate (30%). Subsequent annealing in  $1 \times 10^{-6}$  mbar O<sub>2</sub> partly restores (Ni+Co)/Zn ratio on both substrates, revealing the re-dispersion of Ni-Co islands over ZnO. Decrease of (Ni+Co)/Zn ratio after heating can be

explained by the Ni-Co layer agglomeration typically observed upon annealing metal overlayers on oxides [57]. However similar experimental results could also be obtained if diffusion of Ni-Co into ZnO lattice takes place (or similarly spillover of ZnO over Ni-Co), reported previously for strong metal-support interaction between metal overlayers and oxide supports, e.g. TiO<sub>2</sub> [58]. If the latter arrangement model is valid then the increase of (Ni+Co)/Zn ratio after annealing in O<sub>2</sub> can be rationalized by the re-segregation of subsurface Ni-Co back to the surface.

Focusing on the Ni/Co intensity ratio (Fig. 4.6b), the as-deposited sample is enriched in Ni, while nickel surface segregation is more pronounced on ZnO-O substrate. Upon annealing in UHV, the Ni/Co ratio decreases to 75% and 85% of the initial values for O- and Zn-terminated surface respectively, and becomes similar in both substrates. Subsequent annealing in O<sub>2</sub> induces further decrease of Ni/Co ratio (which is now close to 1) indicating surface segregation of cobalt over nickel. This is coherent to the previously observed behaviour of bulk Ni-Co system where Co surface segregation over Ni took place upon low pressure O<sub>2</sub> exposures [59].

The depth distribution between Ni and Co at different environments was characterized by Co and Ni 3p peaks measured using different photon energies of 200 eV, 620 eV and 890 eV (estimated information depth 1.4, 3 and 4 nm respectively). The Ni/Co atomic ratio for both substrates is presented in fig. 4.6c and d. Depth-dependent measurements indicate a concentration profile between Ni and Co within the overlayer. In particular, at room temperature the Ni/Co ratio decreases as deeper layers are probed, whereas after O<sub>2</sub> treatment the Ni/Co ratio increases in deeper layers. Relatively higher Ni/Co ratio observed by the more surface sensitive mode at room temperature indicates that initially Ni was segregated over Co. After annealing in O<sub>2</sub> the Ni/Co ratio shows the inverse trend, revealing the restructuring of Ni-Co islands upon O<sub>2</sub> annealing, with more cobalt (oxide) towards the surface, likely forming a Ni-core/Co-shell-like structure.

#### **4.4 Discussion**

Bimetallic Ni-Co overlayers supported on polar ZnO surfaces were investigated at room temperature and upon annealing in UHV and O<sub>2</sub> by PES. Our results indicated synergetic interaction between Ni and Co (*alloy effect*) and, to a less extent, influence of the ZnO surface termination (*support effect*), to the oxidation state of the two metals. In particular, upon UHV annealing the oxidation is hampered for bimetallic Ni-Co compared to their monometallic counterparts. The ZnO termination was found to influence more monometallic samples, especially after annealing. Generally, Ni or Co oxidation is enhanced on ZnO-O compared to ZnO-Zn substrate and this is more pronounced at lower coverage (0.25 nm). At elevated temperature the support has an effect also to the diffusion and coalescence of Ni-Co. Oxygen exposure induces total oxidation and formation of a Ni-core/Co-shell structure as indicated by depth dependent measurements. Finally, in UHV Co is relatively easier to oxidize compared to Ni for both mono- and bi- metallic samples.

#### **4.4.1 Metal-support interaction at room temperature**

Oxidation of ZnO supported metal overlayers in UHV has been previously observed for Cu on ZnO [60, 61] and Mn on ZnO-O [62] at room temperature. The interaction of Cu with the support was stronger on ZnO-O than ZnO-Zn [60, 61]. In these studies the effect of hydroxyl species, typically formed on UHV-prepared ZnO, is in general overlooked mainly due to the difficulty to resolve OH species when using laboratory-based PES. However, from other studies it is well established that metal deposition on hydroxylated oxide surfaces (e.g. Al<sub>2</sub>O<sub>3</sub>) produces an intense surface chemical reaction that also leads to laminar growth of metal overlayer. [63] From the O 1s peak of ZnO-Zn and ZnO-O surfaces shown in fig.4.1, it is evident that just before metal deposition both substrates are highly saturated with OH groups. Therefore, it is reasonable to attribute ionic cobalt (Co<sup>δ+</sup>) formation observed at room temperature (fig. 4.2), to the interaction of cobalt adatoms with surface OH groups. This picture can also explain why on ZnO-O substrate relatively higher Co<sup>δ+</sup> amount is observed in relation to the higher OH group concentration on this surface. Furthermore, since the abundance of OH groups is related to the number of exposed O atoms at the outermost surface layer, the O or Zn surface termination indirectly influences the metal-support interaction by controlling the ability of ZnO to form surface hydroxyl groups. At room temperature the (hydr)oxidation is limited at the interface between metal and support, hence is much less pronounced for higher metal loading. The resistance of nickel to oxidation might be explained by its lower affinity to hydroxyl species compared to cobalt ( $[\Delta_f G^\circ \text{Ni(OH)}_2] = -447.3 \text{ kJmol}^{-1}$ ,  $[\Delta_f G^\circ \text{Co(OH)}_2] = -454.4 \text{ kJmol}^{-1}$ ) [64], which under our conditions prevents any direct Ni oxidation. In addition, at room temperature the presence of nickel does not have any profound effect on the extent of cobalt oxidation, which is the expected behavior since Ni does not act competitively to Co in the interaction with surface OH groups.

#### **4.4.2 Thermally induced oxidation in UHV.**

Annealing-induced metal-support interaction has been reported before for Co/ZnO(0001) [19] and Cu/ZnO(10 $\bar{1}$ 0) [22]. Apart from the direct interaction at the metal/substrate interface, substitution of lattice Zn atoms by the Co ions [19] and migration of O ions from the interior of ZnO crystal [22] upon annealing, have been proposed as the overlayer oxidation mechanism. In our study, the substrate has minor effect on the oxidation state of the bimetallic Ni-Co layer at elevated temperature (please compare fig. 4.2 and 4.3). In contrast, on monometallic Ni and Co the effect of the substrate termination to the degree of metal oxidation is clearly evident, in agreement with previous observation on Cu [22] and Co [19]. Since the annealing conditions of mono- and bi-metallic samples were kept identical, kinetic phenomena related to migration of oxygen ions from the interior of the ZnO crystal towards the surface should not account for the observed difference. It is more plausible to propose that Ni-Co synergetic effects prevent the two metals from interacting with ZnO accounting for their resistance to oxidation in UHV. Significant restructuring of Ni-Co layer is induced upon UHV annealing (fig.4.6a) which can be attributed to sintering of the initially

flat Ni-Co layer via Ostwald ripening process and/or diffusion of Ni-Co into the first few atomic layers of ZnO substrate. Interestingly, the higher chemical interaction between ZnO-O substrate and Ni-Co layer (as this is proven by the higher oxidation degree of Co, fig. 4.3) does not introduce stronger adhesion at this interface, given that the Ni-Co layer undergoes even stronger segregation than that on ZnO-Zn (fig. 4.6a). As shown before, at elevated temperatures adsorbed OH groups desorb back to the gas phase [13]. One could speculate that the reorganization of the ZnO surface after OH desorption influence the density of surface defects which are likely to be involved in the surface diffusion of Ni-Co providing nucleation sites [65].

#### **4.4.3 Synergetic effects between Ni and Co in O<sub>2</sub>**

PES do not give direct evidence about the existence or not of a Ni-Co surface alloy, since the shape and binding energies of Ni and Co photoemission peaks from Ni-Co alloy are identical to those obtained for the individual metals [66]. Nevertheless, the dependence of Ni/Co ratio to the information depth (figs. 4.6c and d) as well as the dissimilarities of the oxidation state between mono and bimetallic samples observed upon annealing in UHV (fig. 4.3), are indirect indications that the Ni and Co are in close contact to each other. The Ni-Co layer is readily oxidized upon annealing in  $1 \times 10^{-6}$  mbar of oxygen followed by cobalt segregation over nickel (fig. 4.6c and d). This is in agreement with our previous study on the oxidation of polycrystalline Ni-Co foil [59], where it was shown that as Ni is coupled with Co, Ni oxidation by gas phase oxygen is suppressed [59]. Annealing in O<sub>2</sub> also introduces a redispersion effect on the Ni-Co islands (fig. 4.6a). This indicates that annealing in O<sub>2</sub> enable a better wetting effect of Ni-Co (oxides) onto the ZnO substrates. Similar redispersion effect has also been observed for monometallic copper nanoparticles supported on ZnO [67]. It was suggested that the presence of oxidizing agent may help to retain the dispersion of Cu on ZnO. We show here that this is probably a more general phenomenon of ZnO substrate, applied also to bimetallic overlayers.

#### **4.4.4 Implications in catalysis**

As stated in the introduction part bimetallic Ni-Co supported on ZnO could be utilized as a planar model system of a promising ethanol steam reforming (ESR) catalyst. It has been proposed that for ESR, Ni is more selective to methanation than Co [29, 68] and thus more prompt to coke formation, while the stability is improved when using bimetallic Ni-Co [35]. As showed here cobalt is more reactive than nickel to oxidizing species (e.g. OH groups) and therefore in oxidative atmospheres has the tendency to segregate on the surface. During ESR reaction, surface cobalt might preferentially capture oxidizing species (e.g. from water vapors in the ESR reaction stream) and provide them to nickel sites (through a bifunctional mechanism) limiting carbon deposition. Apart from carbon deposition, at elevated temperatures deactivation might be induced by total oxidation of nickel and/or cobalt due to formation of mixed oxides with the support. We showed here that oxidation is hampered for bimetallic Ni-Co (at least due to the interaction with the support) allowing nickel to maintain in the active metallic state. Loss of the active surface area (active sites) either due

to agglomeration or due to substrate-induced oxidation is connected also to lower catalytic activities. Our study indicates that when bimetallic Ni-Co overlayer is supported on ZnO-Zn substrate, both agglomeration due to Ostwald ripening (or spillover of ZnO over the metal) and metal oxidation, are limited. Taking into account the recent progress in the synthesis of tailored ZnO nanostructures, we suggest that polar Zn-terminated ZnO should be the support of choice for more active and durable reforming catalysts.

#### **4.5 Conclusions**

The metal–support interaction and alloy effects of bimetallic Ni-Co nanosized layers supported on polar ZnO surfaces, has been studied by synchrotron-based PES. At room temperature and at low metal coverage (0.25 nm), cobalt is partially oxidized while nickel remains in zero valence. When bimetallic Ni-Co layer was annealed at 773 K in UHV, the oxidation state of Ni and Co is practically unaffected, while significant agglomeration and cobalt surface segregation is observed. In contrast, monometallic Ni and Co undergo extended oxidation, which is more pronounced on ZnO-O compared to ZnO-Zn. The bimetallic layer is completely oxidized when annealed in  $1 \times 10^{-6}$  mbar  $O_2$ , followed by a significant recovery of the surface area of Ni-Co. A schematic representation of the change in Ni-Co overlayer under different annealing condition is shown in figure 4.7. A notable concentration profile of Ni-Co within the layer, with Co being more concentrated at the surface and Ni in the core, was demonstrated. Overall this work provides detailed information on how the surface oxidation state and composition of nanosized Ni-Co may be influenced by the ZnO substrate termination and metal synergetic effects, both in reducing (UHV) and oxidative ( $O_2$ ) conditions.

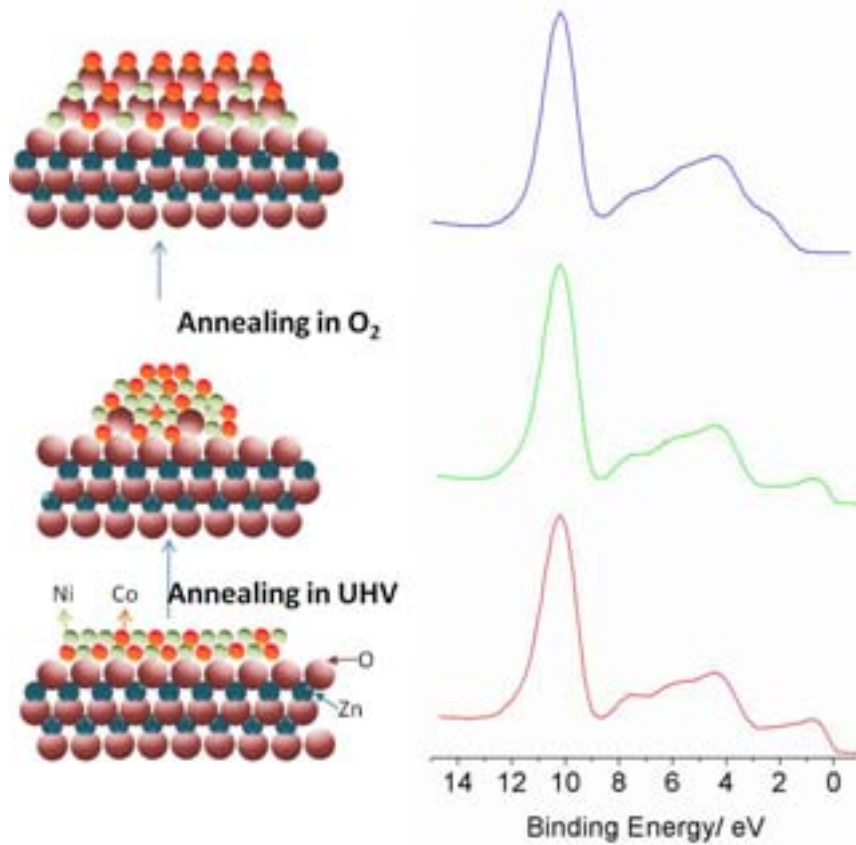


Figure 4.7 Graphical summary of the interaction of Ni-Co overlayer supported on ZnO single crystal. The Co is the as-deposited layer is partially oxidized, and Ni is mainly in metallic form. After annealing in UHV, the layer is agglomerated, lowering its surface coverage over ZnO. When it is annealed in  $O_2$ , the layer is oxidized in to NiO and CoO, with a significant surface redistribution of Ni and Co on ZnO.

## 4.6 References

- [1] K.S. Ahn, S. Shet, T. Deutsch, C.S. Jiang, Y. Yan, M. Al-Jassim, J. Turner, *Journal of Power Sources*. 176 (2008) 387-392.
- [2] X. Yang, A. Wolcott, G. Wang, A. Sobo, R.C. Fitzmorris, F. Qian, J.Z. Zhang, Y. Li, *Nano Letters*. 9 (2009) 2331-2336.
- [3] E.M.P. Steinmiller, K.S. Choi, *Proceedings of the National Academy of Sciences of the United States of America*. 106 (2009) 20633-20636.
- [4] K.S. Leschkies, R. Divakar, J. Basu, E. Enache-Pommer, J.E. Boercker, C.B. Carter, U.R. Kortshagen, D.J. Norris, E.S. Aydil, *Nano Letters*. 7 (2007) 1793-1798.
- [5] W.J.E. Beek, M.M. Wienk, M. Kemerink, X. Yang, R.A.J. Janssen, *Journal of Physical Chemistry B*. 109 (2005) 9505-9516.
- [6] Q. Wan, Q.H. Li, Y.J. Chen, T.H. Wang, X.L. He, J.P. Li, C.L. Lin, *Applied Physics Letters*. 84 (2004) 3654-3656.
- [7] J. Xu, Q. Pan, Y. Shun, Z. Tian, *Sensors and Actuators, B: Chemical*. 66 (2000) 277-279.
- [8] J. Agrell, H. Birgersson, M. Boutonnet, I. Melián-Cabrera, R.M. Navarro, J.L.G. Fierro, *Journal of Catalysis*. 219 (2003) 389-403.
- [9] L. Alejo, R. Lago, M.A. Peña, J.L.G. Fierro, *Applied Catalysis A: General*. 162 (1997) 281-297.
- [10] J.V. Lauritsen, S. Porsgaard, M.K. Rasmussen, M.C.R. Jensen, R. Bechstein, K. Meinander, B.S. Clausen, S. Helveg, R. Wahl, G. Kresse, F. Besenbacher, *ACS Nano*. 5 (2011) 5987-5994.
- [11] O. Dulub, L.A. Boatner, U. Diebold, *Surface Science*. 519 (2002) 201-217.
- [12] O. Dulub, U. Diebold, G. Kresse, *Physical Review Letters*. 90 (2003) 016102.
- [13] M. Kunat, S. Gil Girol, T. Becker, U. Burghaus, C. Wöll, *Physical Review B*. 66 (2002) 081402.
- [14] C. Wöll, *Progress in Surface Science*. 82 (2007) 55-120.
- [15] S. Hövel, C. Kolczewski, M. Wühn, J. Albers, K. Weiss, V. Staemmler, C. Wöll, *Journal of Chemical Physics*. 112 (2000) 3909-3916.
- [16] I. Hegemann, A. Schwaebe, K. Fink, *Journal of Computational Chemistry*. 29 (2008) 2302-2310.
- [17] B. Meyer, D. Marx, *Physical Review B - Condensed Matter and Materials Physics*. 69 (2004) 235420-235421-235420-235427.
- [18] Q. Fu, T. Wagner, *Surface Science Reports*. 62 (2007) 431-498.
- [19] M.P. Hyman, E. Martono, J.M. Vohs, *Journal of Physical Chemistry C*. 114 (2010) 16892-16899.
- [20] J.A. Dumont, M.C. Mugumaoderha, J. Ghijsen, S. Thiess, W. Drube, B. Walz, M. Tolkiehn, D. Novikov, F.M.F. De Groot, R. Sporken, *Journal of Physical Chemistry C*. 115 (2011) 7411-7418.
- [21] K. Ozawa, Y. Oba, K. Edamoto, *Surface Science*. 601 (2007) 3125-3132.
- [22] K. Ozawa, Y. Oba, K. Edamoto, *Surface Science*. 601 (2007) 4053-4057.
- [23] J. Llorca, N. Homs, J. Sales, J.L.G. Fierro, P.R. De La Piscina, *Journal of Catalysis*. 222 (2004) 470-480.
- [24] J. Llorca, P. Ramírez De La Piscina, J.A. Dalmon, J. Sales, N. Homs, *Applied Catalysis B: Environmental*. 43 (2003) 355-369.
- [25] J. Llorca, N. Homs, J. Sales, P. Ramírez de la Piscina, *Journal of Catalysis*. 209 (2002) 306-317.
- [26] P. Bichon, G. Haugom, H.J. Venvik, A. Holmen, E.A. Blekkan, *Topics in Catalysis* (2008) 1-8.
- [27] F. Haga, T. Nakajima, H. Miya, S. Mishima, *Catalysis Letters*. 48 (1997) 223-227.
- [28] S. Freni, S. Cavallaro, N. Mondello, L. Spadaro, F. Frusteri, *Catalysis Communications*. 4 (2003) 259-268.
- [29] A.N. Fatsikostas, X.E. Verykios, *Journal of Catalysis*. 225 (2004) 439-452.

**Chapter 4 Bimetallic nickel-cobalt nanosized layers supported on polar ZnO surfaces: metal-support interaction and alloy effects studied by synchrotron radiation X-ray photoelectron spectroscopy**

- [30]F. Frusteri, S. Freni, V. Chiodo, L. Spadaro, O. Di Blasi, G. Bonura, S. Cavallaro, *Applied Catalysis A: General*. 270 (2004) 1-7.
- [31]F. Frusteri, S. Freni, L. Spadaro, V. Chiodo, G. Bonura, S. Donato, S. Cavallaro, *Catal. Commun.* 5 (2004) 611-615.
- [32]A.M. Karim, Y. Su, J. Sun, C. Yang, J.J. Strohm, D.L. King, Y. Wang, *Applied Catalysis B: Environmental*. 96 (2010) 441-448.
- [33]S.M. De Lima, A.M. Da Silva, L.O.O. Da Costa, U.M. Graham, G. Jacobs, B.H. Davis, L.V. Mattos, F.B. Noronha, *Journal of Catalysis*. 268 (2009) 268-281.
- [34]J. Kugai, S. Velu, C. Song, *Catalysis Letters*. 101 (2005) 255-264.
- [35]N. Homs, J. Llorca, P.R. de la Piscina, *Catalysis Today*. 116 (2006) 361-366.
- [36]F.J. Mariño, E.G. Cerrella, S. Duhalde, M. Jobbagy, M.A. Laborde, *Int. J. Hydrogen Energy* 23 (1998) 1095-1101.
- [37]A. Casanovas, M. Roig, C. De Leitenburg, A. Trovarelli, J. Llorca, *International Journal of Hydrogen Energy*. 35 (2010) 7690-7698.
- [38]H. Song, U.S. Ozkan, *Journal of Catalysis*. 261 (2009) 66-74.
- [39]Z. Zhong, H. Ang, C. Choong, L. Chen, L. Huang, J. Lin, *Physical Chemistry Chemical Physics*. 11 (2009) 872-880.
- [40]S.S.Y. Lin, D.H. Kim, S.Y. Ha, *Catalysis Letters*. 122 (2008) 295-301.
- [41]L. He, H. Berntsen, E. Ochoa-Fernández, J.C. Walmsley, E.A. Blekkan, D. Chen, *Topics in Catalysis*. 52 (2009) 206-217.
- [42]C. Resini, M. Concepción Herrera Delgado, S. Presto, L.J. Alemany, P. Riani, R. Marazza, G. Ramis, G. Busca, *International Journal of Hydrogen Energy*. 33 (2008) 3728-3735.
- [43]R. Vašina, V. Kolařík, P. Doležel, M. Mynář, M. Vondráček, V. Cháb, J. Slezák, C. Comicioli, K.C. Prince, *Nuclear Instruments and Methods in Physics Research, Section A: Accelerators, Spectrometers, Detectors and Associated Equipment*. 467-468 (2001) 561-564.
- [44]J.J. Yeh, *Atomic Calculation of Photoionization Cross-sections and Asymmetry Parameters*, Gordon and Breach Science Publishers, Langhorne, PE, USA, 1993.
- [45]J.J. Yeh, I. Lindau, *Atomic Data and Nuclear Data Tables*. 32 (1985) 1-155.
- [46]S. Tanuma, C.J. Powell, D.R. Penn, *Surface and Interface Analysis*. 20 (1993) 77-89.
- [47]A. Önsten, D. Stoltz, P. Palmgren, S. Yu, M. Göthelid, U.O. Karlsson, *Journal of Physical Chemistry C*. 114 (2010) 11157-11161.
- [48]M. Valtiner, S. Borodin, G. Grundmeier, *Physical Chemistry Chemical Physics*. 9 (2007) 2406-2412.
- [49]K. Ozawa, S. Munakata, K. Edamoto, K. Mase, *Journal of Physical Chemistry C*. 115 (2011) 21843-21851.
- [50]N.S. McIntyre, M.G. Cook, *Analytical Chemistry*. 47 (1975) 2208-2213.
- [51]S.C. Petitto, E.M. Marsh, G.A. Carson, M.A. Langell, *J. Mol. Catal. A: Chem.* 281 (2008) 49-58.
- [52]M.A. Van Veenendaal, G.A. Sawatzky, *Phys. Rev. Lett.* 70 (1993) 2459-2462.
- [53]R.T. Girard, O. Tjernberg, G. Chiaia, S. Söderholm, U.O. Karlsson, C. Wigren, H. Nylén, I. Lindau, *Surface Science*. 373 (1997) 409-417.
- [54]V. Papaefthimiou, T. Dintzer, V. Dupuis, A. Tamion, F. Tournus, A. Hillion, D. Teschner, M. Hävecker, A. Knop-Gericke, R. Schlögl, S. Zafeirotos, *ACS Nano*. 5 (2011) 2182-2190.
- [55]S. Hüfner, J. Osterwalder, T. Riesterer, F. Hulliger, *Solid State Communications*. 52 (1984) 793-796.

**Chapter 4 Bimetallic nickel-cobalt nanosized layers supported on polar ZnO surfaces: metal-support interaction and alloy effects studied by synchrotron radiation X-ray photoelectron spectroscopy**

- [56]Z.X. Shen, J.W. Allen, P.A.P. Lindberg, D.S. Dessau, B.O. Wells, A. Borg, W. Ellis, J.S. Kang, S.J. Oh, I. Lindau, W.E. Spicer, *Physical Review B*. 42 (1990) 1817-1828.
- [57]C.T. Campbell, *Surface Science Reports*. 27 (1997) 1-111.
- [58]O. Dulub, W. Hebenstreit, U. Diebold, *Physical Review Letters*. 84 (2000) 3646-3649.
- [59]Y.T. Law, T. Dintzer, S. Zafeiratos, *Applied Surface Science*. 258 (2011) 1480-1487.
- [60]J. Yoshihara, J.M. Campbell, C.T. Campbell, *Surface Science*. 406 (1998) 235-245.
- [61]K.H. Ernst, A. Ludviksson, R. Zhang, J. Yoshihara, C.T. Campbell, *Physical Review B*. 47 (1993) 13782-13796.
- [62]M.C. Mugumaoderha, R. Sporken, J. Ghijsen, J.A. Dumont, *Journal of Physical Chemistry C*. 115 (2011) 20603-20609.
- [63]S.A. Chambers, T. Droubay, D.R. Jennison, T.R. Mattsson, *Science*. 297 (2002) 827-831.
- [64]J.A. Dean, *Lange's handbook of chemistry*, 15th Edition ed., McGraw-Hill, Inc., 1999.
- [65]R. Meyer, J. Lockemeyer, R. YeateS, M. Lemanski, D. Reinalda, M. Neurock, *Chem. Phys. Lett*. 449 (2007) 155-159.
- [66]G. Zhang, S. Sun, M. Bostetter, S. Poulin, E. Sacher, *Journal of Colloid and Interface Science*. 350 (2010) 16-21.
- [67]S.V. Didziulis, K.D. Butcher, S.L. Cohen, E.I. Solomon, *Journal of the American Chemical Society*. 111 (1989) 7110-7123.
- [68]M.P. Hyman, J.M. Vohs, *Surf. Sci.* . 605 (2011) 383-389.

---

## Chapter 5

Insight for ethanol steam  
reforming reaction  
pathways and  
intermediates:

Ethanol desorption on ZnO  
supported Ni-Co bimetallic  
model catalyst

---

---

---

## **Chapter 5. Insight for ethanol steam reforming reaction pathways and intermediates: Ethanol desorption on ZnO supported Ni-Co bimetallic model catalyst**

### **5.1 Introduction**

Reaction of ethanol over model catalyst is of great interest of study in catalysis. Ethanol is utilized as a biological feedstock for renewable hydrogen production by ethanol steam reforming reaction (ESR). It involves several major intermediates and by-products such as acetaldehyde, methane, ethylene and carbon monoxide. Nickel (Ni) and Cobalt (Co) are very promising transition metal catalysts [1-6] and the application of bimetallic catalyst composed of these two metals is of particular interests [7-10] for the improvement of catalytic activity and deactivation resistance. In addition Ni and Co supported on metal oxides such as ZnO show remarkable ethanol conversion efficiency and hydrogen selectivity [11, 12].

The reaction mechanism and the active role of metal oxide supported Ni and Co catalysts has been widely studied but yet still requires further understanding as the metal-support interaction changes significantly the reaction pathway. This also leads to the various results observed on different catalytic studies. In the catalytic studies of Freni et al. [13], Ni/MgO shows higher activity than Co/MgO due to the lower tendency of Ni oxidation and suppression of ethanol decomposition and CO methanation. On the other hand, the study by Bichon et al.[14] on Ni and Co supported on Al<sub>2</sub>O<sub>3</sub> shows that the amount of carbon deposition is significantly lower on Co/Al<sub>2</sub>O<sub>3</sub>. Padilla et al.[15] has investigated the major reaction intermediates involved on Co/ZrO<sub>2</sub> and Ni/ZrO<sub>2</sub> catalysts promoted with lanthana by temperature programmed reaction-desorption. They proposed that adsorbed ethanol is dehydrogenated to acetaldehyde, which undergoes different evolution mechanism on the two catalyst systems. For Co-based catalyst, reforming of acetaldehyde occurs as the major reaction, while ethylene and high amount of acetone was produced for nickel based catalyst. The catalytic activity of Ni and Co as a bimetallic working metal catalyst has been studied by Resini et al. [9]. They have shown that methane formation was reduced with the addition of Co to Ni/YSZ and hydrogen ratio at low temperature was improved. On the other hand, the studies from Chen et al. [8] has found that the addition of Co does not improve the activity of Ni catalyst (supported on Ca- $\gamma$ -Al<sub>2</sub>O<sub>3</sub> and ZrO<sub>2</sub>). Influence of the alloying of the two metals on ESR remains to be resolved.

Therefore, identification of the intermediate reactions on the surface can facilitate the determination of the desirable reaction pathway and improve catalyst design. The conversion of ethanol involves a series of intermediate reaction pathways and meta-stable intermediate species on the catalyst surface. The reaction involves several bond dissociations, i.e. C-H, C-C, O-H and C-O. The reaction of ethanol on Nickel [16, 17] and Cobalt [18, 19] single crystal or a model catalyst has been studied with surface techniques such as thermal desorption spectroscopy (TDS) and X-ray photoelectron spectroscopy (XPS).

Ni has been regarded as a catalyst efficient in C-C bond scission in ESR. It has been proposed that on Ni (111) surface C-C scission is a major ethanol decomposition pathway, generating methane as one of the major by-products[20]. The study by Hyman et al.[18] on ethanol thermal decomposition on Co (0001) has shown that acetaldehyde, CO and H<sub>2</sub> were the major decomposition products. However it still lacks other spectroscopic supports on the actual intermediates involved which can result in these decomposition products. The influence of the metal oxide support is very critical concerning the catalyst stability. ZnO is regarded as an appropriate support for ESR catalyst thanks to its mild acidity[21]. TDS studies on ZnO nanorod shows that ethanol is mainly decomposed through dehydrogenation and form acetaldehyde [22], but is not active for further decomposition. Despite its rather inert role in catalytic reaction, mobility of oxygen in metal oxide support could be an advantage in decreasing coke formation on catalyst [23-25].

Most of the studies on ethanol surface chemistry have been conducted on metal single crystals. In order to make proper correspondence to the catalytic properties of a working catalyst, thin metal film supported on well-ordered ZnO substrate would be an appropriate model system. Study of surface reaction on such model system by TDS is a direct method to obtain information on the reaction products. The objective of this work is to investigate the mechanism of ethanol adsorption and reaction over ZnO supported Ni-Co surface. A model catalyst system based on Ni-Co thin overlayer deposited on ZnO(0001)-Zn (denoted as ZnO-Zn in the following text) was developed. TDS allows us to understand the reaction intermediate and the decomposition pathway of ethanol on the model catalyst system. In order to account for the changes on the chemical composition of the Ni-Co film brought by the heating effect during TDS, XPS was used to characterize the changes of chemical status of the surface.

## **5.2 Experimental methods**

A one sided polished ZnO-Zn single crystal (10x10x0.33mm, Crystec) was used as a substrate for Ni-Co deposition. Prior to metal evaporation, the ZnO-Zn substrates were cleaned by repeated cycles of Ar<sup>+</sup> sputtering followed by annealing at 773 K in 1x10<sup>-6</sup> mbar O<sub>2</sub> until no C 1s peak intensity could be observed from XPS. Ni-Co overlayers supported on ZnO-Zn single crystal were prepared by e-beam evaporation. A commercial e-beam evaporator (QUAD-EV-C, Mantis Deposition Ltd.) was installed in the preparation chamber where the base pressure was maintained at 1x10<sup>-9</sup> mbar. Electron beams produced by tungsten filaments are targeted onto Ni and Co rods (99.995% Alfa Aesar) biased at 2000 eV. The water-cooled evaporator head is composed of 4 electrically independent pockets which can operate simultaneously for co-evaporation. The metal rod is heated and evaporates by electron bombardment. It is equipped with a manual shutter which maintains a well-timed evaporation period at a controlled evaporation flux. Integrated flux monitoring plates in each pocket allows real-time feedback of the deposition rate during evaporation.

XPS measurement was carried out in an analysis chamber (base pressure < 2x10<sup>-9</sup> mbar) equipped with a VG MicrotechClam2 electron analyser, and a non-monochromatic dual

anode (Al  $K\alpha$  and Mg  $K\alpha$ ) X-ray source. The power of Al  $K\alpha$  X-ray source was 62.5 W (12.5 kV and 5 mA) for measurement of XPS spectra. All the spectra were obtained using pass energies 20 eV. The spectra obtained were processed with background subtraction by Shirley method. The atomic ratio between elements were obtained from the corresponding peak intensity normalized by atomic sensitivity factors [26]. The composition of metallic and metal oxide components of Ni  $2p_{3/2}$  and Co  $2p_{3/2}$  was estimated by the subtraction of the metallic component based on reference spectra of bulk Ni and Co in metallic state. The mean valence of Ni and Co was obtained from the average of the oxidation state of metal and metal oxide content. The thickness of the as deposited Ni-Co, Ni and Co layers was estimated from the change in intensity of the Zn  $2p$  substrate signal after deposition supposing its exponential attenuation with overlayer thickness (Please refer to the appendice for the detailed calculation method). The Atomic Force Microscope (AFM) in contact mode (Model: RTH Technology SPM 100) was used to study the surface profile. The sample for AFM was prepared using the Ni-Co deposition procedure described above. The surface morphology of an as-deposited Ni-Co layer was compared to a sample of the same amount of Ni-Co but annealed in UHV at 623 K for 5 min.

The TDS experiments of ethanol on the ZnO-Zn supported Ni, Co and Ni-Co layer were performed in the UHV chamber same as XPS analysis. The sample was mounted on a molybdenum sample holder which could be heated at the back side by electron bombardment. The temperature was monitored with chromel/alumel thermocouple (K-type) attached on the surface of the ZnO crystal. The sample was cooled down to 125 K via a liquid nitrogen reservoir in contact with the sample holder. In order to avoid accumulation of water on the sample during cooling (originated from residual water vapour in the UHV chamber), prior to TDS experiment the sample was flash annealed to 323 K and cool down quickly before ethanol dosing. The ethanol was provided by Carlo Erba (purity 99.7%) and was subjected to several freeze-pump cycles to remove any diluted gas in the ethanol reservoir before being introduced into the vacuum chamber. Dosing was performed via a stainless steel tube (6 mm diameter) directed above the sample surface with a distance of 2 mm during dosage. A pinhole diaphragm (pin hole diameter 15  $\mu\text{m}$ ) at the end of the dosage tube was used to assure uniform exposure of ethanol vapour to the sample. In addition this system allows exposure of gases or vapour locally on the sample surface, with almost negligible gas load to the vacuum and a minimum contamination of the sample holder and the chamber walls. The pinhole doser was connected to the ethanol reservoir through a leak valve for the control of the overall gas dosing. For all exposure of ethanol in this chapter, the leak valve was kept open for a fixed time period of 10 sec. This produces saturated multilayer ethanol exposure on the sample as judged by the presence of physisorbed ethanol desorption peak.

The detection of the mass desorption signal was carried out by a computer controlled Thermo Scientific VGQ100 quadrupole residual gas analyser mass spectrometer (QMS). It is equipped with an pumped cylindrical tube ending in a cone with a hole of 1 cm with an

oblique angle of 45° at its end. Just before sample annealing and TDS spectra recording, the sample was positioned in front of the mass spec tube hole at a distance of about 1 mm. This allows an almost background-free measurement of desorption products from the sample's surface, which was not possible with a non-shielded QMS.

In a typical TDS experiment, the QMS was moved to the front of the sample surface after dosing. The sample was linearly and uniformly heated by electron bombardment. The heater is controlled by a power supply (Prevac Heat 2PS) with an integrated PID controller. The temperature, the desorbed species and the time of measurement were recorded during heating by mass spectrometry software. A linear heating rate of 1 K/s was used in TDS experiments. The following mass fragments were recorded for the identification of major ethanol decomposition products: H<sub>2</sub> (m/z=2), CH<sub>4</sub> (m/z=16), C<sub>2</sub>H<sub>4</sub>O (m/z=29), CO (m/z=28) and CO<sub>2</sub> (m/z=44). The mass to charge ratio designated for each gas corresponds to the mass fragments with the maximum intensity. The following gases: CH<sub>4</sub>, C<sub>2</sub>H<sub>4</sub>O, CO and CO<sub>2</sub> were tested individually in order to calculate the relative intensities of all the mass fragments generated from ionization at different gas pressure and to estimate the instrumental sensitivities. The following TDS signals were calculated by subtracting the contribution of mass fragments from other desorption products for overlapping signals:

*Table 5.1 Respective mass fragment generated from desorption products*

<b>Desorption products</b>	<b>Other mass fragment generated</b>
<b>CO-m/z 28</b>	m/z 16
<b>C<sub>2</sub>H<sub>4</sub>O-m/z 29</b>	m/z 16, 27, 28, 44
<b>C<sub>2</sub>H<sub>5</sub>OH-m/z 31</b>	m/z 27, 29
<b>CO<sub>2</sub>-m/z 44</b>	m/z 16, 28

Since there is a significant overlapping between the mass fragments of possible desorption products, the exact contribution of fragments to each desorption mass is critical and should be estimated as accurately as possible. For this purpose, separate calibration experiments of the QMS were performed, in which all the possible desorption products were individually introduced into the chamber and their fragmentation pattern by the VGQ100 mass spectrometer was measured.

Figure 5.1 (a) shows the relative intensity of the mass fragments for possible product of ethanol desorption. For comparison, the fragmentation pattern due to electron ionization given by the NIST database (<http://webbook.nist.gov/>) is also shown in the bar graph. It should be noted that the fragmentation pattern from NIST involves more mass fragments for the cracking of C<sub>2</sub>H<sub>5</sub>OH and C<sub>2</sub>H<sub>4</sub>O, but only the relative intensity of the fragments which coincide with masses of other possible products were shown. Figure 5.1(b) shows a characteristic example of a TDS experiment before and after fragment subtraction. Intense peak of mass signal 44(CO<sub>2</sub>) at 260 K derived from the fragment of C<sub>2</sub>H<sub>4</sub>O and the two peaks of mass 16 (CH<sub>4</sub>) at 320 K and 450 K, derived from the fragments of CO could be successfully eliminated by the subtraction process.

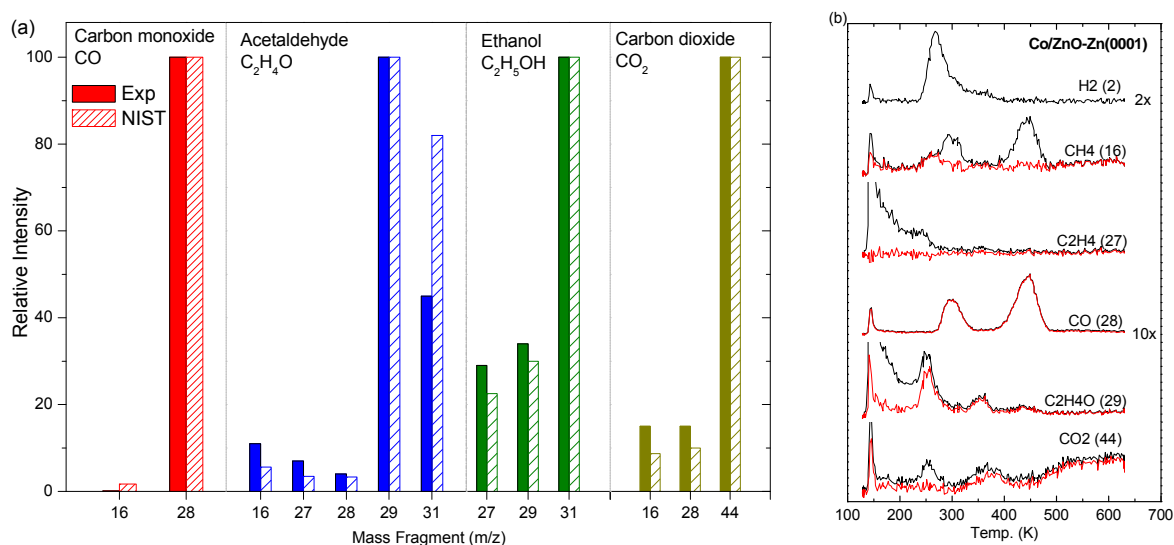


*Figure 5.1 (a) Relative intensity of mass fragment vs. main peak intensity (100%) to be subtracted for mass signal correction. Experimental values were obtained from measurement of respective gas decomposition and used for data subtraction in the spectra shown afterwards. The results were shown with the values obtained from NIST chemistry webBook [27] (b) TDS spectra of ethanol on Co/ZnO-Zn before (black) and after (red) subtraction of mass fragments*

A blank experiment of ethanol thermal desorption on an inert substrate (clean gold foil) was performed in order to estimate the impact of background gas traces to the desorption spectra. A polycrystalline gold foil was cleaned by repeated cycles of sputtering and annealing until no C 1s peak intensity was observed by XPS. The sample was subjected to an identical ethanol exposure and temperature ramping as ZnO based samples and the resultant TDS spectra were shown in Figure 5.2. Desorption of water was observed at low temperature (<150K). Desorption peaks of molecular ethanol and the decomposition products (C<sub>2</sub>H<sub>4</sub>O, CO and CO<sub>2</sub>) appear at the same maximum temperature (200 K). These products could be attributed to the cracking of ethanol by the filament of mass spectrometer. No ethanol related decomposition or cracking products was observed at higher temperature. This indicates that the QMS signal derived from processes not related to the reaction on sample (background signal) is practically negligible and all desorption peaks after fragment subtraction could be attributed to processes related to the sample's reactivity. To facilitate the presentation and comprehension of the TDS results, only QMS signal after subtraction of the fragments from other desorption products will be presented hereafter.

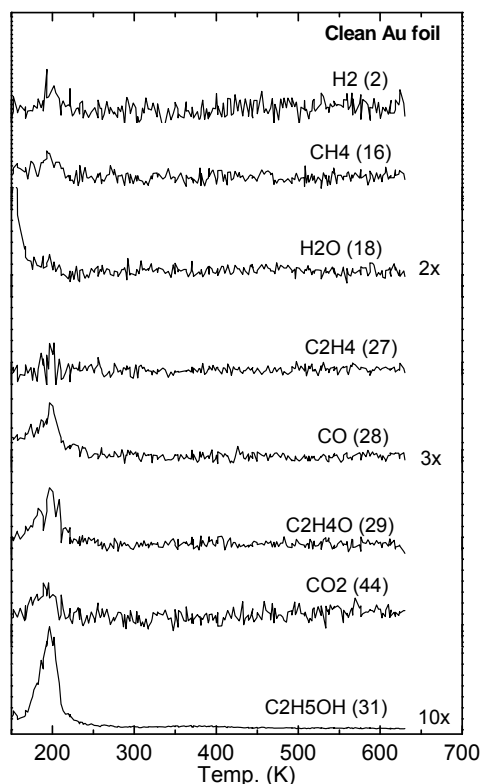


Figure 5.2 Ethanol thermal desorption spectra on Clean Au foil, after saturation ethanol exposure (reference experiment)

## 5.3 Results

### 5.3.1 Ethanol desorption from ZnO-Zn

As shown in our previous work [28], the surface of the Ni and Co metallic nanoparticles deposited on ZnO-Zn undergoes dynamic changes during thermal treatment. This involves both agglomeration of the initially planar thin film and change of its oxidation state (partial oxidation). Consequently, the availability of the active surface of the catalyst and support during ethanol desorption is influenced by the presence of several surfaces and interphases namely, ZnO single crystal, metallic Ni-Co alloy, and possibly Ni-Co oxide formed due to metal support interaction. In order to characterize the reactivity of uncovered ZnO substrate area, the surface reaction of ethanol on bare ZnO-Zn substrate was studied by TDS and the corresponding spectra of H<sub>2</sub>, CH<sub>4</sub>, H<sub>2</sub>O, C<sub>2</sub>H<sub>4</sub>, CO, C<sub>2</sub>H<sub>4</sub>O, C<sub>2</sub>H<sub>5</sub>OH, and CO<sub>2</sub>, taken from mass signal of  $m/z=2, 16, 18, 27, 28, 29, 31, 44$  respectively, were shown in Figure 5.3.

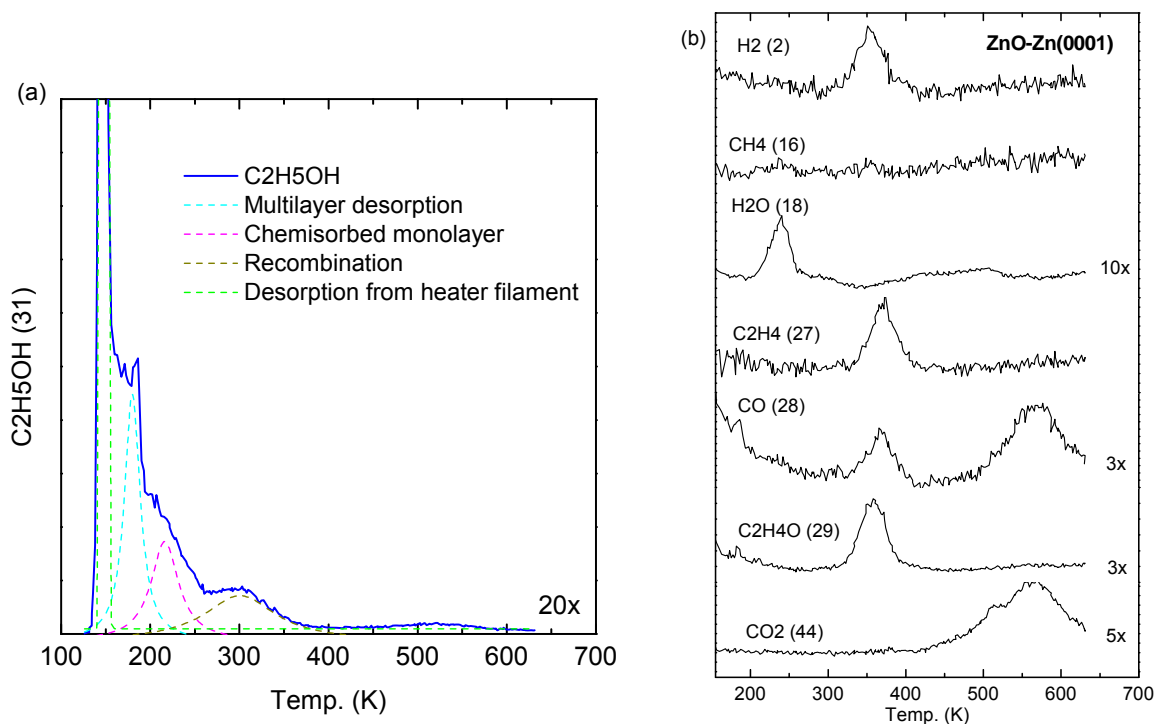
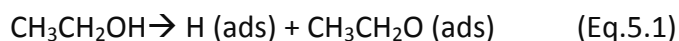


Figure 5.3 (a) Thermal desorption spectra from ethanol adsorbed on ZnO-Zn 125 K. (b) The desorption of respective decomposition products:  $H_2$  ( $m/z=2$ ),  $CH_4$  ( $m/z=16$ ),  $H_2O$  ( $m/z=18$ ),  $C_2H_4$  ( $m/z=27$ ),  $CO$  ( $m/z=28$ ),  $C_2H_4O$  ( $m/z=29$ ),  $C_2H_5OH$  ( $m/z=31$ ),  $CO_2$  ( $m/z=44$ ) were shown

The first peak of ethanol desorption from ZnO-Zn surface is observed at 173 K, which corresponds to physisorbed multi-layer ethanol. Ethanol desorption lower than this temperature should be related to ethanol desorption from the heater filament. A broader desorption peak from 200 to 260 K is from chemisorbed molecular ethanol. A 3<sup>rd</sup> peak of lower intensity is found between 260 and 380 K. This is contributed by the recombination of ethoxy group with surface hydrogen formed from dissociative adsorption of ethanol on ZnO surface. Similar recombination phenomena were observed in other studies on ZnO surface [22, 29, 30]. This has reinforced the proposition of the initial pathway of ethanol decomposition via the dehydrogenation of the –OH group, which leads to the formation of adsorbed ethoxyd group as the major intermediate [31]:



The surface ethoxy groups are consumed via the following reaction pathways:

(1) **Dehydration:** Desorption of  $H_2O$  ( $m/z$  18) and  $C_2H_4$  ( $m/z$  27 and 28) were found at 240 K and 365 K respectively. They are products from ethanol dehydration. It is triggered by the adsorption of oxygen from ethanol at the oxygen vacancy on the steps or kinks of ZnO. Surface hydroxyl groups are formed due to the scission of C-OH bond. The remaining ethyl group undergoes  $\beta$ -hydrogen elimination, resulting in desorption of ethylene. The hydroxyl group formed then interacts with hydrogen from other surface hydroxyl group or surface hydrogen and forms water. The proposed reaction scheme is given by equation (Eq. 5.2) and in the schematic representation in Figure 5.4.

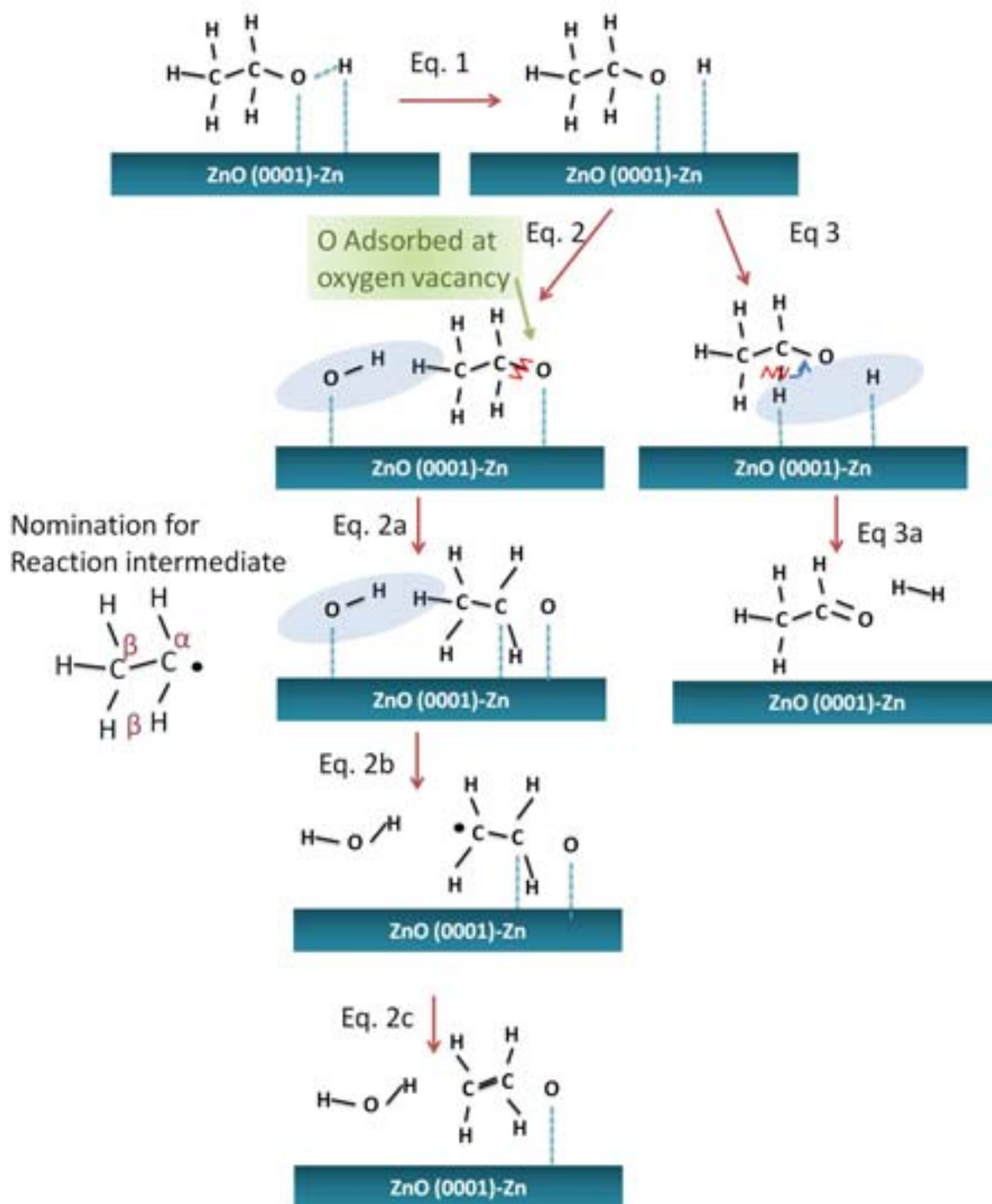
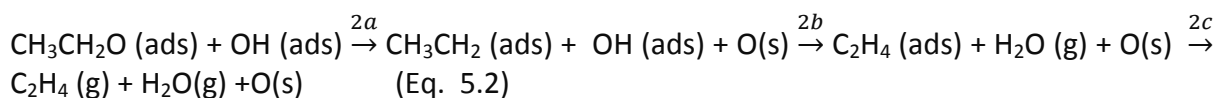
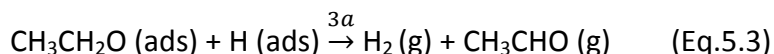


Figure 5.4 Schematic representation of the decomposition of ethanol on ZnO-Zn

(2) **Dehydrogenation:** This reaction path leads to the formation of hydrogen and acetaldehyde. The desorption peaks of  $\text{C}_2\text{H}_4\text{O}$  and  $\text{H}_2$  were observed at 358 K. Dehydrogenation by the removal of  $\alpha$ -hydrogen from the ethoxy group leads to the formation of acetaldehyde and hydrogen atom. Simultaneously, this hydrogen interacts

with surface hydrogen and desorbs as hydrogen gas molecule as shown in Eq. 5.3 and figure 5.4:

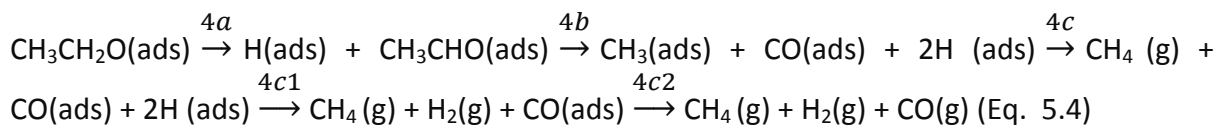


Apart from the major decomposition products described above, a CO<sub>2</sub> desorption peak is also observed at 570 K. The increase in CO<sub>2</sub> intensity extended over a wide temperature range, thus it is rather improbable that its formation is due only to a specific reaction path. Since such a peak has not been observed in the blank experiment on Au foil (see Figure 5.2) background desorption cannot be accountable for its origin. It is more appropriate to associate this desorption peak to the oxidation of surface carbonaceous species deposited at different surface sites during previous decomposition process.

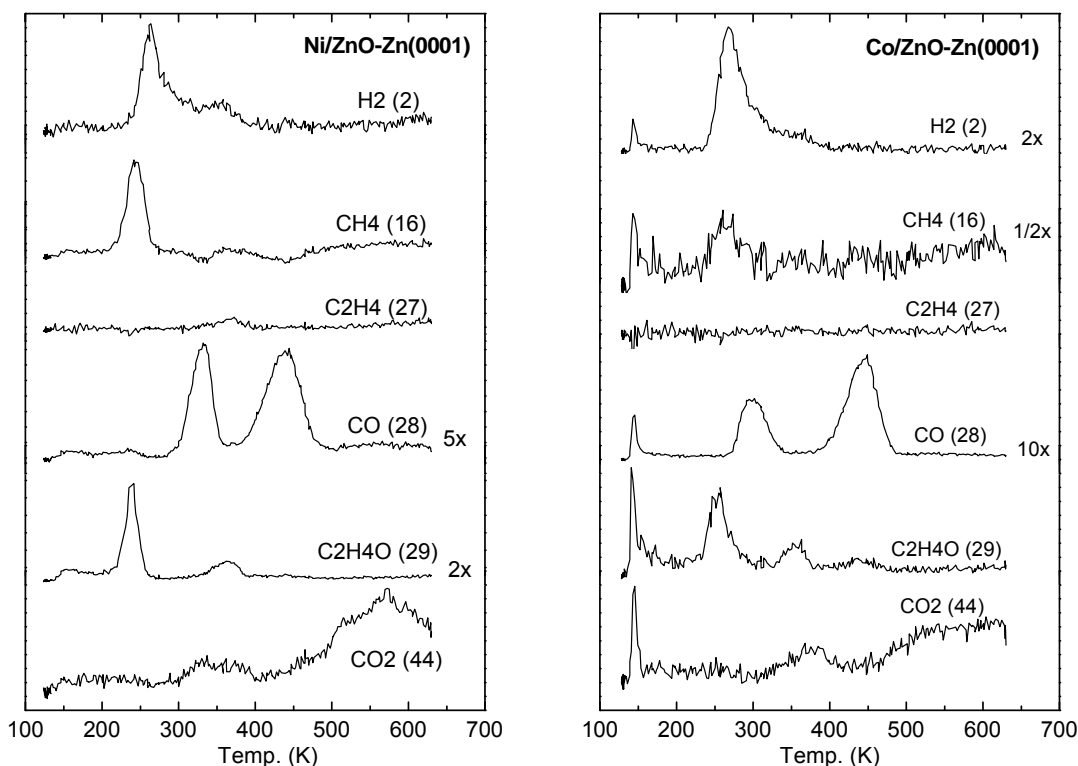
### **5.3.2 Thermal decomposition of ethanol on monometallic Ni and Co layer supported on ZnO**

Figure 5.5 shows the resulting TDS spectra from ethanol desorption on monometallic Ni and Co overlayer supported on ZnO-Zn. The nominal film thickness of Ni and Co layer is 1.3 nm and 1nm respectively as estimated by XPS. The temperature of desorption ( $T_{\text{des}}$ ) of acetaldehyde is much lower (250 K) than when ethanol is adsorbed on ZnO-Zn, indicating that Ni and Co facilitate dehydrogenation reaction (Eq. 5.3). The fact that the dehydrogenation of -O-H appears commonly as the first step in the bond decomposition sequence [16, 32, 33] could be explained by the relatively low dissociation energy barrier of CO-H bond and the relatively high stability of the remaining ethoxy group as an intermediate, as has estimated by recent theoretical studies[34]. Unlike the observations on bare ZnO-Zn substrate, ethylene desorption was not observed on Ni and Co decorated ZnO-Zn. The breaking of C-O bond of ethoxy species involves a higher energy in comparison to other bond dissociation energies and is not a preferential pathway on the Ni or Co surfaces [34]. In contrast, oxygen vacancies on ZnO substrate can facilitate C-O scission. This indicates that either ZnO substrate is completely covered by Ni and Co deposit or if not that oxygen vacancy sites on the ZnO-Zn substrate act as nucleation sites for Ni and Co deposit and therefore are no longer available as ethanol adsorption sites.

The initial step of ethanol adsorption and ethoxy species formation is the same for both ZnO-Zn supported Ni and Co. The subsequent reactions parted to different bond breaking mechanism. The 2<sup>nd</sup> decomposition product observed on Ni/ZnO-Zn is methane (243 K). The breaking of C-C bond is the key step for methane formation. Similar decomposition products have been observed for ethanol decomposition on Ni(111) single crystal[17]. In addition, formation of methane via C-C bond scission has been reported also for single crystal metal surfaces, such as Pt(111), Pt(331), Ni/Pt(111), Pd(110) and Pd(111)[35-37]. The remaining CO group desorbs at higher temperature (332 K). Surface adsorbed hydrogen from previous decomposition process recombines and is desorbed as H<sub>2</sub> at 260 K.



The hydrogen desorption peaks at 260 K is asymmetric and is extended at the higher temperature side, as surface hydrogen is generated not from a single step reaction, but from several successive processes. Surface adsorbed hydrogen is generated by the dissociative adsorption of ethanol and the dehydrogenation of ethoxy species at lower temperature. The 2<sup>nd</sup> contribution of hydrogen desorption is from the hydrogen abstraction from  $\alpha$ - carbon on the adsorbed acetaldehyde group which initiates methane formation, especially on Ni thin layers. Gates et al. [17] identified the abstraction of hydrogen of  $\alpha$ -carbon in (CH<sub>3</sub>-CHO-) group as the controlling factor of C-C bond breaking and the threshold of T<sub>des</sub> of methane on Ni (111) surface.



**Figure 5.5** TDS spectra from ethanol adsorbed on 1.2nm Ni /ZnO-Zn and Co/ZnO-Zn.

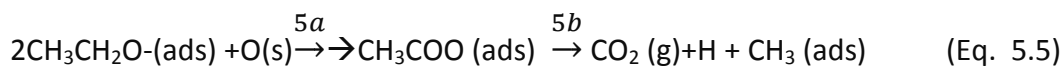
Decomposition of ethoxy group on Co/ZnO-Zn surface follows different paths relative to Ni. On Co/ZnO-Zn, the major desorption products are CO and H<sub>2</sub> and relatively low amount of methane desorption is observed. The desorption of hydrogen is found at 267 K and CO desorption peak at 294 K. C-C bond breaking results only in CO desorption in the absence of methane production. Similar ethanol decomposition products were observed for ethanol decomposition on Ru(0001)[38] and Rh(111) [32] surfaces. The study of ethanol and acetaldehyde decomposition on Rh (111) by Houtman et al.[32] has illustrated similar behaviour, where the dehydrogenation of the ethoxy group involves primarily the dehydrogenation of the methyl group instead of hydrogen abstraction of the methylene

group as on Ni surface. It was proposed that ethoxy group transforms to oxametallacycle intermediate on Rh (111) surface, where the dehydrogenated acetaldehyde is adsorbed through both the methyl C and the oxygen on metal surface. The formation of the oxametallacycle intermediate has been verified by reflection-absorption infrared spectroscopy in the work of Sturm et al. [38] on Ru (111) and by HREELS on Rh (111) [32]. The decomposition products on both metal surfaces are highly similar to those observed on Co/ZnO-Zn. The reaction products are also coherent to those observed on Co/ZnO-Zn in our study and the ethanol TDS study on Co(0001) by Hyman et al.[18], in which similar reaction mechanism was proposed. Theoretical estimation of the energy barrier of dehydrogenation of methyl group on Co is lowered than Ni[34], which also supports the proposition that dehydrogenation of the methyl group occurs mainly on Co surface in comparison to Ni.

A 2<sup>nd</sup> CO desorption peak is observed at higher temperature (ca. 450 K) on both Ni/ZnO-Zn and Co/ZnO-Zn. This 2<sup>nd</sup> CO peak has been attributed to the oxidation of surface carbonaceous species by surface oxygen in other TDS studies[18, 19]. It was proposed that the amount of 2<sup>nd</sup> CO desorption depends on the availability of surface oxygen and carbon produced by previous decomposition process[18]. The carbon and oxygen combines at higher temperatures to give CO. In the studies of Bowker et al. on ethanol oxidation on Pd (110) [39], a 2<sup>nd</sup> CO desorption is also observed in the absence of oxygen on Pd surface. They suggested that surface oxygen could be created by C-O scission, and it recombines with carbon species generated by the dehydrogenation of methyl group and desorbs later as CO. The possibility of C-O bond breaking on Co(0001) surface has been estimated in the theoretical studies of Westrate et al. [40]. It was shown that C-O scission is energetically feasible on a C<sub>x</sub>H<sub>y</sub>-O moiety, and C-O scission was observed experimentally in their studies on ethanol and propanol. The intensity of the 2<sup>nd</sup>CO desorption peak differs between metal oxide supported catalyst and pure metal catalyst [18, 41]. Lower intensity of the 2<sup>nd</sup> CO desorption peak is also observed on Co (0001)[18] compared to metal oxide supported cobalt e.g. Co/CeO<sub>2</sub>/YSZ(100)[41]. The difference could be rationalized as the oxidation of surface carbon by the oxygen generated through the reduction of CeO<sub>2</sub> to Ce<sub>2</sub>O<sub>3</sub>. It could be deduced that on ZnO supported thin film, oxygen is diffused from ZnO support (at elevated temperatures) to the thin film layer and is utilised for carbon oxidation. This is also supported by the oxidation of Ni and Co film observed from XPS after TDS. On Co surface, this surface carbon is generated mainly due to the dehydrogenation of methyl group obtained from the decomposition of oxametallacycle intermediate. Dehydrogenation of -CH<sub>2</sub>- eventually leads to the accumulation of C atoms on the surface. Though it was shown before on Ni/ZnO-Zn the methyl group tends to recombine with hydrogen and desorbs as methane, C-H bond scission is also feasible and has been proven by isotope exchange[17]. In addition, a low quantity (1-2%) of C-O group from ethanol can undergo C-O bond scission and is remained eventually as surface carbon.

The CO<sub>2</sub> desorption peak is observed at 353 K on Ni/ZnO-Zn and 375 K on Co/ZnO-Zn with relatively low intensity with respect to the high temperature CO<sub>2</sub> desorption peak at about

623 K. This suggests the possibility of oxidation of ethoxy group to CO<sub>2</sub> via the formation of carboxyl group (COO-) intermediate. The source of oxygen could come from the diffusion of O in ZnO lattice or Ni or Co oxide formed during TDS. The ethoxy intermediate transforms into carboxyl group by interaction with oxygen from the steps or kink sites of ZnO surface. The presence of COO- species has been observed in other studies by XPS [31]. This involves firstly removal of α hydrogen as shown in equation 5 (reaction 5a), followed by the formation of COO- group through the nucleophilic attack by surface O. The carboxyl group remains adsorbed and is transformed to CO<sub>2</sub> by C-C bond scission, and is liberated CO<sub>2</sub> molecules at high temperature.



The remaining methyl group could undergo dehydrogenation which eventually deposit on the surface as carbon.

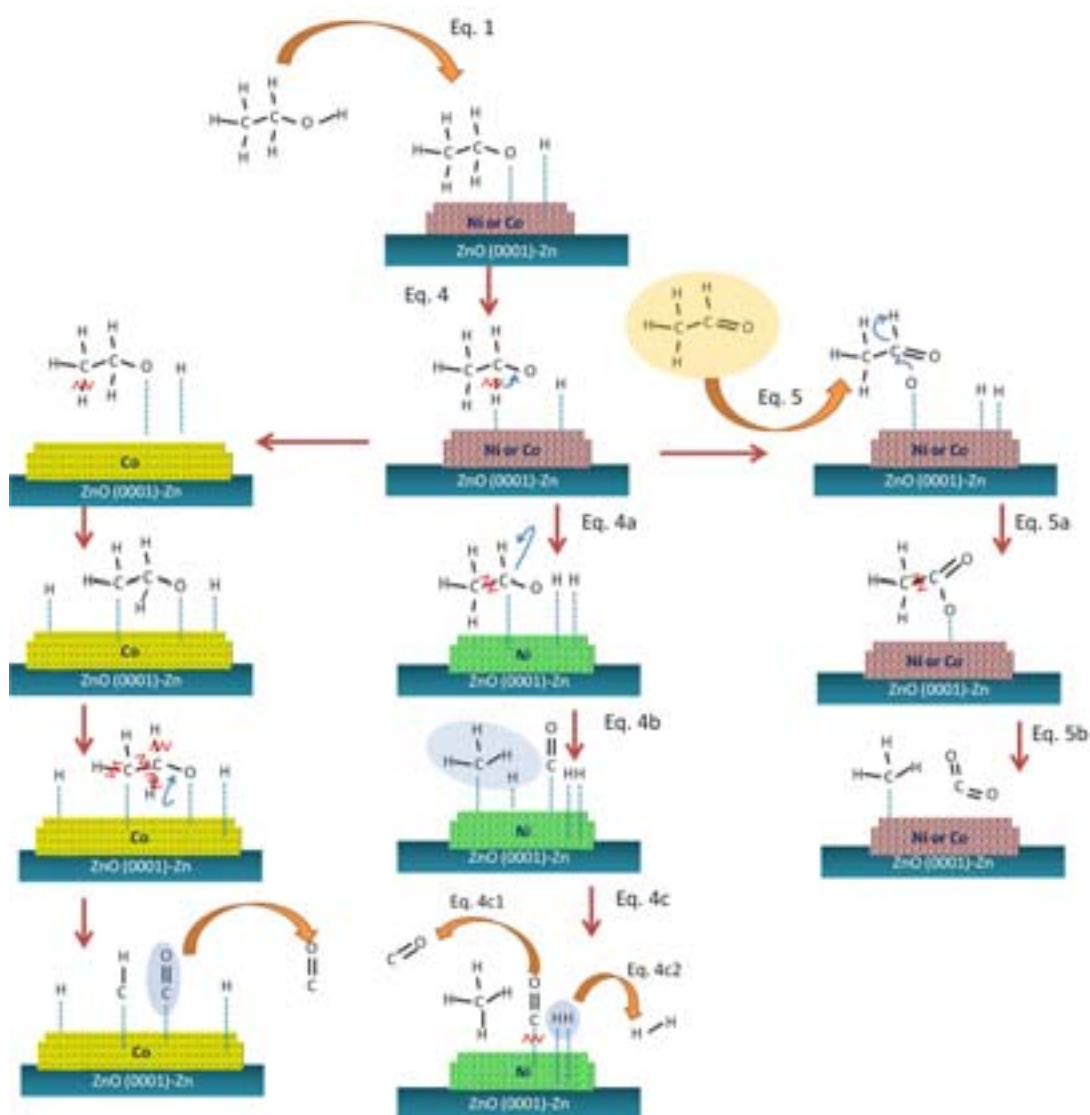


*Figure 5.6 Schematic representation of the proposed reaction mechanism of Ni and Co monometallic overlayer supported on ZnO.*

Hyman et al. [18] showed that the desorption of CO<sub>2</sub> is only observed on Co(0001) surface pre-adsorbed with O<sub>2</sub>. Similar oxidizing effect can be expected on ZnO supported Ni and Co catalyst, as thin metal layer could be oxidized by metal support interaction.

### 5.3.3 Ethanol decomposition on bimetallic Ni-Co alloy overlayer

In order to understand the behaviour of bimetallic materials on ethanol desorption for ZnO supported thin film, the TDS results from different composition of Ni-Co overlayer were compared (see table 5.2). Several Ni to Co mixing ratios were investigated, while the overall thickness of the Ni-Co layer was kept at  $1.2 \pm 0.2$ nm.

*Table 5.2. Estimated thickness of Ni, Co and Ni-Co metal layer deposited on ZnO(0001)-Zn single crystal for ethanol TDS*

<b>Metal overlayer deposited on ZnO(0001)-Zn</b>	<b>Ni:Co atomic ratio</b>	<b>Estimated thickness of the layer(nm)</b>
<b>Ni</b>	-	1.34
<b>Co</b>	-	1.02
<b>Ni-Co</b>	0.6	1.25
<b>Ni-Co</b>	1.2	1.39
<b>Ni-Co</b>	1.8	1.29

The oxidation state and the surface coverage of the Ni-Co overlayers are strongly influenced by metal support interaction and temperature, as discussed in previous chapters of this thesis. Thus, the change of the composition and metal distribution on the surface brought by TDS experiment were investigated by XPS. The bottom part of Figure 5.7 shows the Ni 2p<sub>3/2</sub> and Co 2p<sub>3/2</sub> XPS spectra of Ni-Co layers deposited on ZnO-Zn. Although the background pressure during TDS experiments never exceeded  $5 \times 10^{-8}$  mbar, in order to verify that the modifications of Ni-Co overlayer was exclusively due to the interaction with ZnO-Zn and not an effect of residual species in the UHV chamber, reference experiments were performed by Ni-Co deposition on an inert substrate. Same amount of Ni and Co were deposited under identical conditions on Au foil and heated with the same temperature program as TDS on ZnO-Zn supported samples (125K to 623 K, ramp rate= 1 K/s). In order to obtain the same amount of Ni and Co on the Au substrate as on ZnO-Zn, the ion flux for Ni-Co deposition and the deposition time were identical to the deposition of Ni-Co (1:1) overlayer on ZnO-Zn. The Ni-Co thin film on Au is of a similar thickness as those deposited on Au.

*Table 5.3 Estimated thickness of Ni, Co and Ni-Co metal deposition on Au foil*

	<b>Ni:Co atomic ratio</b>	<b>Estimated thickness of (nm)</b>
<b>Ni-Co/Au</b>	1.25	1.18

The corresponding Ni and Co 2p XPS spectra are shown at the top of Figure 5.7.

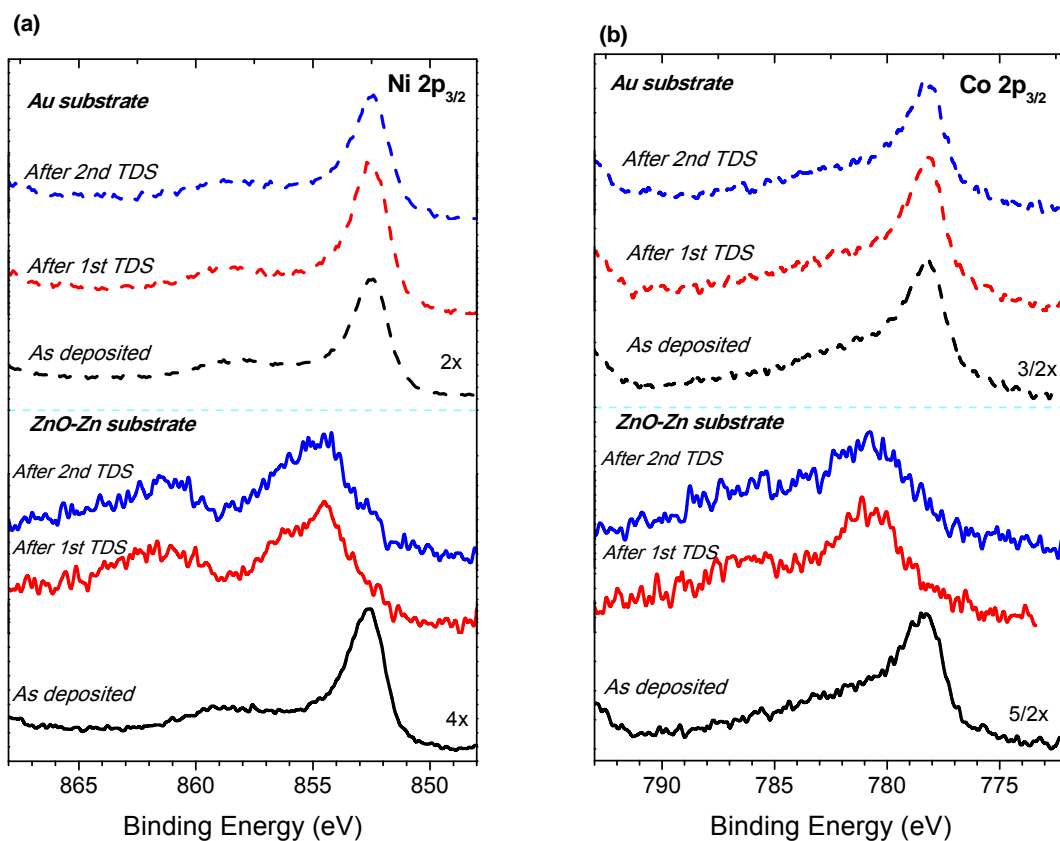
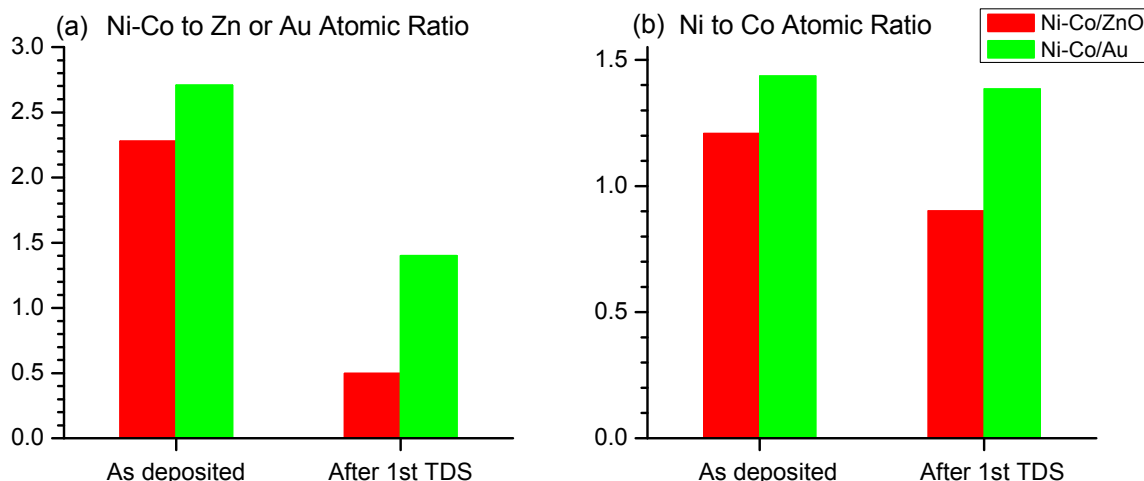


Figure 5.7 (a) Ni  $2p_{3/2}$  (b) Co  $2p_{3/2}$  spectra of 1.2nm Ni-Co layers deposited on ZnO-Zn (lower) and deposited on Gold foil. (upper)

The as deposited Ni-Co layer, is mainly in the metallic state, as indicated by the binding energy (B.E.) of the Ni  $2p_{3/2}$  at 852.7 eV[42, 43]. Similarly, the B.E. of the main peak of Co  $2p_{3/2}$  at 778.3 eV also corresponds well to characteristic B.E. of metallic cobalt. The broadening of the Co  $2p_{3/2}$  at high B.E. side is due to the formation of CoO[44, 45]. This is coherent to our previous studies (chapter 4) of a similar system [28, 46], in which oxidation of metal thin films was induced by metal support interaction. After the TDS cycles the Ni  $2p_{3/2}$  and Co  $2p_{3/2}$  photoelectron peaks are significantly modified. In particular the metallic components of both elements are largely suppressed. XPS features of nickel and cobalt oxides, with binding energy of Ni  $2p_{3/2}$  at 854.6 eV and Co  $2p_{3/2}$  at 780.6 eV peaks and their characteristic shake-up satellite structure at higher BEs, appear. This indicates that the thermal treatment imposed by TDS (maximum temperature at 623 K) induces an oxidizing effect on Ni-Co layer. In contrast to the Ni-Co layer deposited on gold, the TDS cycles have no influence to the metal oxidation state. This is proven by the Ni and Co  $2p_{3/2}$  photoelectron spectra which retain their metallic state even after 2 TDS treatment. This is solid evidence that Ni and Co oxidation is solely an effect of the ZnO support, probably due to the effective spillover of oxygen from ZnO to the Ni-Co layer. The reference experiment on Au substrate also shows that the surface reaction of ethanol during the TDS treatment does not cause any major change in the oxidation state of NiCo the adlayer.

In chapter 4, it has been shown that significant agglomeration of Ni-Co on ZnO occurs after annealing [28]. The change of surface coverage of Ni-Co after TDS is assessed by the surface atomic ratio of Ni-Co to Zn calculated from the corresponding XPS peak intensity. In Figure 5.8 Ni-Co atomic ratio on ZnO are shown with that on Au substrate. It should be noted that qualitatively similar results were found for all other Ni-Co mixing ratio, but for clarity only the layer with Ni:Co ratio 1.2 is presented.



*Figure 5.8 The atomic ratio of (a) Ni, Co and Ni-Co overlayer to Zn or Au and (b) the atomic ratio of Ni to Co. Ni-Co thin layer of thickness about 1.2 nm was deposited on ZnO-Zn and Au. The ratio shown refers to an as-deposited layer and the sample after TDS treatment*

The drop in Ni-Co to Zn atomic ratio represents a decrease in the surface coverage of the monometallic and bimetallic layers after TDS for Ni-Co. Agglomeration of the Ni-Co film into particles on ZnO surface is probable as the materials were heated briefly during TDS (623 K). In addition, after TDS, the metal overlayers are heavily oxidized, showing that migration of oxygen from ZnO-Zn to Ni-Co is facilitated at high temperature. The surface atomic ratio of the bimetallic layers has decreased by 80% after TDS experiment (Figure 5.8a).

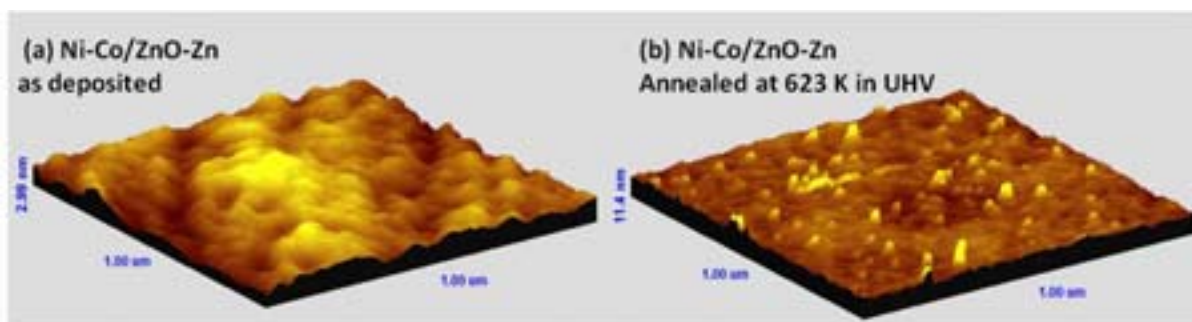


*Figure 5.9 AFM images of 1nm of Ni-Co(Ni:Co ratio =0.95) overlayers supported on ZnO-Zn substrate (a) as deposited Ni-Co thin layer (b)Ni-Co thin layer annealed in UHV at 623 K*

The change in surface morphology of Ni-Co/ZnO-Zn upon heating has been studied by AFM. The corresponding images were shown in Figure 5.9. The images were recorded from an area of 1um x 1um at the center of the sample. The amplitude of height variation of Ni-Co

layer has increased after annealing. Some high-thickness cluster-like structure scatters over the sample surface on the annealed sample. This corresponds well to the finding of XPS, Ni-Co layer agglomerates into cluster structure after annealing.

The agglomeration of Ni-Co layer caused by the annealing from TDS up to 623 K leads to the re-exposure of ZnO surface and the reduction of Ni-Co surface area. In addition to agglomeration, the decrease of the Ni:Co atomic ratio (Figure 5.8b) indicates that the Ni-Co overlayer composition has also changed by surface enrichment of Co over Ni. Upon flash annealing during the TDS cycle, the interaction of the bimetallic overlayer with ZnO substrate leads to the agglomeration and oxidation of Ni-Co thin film, and surface enrichment of cobalt in the agglomerates.

In the comparison experiment conducted on Ni-Co/Au, the decrease in Ni-Co surface coverage after TDS, not as high as thin layers on ZnO-Zn (45% instead of 80 %) (Figure 5.8a). Taking into account that Au is an inert substrate, and ZnO induces a stronger metal/support interaction (as proven by metal oxidation), one should expect the reverse trend, namely extended high level of agglomeration and drop of Ni-Co coverage on Au substrate. This discrepancy can be explained by two surface arrangement models: (i) large 3D NiCo particles are formed on Au just after deposition compared to 2D film on ZnO, which induces much less agglomeration effect and/or (ii) on ZnO substrate the reduction of NiCo coverage is not only the effect of agglomeration, but also the spillover of ZnOx which further contributes to the reduction of NiCo XPS signal. In addition, there is almost no change in the Ni to Co ratio after TDS on Au substrate (Figure 5.8b). This is a clear evidence that surface segregation of Co over Ni is driven by the difference in the rate of oxidation of the two metals and is not due to kinetic limitation imposed by the low deposition temperature (300 K).

After ethanol desorption, no surface carbon was observed by XPS on ZnO supported Ni-Co layer. As previously observed from monometallic Ni and Co/ZnO, oxidation of carbonaceous species by lattice oxygen from ZnO takes place at high temperature. This shows that the oxidizing effect could remove surface carbonaceous species to a level lower than the detection limit of XPS. A very low level of C was observed on Au supported Ni-Co layer. This comparison indicates that there is an efficient transfer of oxygen from ZnO to the metal layer and the surface Ni-Co, which produces a strong oxidizing effect that leads to metal oxidation and carbon oxidation.

Figure 5.10 shows the desorption spectra of the decomposition product of ethanol on 1.4 nm of Ni-Co layer on ZnO-Zn. The major decomposition products are H<sub>2</sub>, CH<sub>4</sub>, CO, C<sub>2</sub>H<sub>4</sub>O and CO<sub>2</sub>. Acetaldehyde, which desorbs at 242 K, is the first decomposition product observed. The first step of ethanol decomposition on Ni-Co/ZnO-Zn is equivalent to monometallic Ni and Co/ZnO-Zn (reaction 1 and 3), in which ethoxide formation takes place by the breaking of O-H bond and acetaldehyde forms through  $\alpha$ -hydrogen elimination. The subsequent decomposition of ethoxy group leads to the formation of methane, which desorbs at 243 K, H<sub>2</sub> (desorbs at 258 K) and CO (desorbs at 312 and 440 K). The desorption of methane indicates that the formation of methyl group via decarbonylation of ethoxy group [47] has

taken place, as for the decomposition of ethanol on Ni/ZnO-Zn. As this is not the preferential pathway for Co/ZnO-Zn, desorption of methane demonstrates clearly the influence of Ni in dominating the selectivity of the reaction pathway of the Ni-Co bimetallic layer. The subsequent desorption of H<sub>2</sub> and CO should contain also the contribution from decomposition via C-C scission as on monometallic Ni/ZnO-Zn (described previously in eq. 5.5).

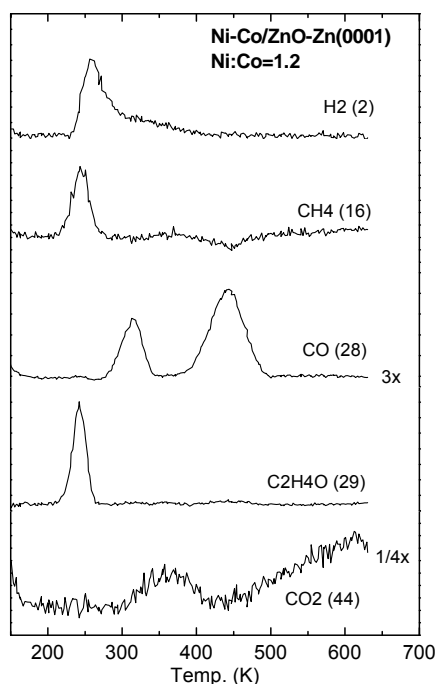


*Figure 5.10 TDS spectra of decomposition products from ethanol adsorbed on Ni-Co/ZnO-Zn (Ni:Co atomic ratio =1.2)*

It is however more difficult to distinguish the effect of the addition of Co to ethanol decomposition, as the major products CO and H<sub>2</sub>, also desorbs in the same temperature range. The desorption products observed on Ni-Co/ZnO-Zn with different Ni-Co composition are highly similar. Hence one could expect that the reaction pathways of ethanol on Ni-Co alloy thin layer are highly comparable at all Ni-Co composition and should be composed of the major ethanol decomposition mechanism as described previously for monometallic Ni and Co overlayer on ZnO. The major decomposition products from the 5 different composition of Ni-Co thin film are compared and shown in the following section in order to distinguish the correlation of Ni and Co composition to the selectivity and the reaction mechanism.

#### **5.3.4 Desorption products of ethanol on Ni-Co/ZnO-Zn of different Ni:Co ratio**

Though different reaction pathways are involved, CO, H<sub>2</sub>, and C<sub>2</sub>H<sub>4</sub>O are the common decomposition products on both Ni/ZnO and Co/ZnO. The major difference of ethanol decomposition pathway between Ni/ZnO-Zn and Co/ZnO-Zn is the more pronounced formation of methane on Ni/ZnO-Zn. The desorption spectra of C<sub>2</sub>H<sub>4</sub>O (m/z= 29), H<sub>2</sub> (m/z=2), CO (m/z=28) and CH<sub>4</sub> (m/z=16) for samples with different Ni-Co composition are

compared in Figure 5.11 and Figure 5.12 respectively. Ethoxy group formation and acetaldehyde desorption are the primary and common reaction pathways of ethanol decomposition on both monometallic Ni and Co layer. The high level of coherence of the primary desorption products, acetaldehyde and hydrogen, shows that there is no deviation of the initial activation of ethanol surface reaction on monometallic or bimetallic Ni-Co layer.

There is an additional desorption peak of  $C_2H_4O$  with lower intensity at 350 K on Co/ZnO-Zn and Ni-Co/ZnO-Zn (Ni:Co=0.6), which coincides with the  $T_{des}$  found on bare ZnO-Zn (see Figure 5.3 b). Therefore the second desorption peak at 350 K could be assigned to the minor adsorption of ethanol on exposed ZnO substrate. The main hydrogen desorption peak (264 K) is asymmetric and a broad extension of the peak is observed from 200 to 400 K. On both Ni and Co/ZnO-Zn metal layer, hydrogen desorption is primarily the result of ethanol O-H group dehydrogenation and ethoxy group dehydrogenation. Additional dehydrogenation process of methyl group occurs mainly on Co/ZnO-Zn. These sequential dehydrogenation process could contribute to the wide  $H_2$  desorption peak on bimetallic Ni-Co layer.

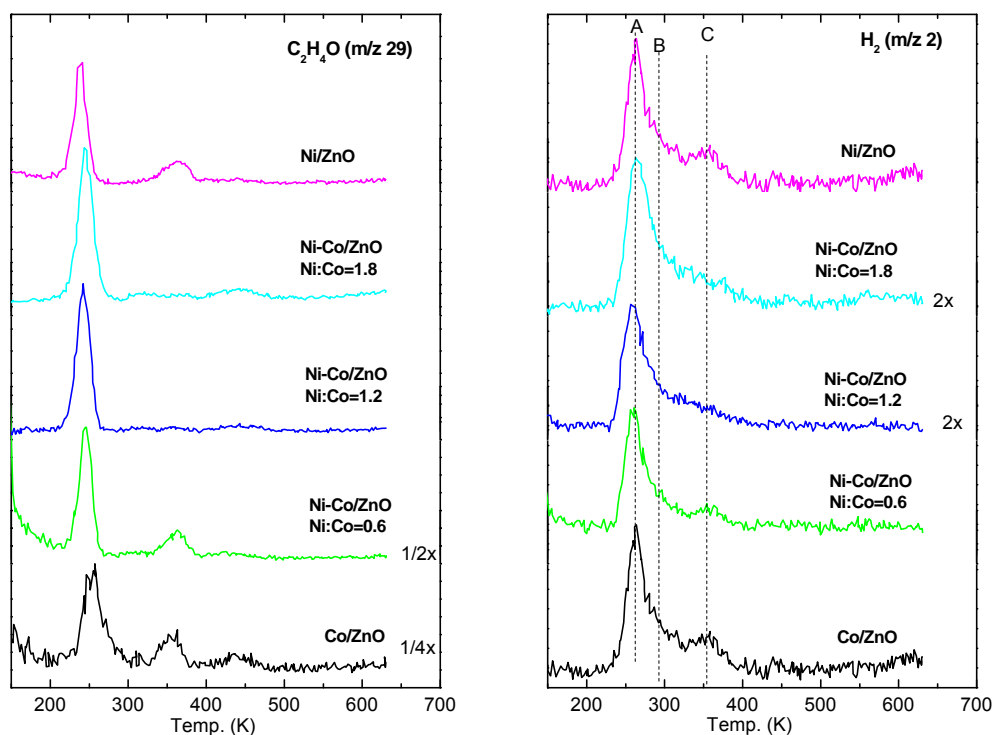


Figure 5.11 (left) TDS of  $C_2H_4O$  ( $m/z$  29, left) and  $H_2$  ( $m/z$  2, right) resulted from ethanol decomposition on Ni and Co layer on ZnO-Zn of composition Ni:Co=0, 0.6, 1.2, 1.8 and pure Ni/ZnO-Zn.

As shown in figure 5.12, desorption of  $CH_4$  on Co/ZnO-Zn is rather minor in comparison to Ni containing layer. Thus Co should play a relatively minor role in the generation of methane in the bimetallic Ni-Co layer. The substantial methane desorption observed for Ni-containing layers should be a consequence of the presence of Ni. The correlation of CO and  $CH_4$

desorption is important for clarifying the influence of bimetallic interaction to the decomposition of the reaction intermediate ethoxy group. Shown in Figure 5.5 and Figure 5.10, there is a clear difference in the  $T_{des}$  between  $CH_4$  and CO. In particular the  $T_{des}$  of  $CH_4$  is at about 250 K for all samples, which is much lower than the  $T_{des}$  of CO which appears above 300 K. Formation of adsorbed methyl and CO groups is induced from the same single step of C-C bond scission. The difference in  $T_{des}$  ( $CH_4$ ) and  $T_{des}$  (CO) shows that after C-C bond scission,  $CH_4$  desorbs immediately while CO group remains adsorbed on the surface and desorbs at higher temperature. This suggests that desorption of CO is likely to be affected by the bond strength between CO and the metal surface. Higher  $T_{des}$  (CO) represents stronger CO/metal bond strength. A 2<sup>nd</sup> and broader CO desorption peak is found at 450 K. As mentioned before, this is likely to be caused by the oxidation of the carbon species on the catalyst surface by lattice oxygen from the substrate. High temperature enhances ZnO lattice oxygen diffusion and facilitates the production of CO and desorption of a 2<sup>nd</sup> peak. Since oxygen diffusion depends mainly on the substrate, there is no pronounced difference between different Ni-Co ratios.

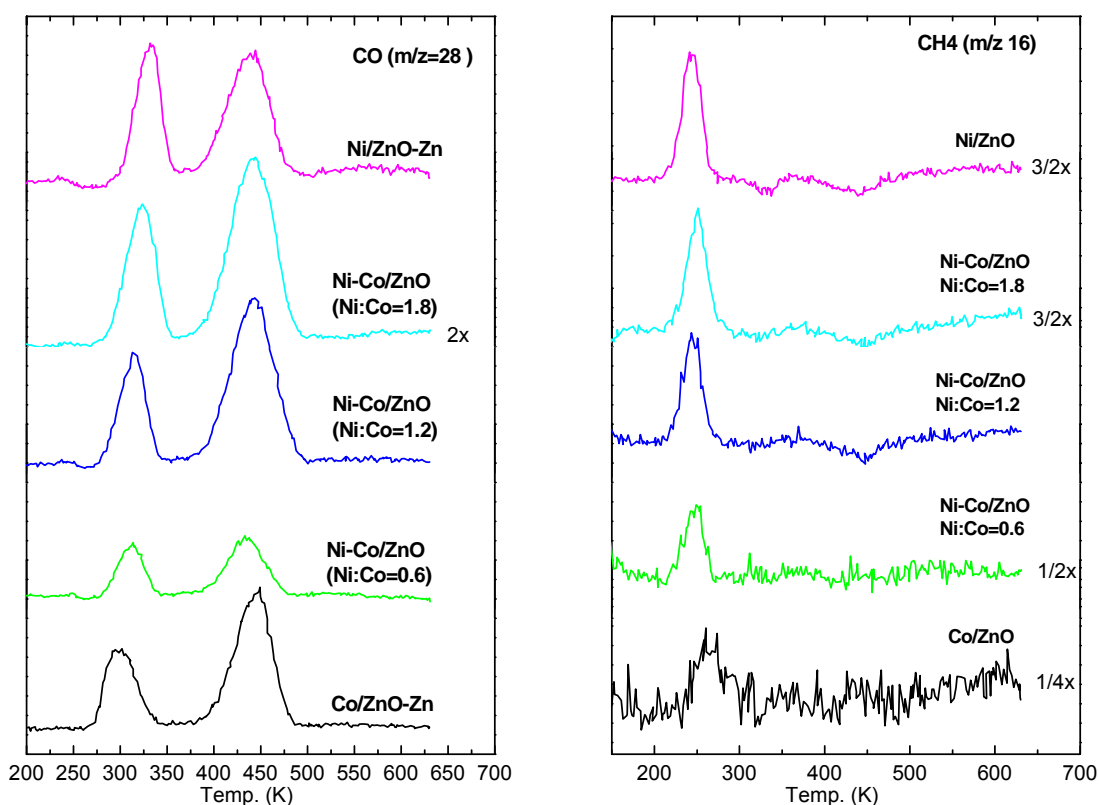


Figure 5.12. TDS of CO ( $m/z$  28, right) and  $CH_4$  ( $m/z$ 16, left) resulted from ethanol decomposition on Ni and Co layer on ZnO-Zn of composition Ni:Co=0, 0.6, 1.2, 1.8 and pure Ni /ZO-Zn

The  $T_{des}$  of acetaldehyde and 1<sup>st</sup> CO desorption peak for layers of all Ni-Co surface composition were compared in Figure 5.12. The  $T_{des}$  of  $C_2H_4O$  on Ni-Co/ZnO-Zn does not deviate significantly from that on monometallic Ni/ZnO-Zn. However compared to Co/ZnO-

Zn, the  $T_{des}$  of Ni-Co/ZnO and monometallic Ni/ZnO-Zn is lower by 10 K. The proximity of the temperature of bimetallic Ni-Co layer with monometallic Ni overlayer indicates that Ni exerts a dominating influence at this step. This can be rationalized either by preferential adsorption on ethanol on Ni surface sites, or simply by segregation of nickel over cobalt on the as-deposited surface. Whichever case it is, the intermixing of Co to Ni does not induce significant electronic effect in the two metals that could influence the adsorption strength of  $C_2H_4O$ .

On the other hand there is about 30 K difference between the  $T_{des}$  of CO on Ni and Co. The  $T_{des}$  of CO increases linearly to higher temperature with increasing Ni content. The adsorption energy of CO on Ni and Co single crystal surface has been estimated by DFT calculation[48], and the adsorption energy of CO on Co(0001) more positive than Ni (111):

Table 5.4 Adsorption energy of CO on Ni and Co single crystal of different adsorption site estimated by DFT[48]

	Adsorption energy (eV)	
	Hollow fcc	Hollow hcp
<b>Co(0001)</b>	-1.38	-1.39
<b>Ni(111)</b>	-1.59	-1.62

The decrease in adsorption energy of CO on Ni (111) by the addition of Co has also been estimated from theoretical calculations by Liu et al [49]. The linear change of  $T_{des}$  of the 1<sup>st</sup> CO peak could correspond to the weakening of CO bond to Ni-Co as Co content increase in the layer. The difference between the trend of the CO and  $C_2H_4O$  indicates that the two reaction intermediates probably involve different surface adsorption sites. Therefore the synergistic effect between the two metals affects preferentially desorption certain products.

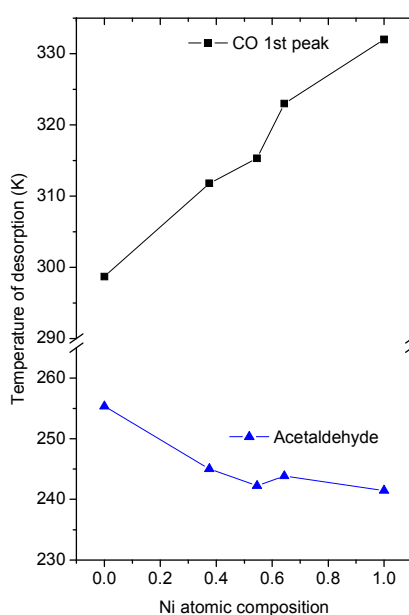


Figure 5.13.  $T_{des}$  of acetaldehyde and 1st CO desorption peak on Ni-Co/ZnO-Zn of various Ni composition.

### 5.3.5 Susceptibility to Carbon formation

The desorption spectra of CO<sub>2</sub> (m/z 44) is shown in figure 5.14. A broad desorption peak with relatively low intensity is observed at 368 K on all metal layers. As illustrated previously CO<sub>2</sub> could be generated from the decomposition of acetate, formed by the oxidation of ethoxy group. As shown in Figure 5.7, Ni and Co oxides are formed during TDS due to metal support interaction, and this could be the source of oxygen for this reaction. Above 450 K, the CO<sub>2</sub> intensity undergoes a gradual increase with temperature notably on Ni-Co bimetallic layer of high Ni content. Desorption of CO<sub>2</sub> due to oxidation of surface carbonaceous species, was also observed on ZnO-Zn (Figure 5.3) in this temperature range. Similar effects can also be expected on thin film deposited ZnO-Zn. As shown earlier the change in the atomic ratio of Ni and Co to Zn after TDS, significant surface area of ZnO is restored after TDS. The recovery of ZnO at the surface can enhance the interaction between oxygen from ZnO and surface carbon, which led to significant carbon oxidation. Utilisation of oxygen from the support has been reported on other metal-oxide supported catalysts [23, 24, 50] and the improvement in reducing coke deposition by oxidization has been observed. The generation of CO<sub>2</sub> on Co rich bimetallic layer is more limited. It could be an indication for the lower amount of C remained on Co rich surface.

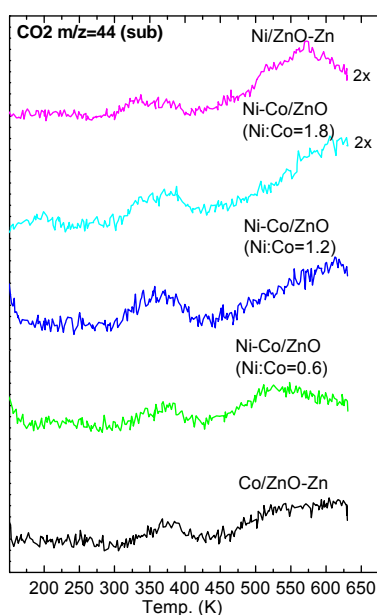


Figure 5.14. (left) TDS of CO<sub>2</sub>( m/z 44, left) resulted from ethanol decomposition on monometallic Co on ZnO-Zn, Ni-Co on ZnO-Zn (Ni to Co atomic ratio =0.6,) Ni-Co on ZnO-Zn (Ni to Co atomic ratio =1.2), Ni-Co on ZnO-Zn (Ni to Co atomic ratio =1.8)and monometallic Ni on ZnO-Zn

### 5.3.6 Preferences of reaction pathway on Ni-Co/ZnO-Zn of different composition

Figure 5.15 shows the ratios of CH<sub>4</sub> desorption with respect to the other decomposition products: C<sub>2</sub>H<sub>4</sub>O, CO and H<sub>2</sub>. As CH<sub>4</sub> production is involved primarily on nickel surface and all other products are commonly found on both Ni and Co, the comparison of CH<sub>4</sub> desorption

to the quantity of other decomposition products can assist in discerning the influence of bimetallic Ni-Co to the reaction.

In general, the ratio of CH<sub>4</sub> to all other products increases with increasing Ni content (see Figure 5.15). CO, CH<sub>4</sub> and H<sub>2</sub> are generated from the same intermediate species (ethoxy group). Hence, methane is produced in the expense of CO and H<sub>2</sub>. The ratio of CH<sub>4</sub> to CO (1<sup>st</sup> desorption peak) production, expressed as the ratio of respective desorption peak area, approaches an almost linear relationship in comparison to CH<sub>4</sub>/CO (2<sup>nd</sup>) and CH<sub>4</sub>/H<sub>2</sub>. The 1<sup>st</sup> CO desorption peak originates from two different reaction pathways: 1) α-hydrogen abstraction and C-C bond breaking of acetaldehyde, mainly found on Ni/ZnO-Zn and 2) C-C bond breaking from oxametallacycle (mainly on Co/ZnO-Zn). The linear correlation of CH<sub>4</sub>/CO with Ni content reveals that the presence of Co changes the selectivity of the layer to methane production. Since the generation of methane through the C-C bond scission (reaction 4) is dominant on Ni, dilution of surface nickel sites by introduction of Co, influences the selectivity to methane mainly by reducing the surface area of Ni.

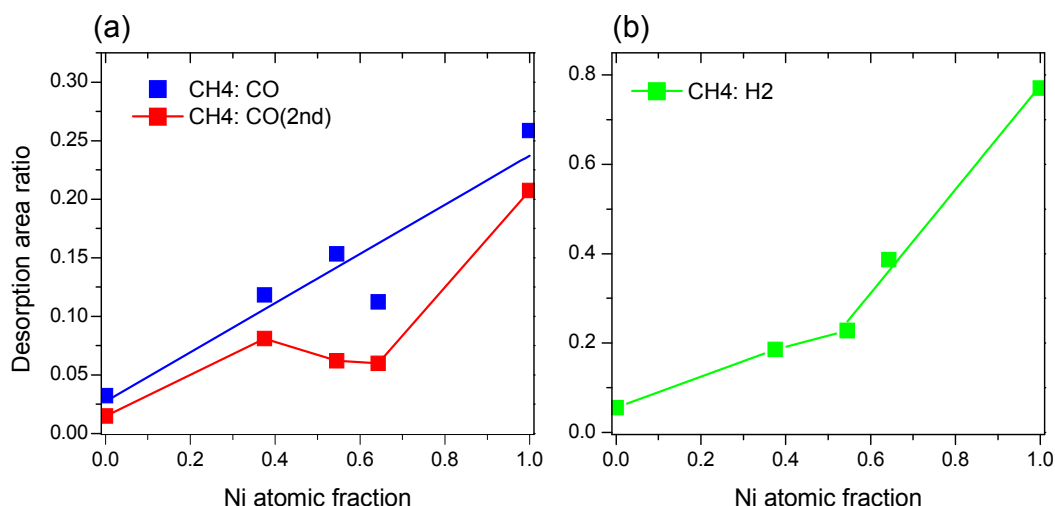


Figure 5.15. Ratio of desorption peak area of (a) CH<sub>4</sub> to CO (1<sup>st</sup> and 2<sup>nd</sup> desorption peak respectively) (b) CH<sub>4</sub> to H<sub>2</sub> on Ni-Co/ZnO-Zn of various composition.

On Ni-Co bimetallic layer, hydrogen desorption is contributed from several reaction pathways: 1) the dehydrogenation of -OH group, 2) dehydrogenation of ethoxy group during formation of acetaldehyde group, 3) dehydrogenation of methyl group, predominantly observed on Co/ZnO-Zn. The first two paths are common on Ni/ZnO-Zn and Co/ZnO-Zn. Figure 5.15 b shows that by adding Co into Ni the hydrogen production is favoured compared to that of methane. Desorption of CH<sub>4</sub> limits the selectivity to methyl group dehydrogenation and reduces hydrogen generation. As shown clearly in Figure 5.15 b, the ratio of methane to hydrogen is not linearly correlated to the Ni content in the layer. There is an evident change in the slope of the production ratio of CH<sub>4</sub>/H<sub>2</sub> when Ni atomic fraction is above 0.6. When Co is in abundance in the layer, the selectivity to methane is subjected to a less influenced by the addition of Ni to the layer. The influence of addition to methane production becomes significant only when the fraction of Ni in the layer surpasses

0.6. This can be comprehended as the suppression of reaction pathway to C-C bond scission or the favouring of methyl group dehydrogenation by the formation of oxometallate cycle when cobalt content becomes a major component in the bimetallic layer.

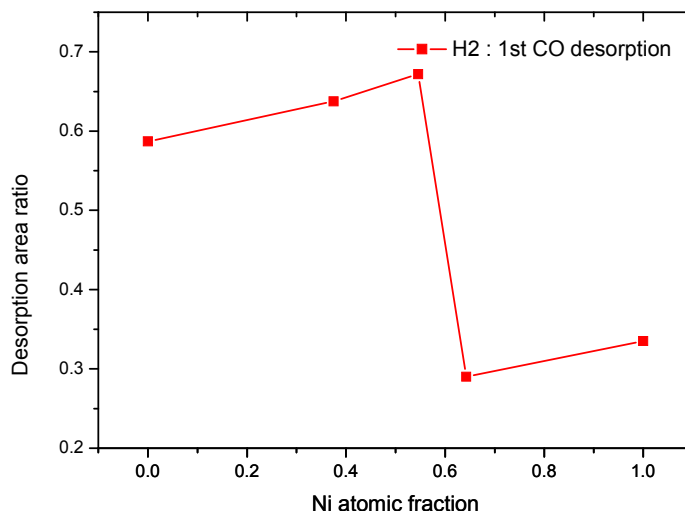


Figure 5.16 Ratio of desorption peak area of (a)  $H_2$  to CO (1<sup>st</sup> desorption peak)

Figure 5.16 shows the desorption ratio of  $H_2$  to the first desorption peak of CO (please refer to Figure 5.11 for the original spectra). As in the case of  $CH_4/H_2$  ratio, there is a break at Ni fraction of 0.6. The ratio of  $H_2$  to CO increases mildly in low Ni content layers. When the fraction of nickel is above 60%,  $H_2/CO$  ratio drops by 50%. This shows that for layers with Ni fraction below 0.6,  $H_2$  production is only slightly affected by the competition of methane production. In combination with the results of  $CH_4/H_2$  (Figure 5.15b), the fraction of Co in the layer has to surpass a critical level in order to obtain high selectivity to hydrogen. It also suggests that the dehydrogenation of methyl group does not vary as a function of the fraction of cobalt in the alloy film. It is better described by a system where the activity of the reaction is separated to two levels depending on Ni/Co content.

In general, the above comparison shows that the selectivity of the reaction pathway is not a simple linear function of the composition of the constituent metal. From the current results, Ni or Co gain significant influence to the overall hydrogen production only when it is sufficiently abundant; and the activity of the less abundant counterpart will be largely suppressed. This could explain the inconsistency in the modification of reaction efficiency and  $H_2$  selectivity on working catalyst system [9, 51]. Improvement of catalytic activities of Ni-Co bimetallic materials would require precise selection of the composition between the two elements.

## 5.4 Conclusions

The surface reaction of ethanol on ZnO-Zn supported monometallic Ni, Co and bimetallic Ni-Co thin film was studied by XPS and TDS. On bare ZnO-Zn single crystal surface, the major reaction involved is dehydration and dehydrogenation, generating  $C_2H_4O$ ,  $H_2O$ ,  $H_2$  and  $C_2H_4$ .

Further decomposition of the  $C_2H_4O$  group is very limited on ZnO-Zn. The deposition of Ni and Co increases significantly the efficiency in C-C bond breaking and C-H bond breaking. The major difference in the reaction pathway of the two metal layers is the formation of methane, which is observed almost exclusively on Ni/ZnO-Zn. Thus, ethoxy intermediate formed on Ni/ZnO-Zn and Co/ZnO-Zn undergoes two different decomposition mechanisms. On Ni/ZnO-Zn, the major reaction is C-C scission, which leads to high amount of methane desorption. On Co/ZnO-Zn, ethoxy intermediate transforms into oxametallate cycle, which further decomposes into CO and  $H_2$  by the dehydrogenation of methyl group. The reaction pathways of bimetallic Ni-Co layer on ZnO-Zn are affected by the reaction pathway of both Ni/ZnO-Zn and Co/ZnO-Zn. The relative amount of methane to CO desorption varies as a function of the quantity of Ni in the thin layer. Desorption of hydrogen is inversely proportional to methane desorption as the reaction pathway for hydrogen formation is in competition with methane. The selectivity of reaction pathway is determined by a threshold concentration (Ni atomic fraction  $>0.6$ ), above which hydrogen selectivity decreases in a high proportion than on Ni-Co layer with lower Ni atomic fraction. This has reveals that precision on Ni-Co composition is required for catalyst design.

## 5.5 References

- [1] J.D.A. Bellido, E.M. Assaf, *Journal of Power Sources*. 177 (2008) 24-32.
- [2] K. Urasaki, K. Tokunaga, Y. Sekine, M. Matsukata, E. Kikuchi, *Catalysis Communications*. 9 (2008) 600-604.
- [3] C. Resini, T. Montanari, L. Barattini, G. Ramis, G. Busca, S. Presto, P. Riani, R. Marazza, M. Sisani, F. Marmottini, U. Costantino, *Applied Catalysis A: General*. 355 (2009) 83-93.
- [4] H. Song, L. Zhang, R.B. Watson, D. Braden, U.S. Ozkan, *Catalysis Today*. 129 (2007) 346-354.
- [5] S.S.Y. Lin, D.H. Kim, S.Y. Ha, *Catalysis Letters*. 122 (2008) 295-301.
- [6] A. Machocki, A. Denis, W. Grzegorzczak, W. Gac, *Applied Surface Science*. 256 (2010) 5551-5558.
- [7] N. Homs, J. Llorca, P.R. de la Piscina, *Catalysis Today*. 116 (2006) 361-366.
- [8] L. Chen, C.K.S. Choong, Z. Zhong, L. Huang, Z. Wang, J. Lin, *International Journal of Hydrogen Energy* (2012).
- [9] C. Resini, M. Concepción Herrera Delgado, S. Presto, L.J. Alemany, P. Riani, R. Marazza, G. Ramis, G. Busca, *International Journal of Hydrogen Energy*. 33 (2008) 3728-3735.
- [10] L. He, H. Berntsen, E. Ochoa-Fernández, J.C. Walmsley, E.A. Blekkan, D. Chen, *Topics in Catalysis*. 52 (2009) 206-217.
- [11] A. Chica, S. Sayas, *Catalysis Today*. 146 (2009) 37-43.
- [12] J.F. Da Costa-Serra, R. Guil-López, A. Chica, *Int. J. Hydrogen Energy*. 35 (2010) 6709-6716.
- [13] S. Freni, S. Cavallaro, N. Mondello, L. Spadaro, F. Frusteri, *Catalysis Communications*. 4 (2003) 259-268.
- [14] P. Bichon, G. Haugom, H.J. Venvik, A. Holmen, E.A. Blekkan, *Topics in Catalysis*. 49 (2008) 38-45.
- [15] R. Padilla, M. Benito, L. Rodríguez, A. Serrano, G. Muñoz, L. Daza, *International Journal of Hydrogen Energy*. 35 (2010) 8921-8928.
- [16] J. Xu, X. Zhang, R. Zenobi, J. Yoshinobu, Z. Xu, J.T. Yates Jr, *Surface Science*. 256 (1991) 288-300.
- [17] S.M. Gates, J.N. Russell Jr, J.T. Yates Jr, *Surface Science*. 171 (1986) 111-134.
- [18] M.P. Hyman, J.M. Vohs, *Surf. Sci.* . 605 (2011) 383-389.
- [19] E. Martono, M.P. Hyman, J.M. Vohs, *Physical Chemistry Chemical Physics*. 13 (2011).
- [20] T. Kratochwil, M. Wittmann, J. Küppers, *Journal of Electron Spectroscopy and Related Phenomena*. 64-65 (1993) 609-617.
- [21] Z. Zhong, H. Ang, C. Choong, L. Chen, L. Huang, J. Lin, *Physical Chemistry Chemical Physics*. 11 (2009) 872-880.
- [22] K. Geunjae, Y. Kijung, *Journal of Physical Chemistry C*. 112 (2008) 3036-3041.
- [23] H. Song, U.S. Ozkan, *Journal of Catalysis*. 261 (2009) 66-74.
- [24] H. Song, U.S. Ozkan, *Journal of Physical Chemistry A*. 114 (2010) 3796-3801.
- [25] C. Zhang, S. Li, M. Li, S. Wang, X. Ma, J. Gong, *AIChE Journal*. 58 (2012) 516-525.
- [26] C.D. Wagner, L.E. Davis, M.V. Zeller, J.A. Taylor, R.H. Raymond, L.H. Gale, *Surface and Interface Analysis*. 3 (1981) 211-225.
- [27] P.J. Linstrom, W.G. Mallard, *NIST Standard Reference Database No. 69*, June 2005 ed., National Institute of Standards and Technology, Gaithersburg, MD, 20899, 2005.
- [28] Y.T. Law, T. Skala, I. Pis, V. Nehasil, M. Vondracek, S. Zafeiratos, *Journal of Physical Chemistry C*. 116 (2012) 10048-10056.

**Chapter 5 Insight for ethanol steam reforming reaction pathways and intermediates: Ethanol desorption on ZnO supported Ni-Co bimetallic model catalyst**

- [29] A.M. Nadeem, J.M.R. Muir, K.A. Connelly, B.T. Adamson, B.J. Metson, H. Idriss, *Physical Chemistry Chemical Physics*. 13 (2011) 7637-7643.
- [30] J. Llorca, N. Homs, P. Ramirez de la Piscina, *Journal of Catalysis*. 227 (2004) 556-560.
- [31] J.M. Vohs, M.A. Barteau, *Surface Science*. 221 (1989) 590-608.
- [32] C.J. Houtman, M.A. Barteau, *Journal of Catalysis*. 130 (1991) 528-546.
- [33] E. Vesselli, A. Baraldi, G. Comelli, S. Lizzit, R. Rosei, *ChemPhysChem*. 5 (2004) 1133-1140.
- [34] J.H. Wang, C.S. Lee, M.C. Lin, *Journal of Physical Chemistry C*. 113 (2009) 6681-6688.
- [35] A.F. Lee, D.E. Gawthrope, N.J. Hart, K. Wilson, *Surface Science*. 548 (2004) 200-208.
- [36] Y. Cong, V. Van Spaendonk, R.I. Masel, *Surface Science*. 385 (1997) 246-258.
- [37] R. Shekhar, M.A. Barteau, *Catalysis Letters*. 31 (1995) 221-237.
- [38] J.M. Sturm, C.J. Lee, F. Bijkerk, *Surface Science*.
- [39] M. Bowker, R.P. Holroyd, R.G. Sharpe, J.S. Corneille, S.M. Francis, D.W. Goodman, *Surface Science*. 370 (1997) 113-124.
- [40] C.J. Weststrate, H.J. Gericke, M.W.G.M. Verhoeven, I.M. Ciobîcă, A.M. Saib, J.W. Niemantsverdriet, *The Journal of Physical Chemistry Letters*. 1 (2010) 1767-1770.
- [41] E. Martono, J.M. Vohs, *Journal of Catalysis*. 291 (2012) 79-86.
- [42] M.C. Biesinger, B.P. Payne, L.W.M. Lau, A. Gerson, R.S.C. Smart, *Surface and Interface Analysis*. 41 (2009) 324-332.
- [43] A.R. González-Elipe, J.P. Holgado, R. Alvarez, G. Munuera, *J. Chem. Phys.* . 96 (1992) 3080-3086.
- [44] A.W. Moses, H.G.G. Flores, J.-G. Kim, M.A. Langell, *Applied Surface Science*. 253 (2007) 4782-4791.
- [45] S.C. Petitto, E.M. Marsh, G.A. Carson, M.A. Langell, *J. Mol. Catal. A: Chem.* 281 (2008) 49-58.
- [46] K. Ozawa, Y. Oba, K. Edamoto, *Surface Science*. 601 (2007) 3125-3132.
- [47] J.M. Guil, N. Homs, J. Llorca, P.R. De La Piscina, *Journal of Physical Chemistry B*. 109 (2005) 10813-10819.
- [48] F. Abild-Pedersen, M.P. Andersson, *Surface Science*. 601 (2007) 1747-1753.
- [49] H. Liu, R. Zhang, F. Ding, R. Yan, B. Wang, K. Xie, *Applied Surface Science*. 257 (2011) 9455-9460.
- [50] H. Song, X. Bao, C.M. Hadad, U.S. Ozkan, *Catalysis Letters*. 141 (2011) 43-54.
- [51] A. Casanovas, M. Roig, C. De Leitenburg, A. Trovarelli, J. Llorca, *International Journal of Hydrogen Energy*. 35 (2010) 7690-7698.

---

Chapter 6  
Ambient Pressure  
Photoemission  
Spectroscopy (APPEs) and  
Near-Edge X-ray Absorption  
Spectroscopy (NEXAFS)  
study of Ni-Co bimetallic  
catalyst for ethanol steam  
reforming

---

---

---

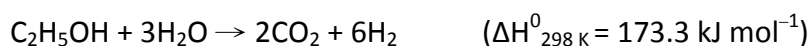
---

## **Chapter 6. Ambient Pressure Photoemission Spectroscopy (APPEs) and Near-Edge X-ray Absorption Spectroscopy (NEXAFS) study of Ni-Co bimetallic catalyst for ethanol steam reforming**

### **6.1 Introduction**

Ethanol is a very suitable choice as the feedstock for renewable hydrogen production among most biomass derived fuel. It has high hydrogen content. It is non-toxic and easy to be handled and stored. In addition, the production of ethanol from biomass like sugar is a well-developed process. Its practical conveniences make it a promising feedstock for the on-demand production of hydrogen for fuel cells.

Steam reforming process converts ethanol into hydrogen and carbon dioxide. It is an endothermic reaction and the ideal reaction requires an input of ethanol and water in a molecular ratio 1:3, forming H<sub>2</sub> and CO<sub>2</sub> as the only products:



The practical ethanol steam reforming (ESR) involves a complex reaction network, in which the reaction pathways are strongly influenced by the nature of the catalysts and the operating condition. Nickel [1, 2] and cobalt [3-6] based catalysts have been regarded as the most promising and effective non-noble metal catalysts for ESR reaction. High ethanol conversion efficiency at relatively low temperatures and H<sub>2</sub> selectivity comparable to noble metal catalysts, such as Rhodium, has been achieved [7, 8]. However, a major short-coming of transition metal catalysts is their fast deactivation due to sintering [9] and surface coke formation [10, 11]. Utilization of bimetallic catalysts [12-15] and suitable metal oxide support [16-18] can improve catalyst stability.

Reaction intermediates such as C<sub>2</sub>H<sub>4</sub>O or undesirable intermediates such as CO, CH<sub>4</sub>, C<sub>2</sub>H<sub>4</sub>, are generated in ESR process, depending on the nature of the catalyst and the support. The reaction pathway over monometallic Nickel (Ni)[1, 19] and Cobalt (Co)[20-22] catalyst supported on different metal oxide substrate has been studied by methods such as temperature programmed desorption[23-25] and Infrared spectroscopy[25, 26]. Adsorption of ethanol through dehydrogenation, forming hydrogen and ethoxide is the main initial step and takes place readily at low temperature [20, 27]. The ethoxide group can either decompose further into CO, H<sub>2</sub> and CH<sub>4</sub> by decarbonylation [20, 21]; or form acetaldehyde[28] by dehydrogenation. Formation of other acetyl group containing compound such as acetone and acetic acid[24] is also possible. Observed in most catalytic studies, Ni based catalysts are very selective to CH<sub>4</sub> production [1, 19] due to its lower energy barrier to C-C bond scission. From the ethanol thermal desorption studies by Verykios et al. [1], C-C bond cracking of acetaldehyde takes place readily at low temperature (<420 K), while acetaldehyde decomposition via dehydrogenation takes place at higher temperature (~470 K). The generation of CO and CO<sub>2</sub> through this decomposition pathway

increases with temperature. On the other hand, dehydrogenation of ethoxy group is more active on Co based catalyst [20].

The role of Ni and Co oxide in the ESR is a rather disputable issue. Oxidation of a metal catalyst supported on metal oxide (common ESR catalyst supports such as ZnO, CeO<sub>2</sub>, MgO) is frequently observed due to metal support interaction. The oxidation state of cobalt is a determining factor for the reaction pathway. Apart from Co oxide formed due to metal-support interaction [29, 30], metal species are oxidized spontaneously in ESR gases at low temperature [31]. A recent study from Avila et al. [31] reveals that cobalt is oxidized into rock salt structured CoO in ESR reaction mixture at low temperatures (>430 K) and is reducible spontaneously as temperature of reaction increases. Spinel Co<sub>3</sub>O<sub>4</sub> was found to be rather inactive to ESR and can be easily reduced to CoO under reaction condition [32]. It was shown by *in-situ* XRD that when Co<sub>3</sub>O<sub>4</sub> is the predominant phase, ethanol conversion is below 30%, and is selective mainly to H<sub>2</sub> and acetaldehyde production. Hyman et al. has studied the ESR reaction pathway over metallic Co and Co oxides [20] on polycrystalline cobalt foil by thermal desorption spectroscopy. They showed that Co<sup>2+</sup> is selective to dehydrogenation of ethoxide and formation of acetaldehyde, while metallic cobalt favours the subsequent decarbonylation of ethoxide. Yet, the reaction efficiency and mechanism over CoO are still under question. The activity of NiO in ESR has also been seldom studied. The active role of the ionized Ni and Co species in the reaction requires further study.

Life time of Ni and Co based catalysts is rather limited in comparison to noble metal such as Rh [10]. The major cause of Ni and Co deactivation is high level of coke formation. Frusteri et al. compared the catalytic performance of MgO supported Pd, Rh, Ni and Co and the amount of carbon formed over Ni and Co is at least two times higher than that formed on Rh [9]. The addition of another active metal to form bimetallic catalyst is an approach to promote catalytic performance and catalysts' stability. Improvement on coke formation has been observed on Ni-Co bimetallic catalyst [12, 13, 33, 34]. Studies of such systems are, however, complicated due to the difference in the two metal's catalytic activity, bimetallic synergetic effects and their interaction towards the support.

In this respect, we aim at investigating a model catalyst of Ni-Co nanopowder by *in-situ* method, such that information of the real-time active state of the catalyst and the reaction products can be obtained. *In-situ* ambient pressure photoelectron spectroscopy (APPEs) measurement and mass spectroscopy were used simultaneously to investigate the correspondence of the active state of the catalyst surface and the reaction product released in the process. A direct comparison of the relative selectivity of the key products of ESR reaction from 373 K- 623 K on Ni-Co bimetallic alloy powder to its monometallic counterparts (Ni and Co nanopowders) were made for a better understanding of the influence of Ni-Co bimetallic synergy to the reaction.

## 6.2 Experimental methods

The surface chemistry of Ni (99.9%, <100nm, Sigma Aldrich), Co (99%, 50-80nm, Alfa Aesar) and Ni-Co (99%, <150nm, Sigma Aldrich) nanopowders were studied under ambient pressure H<sub>2</sub>, O<sub>2</sub> and ESR reaction mixture in this chapter. In situ X-ray photoelectron spectroscopy (XPS) and NEXAFS measurement were performed at ISS beamline at BESSY synchrotron facility in Helmholtz Zentrum, Berlin (Germany). Description of the setup was given in chapter 2. The nanopowder was pressed into a pellet and was mounted to the sample holder. The sample was heated at the rear by infrared laser and the temperature was measured by a K-type thermocouple fixed on the sample surface. The sample temperature was raised at a constant heating rate (20 K/min.) until it reached the target temperature.

Core-level photoelectron and NEXAFS spectra were measured *in-situ* in different reaction gases. The reduction of Ni, Co and Ni-Co powder in H<sub>2</sub> was monitored *in-situ* by XPS, where spectra were recorded at constant time intervals in the temperature range from 373 K to 623 K. The temperature ramp was 20 K /min. Ni 2p, Co 2p, C 1s and O 1s spectra were recorded at selected photon energy such that the emitted photoelectrons were of the same kinetic energy at about 145 eV. All binding energies (BE) given were calibrated with respect to the Fermi edge of the analyzer. Background subtraction was carried out by Shirley method. For the quantitative evaluation of atomic ratio between the elements, the spectra were normalized to the incident photon flux and the photo-ionization cross-sections [35, 36]. The catalysts were studied with *in-situ* XPS in ESR gas mixture with a temperature program from 373 K – 623 K (ramp rate 20 K/min) and also at two constant temperature level. Spectra were collected with short acquisition time at chosen time interval during the temperature program. Two temperature levels (543 K and 623 K), at which the catalysts were at different oxidation state, was chosen for detailed XPS study.

The gas phase composition was monitored by on-line mass spectrometry with a differentially pumped quadrupole mass spectrometer (Balzers). Mass flow controllers were used to control the gas flow into the reaction cell. The pressure of the gas mixture introduced to the reaction cell was kept constant at 0.2 mbar. An ethanol to water (H<sub>2</sub>O) flow ratio of 1:3 was used as the ESR reaction mixture. As ionization of gas molecules by mass spectrometer filament generates a wide spectra of mass fragment, the mass signals of methane (CH<sub>4</sub>), acetaldehyde (C<sub>2</sub>H<sub>4</sub>O), carbon monoxide (CO) and carbon dioxide (CO<sub>2</sub>) were corrected by subtraction of fragments from other products that overlaps with the highest intensity mass fragment of the above species. Details of the correction factors for each fragment were given in the Table 6.1. The above spectrum of the mass fragments for the above species was collected by the online measurement of the corresponding pure gas or vapour in the same reaction cell at the same pressure. The conversion of ethanol and water was expressed as gas pressure. The mass signal has been converted from ion current to partial pressure (Torr) for the calculation of ethanol consumption. This conversion was

estimated by varying the ethanol to water feed ratio while keeping the same overall pressure.

In addition to synchrotron based measurements, temperature programmed reduction (TPR) was performed to study the reducibility of the Ni-Co nanopowder in the bulk. The measurement was performed using Micrometrics Autochem II analyser. 20 mg of the sample powder was used for this analysis. Before measurement, the samples were oxidized for 15 min in flowing O<sub>2</sub> at 623 K. The sample was then cooled in flowing He to room temperature. Subsequently the sample was purged by carrier gas (50 cm<sup>3</sup>/min Ar) until the baseline stabilized. 5% H<sub>2</sub>/Ar at flux rate 50 cm<sup>3</sup>/min was used as reaction gas. The temperature ramp was 40 K/min from ambient temperature to 1173 K. The hydrogen uptake was measured by thermal conductivity detector.

*Table 6.1 Relative intensity of mass fragment from ESR products*

<b>Reaction products studied</b>	<b>Overlapping mass fragment from other products (percentage of mass signal contributed by these products)</b>
<b>CH<sub>4</sub>-m/z16</b>	CO (1%), CO <sub>2</sub> (10%)
<b>CO-m/z 28</b>	C <sub>2</sub> H <sub>5</sub> OH (51%), CO <sub>2</sub> (14%)
<b>C<sub>2</sub>H<sub>4</sub>O-m/z 29</b>	C <sub>2</sub> H <sub>5</sub> OH (84%), CO (2%)
<b>CO<sub>2</sub>-m/z 44</b>	C <sub>2</sub> H <sub>5</sub> OH (32%)

## 6.3 Results

### 6.3.1 Reduction of Ni-Co nanopowders in ambient pressure H<sub>2</sub>

The redox behavior of Ni-Co bimetallic system has been previously studied experimentally using ex-situ XPS [37] and has been described in chapter 3. It was shown that in oxidative environment Co undergoes preferential oxidation due to the higher availability of Co cation vacancies and surface segregation of cobalt. In reducing environment, reduction of Ni-Co takes place in two stages. Figure 6.1 shows a comparison of the reduction behavior of Ni-Co alloy nano-powders with monometallic Ni and Co nano-powders. The Ni and Co mean valence value was obtained from the relative composition of its metallic form and oxidized form deconvoluted from Ni 2p<sub>3/2</sub> and Co 2p<sub>3/2</sub> peak. (For the respective spectra, please refer to the Appendix). Monometallic Ni, Co and bimetallic Ni-Co nanopowders were pre-oxidized in 0.2 mbar O<sub>2</sub> to form NiO and Co<sub>3</sub>O<sub>4</sub> before reduction.

Complete reduction of nickel oxide takes place at a lower temperature compared to cobalt and Ni-Co oxides. Co<sub>3</sub>O<sub>4</sub> is a spinel oxide which consists of cobalt at 2+ and 3+ oxidation states. Co<sup>2+</sup> occupies tetrahedral sites and Co<sup>3+</sup> occupies octahedral sites. Reduction of Ni is initiated at 500 K and the complete reduction occurs at around 550 K. Reduction of Co<sub>3</sub>O<sub>4</sub> involves firstly the transformation of Co<sub>3</sub>O<sub>4</sub> to CoO at lower temperature and subsequently complete reduction of CoO to metallic cobalt, which occurs at 623 K. Similar to cobalt oxide, bimetallic Ni-Co oxide reduces also in two consecutive steps. At first reduction of Co<sub>3</sub>O<sub>4</sub> to CoO is completed at 550K, without affecting surface composition of the alloy or the

oxidation state of NiO. The second step involves the reduction of CoO and NiO to metallic Ni and Co which is completed almost simultaneously at 630K. As Ni-Co is reduced to metallic form, the surface of catalyst also undergoes strong restructuring in which Ni to Co ratio increases from 0.3 to 1, reaching the bulk Ni-Co composition. Surface segregation of cobalt of Ni-Co alloy in oxidative environment was led by the fast oxidation of cobalt compared to Ni and it has been previously observed in  $10^{-6}$  mbar and atmospheric pressure oxygen [37]. In reducing environment, surface segregation of cobalt is reversed that the Ni to Co atomic ratio is restored. According to a DFT studies on the segregation energy of transition metal surface by Ruban et al. [38], for bulk Ni-Co alloy, surface segregation of Ni is more favourable in the absence of any adsorbents. The results obtained here suggest that surface segregation of nickel is favoured at reducing environments, while in oxidative atmospheres segregation follows the reverse trend.

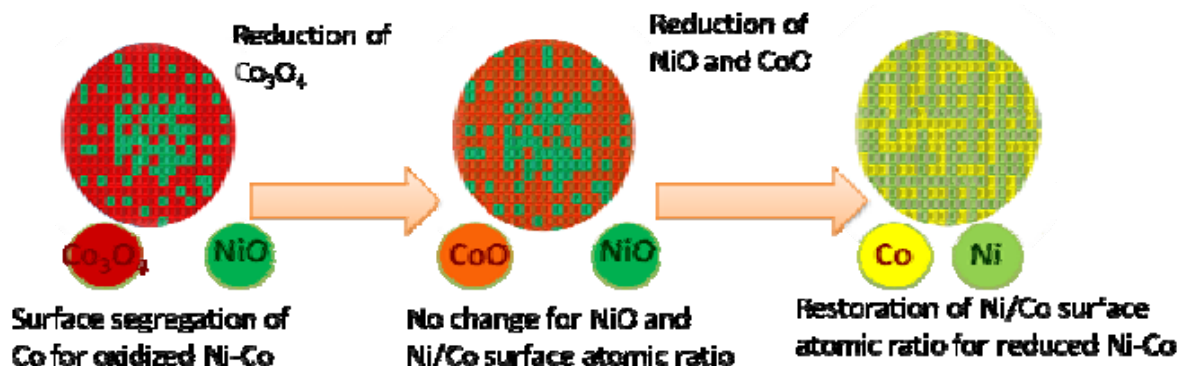
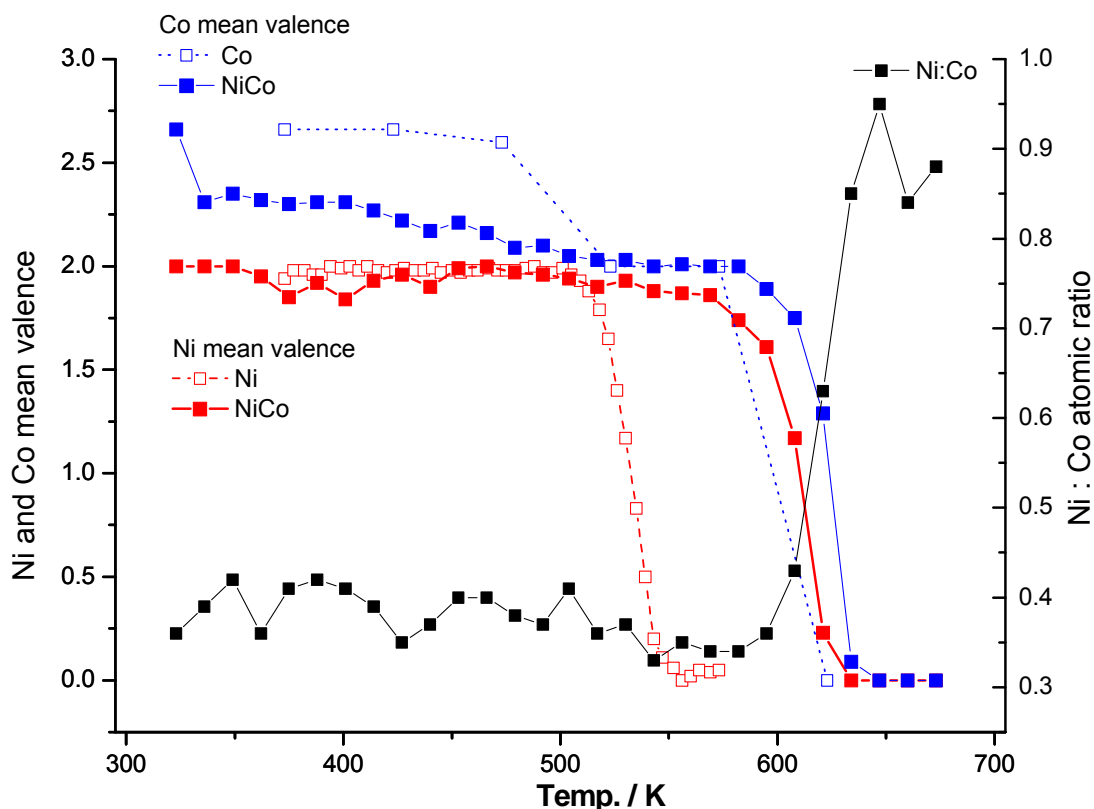


Figure 6.1 Mean valence value of Ni (Red) and Co (Blue) and surface atomic ratio of Ni to Co of monometallic Ni, monometallic Co and Ni-Co nanopowders (all has been pretreated in  $\text{O}_2$ ) annealed in 0.2 mbar  $\text{H}_2$  between temperature 370 – 623 K with temperature ramp 20 K/min.

Shown in figure 6.1, the temperature of reduction for monometallic nanopowder is lower than that of Ni-Co nanopowders, with a larger difference between Ni and Ni-Co than that of Co. This shows that the bimetallic interaction has raised the barrier for the reduction of its respective metals, especially for nickel. The Gibbs free energy of Ni and Co oxide formation shows that  $\text{Co}_3\text{O}_4$  formation from  $\text{CoO}$  is the least favourable reaction, leading to its reduction prior to other oxide species:

$$\Delta G_f^0 (\text{NiO}) = -211.7 \text{ kJmol}^{-1}$$

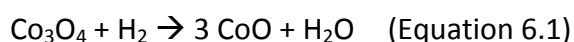
$$\Delta G_f^0 (\text{CoO}) = -214 \text{ kJmol}^{-1}$$

$$\Delta G_f^0 (\text{Co}_3\text{O}_4) = -744 \text{ kJmol}^{-1} \quad [39]$$



The difference in the free energy of formation of NiO and CoO is relatively small, which explains the proximity of the reduction temperature of NiO and CoO in an alloy. The NEXAFS spectra show that the CoO formed during the reduction process is in rocksalt structure. It should be noted that the difference in the reduction temperature of monometallic NiO and CoO oxides is probably due to kinetic reason since the reduction rate of  $\text{Co}_3\text{O}_4$  under the experimental condition is probably slower than the temperature ramp.

The reduction of bulk Ni, Co and Ni-Co nanopowder was also tested under atmospheric pressure. The hydrogen uptake for Ni reduction is represented as one sharp peak while reduction of Co involves firstly a lower intensity shoulder at 735 K and a higher  $\text{H}_2$  uptake peak at 830 K. Though the threshold of reduction temperature is different from that observed from XPS, the TPR results still represent very coherently the two step reduction process of Co oxides. In addition, the first step of reduction (Equation 6.1) requires less quantity of hydrogen, which is coherent to the reduction of  $\text{Co}_3\text{O}_4$  to CoO that produces CoO in a stoichiometric ratio of 1:3 by 1 mole of  $\text{H}_2$ . Complete reduction of Co from CoO to Co would then show a higher hydrogen uptake.



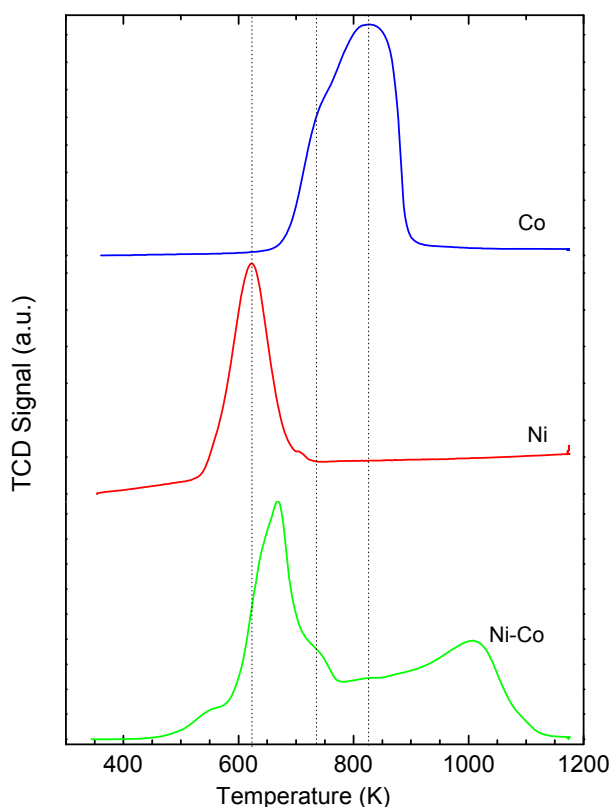


Figure 6.2 temperature programmed reduction of Ni-Co, Ni and Co nanopowder in 5% H<sub>2</sub>/Ar.

H<sub>2</sub> uptake for reduction of bulk Ni-Co nanopowder distributes over a wide temperature range. This is associated with the more complicated form of oxide present in bimetallic materials. Through oxidation pretreatment, Ni and Co should be oxidized to NiO and Co<sub>3</sub>O<sub>4</sub>. Presence of another spinel oxide NiCo<sub>2</sub>O<sub>4</sub> cannot be neglected, especially when oxidation takes place in O<sub>2</sub> gas of atmospheric pressure (see chapter3). The reduction of Ni oxide is initiated by the adsorption of hydrogen to nickel atoms adjacent to oxygen vacancy. The hydrogen reduces NiO and desorbs as water. The reduced Ni nucleates into large domains on Ni oxide surface and this continues as an autocatalytic reduction as more metallic Ni is formed [40, 41]. Eventually, agglomerates of Ni metal crystallites displace the diminishing NiO domains. Therefore the reduction of Nickel takes place mainly at the Ni/NiO interface. The reduction of Co oxides relies mainly on the reduction of Co oxide in the bulk as Co oxide has a much lower surface tension and tends to segregate to the surface. Therefore reduction of bulk Co oxide is necessary prior to surface Co oxide reduction. This is facilitated by electron diffusion to bulk CoO which reduces internal Co cation and the outward oxygen diffusion through vacancies or grain boundaries to the surface[42]. Therefore the wide reduction peak at high temperature is a result of the complex diffusion process of metal species towards to bulk and the outward diffusion of oxygen.

### 6.3.2 Coordination of Ni-Co in ethanol steam reforming mixture

The oxidation state of the metal catalyst has a critical effect to the reaction pathway of a catalytic reaction and activity, as the difference in the electronic structure induces different bonding structure between the catalyst and gas phase molecules. In order to understand the effect of oxide formation to the reaction, the catalysts were pretreated either in oxygen or in hydrogen to form an initial surface Ni-Co oxide or metallic Ni-Co layer on the Ni-Co catalysts prior to reaction. However, it was soon found that independent of the pretreatment, exposure of catalysts to the reaction mixture modifies the surface oxidation state and composition of the catalyst. In particular, pre-reduced catalysts were partly oxidized when the reaction mixture was introduced at low temperature (370 K), while pre-oxidized catalysts were reduced in reaction mixture upon heating, as shown in the Ni  $2p_{3/2}$  and Co L-edge spectra in figure 6.3.

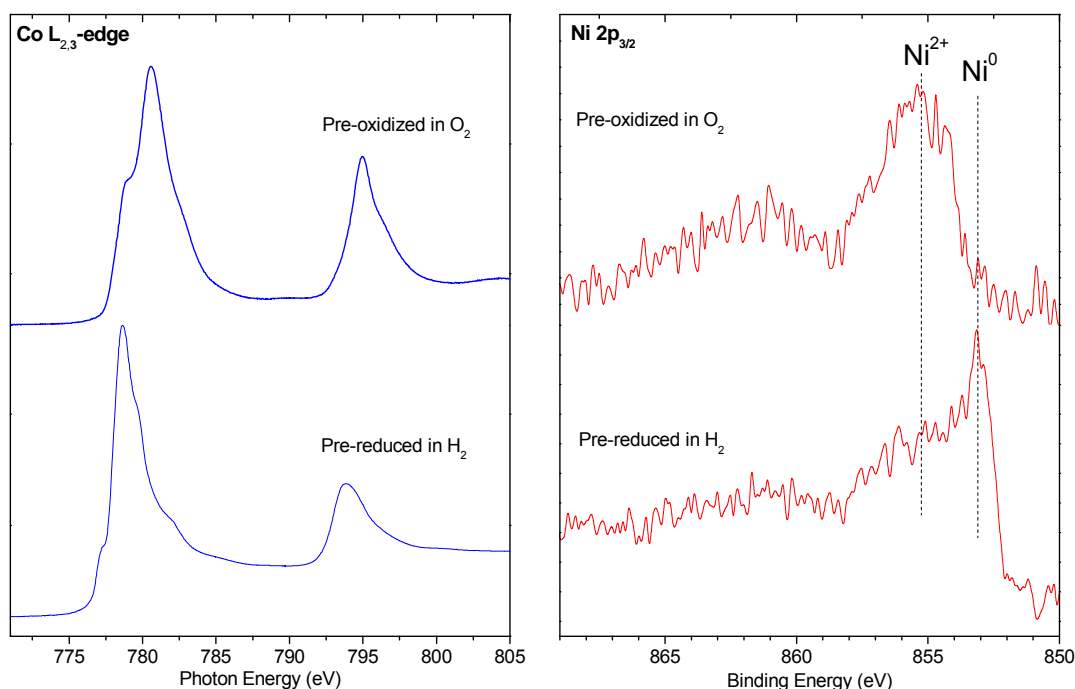


Figure 6.3 Ni  $2p_{3/2}$  and Co L-edge spectra of pre-reduced and pre oxidized Ni-Co nanopowder in ESR gases at 373 K (initial temperature of ESR gas introduction)

The oxidation of pre-reduced cobalt-based catalysts has been observed experimentally in other studies [43, 44]. In the thermodynamic analysis by Avila et al. [31], they indicated that  $H_2O$  acts as oxidant at low temperature for oxidizing Co metal to CoO, which is reduced spontaneously above 430K. The reduction of pre-oxidized catalysts, both in mono- or bimetallic form, takes place in a similar fashion in ESR gases as in  $H_2$ . Increase in surface Ni to Co atomic ratio on bimetallic Ni-Co catalyst surface also occurs when the metal oxide reduction starts in ESR gas mixture, as in the case of  $H_2$ . The Ni to Co atomic ratio reaches close to 1:1 as the alloy powder is in metallic state. Both the reduction and surface segregation behaviour indicates that the ESR gases create a reducing environment under reaction conditions.

Pre-oxidized catalysts maintain their oxidation state under reaction conditions up to 540 K. Therefore the catalytic reaction was tested at 540 K in order to probe the effect of surface oxidation state to the catalytic performance. At this temperature the conversion of ethanol (catalytic activity) is relatively low, therefore results obtained at 540 K was used just to probe the effect of surface oxidation state to the reaction paths. The difference between bimetallic and monometallic catalyst to ESR activity and selectivity was investigated also based on measurements performed at higher temperature (620 K), where the catalytic activity is higher.

### **6.3.3 Influence of oxidation state of Ni and Co on the catalytic performance of Ni-Co**

There has been a long discussion on how the oxidation state of nickel and cobalt catalyst affects the catalytic activities of ESR [32, 43-45]. Our results show that the surface oxide on both cobalt and nickel can be easily reduced in ethanol reforming mixture even at relatively low temperature (600 K). Therefore the surface of the catalysts should be in metallic state under industrially relevant reaction conditions. On the other hand it is likely that nanosized particles might be oxidized due to the interaction with oxide support. Therefore it is important to clarify the effect of ionic cobalt and nickel (oxidized) to the selectivity and activity of the reaction. Ni, Co and NiCo powders pretreated in O<sub>2</sub> and H<sub>2</sub>, were tested in ESR mixture at 540 K, which is the highest possible temperature that nickel and cobalt oxides are stable in the reaction mixture. Above this temperature the oxides were reduced by the reaction mixture into metals.

Pretreatment in hydrogen and oxygen gas converts the initial surface state of Ni and Co to either metal form (H<sub>2</sub> treatment) or oxide form (NiO and Co<sub>3</sub>O<sub>4</sub> for Ni, Co and Ni-Co in O<sub>2</sub>). Corresponding NEXAFS spectra of Co L-edge and XPS spectra of Ni 2p<sub>3/2</sub> are shown in figure 6.4. As the binding energy of the main peak of Co 2p<sub>3/2</sub> XPS spectra for Co<sup>0</sup>, Co<sup>2+</sup> and Co<sup>3+</sup> [46-48] is very close, Co L-edge NEXAFS spectra are shown as it contains more distinct features for Co at each oxidation state [49]. In addition the coordination of Co<sup>2+</sup>, tetrahedral or octahedral coordination, can be better distinguished by NEXAFS. Pre-oxidized Co in either monometallic or bimetallic form is reduced to CoO in ESR gases at 534 K.

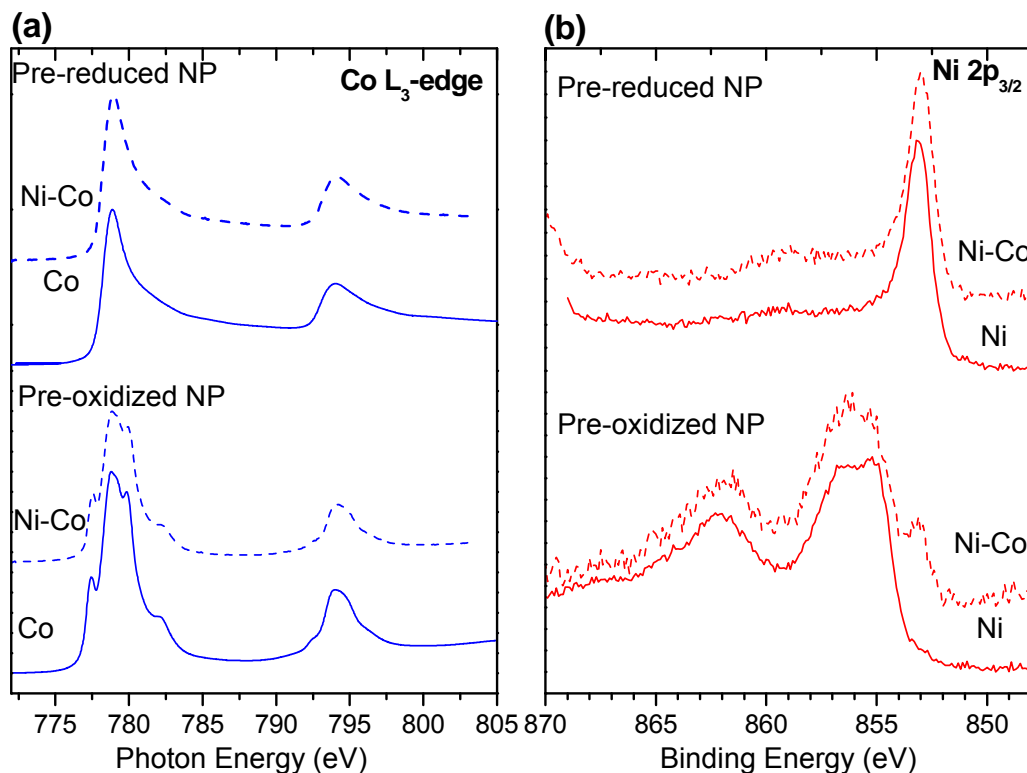
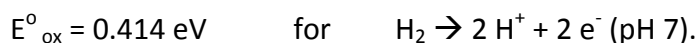


Figure 6.4 (a) Co L<sub>3</sub> edge of pre-oxidized (O<sub>2</sub>, 543 K) and pre-reduced (H<sub>2</sub>, 543 K) Co nanopowder (NP) and Ni-Co NP (b) Ni 2p<sub>3/2</sub> spectra of Ni NP and Ni-Co NP in ESR reaction gas mixture (ethanol to steam ratio=1:3) at 543 K.

Ni is mainly in form of NiO, but small amount of metallic Ni builds up on Ni-Co NPs. Ethanol is also a reducing agent, though the oxidation potential is slightly inferior to H<sub>2</sub>



Reduction at this temperature could be a slow process unlike in H<sub>2</sub> gases (shown in figure 6.1) due to the presence of water. Pre-reduced Ni, Co and Ni-Co, which is partially oxidized in presence of water at 373 K, readily transformed to pure metal phase at 543 K.

Apart from the differences in the valence state, oxidative pretreatment also leads to surface segregation of Co over Ni due to its rapid oxidation. The surface atomic ratio of pre-reduced Ni-Co is higher than the pre-oxidized sample by more than 50% (figure 6.5). Even though Co<sub>3</sub>O<sub>4</sub> reduces to CoO at 543 K in the reaction mixture, there is no significant rearrangement in the surface layers or change in surface Ni and Co content since the Ni:Co atomic ratio remains similar to the initial state (373 K). This is also coherent with the behaviour of reduction of Ni-Co in H<sub>2</sub>, where diffusion of Ni back to the surface was initiated only during the reduction of NiO and CoO to metallic Ni and Co and remains stable during the reduction of Co<sub>3</sub>O<sub>4</sub> to CoO.

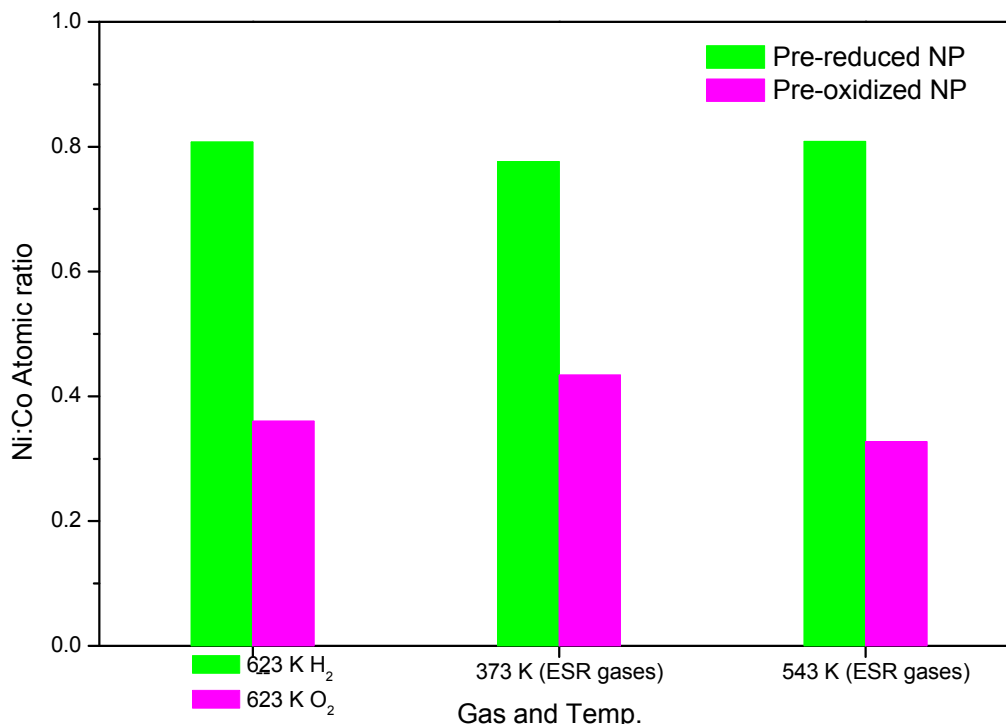
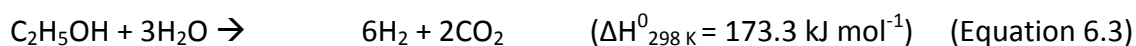


Figure 6.5 Ni to Co atomic ratio of pre-reduced and pre-oxidized Ni-Co bimetallic nanopowder in 0.2 mbar ethanol steam reforming gases (ethanol : steam ratio =1:3) at 373 K and 543 K

The ethanol and water consumption for monometallic and bimetallic Ni and Co samples pretreated in O<sub>2</sub> and H<sub>2</sub> and the relative production of corresponding reaction products are presented in figure 6.6. In general, Co shows higher ethanol consumption compared to Ni and Ni-Co. However comparison of the consumption of ethanol and water between the samples shows that ethanol consumption is much higher than the expected 1:3 stoichiometry for an ideal ESR reaction (equation 6.3), indicating that other reactions like dehydrogenation (equation 6.4), decomposition (equation 6.5), and dehydration (equation 6.6), are involved.



Since C<sub>2</sub>H<sub>4</sub> was not detected among the products, dehydration (Equation 6.6) is negligible. The considerable amount of CO and CH<sub>4</sub> produced (presented in figure 6.6b) suggests that the decomposition of ethanol at this temperature is a significant reaction pathway for all samples. This is coherent the thermodynamic considerations presented in chapter 1. Ethanol decomposition is an exothermic reaction, so it is favoured at low temperature in

contrast to ethanol steam reforming (endothermic reaction) which requires higher temperature.

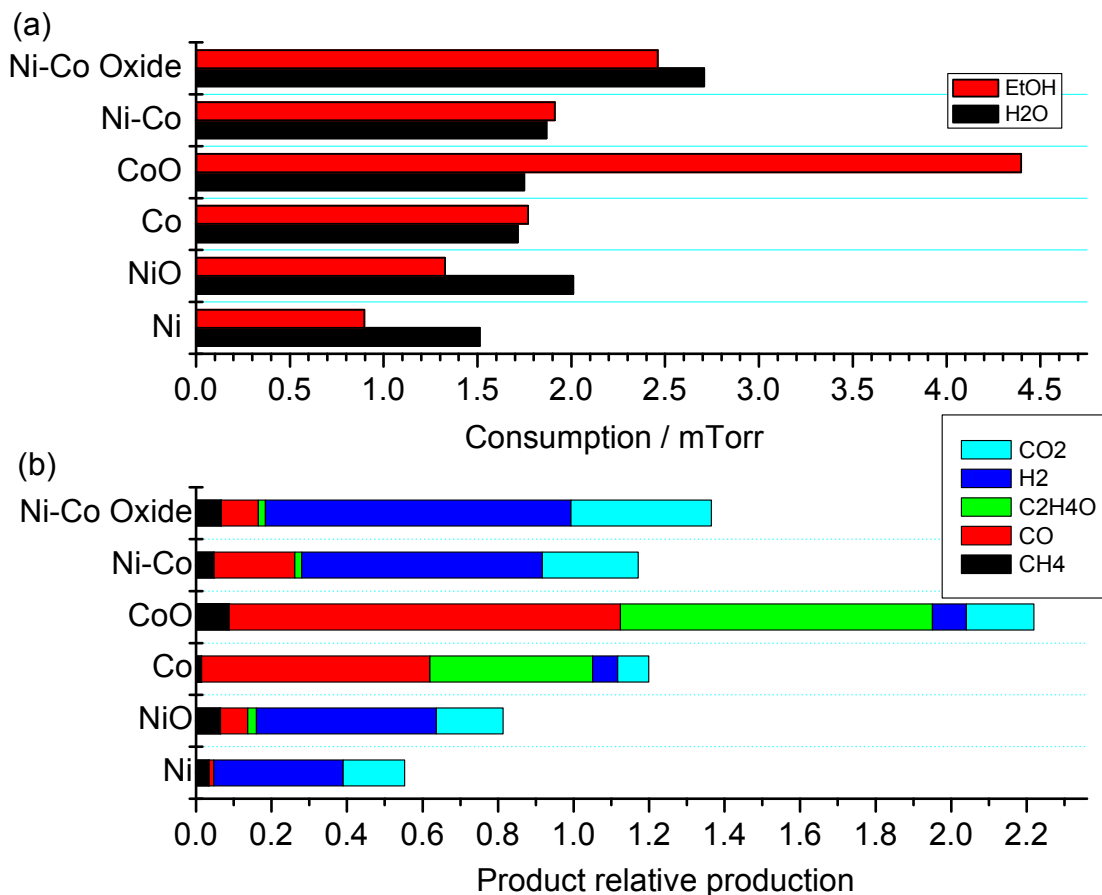


Figure 6.6 (a) Steady state water and ethanol consumption, which is expressed in terms of the change in partial pressure of ethanol and water calculated based on the calibration procedure mentioned in section 6.2 (b) Relative production of ethanol steam reforming product on pre-reduced and pre-oxidized Ni, Co and Ni-Co nanopowder at 543 K.

Among all three materials studied (Ni, Co and NiCo), pre-oxidized samples show higher ethanol conversion than their reduced counterpart under the conditions examined. Product selectivity for oxidized sample is very similar to the reduced sample. The higher ethanol conversion observed could be the result of ethanol oxidation on oxidized metal surfaces (equation 6.8 and 6.9):



The APPEs C 1s spectra can be used to identify the surface adsorbed species in the course of the reaction. The C 1s peak (figure 6.7) can be deconvoluted into 5 components: (1) graphitic carbon due to coke formation (284.3-284.8 eV) [50] (2) alkyl group CH<sub>x</sub> corresponding to methyl group formed by the cracking of the C-C bond (285.2 eV) [51-53] (3) the α carbon from ethoxide group -CH<sub>2</sub>O- from dissociative ethanol adsorption (286.5-

286.8 eV [54] (4) HCOO- formate group at (288 eV) and (5) acetate groups CH<sub>3</sub>COO- (288.9-289.5 eV) [51, 54-56], which are both intermediates of the reaction of surface oxygen with ethoxy group [57]. Acetate group is present only on oxidized Ni-Co surface. Formation of CH<sub>3</sub>COO- group by interaction of un-desorbed acetaldehyde with lattice oxygen or hydroxyl group has been observed elsewhere [58, 59]:



The acetate group can be then consumed by decomposition into CO<sub>2</sub> and methyl group. Acetate formation by oxidation was also observed on other catalysts [59]. Therefore this is very likely to be the contributing factor for the higher ethanol conversion on oxide surface.

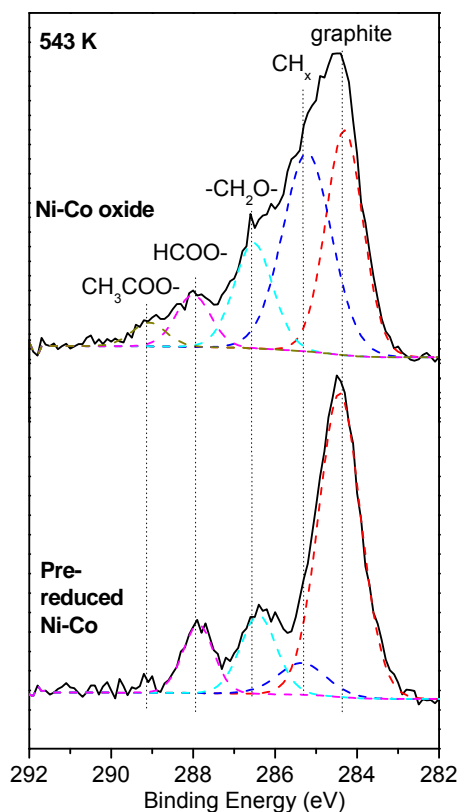


Figure 6.7 C 1s spectra of pre-reduced Ni-Co and Ni-Co oxide

In addition, the relative proportion of CH<sub>x</sub> and graphitic species on oxidized and reduced samples are very different. Although the overall carbon surface coverage is similar on both samples, graphitic carbon are the main carbon species on reduced samples, while much higher proportion of CH<sub>x</sub> is observed on oxidized samples. This also suggests the possibility of methyl group dehydrogenation over metallic Ni-Co at this temperature, which leads to the accumulation of graphitic carbon on the surface.

Acetaldehyde from dehydrogenation (Equation 6.4) is the major product and reaction for CoO and Co catalyst. The energy requirement of this reaction is relatively low [60] compared to other reaction paths, and is commonly involved as initial step in ethanol surface reaction. Formation of acetaldehyde as a major reaction intermediate over Co catalyst has been observed on supported Co catalysts at low temperature elsewhere [8]. The correlation of Co and Co<sup>2+</sup> to ethanol dehydrogenation has been investigated by TPD on Co model catalyst supported on YSZ [61, 62]. It was observed that both Co and Co<sup>2+</sup> are active for dehydrogenation and selective to acetaldehyde formation, which is also coherent to our study at ambient pressure. The high amount of acetaldehyde produced also reveals that acetaldehyde formed cannot be activated for further reforming or decomposition at this temperature. The low amount of water utilization relative to ethanol over Co oxide also implies that reforming reaction is a minor reaction under this condition (in accordance with thermodynamic considerations). According to reaction stoichiometry, 6 hydrogen molecules are produced in an ideal ESR reaction. The production of hydrogen is higher when reforming reaction is involved. This also explains the relatively minor hydrogen production with the high level of ethanol consumption on Co oxide.

The relative selectivity of CO is the lowest over metallic Nickel. Methane is the resultant product of ethanol decomposition, which also produces CO and H<sub>2</sub> (equation 6.5). Since production of CO is rather minor relative to CH<sub>4</sub>, some of the CO could have further reacted with H<sub>2</sub>O by water-gas shift reaction. This is a viable pathway given the exothermic and less energy dependent nature of the reaction. An opposite tendency is shown over Co and Co oxide as CO production is much more significant relative to CH<sub>4</sub>. It can also be noted that although a significant surface fraction on Ni-Co powder is composed by Co, the reactivity pattern is rather different from Co catalyst since production of acetaldehyde is almost negligible. In addition, selectivity to hydrogen on Ni and Ni-Co is much higher. Despite the significant surface atomic fraction of Co, Ni is the component that dominates the reactivity of bimetallic Ni-Co.

The O 1s spectra of Ni, Ni-Co nanopowder, Ni and Co planar surface under reaction conditions at 543 K are shown in figure 6.8. The components at binding energy higher than 534 eV originate mainly from gas phase water and ethanol. The rest of the O 1s peak can be deconvoluted into the following components: (1) surface adsorbed carbonyl group (530.5 eV, [63]) (2) hydroxyl group (531.8-532 eV, [64]) and adsorbed water (533 eV, [64]). The proportion of each O 1s component on Ni-Co and Ni powder is highly comparable. The proportion of adsorbed -OH group to the overall O 1s peak on Co, however, is significantly lower than that on Ni foil (figure 6.8b). Water can adsorb by dissociation into surface hydrogen atom and hydroxyl group on metal surface. The dissociation is reversible when hydroxyl group and hydrogen are formed as products of water dissociation. It can also take place as irreversible dissociation, where water molecule is dissociated as Hydrogen gas and O atom. At low temperature, water tends to adsorb as molecule on both Ni and Co. Water dissociation into adsorbed atomic oxygen and hydrogen has been observed on Co (0001)

[65] at room temperature. Below this temperature water dissociation is reversible. Water can be decomposed into H and O at temperature as low as at 210 K on Co (1120) or polycrystalline Co[66]. The dissociation of water depends largely on the surface structure and the availability of defect sites of the metals. The interaction of water on Co oxide is much lower and water is adsorbed molecularly on oxidized Co (0001)[65]. This is coherent with the low water consumption observed on oxidized Co nanopowder shown in figure 6.6. Irreversible dissociation of water into atomic H and O has been observed on a few single crystal surfaces such as Ni (760) [67] and Ni (110) [68, 69], but at a higher temperature (>400 K). It is generally believed that water dissociation on Ni surface is an auto-catalytic reaction, that dissociation can only be accelerated on surface pre-adsorbed with O[67]. This could be a reason for the high amount of surface hydroxyl group observed on Ni and Ni-Co powder, which are produced as a result of reversible water dissociation. Due to the relatively high amount of carbon deposition on Co powder, the signal to noise ratio of the C 1s peak on Co has been affected. Therefore the O 1s spectra from planar Ni and Co were shown in figure 6.8. The different in surface geometry of Co single crystal to Ni foil to water adsorption may also contribute to the difference in water adsorption on these two metals.

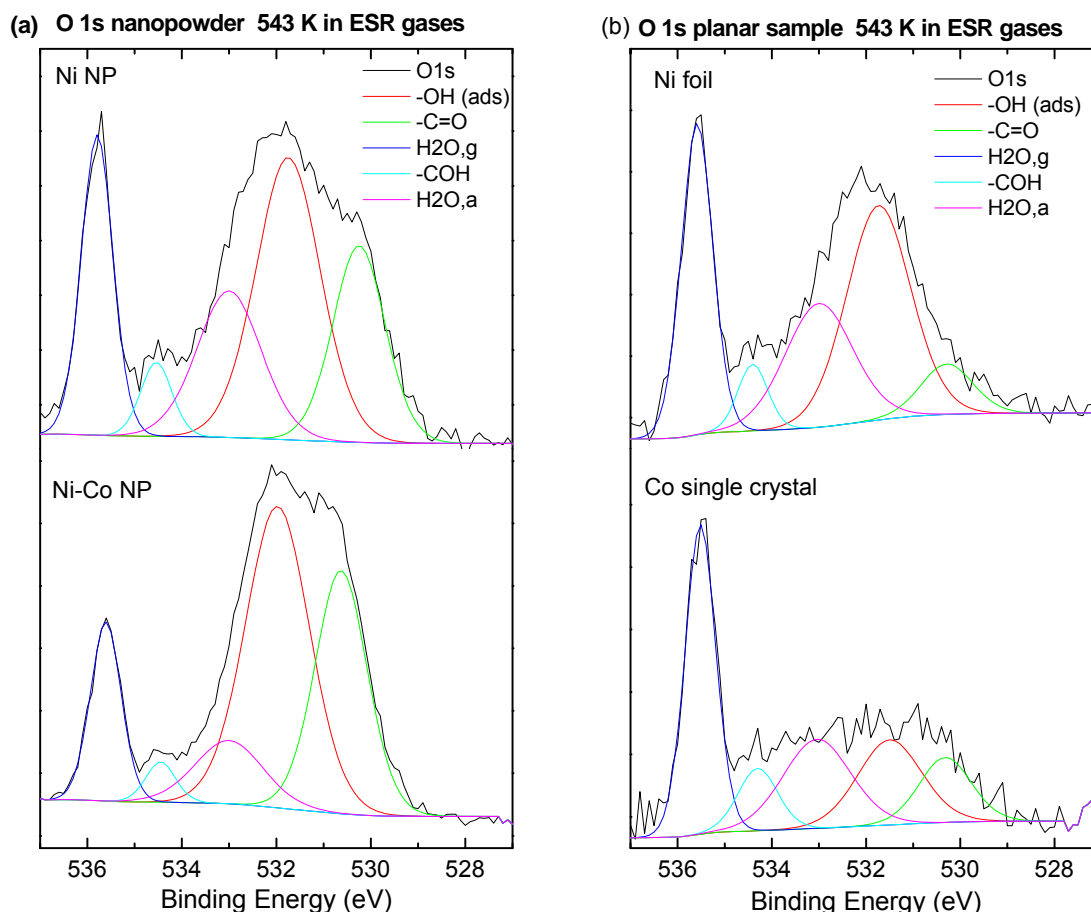


Figure 6.8 (a) O 1s spectra of pre-reduced Ni and Ni-Co nanopowder in ESR gases (0.2 mbar ethanol+water in ratio 1:3) at 543 K (b) O 1s spectra of pre-reduced Ni foil and Co single crystal in ESR gases (0.2 mbar ethanol+water in ratio 1:3) at 543 K

The number of surface –OH group influences the reforming reaction. Therefore for Co surface, where the available of surface OH- group is lower, products resulting from reforming reaction are also lower. Thus on Ni and Ni-Co nanopowder, where there is higher contribution of adsorbed water, enjoys higher ethanol reforming and less decomposition.

### 6.3.4 Steady state reaction of 623 K

As mentioned before, at 623 K, samples are reduced to metallic Ni and Co in ESR gases independent of their pretreatment. The Co L-edge and Ni  $2p_{3/2}$  spectra under reaction conditions at 623 K are shown in figure 6.9a and 6.9b. In comparison to reaction at 543 K, surface atomic ratio of Ni/Co has increased significantly as Ni-Co is reduced in ESR gases. At steady state, the atomic ratio of Ni:Co between the samples pretreated in  $O_2$  and  $H_2$  is very similar (figure 6.9c). The surface oxidation state and composition of Ni and Co in ESR stream at this temperature resembles very much the Ni-Co powders reduced in  $H_2$  at similar temperature (shown in figure 6.1).

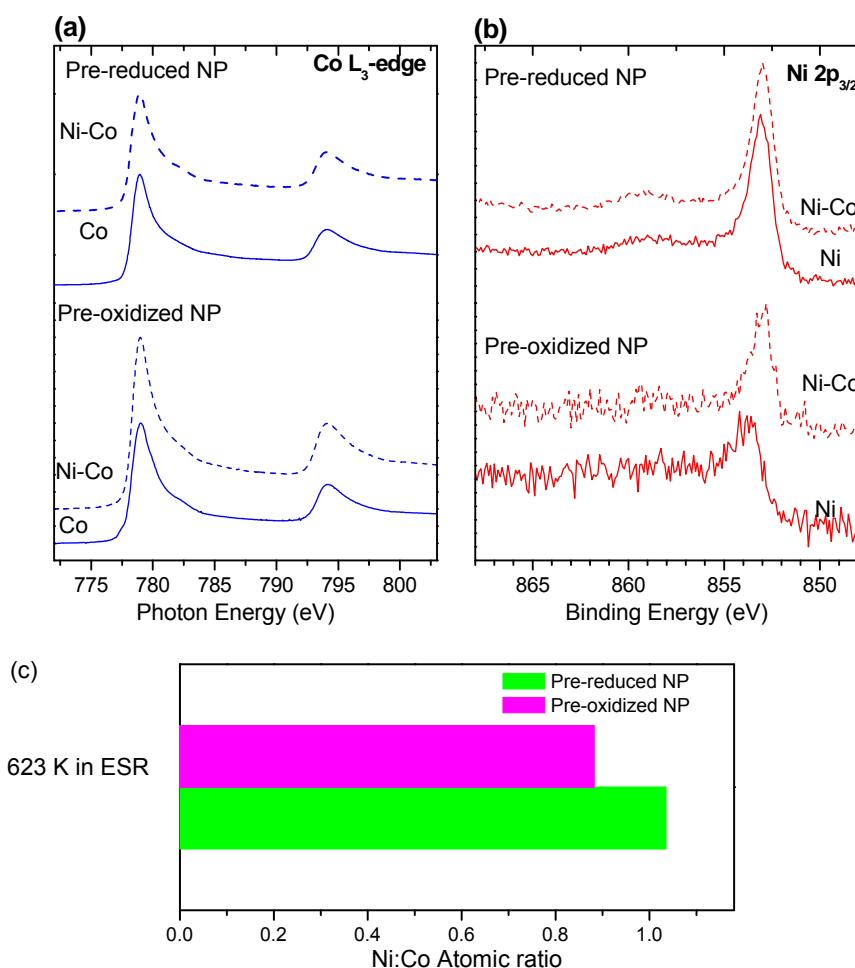
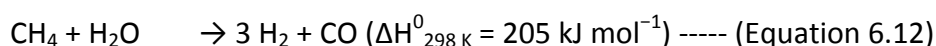


Figure 6.9 (a) Co L3 edge of pre-oxidized ( $O_2$ , 623 K) and pre-reduced ( $H_2$ , 623 K) Co nanopowder(NP) and Ni-Co NP (b) Ni  $2p_{3/2}$  spectra of Ni NP and Ni-Co NP in ESR reaction gas mixture (ethanol to steam ratio=1:3) at 623 K. (c) atomic ratio of Ni-Co bimetallic nanopowder

As the samples pretreated by oxidation and reduction are both in metallic state under reaction conditions and show very similar reactivity pattern, only results on pre-reduced sample are shown at this reaction temperature. The overall ethanol conversion on all materials is significantly higher at 623 K than 543 K. The ethanol consumption on nickel is the lowest. However in comparison to reaction at 543 K, conversion over bimetallic catalyst becomes the highest among all materials. In addition, the consumption of water on Ni and Ni-Co surpasses the consumption of ethanol. This gives evidence to the increase in the activity of steam reforming reaction compared to other reaction pathway in comparison to the reaction at 543 K.

Observed from other catalytic studies on Ni and Co catalysts [1, 70] and thermodynamic studies of ESR [71, 72], ethanol tends to undergo decomposition at low temperature as most decomposition pathways are exothermic. Steam reforming reactions on ethanol or other intermediates such as methane and acetaldehyde are endothermic, and are favoured at higher temperature. This can be reflected particularly on reaction products over Ni and Ni-Co, where the relative selectivity to methane compared to reaction at 543 K has reduced to a very low level. The selectivity pattern of all catalyst is similar to that found at lower temperature, but being less selective to intermediate like acetaldehyde and methane.

The major reaction products over Ni and Ni-Co catalysts are CO, CO<sub>2</sub> and H<sub>2</sub> at 623 K, while the relative selectivity of methane is reduced. The methyl group in ethanol molecule is the major group leading to methane formation. As temperature increases, the methyl group, which desorbs as methane at low temperature, may further decompose to hydrogen and carbon. Reforming of methane may also be a probable reaction to the increase in production of CO and H<sub>2</sub>:



Co metal is less selective to H<sub>2</sub> and CO<sub>2</sub> in comparison to Ni and Ni-Co, and the overall reaction remains to be very selective to C<sub>2</sub>H<sub>4</sub>O and CO as at 543 K. From figure 6.10a, water consumption on Co is still inferior to ethanol consumption, showing that decomposition of ethanol remains still as the more important reaction path on cobalt despite the increase in overall ethanol conversion at this temperature. In addition, the production of CO relative to C<sub>2</sub>H<sub>4</sub>O has increased at 623 K, which also suggests that CO is produced in the expense of C<sub>2</sub>H<sub>4</sub>O, that acetaldehyde is utilized by further reaction. Shown in the ethanol thermal desorption study in previous chapter, CO and H<sub>2</sub> is the major product from ethanol decomposition on Co. Therefore acetaldehyde decomposition is one of the possible pathway. In addition, reforming of acetaldehyde on cobalt based catalyst in this temperature range has been observed in some other studies [73, 74]. This suggests the likelihood of the reforming acetaldehyde or the ethoxy group on Co:



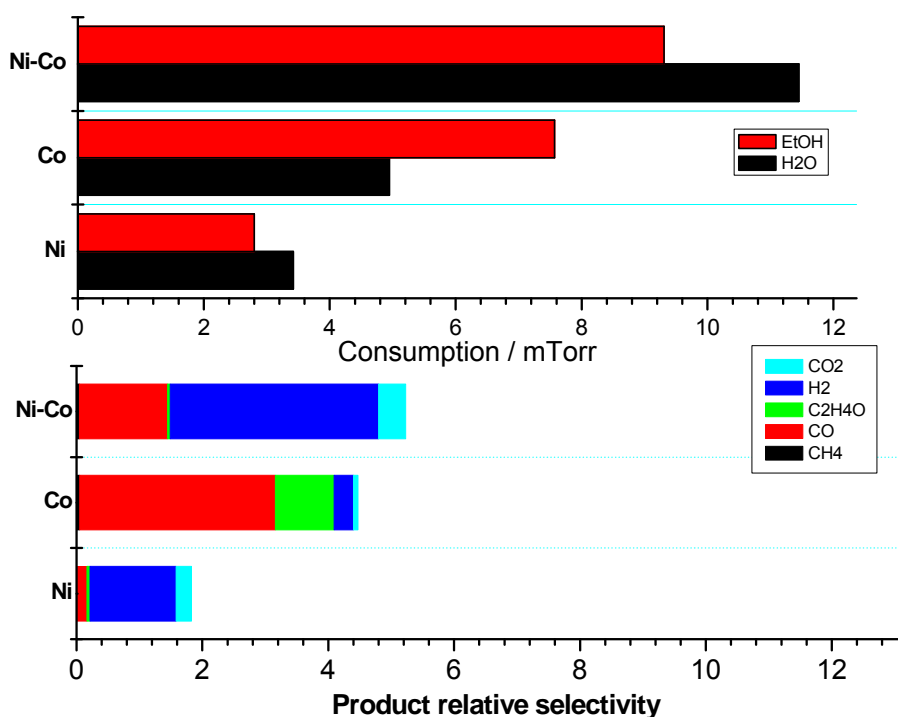
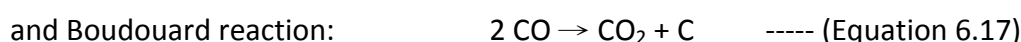
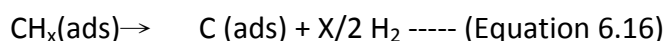


Figure 6.10 (a) Steady state water and ethanol consumption (b) Relative production of ethanol steam reforming product on Ni, Co and Ni-Co nanopowder pretreated in 0.2 mbar of  $H_2$

### 6.3.5 Carbon formation during ESR process in different temperature range

Carbon formation is the major disadvantage for Ni and Co based catalyst for ESR. The major carbon formation pathways include methane or adsorbed methyl group decomposition:



The level of surface carbon formation can be studied by the analysis of carbon C 1s peak, which is shown in figure 6.11. The deconvolution of C 1s peak has been described earlier. The intensity of C1s peak is much lower at 543 K, showing that carbon formation is at a lower level at low temperature. The carbon to metal atomic ratio is less than 2 at 543 K, in which the high intensity C 1s component is from graphitic carbon.

The intensities of ethoxide groups ( $-CH_2O-$ ) and carboxyl groups ( $CH_3COO-$  and  $HCOO-$ ) remain quite stable during reaction at both 543 K and 623 K. The most apparent difference is the vast increase of graphitic carbon and  $CH_x-$  group. As ethanol conversion increases at 623 K, graphitic carbon builds up in a very high amount. On reduced Ni-Co, it is obvious that  $CH_x-$  group at 543 K is of low intensity in comparison to other adsorbed carbon species. Its composition to C 1s increases as reaction temperature increases, surpassing other C species

at 623 K apart from graphitic carbon. As methane production decreases at 623 K, it is likely that the methyl group desorbs as methane at low temperature and undergoes dehydrogenation as temperature rises (equation 6.16). Thus at high temperature, surface adsorbed methyl group and the amount of graphitic carbon increases, and the relative selectivity to hydrogen also increases.

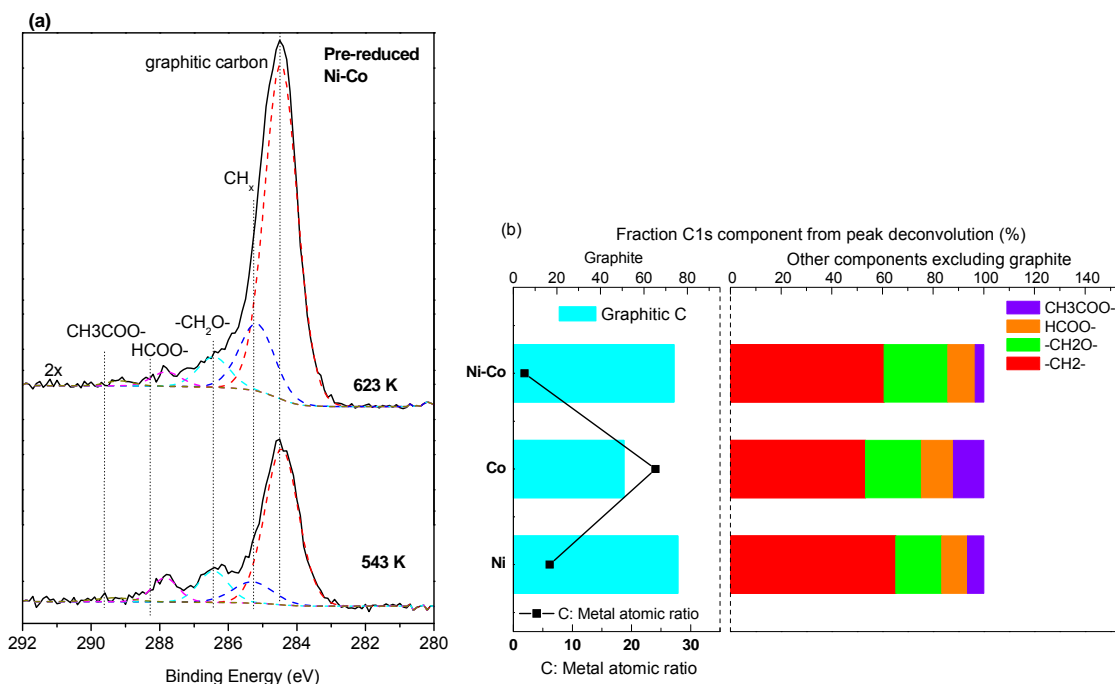


Figure 6.11 (a) C 1s spectra and deconvolution of pre-reduced Ni-Co at 543 K and 623 K. (b) Surface carbon ratio(■) and the fraction of graphitic C to the C 1s spectra, the fraction of other carbon species to the C 1s peak (calculated excluding graphitic C) over pre-reduced Ni, Co and Ni-Co catalysts in ESR gases (0.2 mbar ethanol and H<sub>2</sub>O in ratio 3:1) at 623 K.

The right side of Figure 6.11 summarizes the proportion of different carbon species to C1s peak calculated based only on the deconvoluted peaks other than graphitic carbon. The surface carbon to metal atomic ratio on Ni, Co and Ni-Co at 623 K is shown on the left side. At 623 K, over Ni-Co catalyst the lowest amount of carbon is generated while cobalt is the most susceptible to carbon formation. Carbon deposition on Co is the highest among all metals. As the level of CO production on Co is much higher than other metal catalysts, Boudouard reaction could be a probable reaction path for carbon deposition on Co. As shown in figure 6.10, CO production on Ni containing catalyst is much more limited. This can rationalize the improvement in carbon formation on bimetallic materials.

## 6.4 Conclusions

In this study, ethanol steam reforming on Ni, Co and Ni-Co nanopowder was studied under working condition (0.2 mbar of reaction gases) by *in-situ* APPEs, NEXAFS and online mass spectroscopy in order to understand the influence of bimetallic synergy to the catalytic performance. The impact of oxide formation to the catalyst has also been discussed. The redox properties of Ni-Co nanopowder were also studied in pure H<sub>2</sub> in order to understand

the basic bimetallic interaction of Ni-Co with respect to its monometallic counterpart in this pressure range. Reduction of cobalt in either monometallic form and bimetallic form proceeds in a similar way, while nickel oxide reduction for bimetallic Ni-Co takes place at a much higher temperature compared to monometallic nickel. For bimetallic Ni-Co oxide, reduction of  $\text{Co}_3\text{O}_4$  proceeds in prior to other reaction as reduction of  $\text{Co}_3\text{O}_4$  to CoO is thermodynamically the most favourable reaction. Ethanol steam reforming mixture (0.2 mbar with ethanol and water in a flow ratio of 1:3) provides a reducing environment, in which Ni, Co and Ni-Co oxides are reduced. At 543 K,  $\text{Co}_3\text{O}_4$  is reduced to CoO, while NiO remains oxidized. At 623 K, all surface metal oxides are reduced to metal form.

$\text{H}_2$ ,  $\text{CH}_4$ , CO,  $\text{C}_2\text{H}_4\text{O}$  and  $\text{CO}_2$  are the major products generated when the catalysts are exposed to the reaction gases. At low temperature (543 K), ethanol conversion is higher on oxidized catalysts as apart from ethanol reforming or decomposition. Ethanol could be consumed additionally through oxidation. Relative product selectivity to  $\text{C}_2\text{H}_4\text{O}$  and CO is much higher on Co than Ni and Ni-Co, while production of  $\text{CH}_4$  is more pronounced on Ni containing catalyst. Though cobalt surface atomic ratio is more than 50% on both pre-reduced and pre-oxidized Ni-Co powder, its influence to the product selectivity of bimetallic catalysts seems rather limited. One possible reason is that the availability of hydroxyl groups on Ni containing catalyst is higher and can promote reforming reaction more efficiently. Thus there is no dominance of ethanol dehydrogenation on bimetallic materials. At 623 K, selectivity to intermediate products such as  $\text{C}_2\text{H}_4\text{O}$  and  $\text{CH}_4$  is largely reduced. On Ni and Ni-Co, the consumption of water and production of  $\text{H}_2$  and  $\text{CO}_2$  increase, indicating the increasing importance of reforming reaction to the overall ethanol conversion against other reaction pathways. The carbon level at 623 K also increases largely. One of the major causes for carbon deposition is methyl group decomposition, which increases with temperature. The high level of carbon deposition on Co and its high relative selectivity to CO also suggests that Boudouard reaction could be an important factor for carbon contamination over Co based catalysts.

## 6.5 References

- [1] A.N. Fatsikostas, X.E. Verykios, *J. Catal.* 225 (2004) 439-452.
- [2] F. Frusteri, S. Freni, V. Chiodo, L. Spadaro, O. Di Blasi, G. Bonura, S. Cavallaro, *Appl Catal A Gen.* 270 (2004) 1-7.
- [3] J. Llorca, N. Homs, J. Sales, P. Ramírez de la Piscina, *Journal of Catalysis.* 209 (2002) 306-317.
- [4] P. Bichon, G. Haugom, H.J. Venvik, A. Holmen, E.A. Blekkan, *Top. Catal.* (2008) 1-8.
- [5] F. Haga, T. Nakajima, H. Miya, S. Mishima, *Catal. Lett.* 48 (1997) 223-227.
- [6] S. Freni, S. Cavallaro, N. Mondello, L. Spadaro, F. Frusteri, *Catalysis Communications.* 4 (2003) 259-268.
- [7] J. Sun, X.P. Qiu, F. Wu, W.T. Zhu, *Int. J. Hydrogen Energy* 30 (2005) 437-445.
- [8] J. Llorca, P. Ramírez De La Piscina, J.A. Dalmon, J. Sales, N. Homs, *Applied Catalysis B: Environmental.* 43 (2003) 355-369.
- [9] F. Frusteri, S. Freni, L. Spadaro, V. Chiodo, G. Bonura, S. Donato, S. Cavallaro, *Catal. Commun.* 5 (2004) 611-615.
- [10] A.M. Karim, Y. Su, J. Sun, C. Yang, J.J. Strohm, D.L. King, Y. Wang, *Applied Catalysis B: Environmental.* 96 (2010) 441-448.
- [11] S.M. De Lima, A.M. Da Silva, L.O.O. Da Costa, U.M. Graham, G. Jacobs, B.H. Davis, L.V. Mattos, F.B. Noronha, *Journal of Catalysis.* 268 (2009) 268-281.
- [12] J. Kugai, S. Velu, C. Song, *Catalysis Letters.* 101 (2005) 255-264.
- [13] N. Homs, J. Llorca, P.R. de la Piscina, *Catalysis Today.* 116 (2006) 361-366.
- [14] F.J. Mariño, E.G. Cerrella, S. Duhalde, M. Jobbagy, M.A. Laborde, *Int. J. Hydrogen Energy* 23 (1998) 1095-1101.
- [15] A. Casanovas, M. Roig, C. De Leitenburg, A. Trovarelli, J. Llorca, *International Journal of Hydrogen Energy.* 35 (2010) 7690-7698.
- [16] H. Song, U.S. Ozkan, *Journal of Catalysis.* 261 (2009) 66-74.
- [17] Z. Zhong, H. Ang, C. Choong, L. Chen, L. Huang, J. Lin, *Physical Chemistry Chemical Physics.* 11 (2009) 872-880.
- [18] S.S.Y. Lin, D.H. Kim, S.Y. Ha, *Catalysis Letters.* 122 (2008) 295-301.
- [19] J.W.C. Liberatori, R.U. Ribeiro, D. Zanchet, F.B. Noronha, J.M.C. Bueno, *Applied Catalysis A: General.* 327 (2007) 197-204.
- [20] M.P. Hyman, J.M. Vohs, *Surf. Sci.* 605 (2011) 383-389.
- [21] E. Martono, M.P. Hyman, J.M. Vohs, *Physical Chemistry Chemical Physics.* 13 (2011) 9880-9886.
- [22] A.M. Karim, Y. Su, M.H. Engelhard, D.L. King, Y. Wang, *ACS Catalysis.* 1 (2011) 279-286.
- [23] E. Martono, M.P. Hyman, J.M. Vohs, *Physical Chemistry Chemical Physics.* 13 (2011).
- [24] H. Song, X. Bao, C.M. Hadad, U.S. Ozkan, *Catalysis Letters.* 141 (2011) 43-54.
- [25] J. Xu, X. Zhang, R. Zenobi, J. Yoshinobu, Z. Xu, J.T. Yates Jr, *Surface Science.* 256 (1991) 288-300.
- [26] J.M. Guil, N. Homs, J. Llorca, P.R. De La Piscina, *Journal of Physical Chemistry B.* 109 (2005) 10813-10819.
- [27] J. Llorca, J.A. Dalmon, P. Ramírez De la Piscina, N. Homs, *Appl. Catal. A Gen.* 243 (2003) 261-269.
- [28] J. Llorca, N. Homs, P. Ramirez de la Piscina, *Journal of Catalysis.* 227 (2004) 556-560.
- [29] M.P. Hyman, E. Martono, J.M. Vohs, *Journal of Physical Chemistry C.* 114 (2010) 16892-16899.

**Chapter 6 Ambient Pressure Photoemission Spectroscopy (APPEs) and Near-Edge X-ray Absorption Spectroscopy (NEXAFS) study of Ni-Co bimetallic catalyst for ethanol steam reforming**

- [30] Y.T. Law, T. Skála, I. Píš, V. Nehasil, M. Vondráček, S. Zafeiratos, *Journal of Physical Chemistry C*. 116 (2012) 10048-10056.
- [31] C.N. de Ávila, C.E. Hori, A.J. de Assis, *Energy*. 36 (2011) 4385-4395.
- [32] V.A. de la Peña O'Shea, N. Homs, E.B. Pereira, R. Nafria, P. Ramírez de la Piscina, *Catalysis Today*. 126 (2007) 148-152.
- [33] L. He, H. Berntsen, E. Ochoa-Fernández, J.C. Walmsley, E.A. Blekkan, D. Chen, *Topics in Catalysis*. 52 (2009) 206-217.
- [34] C. Resini, M. Concepción Herrera Delgado, S. Presto, L.J. Alemany, P. Riani, R. Marazza, G. Ramis, G. Busca, *International Journal of Hydrogen Energy*. 33 (2008) 3728-3735.
- [35] J.J. Yeh, *Atomic Calculation of Photoionization Cross-sections and Asymmetry Parameters*, Gordon and Breach Science Publishers, Langhorne, PE, USA, 1993.
- [36] J.J. Yeh, I. Lindau, *Atomic Data and Nuclear Data Tables*. 32 (1985) 1-155.
- [37] Y.T. Law, T. Dintzer, S. Zafeiratos, *Applied Surface Science*. 258 (2011) 1480-1487.
- [38] A.V. Ruban, H.L. Skriver, J.K. Nørskov, *Physical Review B - Condensed Matter and Materials Physics*. 59 (1999) 15990-16000.
- [39] *Lange's handbook of chemistry*, 15th Edition ed., McGraw-Hill, Inc., 1999.
- [40] Q. Jeangros, T.W. Hansen, J.B. Wagner, C.D. Damsgaard, R.E. Dunin-Borkowski, C. Hébert, J. Van herle, A. Hessler-Wyser, *Journal of Materials Science* (2012) 1-15.
- [41] J.T. Richardson, R. Scates, M.V. Twigg, *Applied Catalysis A: General*. 246 (2003) 137-150.
- [42] J. Łojewska, W. Makowski, T. Tyszewski, R. Dziembaj, *Catalysis Today*. 69 (2001) 409-418.
- [43] B. Bayram, I.I. Soykal, D. Von Deak, J.T. Miller, U.S. Ozkan, *Journal of Catalysis*. 284 (2011) 77-89.
- [44] S.S.Y. Lin, D.H. Kim, M.H. Engelhard, S.Y. Ha, *Journal of Catalysis*. 273 (2010) 229-235.
- [45] S. Tuti, F. Pepe, *Catalysis Letters*. 122 (2008) 196-203.
- [46] S.C. Petitto, E.M. Marsh, G.A. Carson, M.A. Langell, *J. Mol. Catal. A: Chem.* 281 (2008) 49-58.
- [47] G.A. Carson, M.H. Nassir, M.A. Langell, 1995, pp. 163-168.
- [48] T.J. Chuang, C.R. Brundle, D.W. Rice, *Surf. Sci.* . 59 (1976) 413-429.
- [49] V. Papaefthimiou, T. Dintzer, V. Dupuis, A. Tamion, F. Tournus, A. Hillion, D. Teschner, M. Hävecker, A. Knop-Gericke, R. Schlögl, S. Zafeiratos, *ACS Nano*. 5 (2011) 2182-2190.
- [50] C.J. Powell, *Journal of Electron Spectroscopy and Related Phenomena*. 185 (2012) 1-3.
- [51] M. Ebrahimi, J. Fernando Rios, K.T. Leung, *The Journal of Physical Chemistry C*. 113 (2008) 281-289.
- [52] Y.K. Kim, C.-C. Hwang, *Surface Science*. 605 (2011) 2082-2086.
- [53] L. Liu, B.R. Quezada, P.C. Stair, *The Journal of Physical Chemistry C*. 114 (2010) 17105-17111.
- [54] A.M. Nadeem, J.M.R. Muir, K.A. Connelly, B.T. Adamson, B.J. Metson, H. Idriss, *Physical Chemistry Chemical Physics*. 13 (2011) 7637-7643.
- [55] S. Zafeiratos, T. Dintzer, D. Teschner, R. Blume, M. Hävecker, A. Knop-Gericke, R. Schlögl, *Journal of Catalysis*. 269 (2010) 309-317.
- [56] K.W. Wulser, M.A. Langell, *Catalysis Letters*. 15 (1992) 39-50.
- [57] C. Resini, T. Montanari, L. Barattini, G. Ramis, G. Busca, S. Presto, P. Riani, R. Marazza, M. Sisani, F. Marmottini, U. Costantino, *Applied Catalysis A: General*. 355 (2009) 83-93.
- [58] J. Raskó, M. Dömök, K. Baán, A. Erdőhelyi, *Applied Catalysis A: General*. 299 (2006) 202-211.
- [59] M. Dömök, M. Tóth, J. Raskó, A. Erdőhelyi, *Applied Catalysis B: Environmental*. 69 (2007) 262-272.
- [60] J.H. Wang, C.S. Lee, M.C. Lin, *Journal of Physical Chemistry C*. 113 (2009) 6681-6688.

**Chapter 6 Ambient Pressure Photoemission Spectroscopy (APPEs) and Near-Edge X-ray Absorption Spectroscopy (NEXAFS) study of Ni-Co bimetallic catalyst for ethanol steam reforming**

- [61] E. Martono, J.M. Vohs, *Journal of Catalysis*. 291 (2012) 79-86.
- [62] E. Martono, J.M. Vohs, *ACS Catalysis*. 1 (2011) 1414-1420.
- [63] D. Teschner, A. Wootsch, O. Pozdnyakova-Tellingner, J. Kröhnert, E.M. Vass, M. Hävecker, S. Zafeiratos, P. Schnörch, P.C. Jentoft, A. Knop-Gericke, R. Schlögl, *Journal of Catalysis*. 249 (2007) 318-327.
- [64] J.T. Newberg, D.E. Starr, S. Yamamoto, S. Kaya, T. Kendelewicz, E.R. Mysak, S. Porsgaard, M.B. Salmeron, G.E. Brown Jr, A. Nilsson, H. Bluhm, *Surface Science*. 605 (2011) 89-94.
- [65] L. Xu, Y. Ma, Y. Zhang, B. Chen, Z. Wu, Z. Jiang, W. Huang, *Journal of Physical Chemistry C*. 114 (2010) 17023-17029.
- [66] J.M. Heras, H. Papp, W. Spiess, *Surface Science*. 117 (1982) 590-604.
- [67] R.V. Kasza, K. Griffiths, J.G. Shapter, P.R. Norton, D.A. Harrington, *Surface Science*. 356 (1996) 195-208.
- [68] L. Olle, M. Salmeron, A.M. Baro, *Journal of Vacuum Science & Technology A: Vacuum, Surfaces, and Films*. 3 (1985) 1866-1870.
- [69] B.W. Callen, K. Griffiths, P.R. Norton, D.A. Harrington, *Journal of Physical Chemistry*. 96 (1992) 10905-10913.
- [70] H. Song, L. Zhang, R.B. Watson, D. Braden, U.S. Ozkan, *Catalysis Today*. 129 (2007) 346-354.
- [71] V. Mas, R. Kipreos, N. Amadeo, M. Laborde, *International Journal of Hydrogen Energy*. 31 (2006) 21-28.
- [72] K. Vasudeva, N. Mitra, P. Umasankar, S.C. Dhingra, *International Journal of Hydrogen Energy*. 21 (1996) 13-18.
- [73] R. Padilla, M. Benito, L. Rodríguez, A. Serrano, G. Muñoz, L. Daza, *International Journal of Hydrogen Energy*. 35 (2010) 8921-8928.
- [74] M. Benito, R. Padilla, A. Serrano-Lotina, L. Rodríguez, J.J. Brey, L. Daza, *Journal of Power Sources*. 192 (2009) 158-164.

---

# Chapter 7

## General conclusions and perspectives

---

---

---

---

## Chapter 7. General conclusions and perspectives

### 7.1 General conclusions

Bimetallic catalysts are developed for chemical processes to improve the overall efficiency of the catalyst by the synergetic effects between the two metals. The bimetallic interaction causes formation of different structures, which modify reactant adsorption on the catalysts. The interest of this study is to comprehend how bimetallic interaction is manifested in different environments and its potential influence to the catalytic process. Benefits of bimetallic interaction on the improvement of carbon resistance and enhancement of catalytic activity on ethanol steam reforming have been observed [1-5]. Attention was also drawn to the choice of metal oxide support, which has been proven to be a critical factor for catalyst deactivation [6, 7]. In this work, surface techniques were applied to carry out a detailed characterization of Ni-Co based bimetallic catalyst supported on ZnO single crystal and to investigate its dynamic behaviour in reaction environment.

This work started with material characterization and investigation of bimetallic interaction between Ni and Co as a bulk material, followed by the study of metal support interaction between Ni-Co thin overlayer and ZnO substrate. Having obtained the fundamental knowledge on Ni-Co and Ni-Co/ZnO in a material perspective, the investigation was extended to the study of catalytic reactions. Surface adsorption and reaction pathway of ethanol on ZnO supported Ni-Co was studied by TDS. Most studies of the model catalyst were conducted in UHV, where the surface phenomena observed may not correspond directly to actual operation conditions. Thus the catalytic performance of Ni, Co and Ni-Co and the reaction mechanism were also studied by *in-situ* ambient pressure XPS, in order to understand the surface characteristics of Ni-Co in reaction conditions at different pressure range.

The synergetic effect between the two bimetallic components during the initial stages of oxidation was investigated and presented in chapter 3. Oxidation of planar polycrystalline NiCo bimetallic foil was studied under two pressure regimes,  $5 \times 10^{-10}$  and  $5 \times 10^{-1}$  bar, by X-ray photoelectron spectroscopy (XPS). At low oxygen pressure, preferential oxidation of cobalt takes place while oxidation of nickel is largely suppressed on Ni-Co bimetallic foil compared to pure Ni or Co. The dominating species on the surface is CoO but small amount of metallic cobalt still remains even after prolonged oxidation at 670 K. Co surface segregation occurs in oxidative environment and the surface composition of Ni to Co decreases. In high O<sub>2</sub> pressure (0.5 bar), Ni-Co oxidation at low temperature is coherent to its behaviour at low O<sub>2</sub> pressure. From 420 K to 520 K, surface cobalt is oxidized as CoO and Ni:Co atomic ratio at the surface decreases and approaches a minimum, similar to the observations in low pressure regime. At higher temperatures (from 520K to 720K), CoO is further oxidized to Co<sub>3</sub>O<sub>4</sub>. Nickel is re-segregated onto the surface and surface Ni:Co atomic ratio rebounds. Formation of mixed Ni-Co-O spinel-like oxides is a probable cause for the re-diffusion of Ni

to the surface at high temperature range. This is also supported by the modifications of the characteristic feature of Ni2p<sub>3/2</sub> satellite peak.

In Chapter 4, the interaction of thin bimetallic Ni-Co layers (0.25 and 1.5 nm) supported on polar (0001)-Zn and (000 $\bar{1}$ )-O ZnO substrates was investigated by synchrotron-based photoelectron spectroscopy (PES) under ultra-high vacuum (UHV) and O<sub>2</sub> environments. Monometallic Ni and Co layers were also characterized to highlight the influence of Ni-Co synergetic effects to the metal-support interaction. For an as-deposited Ni-Co thin layer, cobalt is partially oxidized and nickel is in metallic state. More prominent oxidizing effect was observed on O-terminated ZnO due to the interaction of Ni-Co with the more abundant surface hydroxyl group on ZnO-O surface. Oxidation of monometallic Ni and Co layers is promoted upon annealing at 773 K in UHV, but it has little influence on bimetallic Ni-Co. In addition, significant agglomeration of the Ni-Co overlayer is observed, with higher surface Co content than Ni in this agglomerated layer. Agglomeration of Ni-Co is more pronounced on O-terminated ZnO. Upon annealing in 1x10<sup>-6</sup> mbar O<sub>2</sub> both Ni and Co is readily oxidized and form NiO and CoO, and the agglomerated Ni-Co layer re-disperses over ZnO substrate. Moreover, cobalt tends to segregate over nickel, creating a concentration gradient between the two alloy constituents (probably a core-shell-like structure). Overall our results indicate that the interaction at Ni-Co/ZnO interface is influenced by synergetic effects between the two metals and to a lesser extent by the substrate termination. Metal-support interaction between Ni-Co and ZnO induces oxidation of the bimetallic layer, but the extent of oxidation is more limited in comparison to a pure metal layer. The oxidation behaviour is mainly governed by bimetallic interaction of Ni-Co, that preferential oxidation of Co takes place, as observed for the bulk Ni-Co system in chapter 3.

Chapter 5 is devoted to the investigation of ethanol surface reaction on ZnO-Zn (0001) supported Ni-Co thin layers (~1.2nm) by TDS. The modification on the chemical composition and oxidation state of the Ni-Co film due to heating during TDS was characterized by XPS. Dehydrogenation is the primary reaction step of ethanol decomposition, which results in the formation of adsorbed ethoxy group and hydrogen. The ethoxy group either transforms to acetaldehyde by further dehydrogenation or undergoes further decomposition. On bare ZnO-Zn single crystal surface, ethanol decomposes into C<sub>2</sub>H<sub>4</sub>O, H<sub>2</sub>O, H<sub>2</sub> and C<sub>2</sub>H<sub>4</sub> by two major reaction pathways, namely, dehydration and dehydrogenation. Further decomposition of ethoxy group was not observed on ZnO.

Supported Ni and Co layers are much more efficient in C-C bond breaking and C-H bond breaking than bare ZnO. This results in the further decomposition of ethoxy group, which occurs in different reaction pathway on Ni and on Co layers. H<sub>2</sub> and CO were found to be the common decomposition products of ethoxy decomposition on both Ni and Co thin layers, but the generation of methane takes place almost exclusively on Ni thin layers. Ethoxy group is decomposed via C-C bond scission on supported Ni layers, forming adsorbed methyl group and C-O which desorbs as CH<sub>4</sub> and CO respectively. On Co/ZnO-Zn, ethoxy is adsorbed as oxametallacycle, such that the methyl group remains adsorbed and undergoes further

dehydrogenation. Consequently, the decomposition of ethoxy group results only in desorption of H<sub>2</sub> and CO on Co/ZnO-Zn. Thus desorption of hydrogen is inversely correlated to desorption of methane as the reaction pathway for hydrogen formation is in competition with methane generation. The selection of methane or hydrogen production does not vary linearly with Ni and Co composition, but is determined rather by dominating metal species. Thus at a concentration where Co is more abundant (Ni composition < 0.6), the increase in Ni content only increases mildly the methane to hydrogen production ratio. When Ni content surpasses this critical level and becomes the more abundant species, increase in Ni content affects the production of methane more significantly.

The influence of bimetallic synergy of Ni-Co to activity and product selectivity of ethanol steam reforming was studied by *in-situ* APPEs, NEXAFS and online mass spectrometry and discussed in chapter 6. The oxidation state and surface composition of Ni-Co were confirmed by these *in-situ* techniques. The reduction of Ni-Co nanopowder was studied in 0.2 mbar H<sub>2</sub> in order to understand the basic bimetallic interaction of Ni-Co with respect to its monometallic counterpart in this pressure range. The reduction of cobalt takes place as a two step process. Co<sub>3</sub>O<sub>4</sub> is reduced to CoO firstly at low temperature, followed by the simultaneous reduction of NiO and CoO at higher temperature. According to the thermodynamics of cobalt reduction, reduction of Co<sub>3</sub>O<sub>4</sub> is more favourable than reduction of nickel and takes place as the first step. ESR reaction on pre-reduced and pre-oxidized Ni, Co and Ni-Co were compared and the influence of metal oxide formation to its catalytic activities was discussed. ESR gases (0.2 mbar with ethanol and water in a flow ratio of 1:3) provide a reducing environment, in which Co<sub>3</sub>O<sub>4</sub> is reduced to CoO at low temperature and pre-oxidized Ni and Co is in form of NiO and CoO at 543 K. At 623 K, all reduction of metal oxide is complete and pre-oxidized Ni and Co changes to metallic state.

H<sub>2</sub>, CH<sub>4</sub>, CO, C<sub>2</sub>H<sub>4</sub>O and CO<sub>2</sub> are the major products of ESR. At low temperature (543 K), ethanol conversion is higher on oxidized catalysts as ethanol was consumed additionally through oxidation apart from steam reforming or decomposition. Co is distinctly more selective to C<sub>2</sub>H<sub>4</sub>O and CO production, while production of CH<sub>4</sub> is more pronounced on Ni containing catalyst. Though cobalt surface fraction is above 50% on both pre-reduced and pre-oxidized Ni-Co powder, its influence to the product selectivity of bimetallic catalysts seems rather limited. One possible reason is that the availability of hydroxyl groups on Ni containing catalyst is higher and can promote reforming reaction more efficiently. Thus the dominance of ethanol dehydrogenation on cobalt is not observed on bimetallic materials, though the surface is also enriched with cobalt.

At 623 K, selectivity to intermediate products such as C<sub>2</sub>H<sub>4</sub>O and CH<sub>4</sub> is significantly reduced, notably on Ni and Ni-Co. On Ni and Ni-Co, the consumption of water and production of H<sub>2</sub> and CO<sub>2</sub> increase, indicating the increasing importance of reforming reaction to overall ethanol conversion against other reaction pathways with increase in temperature. The reforming or decomposition of methane and acetaldehyde is also likely to take place and contributes to the production of hydrogen. XPS results reveal that there is a substantial

increase in the level of graphitic carbon built up when temperature increases from 534 to 623 K. The carbon level is the highest on Co. This could be related to the high amount of CO produced on Co, which leads to high amount of carbon formation via Boudouard reaction.

## **7.2 Perspectives**

This work has illustrated the influence of bimetallic interaction of a catalyst to its activities under ethanol steam reforming condition. Results from TDS has demonstrated the difference in ethanol decomposition pathway on Ni and Co. Ni is more active in C-C bond scission, yielding higher methane desorption and Co is more selective to dehydrogenation. However, the oxametallacycle intermediate involved for the decomposition of ethoxy group on Co is difficult to be verified by XPS and TDS. Other spectroscopic techniques such as infrared spectroscopy may help in confirming the presence of oxametallacycle adsorbate. This will also facilitate the determination the quantity of adsorbates that are specific to the constituent metal in the bimetallic film and thus will facilitate the quatification of product yield or catalyst active surface sites.

There are also a few interesting aspects of ZnO substrate for further investigation. The oxidizing and chemical effect brought by metal-support interaction on Ni-Co layer has been discussed in this work. The decrease in surface coverage of Ni-Co on ZnO under high temperature has been clearly shown by XPS, but the mechanism in which this change takes place cannot be easily clarified by the XPS alone. Other possible mechanisms include agglomeration, strong metal-support interaction, or formation of mixed oxide by the displacement of  $Zn^{2+}$  by  $Co^{2+}$ . The exchange of  $Zn^{2+}$  and  $Co^{2+}$  has been observed from our preliminary experiments on Ni-Co/ZnO-Zn under ambient pressure reaction conditions. The  $Co^{2+}$  formed by the substitution of  $Zn^{2+}$  is in different coordination compared to  $Co^{2+}$  in common rocksalt CoO, and may lead to different catalytic activities. It would be interesting to clarify the mechanism of the decrease in surface coverage of Ni-Co. X-ray absorption spectroscopy would be a helpful technique in distinguishing  $Co^{2+}$  coordination in the catalyst.

From the results of TDS, ZnO as catalyst support can facilitate the oxidation of surface carbon species formed during the reaction. The role of lattice O in ZnO and its utilization plays a key role to carbon formation in this TDS study. The mobility of O from ZnO has also led to the high level of oxidation of Ni-Co film. One possible way to compare the availability of lattice O from metal oxide is to change the ZnO support to other metal oxide, such as  $TiO_2$  [8] or  $Al_2O_3$  [9] which are very stable metal oxide with strong bonding to lattice oxygen, or even inert metal substrate such as Au, to establish the correlation between O availability and surface carbon oxidation.

To broaden the scope of study in metal-support interaction, the model catalyst support could be extended to well-ordered nanostructure supports such as ZnO nanowire array [10, 11]. This will improve the current understanding of the influence of substrate morphology on

catalyst properties. Also this allows the narrowing of the "material gap" in catalytic studies. Hence results from research can approach better to a real catalyst system.

### **7.3 References**

- [1] J. Zhang, H. Wang, A.K. Dalai, *Applied Catalysis A: General*. 339 (2008) 121-129.
- [2] V. Palma, F. Castaldo, P. Ciambelli, G. Iaquaniello, *Chemical Engineering Transactions*. 29 (2012) 109-114.
- [3] Q. Shi, B. Li, W. Chen, C. Liu, B. Huang, 2012, pp. 314-319.
- [4] N. Homs, J. Llorca, P.R. de la Piscina, *Catalysis Today*. 116 (2006) 361-366.
- [5] J. Kugai, S. Velu, C. Song, *Catalysis Letters*. 101 (2005) 255-264.
- [6] H.S. Roh, A. Platon, Y. Wang, D.L. King, *Catalysis Letters*. 110 (2006) 1-6.
- [7] H. Wang, Y. Liu, L. Wang, Y.N. Qin, *Chemical Engineering Journal*. 145 (2008) 25-31.
- [8] R.P. Galhenage, H. Yan, S.A. Tenney, N. Park, G. Henkelman, P. Albrecht, D.R. Mullins, D.A. Chen, *The Journal of Physical Chemistry C*. 117 (2013) 7191-7201.
- [9] O. Yabuhara, M. Ohtake, Y. Nukaga, M. Futamoto, *Journal of Physics: Conference Series*. 266 (2011).
- [10] X. Yang, A. Wolcott, G. Wang, A. Sobo, R.C. Fitzmorris, F. Qian, J.Z. Zhang, Y. Li, *Nano Letters*. 9 (2009) 2331-2336.
- [11] K. Geunjae, Y. Kijung, *Journal of Physical Chemistry C*. 112 (2008) 3036-3041.



## I. Appendices

### a. Supplementary information to Chapter 3

#### Bulk XRD Structure of Ni, Co and Ni-Co

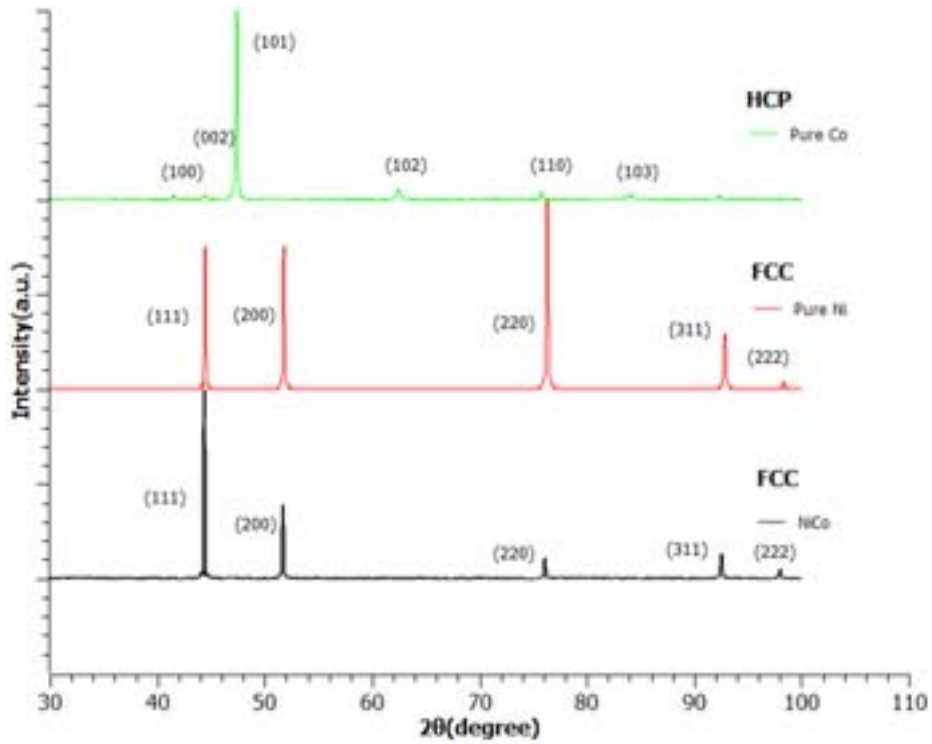


Figure 1.1 XRD patterns of Pure Ni, Pure Co and NiCo alloy foil after annealing at 720K in 0.5bar O<sub>2</sub>.

Co  $2p_{3/2}$  XPS Spectra of Co and Ni-Co annealed in 0.5 mbar O<sub>2</sub>

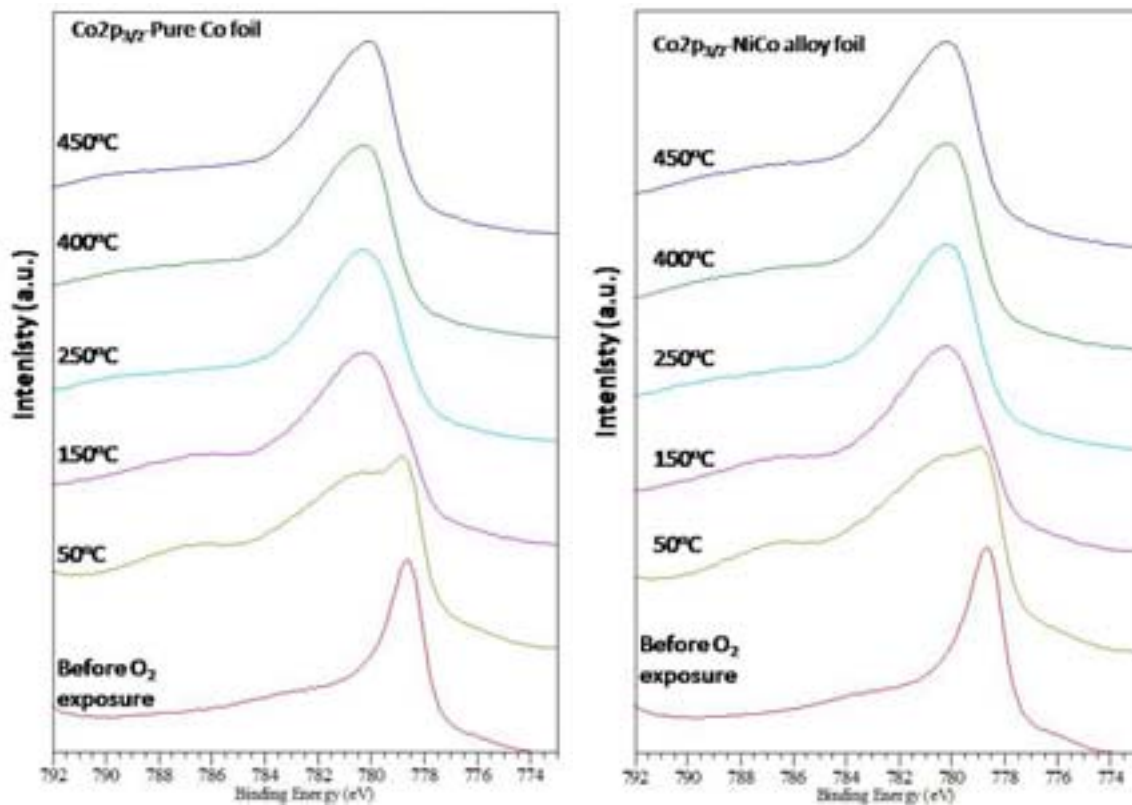


Figure 1.2 (Left) Normalised XPS spectra of  $Co2p_{3/2}$  for Co metal foil exposed to O<sub>2</sub> at 0.5 bar (Right) Normalised XPS spectra of  $Co2p_{3/2}$  for NiCo alloy foil exposed to O<sub>2</sub> at 0.5 bar. The time of O<sub>2</sub> exposure is 5 minutes for temperature 50°C, 150°C, 250°C, 400°C and 450°C

Spectra of Co 2p<sub>3/2</sub> after subtraction of Co metal reference spectra

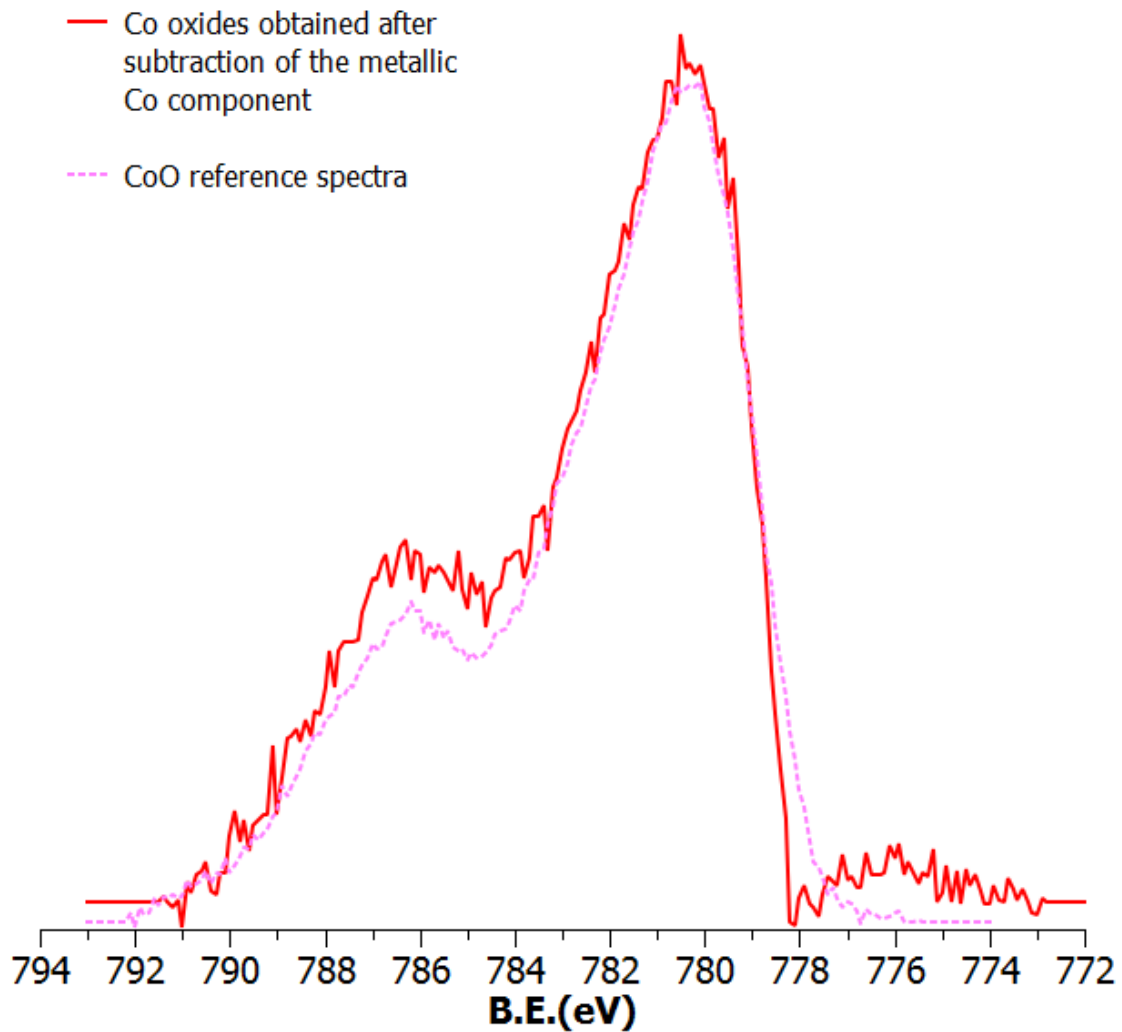


Figure I.3 Fitting of CoO reference spectrum to the Co oxides component obtained from spectrum of Co2p<sub>3/2</sub> for NiCo alloy foil exposed to O<sub>2</sub> at 5x10<sup>-7</sup> mbar at 670 K for 30min. The resultant CoO spectra obtained by subtraction is highly coherent to the reference spectra of CoO

b. Supplementary information to Chapter 4

LEED pattern on clean ZnO (0001)-Zn and ZnO (000 $\bar{1}$ )-O

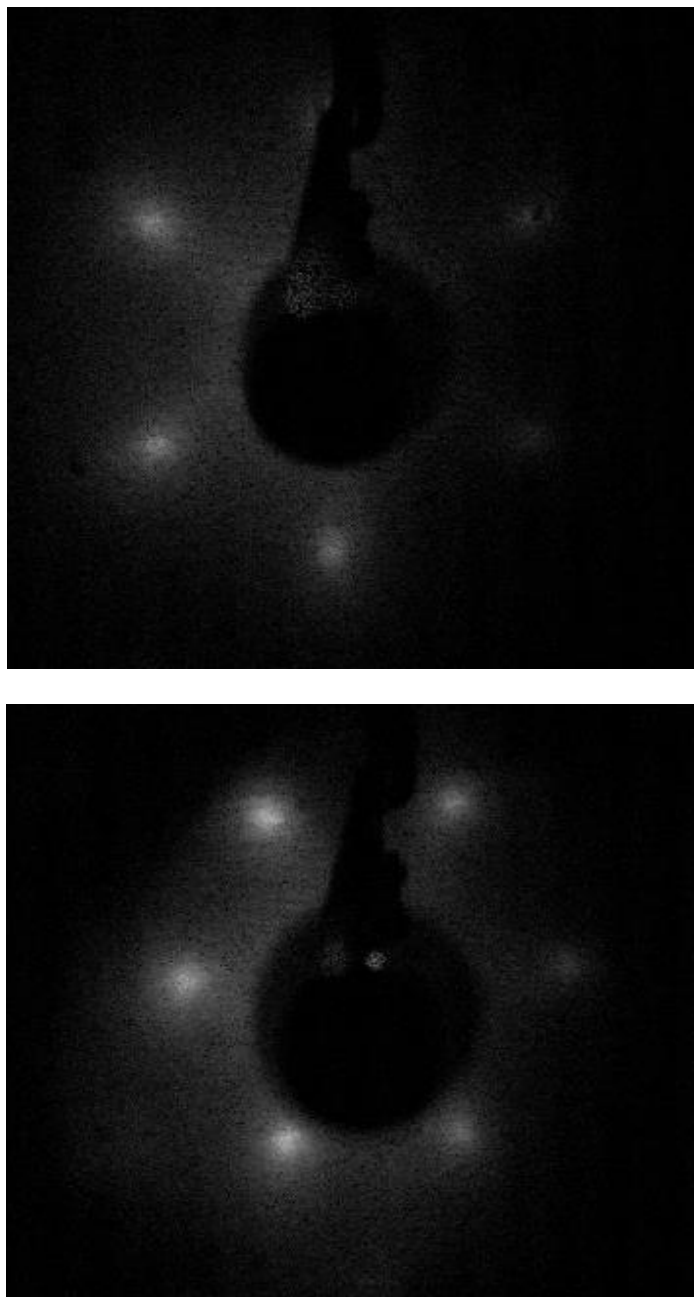


Figure I.4 LEED pattern of (up) ZnO -Zn (0001) and (down) ZnO-O (000 $\bar{1}$ ) obtained after successive cycles of Ar<sup>+</sup> sputtering and annealing in 1x10<sup>-6</sup>mbar O<sub>2</sub>

O 1s spectra measured at different photon energy

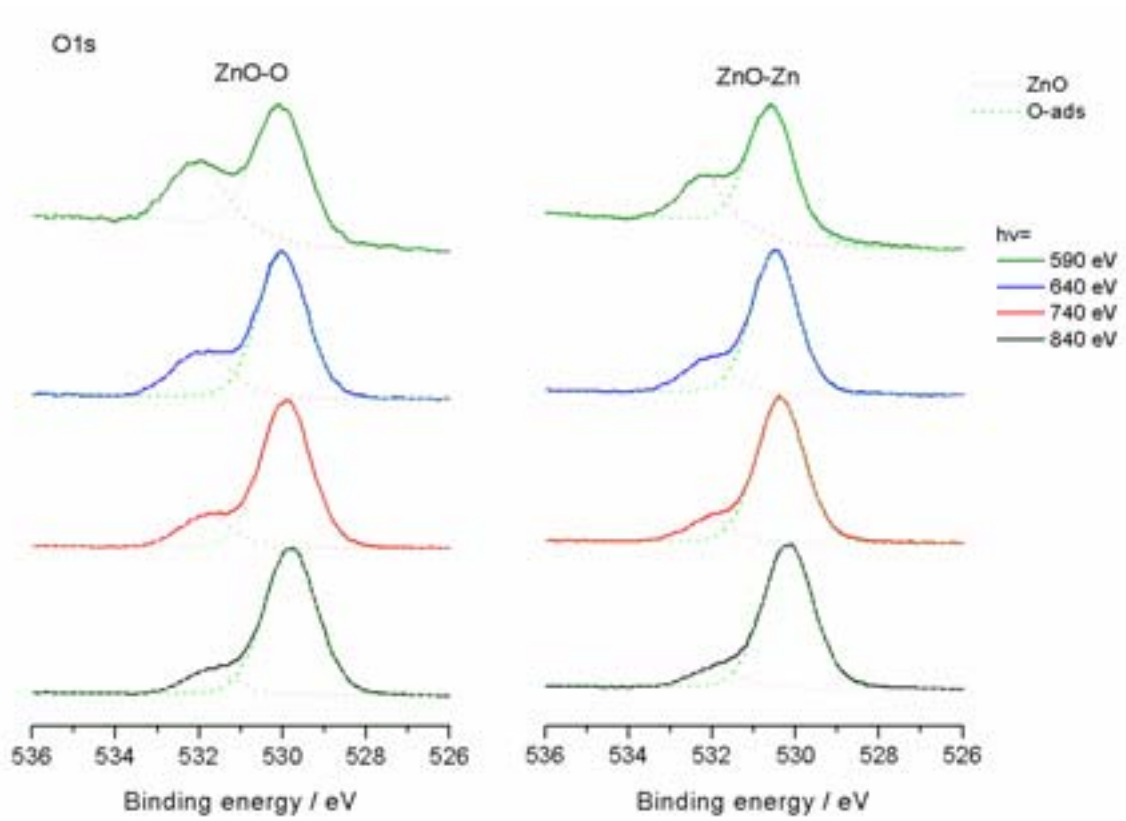
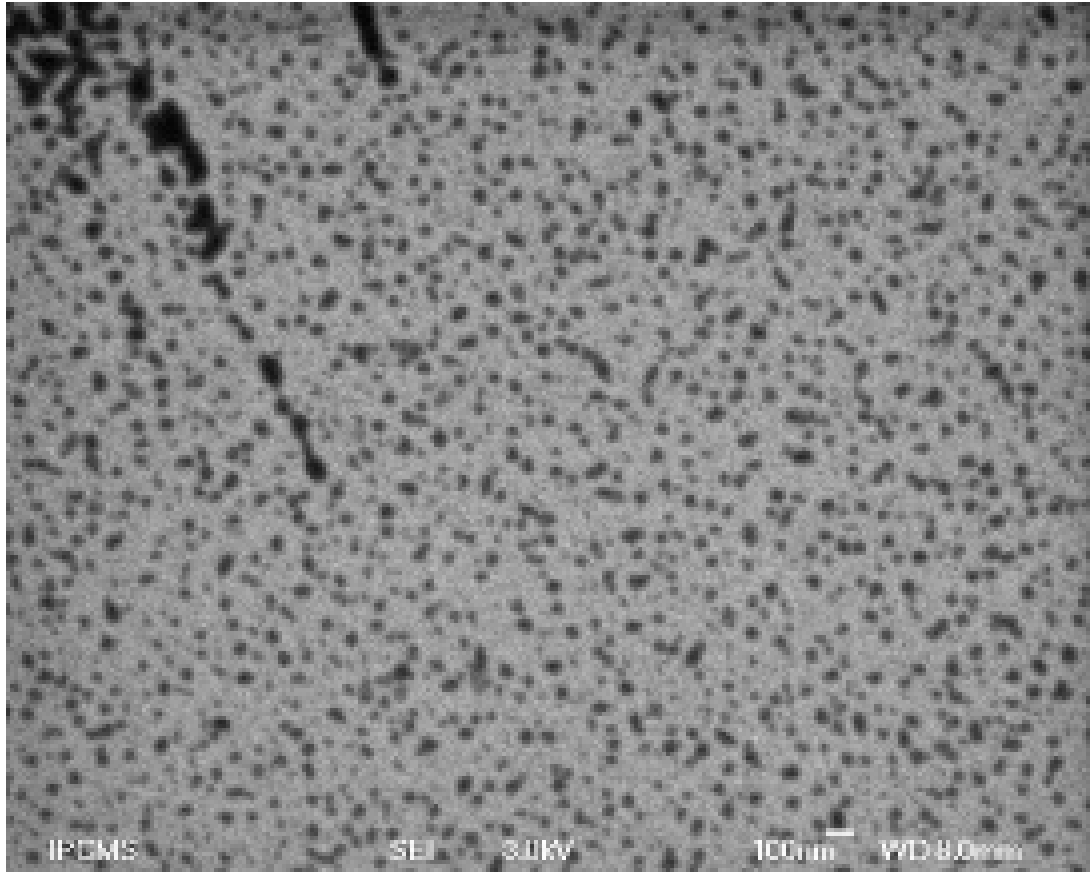


Figure I.5 O1s spectra of clean (right) ZnO –Zn (0001) and (left) ZnO-O (000 $\bar{1}$ ) measured with energy 590 eV-840 eV

**SEM of NiCo overlayer after annealing in O<sub>2</sub>**

The morphology of 1.5 nm Ni-Co overlayer after annealing in O<sub>2</sub> were investigated by SEM. Figure I.6 shows the overall morphology indicating clearly the formation of relatively uniform islands about 30 nm in size over the substrate. The islands formed after oxidation are relatively stable and does not undergo much changes in surface coverage upon the second annealing cycle (data not shown).



*Figure I.6 SEM image of 1.5 nm NiCo/ZnO-Zn (0001) after annealing at 773 K in  $1 \times 10^{-6}$  mbar O<sub>2</sub>*

### Co $2p_{3/2}$ and Ni $2p_{3/2}$ core level spectra of 1.5nm Ni-Co layer deposited on ZnO-Zn and ZnO-O Annealing

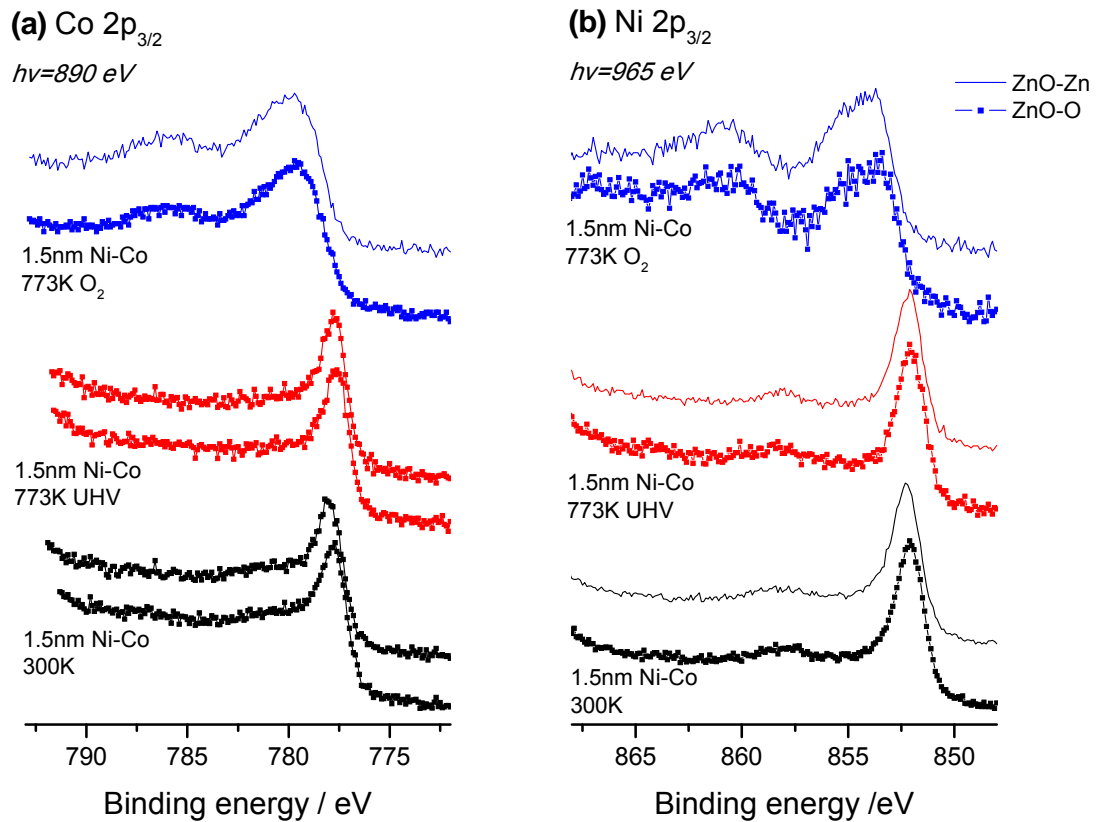


Figure I.7 Co $2p_{3/2}$  **(a)** and Ni  $2p_{3/2}$  **(b)** spectra of 1.5 nm Ni-Co layer on ZnO-Zn(—) and ZnO-O(- -) substrates as deposited (bottom), annealed at 773 K in UHV (middle) and after  $1 \times 10^{-6}$  mbar  $O_2$  at 773 K (top).

Little difference has been observed between the Ni-Co layer deposited on the two types of substrates. The oxidation effect induced by annealing in UHV is much less prominent for deposited layer of this thickness, showing that this oxidation is limited to the interfacial region. Subsequent annealing in  $O_2$  transformed the metallic layer into NiO-CoO.

### Calculation for Ni-Co layer thickness and OH group coverage on ZnO

The thickness of the as deposited NiCo layer is estimated by the attenuation of Zn 3d substrate signal and calculated based on the following formula:

$$I_{Zn} = I_{Zn}^{\infty} \exp[-d_{NiCo} / \lambda_{NiCo} \cos\theta]$$

where  $d_{NiCo}$  is the thickness of the NiCo metal overlayer,  $I_{Zn}^{\infty}$  is the atomic sensitivity factor of Zn 3d line,  $\lambda_{NiCo}$  is the inelastic mean free path of characteristic Zn 3d photoelectrons in the NiCo overlayer and  $\vartheta$  is the emission angle from the surface normal. From TPP2M formula[1]  $\lambda_{Ni} (110 \text{ eV}) = 0.421 \text{ nm} \approx \lambda_{Co} (110 \text{ eV}) = 0.430 \text{ nm}$  and therefore  $\lambda_{NiCo} = 0.425 \text{ nm}$  was used.

The corresponding metal atomic ratio was calculated by on the intensity ratio of the 2 components:

$$X_M = \frac{\frac{I_M}{I_M^{\infty}}}{\sum_M \frac{I_M}{I_M^{\infty}}}$$

The OH groups thickness is estimated based on

$$-d_{OH} = -\lambda_{ZnO} \cos\theta \ln(I_{OH} / I_{Oxide} + 1)$$

$$-\Phi_{OH} = (I_{OH} / I_{Oxide} + 1) \times (1 / (1 - \exp(-a_{OH} / \lambda_{ZnO})))$$

where  $\varphi$  is the coverage of OH groups and  $a$  is OH group monolayer thickness.

c. Supplementary information to Chapter 6

Ni  $2p_{3/2}$  and Co  $2p_{3/2}$  spectra of Ni, Co and Ni-Co nanopowder during reduction in 0.2 mbar  $H_2$  with temperature ramp 20 K/min

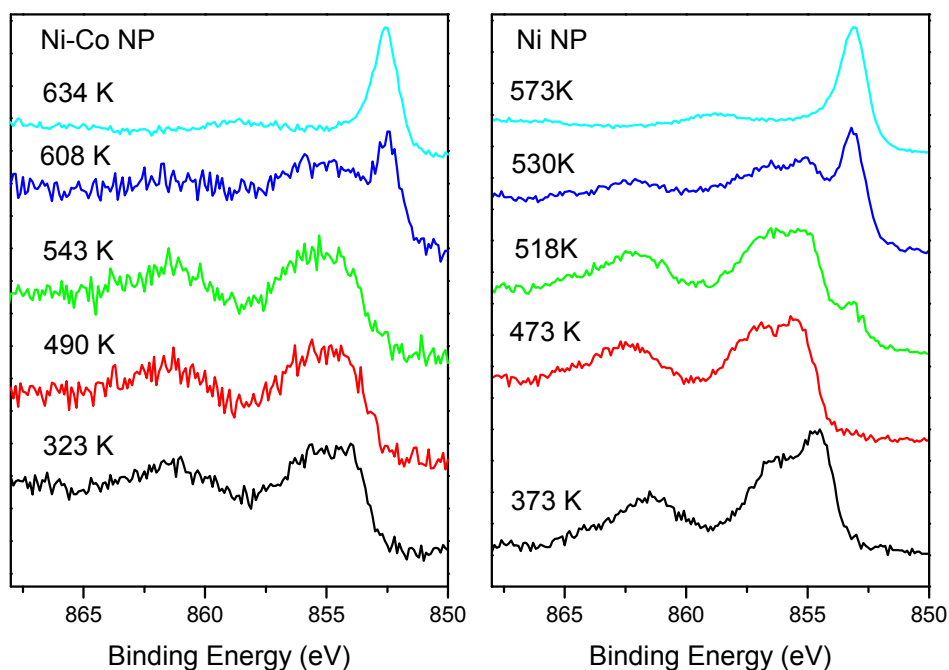


Figure I.8 Ni  $2p_{3/2}$  spectra of Ni-Co nano-powders and Ni nanopowders reduced in 0.2mbar  $H_2$

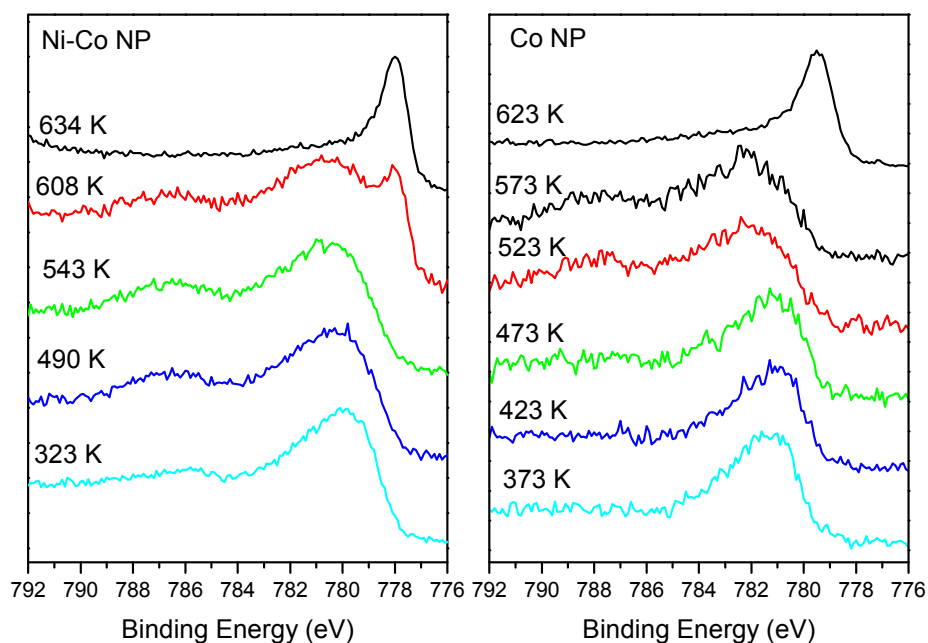


Figure I.9 Co  $2p_{3/2}$  spectra of Ni-Co nano-powders and Co nanopowders reduced in 0.2mbar  $H_2$

**d. References**

- [1] S. Tanuma, C.J. Powell, D.R. Penn, *Surface and Interface Analysis*. 20 (1993) 77-89.

## **II. List of Publications**

### **a. Published articles**

1. Bimetallic Nickel-Cobalt Nanosized Layers Supported on Polar ZnO Surfaces: Metal-Support Interaction and Alloy Effects Studied by Synchrotron Radiation X-ray Photoelectron Spectroscopy. Law, Y. T.; Skala, T.; Pis, I.; Nehasil, V.; Vondracek, M.; Zafeiratos, S., Journal of Physical Chemistry C 2012, 116, 10048-10056.
2. Surface oxidation of NiCo alloy: A comparative X-ray photoelectron spectroscopy study in a wide pressure range. Law, Y. T.; Dintzer, T.; Zafeiratos, S., Applied Surface Science 2011, 258, 1480-1487.

### **b. Article under preparation**

1. Insight for ethanol steam reforming reaction pathway and intermediates: Ethanol desorption on ZnO supported Ni-Co bimetallic model catalyst, Law, Y. T.; Doh, W.H.; Luo, W., Zafeiratos, S.

### **c. Oral presentation**

1. Ambient Pressure Photoemission Spectroscopy (APPEs) and Near-Edge X-ray Absorption Spectroscopy (NEXAFS) study of ZnO supported Ni-Co bimetallic model catalyst (Oral presentation), Y.T. Law, S. Zafeiratos, M. Hävecker, A. Knop-Gericke, 29th ECOSS, Edinburg, September 2012.

### **d. Poster presentation**

1. *In-situ* study of metal-support interaction of bimetallic catalyst: Ni-Co/ZnO-Zn(0001) at ambient pressure (Poster), Y.T. Law, T. Skala, L. Gregoratti, M. Amati, Vondracek, M. Hävecker, A. Knop-Gericke, S. Zafeiratos, Symposium "Progress in the kinetics and mechanisms of chemical reactions at the atomic and molecular levels", Strasbourg, March, 2013.
2. Bimetallic Ni-Co supported on ZnO single crystal: Metal-support interaction studied in UHV and ambient pressure conditions (Poster), Y.T. Law, T. Skala, L. Gregoratti, M. Amati, Vondracek, M. Hävecker, A. Knop-Gericke, S. Zafeiratos, 15th International Congress on Catalysis, Munich, July 2012.
3. Bimetallic Ni-Co alloy overlayers supported on ZnO: Influence of the ZnO surface termination to the metal-support interaction (Poster). Y.T. Law, T. Skala, M. Vondracek, F. Garin, S. Zafeiratos. 6th European Conference Paul Sabatier on Catalysis, Strasbourg/ France, September 2011

## ***II. List of publications***

# Investigation of Reaction Networks and Active Sites in Ethanol Steam Reforming Reaction over Ni and Co-Based Catalysts

## Résumé

Les catalyseurs bimétalliques sont reconnus pour promouvoir les performances de nombreuses réactions catalytiques. Les connaissances des propriétés de surface ; notamment l'interaction entre les couches bimétalliques et le support, composants catalytiques, servent à améliorer le design des catalyseurs. Dans cette thèse, le dépôt de couches minces Ni-Co sur un monocristal ZnO a été étudié en tant que catalyseur modèle pour le vapo-réformage de l'éthanol. L'objectif du travail est d'élargir les connaissances fondamentales de l'influence des propriétés de surface (i) sur le mécanisme et (ii) sur l'efficacité de la réaction. Dans un premier temps, l'interaction entre les atomes Ni et Co sous atmosphère oxydante par **spectrométrie** de photoélectrons de rayons X (XPS) a été étudiée. L'oxydation du Co est favorisée ; la surface est enrichie par CoO sur Ni. Ensuite, les couches minces de Ni-Co sur monocristal polaire ZnO, possédant deux terminaisons -O et -Zn, ont été étudiées par XPS couplé à un synchrotron. L'interaction métal-support a mis en évidence que Co est oxydé dès que celui-ci est déposé à température ambiante. L'interaction entre la molécule d'éthanol et le catalyseur Ni-Co/ZnO-Zn a été étudiée par spectrométrie de masse de thermodesorption (TDS). L'éthanol se décompose par différentes voies sur Ni/ZnO-Zn et Co/ZnO-Zn. Ni/ZnO-Zn favorise la rupture de la liaison C-C et permet la production de méthane, tandis que Co/ZnO-Zn favorise la déshydrogénation du méthyle. Enfin, nous avons étudié le vapo-réformage de l'éthanol sur les nanopoudres de Ni-Co *in-situ* par XPS à pression ambiante. La sélectivité en produits sur Co est très différente de celle du Ni et Ni-Co. De plus, la déshydrogénation du méthyle et la production de CO peut entraîner la formation d'une grande quantité de carbone sur Co

Mots-clés: Nickel, Cobalt, ZnO, Vapo-réformage de l'éthanol, couches bimétalliques, interaction métal-support.

## Résumé en anglais

Bimetallic catalysts have been widely exploited to improve the performance of various catalytic reactions. Understanding the surface properties and in particular, bimetallic interaction and support effect of the catalytic components is an important step towards rational catalyst design. In this thesis, Ni-Co thin film on polar ZnO single crystal was studied as a model catalyst for ethanol steam reforming reaction. The aim is to provide fundamental understanding of how the surface characteristics of the catalyst influence the mechanism and the efficiency of the reaction. This study focused firstly on the study of the interaction between Ni and Co in oxidative environment using X-ray photoelectron spectroscopy (PES). Oxidation of Co is favoured over nickel and the surface is enriched with cobalt oxide. Secondly, Ni-Co thin film supported on polar Zn and O terminated ZnO was studied by synchrotron based PES. The as deposited layer interacts readily with ZnO and Co is partially oxidized upon deposition, even at room temperature. The interaction of ethanol with Ni-Co/ZnO-Zn was studied by thermal desorption spectroscopy (TDS). Ethanol decomposes in different pathways on Ni and Co, in which C-C bond scission and methane production are favoured on Ni/ZnO-Zn while dehydrogenation is favoured on Co/ZnO-Zn. Finally, Ni-Co powder was studied by *in-situ* ambient pressure PES under reaction conditions in order to clarify the correspondence between the active state of the catalyst and the reaction activity. The product selectivity on Co catalyst is distinctly different from Ni and Ni-Co. Also, the decomposition of methyl group and the high amount of CO produced over Co is likely to be the cause for its high level of carbon deposition. Keywords: Nickel, Cobalt, ZnO, Ethanol steam reforming, bimetallic overlayer, metal-support interaction

